Energy Dependence of the Mean Charged Multiplicity in Deep Inelastic Scattering with ZEUS at HERA

by

Michele L. Rosin

A dissertation submitted in partial fulfillment of the
requirements for the degree of

Doctor of Philosophy

(Physics)

at the

University of Wisconsin – Madison

2006

Abstract

The hadronic final state has been investigated in inclusive neutral current deep inelastic ep scattering with the ZEUS detector at HERA, using an integrated luminosity of 38.6 pb^{-1}. The mean charged multiplicity has been measured for the hadrons belonging to the current region of the Breit frame, as well as for those belonging to the photon fragmentation region of the hadronic center of mass frame. The results are compared to leading-logarithm parton-shower Monte Carlo predictions as well as to results of e^+e^-, pp and previous deep inelastic scattering measurements.

ii

Contents

iv

List of Tables

x

List of Figures

Chapter 1

Theoretical Introduction

1.1 The Standard Model

The elementary particles which make up matter are fermions, and are either quarks (which form protons and neutrons) or leptons (such as electrons). There are six quarks (up, down, charm, strange, bottom and top) and six leptons (electron, muon, tau, electron neutrino, muon neutrino, and tau neutrino). For each particle there exists an anti-particle with the same mass but opposite quantum numbers[1]. The quarks and leptons are grouped into three generations or families, with each generation consisting of two particles. The quarks and the massive leptons are electrically charged. Electrical charge comes in one of two types referred to as positive and negative. The quarks exist in three different color "charges", red, blue and green. The term "color" can be misleading as it refers not to colors of visible light but is used as an analogy to color mixing. The quark's color is similar to the electric charge, but where the electric charge has two manifestations (positive and negative), the color "charge" has

---

[1]A quantum number is any one of a set of numbers used to specify the full quantum state of any system in quantum mechanics.

six (red, anti-red, green, anti-green, blue and anti-blue). In a similar way that the combination of a positive and negative electrical charge gives an electrically neutral result, the mixing of a color and its anti-color gives a colorless (uncharged) result. A combination of all three colors (or anti-colors) is also colorless. These properties of the fermions are summarized in table 1.1.

The forces that act on these fundamental particles are the electromagnetic force, the weak force, the strong force and gravity. The strength of these interactions is determined by a coupling constant (denoted by α_{EM} for the electromagnetic force and α_s for the strong force). In quantum field theory, these forces are mediated by bosons. The electromagnetic force is mediated between electrically charged particles by the massless photon. The weak interaction is mediated by the massive Z^0 and $W^\pm$ bosons (the superscripts representing the fact that the W bosons carry electrical charge and the Z boson is electrically neutral, as is the photon). The strong force binds the quarks together to form colorless hadrons. It is mediated between colored particles by bosons called gluons, of which there are 8 types. The gluons do not have mass or electrical charge, but they do carry color. This means that the gluons interact with other gluons, which in turn causes the force to strengthen with increasing distances resulting in the fact that colored objects are only observable as free particles at the microscopic scale. Gravity is the force that acts between particles with mass. At the macroscopic scale it has been successfully described by the general theory of relativity. There are quantum field theories of gravity, which predict that the gravitational field is mediated by a boson called the graviton, but such a particle has not been observed. Gravity is the weakest of the four forces and can be neglected in the high energy

Quarks			
Flavor	**Mass (GeV/c^2)**	**Charge (Q/e)**	**Color**
u	0.003	+2/3	yes
d	0.006	-1/3	yes
c	1.3	+2/3	yes
s	0.1	-1/3	yes
t	175	+2/3	yes
b	4.3	-1/3	yes
Leptons			
Flavor	**Mass (GeV/c^2)**	**Charge (Q/e)**	**Color**
ν_e	$< 1 \times 10^{-8}$	0	no
e	5.11×10^{-3}	-1	no
ν_μ	< 0.0002	0	no
μ	0.106	-1	no
ν_τ	< 0.02	0	no
τ	1.7771	-1	no

Table 1.1: Properties of the basic fermions of the standard model. The masses are from experimental data, while all the other quantities are predicted by the standard model.

regime of particle physics. The properties of the fundamental forces and the bosons that mediate them are summarized in table 1.1.

The unified description of electromagnetism described by Quantum Electrodynamics (QED) and the weak force is called electro-weak theory. The theory describing the strong force is called Quantum Chromodynamics (QCD). The QCD and electro-weak theory are gauge theories that can be derived from symmetry principles. For QCD, the basic symmetry is $SU(3)$ which is connected to the three degrees of freedom given by the three color-charges. The electro-weak theory is based on the $SU(2) \times U(1)$ symmetry. The combined suite of theories comprises the Standard Model.

Boson	Force	Types	Mass (GeV)	Charge (Q/e)	Color
γ (photon)	Electromagnetic	1	0	0	No
$W^\pm$	Weak	2	80.4	± 1	No
Z^0	Weak	1	91.187	0	No
g (gluon)	Strong	8	0	0	Yes

Table 1.2: The bosons which mediate the fundamental forces as predicted by the standard model. The masses are experimentally determined.

1.1.1 Electro-Weak Theory

Quantum Electrodynamics (QED) is the theory that describes electromagnetism. It is mathematically the simplest of the quantum gauge theories. QED is invariant under local U(1) gauge transformations. The predictions of QED can be calculated using perturbation theory since the electromagnetic coupling constant $\alpha_{\mathrm{EM}} \simeq 1/137$ is much smaller then unity. Electrically charged particles can emit and absorb virtual photons which can fluctuate into electron-positron pairs. These charged pairs act as an electric dipole and reposition themselves around the original charge thus partially counteracting or *screening* the field. The consequence of this so-called vacuum polarization is that at larger distances the effective charge is less than at smaller distances. The electromagnetic force grows weaker as charges move farther apart. The electromagnetic and weak interactions were unified into one electro-weak theory by Glashow, Salam and Weinberg [1].

1.1.2 Quantum Chromodynamics (QCD)

The strong interactions are described by Quantum Chromodynamics (QCD). Unlike the electromagnetic force, the strong force has the unusual property that it becomes stronger at larger distances. As colored objects move apart, they are more and

more strongly held together. Therefore the strong coupling constant, α_s, gets stronger as the distance increases, and it this "running" of α_s that explains why quarks are permanently confined within hadrons (color confinement), yet behave as free particles when probed at high energies in scattering experiments. This phenomenon results from a similar effect as the QED screening of charge by virtual electron-positron pairs. In QCD, the same thing happens with virtual quark anti-quark pairs; they tend to screen the color charge. However, because the mediators of the strong force, the gluons themselves, carry color charge, the effects are different. Each gluon carries both a color charge and an anti-color charge. The net effect of polarization of virtual gluons in the vacuum is not to screen the field, but to augment it and affect its color. This is sometimes called *anti-screening*. Getting closer to a quark diminishes the anti-screening effect of the surrounding virtual gluons, so the contribution of this effect would be to weaken the effective charge with decreasing distance. Since the virtual quarks and the virtual gluons contribute opposite effects, which effect wins out depends on the number of different kinds, or flavors, of quarks. For standard model QCD with three colors, and 6 quark flavors, anti-screening prevails and the theory is asymptotically free. This asymptotic freedom was discovered by David Gross, Frank Wilczek, and David Politzer in 1973. For their discovery, Gross, Wilczek and Politzer were awarded the Nobel Prize in Physics in 2004. Asymptotic freedom implies that in high-energy scattering the quarks move within nucleons essentially as free, non-interacting particles.

1.1.3 Limits of the Standard Model

A great deal of experimental evidence has demonstrated the overwhelming success of the standard model. It has yet to be contradicted by any theory which can be confirmed by data. Fundamental tests of the predictions of the standard model have been carried out and its free parameters have been precisely measured. In spite of these successes, the model is incomplete, and there are some experimental results that hint at possible disagreement. Some of the predominant shortfalls of the model follow.

- The masses of the quarks and leptons are not predicted.

- The existence of exactly three families of quarks and leptons can not be explained.

- A quantum level description of gravity is not included nor is any reason for the comparative weakness of the gravitational force.

- The existence of an additional particle, called the Higgs, is required by the model for the generation of the particle masses. This particle has not yet been observed experimentally, but its existence can not be excluded.

- The neutrinos are assumed to be massless, but recent observations of neutrino oscillations can only be easily explained if neutrinos have a non-vanishing mass.

- There is no explanation for the unequal distribution between matter and anti-matter in the universe.

1.2 Deep Inelastic Scattering (DIS)

Deep inelastic scattering (DIS) has made important contributions to the field of particle physics, especially in the early period of the development of QCD. The deep inelastic scattering of leptons and hadrons is an ideal environment to study the strong nuclear force. The two particles interact by the exchange of an electro-weak gauge boson, which breaks up the hadron. Highly virtual bosons act as point-like particles which probe the inner structure of the hadron and the forces that bind it together. The first confirmations of QCD came from fixed target DIS experiments which led to an understanding of how the quarks and gluons are distributed inside the proton. DIS remains an important test of not only QCD, but also the phenomenological models that have been devised to make a connection between the natural domain of QCD, the partons, and the experimentally accessible hadrons.

1.2.1 Kinematic Variables

A DIS process involves the scattering of a high energy lepton (l) on a hadron (h), leading to the general reaction

$$l(k) + h(p) \rightarrow l'(k') + X(p') . \tag{1.1}$$

The initial state particles (l, h) are defined by the experiment and the final state particles (l', X) are determined by the processes which have occurred in the collision.

The DIS collisions that have been analyzed and are presented in this thesis were produced at the HERA collider where the initial state particles are electrons (or positrons) and protons. The high energy electron (or positron) is scattered off a constituent in the proton, breaking the proton into a system of out-going particles,
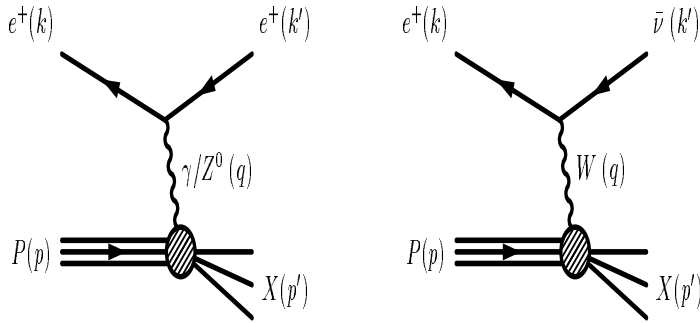
Figure 1.1: Feynman diagrams for the lowest order of electron-proton deep inelastic scattering. In the neutral current process the exchanged boson is a photon (γ) or a Z^0 boson, while in the charged current process a $W^{\pm}$ boson is exchanged.

which observed in the final state as columnated sprays of particles called jets, and a proton remnant, most of which escapes down the beam pipe. The kinematics presented here pertain specifically to deep inelastic ep scattering, with the knowledge that other DIS processes can be described in a very similar way.

When an electron is scattered on a proton two distinct processes can occur. The exchanged boson can be either an electrically charged $W^{\pm}$ (charged current DIS) or an electrically neutral photon, or Z^0 (neutral current DIS). The processes can be distinguished by the final state lepton. In the neutral current process, the final state lepton is the same as the initial one, an electron or positron. In the charged current process, the electric charge of the electron (positron) has been transferred to the exchanged particle and the final state lepton is a(n) (anti-)neutrino. In this thesis only the neutral current processes are considered. The Feynman diagrams for both processes are shown in figure 1.1.

In the figure the four-momenta of the incoming positron and proton are k and

p, which are given explicitly by:

$$k = (E_e, 0, 0, -E_e) \tag{1.2}$$

$$p = (E_p, 0, 0, E_p) \tag{1.3}$$

where E_e and E_p are the electron and proton beam energies respectively. The coordinate system is defined with the incoming protons moving in the positive z direction.

Apart from the center of mass energy squared, $s = (k + p)^2$, which is fixed for any given experimental conditions by the four-momentum of the initial lepton, k, and that of the initial hadron, p, only two independent Lorentz invariant quantities are needed to fully define the kinematics. These are customarily drawn from the set of the following three:

$$Q^2 = -q^2 = -(k - k')^2 \ , \tag{1.4}$$

$$x = \frac{Q^2}{2p \cdot q} \ , \tag{1.5}$$

and

$$y = \frac{p \cdot q}{p \cdot k} \ . \tag{1.6}$$

The virtuality of the exchange boson sets the energy scale of the hard scattering process and is specified by Q^2, the negative square of the momentum transfer. The transverse resolution at which the hadron is probed is inversely proportional to Q. The DIS regime refers to the kinematic region where the photon is highly virtual, i.e. $Q^2 >> m_p^2 \approx 1 \text{ GeV}^2$. If $Q^2 \approx 0$, the process takes place in the photoproduction regime, in which the photon is not virtual, and the collision is between the proton

and a real photon. The photoproduction regime is studied in a slightly different way and not considered in further detail since the analyses described in this thesis are performed in the region where Q^2 is well above 1 GeV^2. Q^2 is bound above by s but the rapid fall off of the DIS cross section with respect to Q^2, (equation 1.17), imposes a more restrictive limit dependent on the statistics of the data.

x is the scaling variable introduced by Bjorken. In an approximation in which a rapidly moving hadron made up of non interacting partons, x is interpreted as the fraction of the proton momentum carried by the struck parton. The approximation is called the Quark Parton Model (QPM) and is introduced section 1.2.3.

Finally, the inelasticity, y, corresponds to the fractional energy transfer from the lepton to the proton in the proton rest frame. Both x and y are dimensionless variables which can vary in the range between 0 to 1.

Q^2, x, and y are related to the center of mass energy (in the approximation of negligible masses of the colliding particles) by:

$$s = (k + p)^2 = 4E_e E_p = \frac{Q^2}{xy} \,, \tag{1.7}$$

In addition to the above variables, the invariant mass squared of the photon-proton ($\gamma^* P$) system,

$$W^2 = (q + p)^2 = sy - Q^2 \,, \tag{1.8}$$

defines the phase space available for particle production in the hadronic center of mass reference frame.

1.2.2 DIS cross section

The general form of the inclusive DIS cross section can be factorized into a leptonic tensor $L_{\mu\nu}$ and a hadronic tensor $W^{\mu\nu}$ (for more details see [2])

$$d\sigma \propto L_{\mu\nu}W^{\mu\nu} . \qquad (1.9)$$

The leptonic tensor, symmetric in μ and ν can be calculated using QED and can be written as:

$$L_{\mu\nu} = \frac{1}{2} \sum_{e\ spins} [\bar{u}(k')\gamma^\mu u(k)] [\bar{u}(k')\gamma^\nu u(k)]^* , \qquad (1.10)$$

where $u(k)$ and $\bar{u}(k')$ are the incoming and outgoing four-momenta of the electron, and the γ^μ and γ^ν are the Dirac matrices. The hadronic tensor, $W^{\mu\nu}$ can be parameterized using a combination of tensors as

$$W^{\mu\nu} = -W_1 g^{\mu\nu} + W_2 \frac{p^\mu p^\nu}{M^2} - iW_3 \frac{\varepsilon^{\mu\nu\lambda\rho}p^\lambda q^{rho}}{M^2} + W_4 \frac{q^\mu q^\nu}{M^2} + W_5 \frac{p^\mu q^\nu + p^\nu q^\mu}{M^2} , \quad (1.11)$$

where p and q are the momenta, M is the mass of the proton and W_i are functions of the two independent scalers q^2 and $p \cdot q$. The antisymmetric terms have been left out because they drop out after insertion into equation 1.9. Conservation of current, given by $\partial_\mu J^\nu = 0$, requires that $q_\mu W^{\mu\nu} = q_\nu W^{\mu\nu} = 0$, which constrains the Lorentz scalers by:

$$W_5 = -\frac{p \cdot q}{q^2} W_2 \ and \ W_4 = \left(\frac{p \cdot q}{q^2}\right)^2 W_2 + \frac{M^2}{q^2} W_1 \qquad (1.12)$$

These are more commonly defined in terms of the structure functions:

$$F_1(x, Q^2) = M \cdot W_1(x, Q^2) \qquad (1.13)$$

$$F_2(x, Q^2) = \frac{Q^2}{2Mx} \cdot W_2(x, Q^2) \qquad (1.14)$$

$$F_3(x, Q^2) = \frac{Q^2}{2Mx} \cdot W_3(x, Q^2) . \tag{1.15}$$

The inclusive differential cross section for inelastic electron-proton scattering can be written as:

$$\frac{d\sigma}{dE'_e d\Omega} = \frac{\alpha^2}{q^4} \frac{E'_e}{E_e} L_{\mu\nu} W^{\mu\nu} , \tag{1.16}$$

where E_e and E'_e are the incoming and outgoing electron energies. Inserting the tensor terms calculated above yields the neutral current ep cross section:

$$\frac{d^2\sigma}{dxdQ^2} = \frac{4\pi\alpha^2}{xQ^4} \left[y^2 x F_1(x, Q^2) + (1 - y)F_2(x, Q^2) \mp y(1 - \frac{y}{2})x F_3(x, Q^2) \right] \tag{1.17}$$

$$= \frac{4\pi\alpha^2}{xQ^4} \left[Y_+ F_1(x, Q^2) - y^2 F_L(x, Q^2) \mp Y_- F_3(x, Q^2) \right] , \tag{1.18}$$

with $F_L = F_2 - 2xF_1$ and $Y_\pm = 1 \pm (1 - y)^2$.

In this form the different contributions to the cross section can be associated with the different functions. F_2 derives from the transversely polarized photon, and is the main contribution to the cross section. F_3 is the parity violating contribution which comes from the Z^0 exchange and is small for $Q^2 \ll M_Z^2$. F_L derives from the absorption of a longitudinally polarized photon and equals 0 in the QPM model, which is described in the next section.

1.2.3   Quark Parton Model

In the late 1960's the first evidence that the nucleon is composed of point-like constituents began to be uncovered from DIS experiments at SLAC [3, 4]. At that time there were two models proposed for describing the structure of the hadrons. The quark-constituent model proposed by Gell-Mann and Zweig [5] relied upon a classification of the observed hadrons to deduce that they are made up of two (mesons)

or three (baryons) quarks [6]. Another model, called the parton model, proposed by Feynman [7], assumed that the proton is made up of quasi-free point-like constituents called partons, and in the scattering process only one of the partons participates while the others do not take part in the interaction (spectator particles).

If the DIS interaction involves free partons, as Feynman's parton model predicts, the total cross section can be written as the sum of the cross sections for elastic scattering off the individual partons. Since the quarks are assumed to be non-interacting static particles confined within the proton, the structure functions are expected to be a function of x but not Q^2 because changes in Q^2 correspond to changes in the scale probed by the exchanged boson, which would be irrelevant for point-like constituents, i.e. $F_i(x, Q^2) = F_i(x)$. This behavior, known as scale invariance, was originally proposed by Bjorken [8], and observed in early fixed target DIS experiments [9].

As experimental evidence pointed to the existence of point-like particles forming the structure of the hadrons, the quarks and partons were associated with each other and the Quark Parton Model (QPM) was formulated. The QPM states that the hard interaction can be expressed as the sum of independent scatterings from non-interacting point-like constituents, which behave as if they were free inside the hadron during the interaction. The QPM explanation of the DIS data as scattering on quasi-elastic partons is done in the frame of a fast moving hadron. Here the scattering occurs over a short time scale of the order $1/Q$ and, due to relativistic time dilation, the photon sees a frozen state of non-interacting quarks. The final hadronization process, which is a direct consequence of the color confinement property of QCD, occurs only much later. In this frame the physical content of the structure function F_2

is in its relation to the probability density, $f_q(x)$, for a quark to carry a longitudinal fractional momentum x:

$$\frac{F_2}{x} = x \sum_q e_q^2 f_q(x) \,, \tag{1.19}$$

where e_q is the charge of parton q and $f_q(x)dx$ is the probability of finding a parton of type q in the momentum range between x and $x + dx$.

Furthermore, the Callan-Gross relation between the two scaling structure functions,

$$2xF_1(x) = F_2(x) \Rightarrow F_L = 0 \,, \tag{1.20}$$

which followed from the fermionic nature (spin $1/2$) of the quarks as postulated by Gell-Mann and Zweig in the quark-constituent model, was also in fact confirmed to hold [4]. The quark-constituent model also predicted that the quarks carry a fractional electrical charge, and this was also positively verified using fixed DIS experiments which looked at the ratio between the respective structure functions measured in νN and eN collisions [4].

The QPM, as described above, was successful in kinematic regions where the effects of the nuclear forces could be ignored. But experiments [10, 4] showed that

$$\sum_q \int_0^1 x f_q(x)dx \approx 0.5 \,, \tag{1.21}$$

indicating that the quarks carry only about half of the momentum of a nucleon [11]. This implies that the hadrons contain a significant admixture of matter transparent to the DIS probes. In order to explain the remainder, the QPM needed to be modified to include the effects of the nucleon binding forces.

The formulation of the quantum field theory of the nucleon binding forces began with the introduction of a new degree of freedom, color, for the quarks, along with
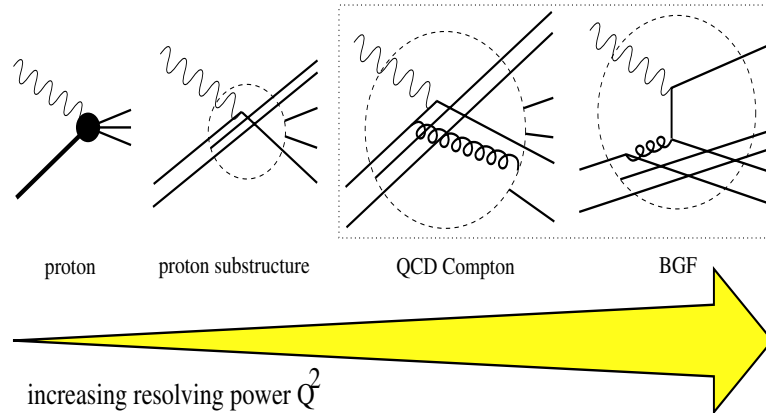
Figure 1.2: Illustration of scaling violation. Higher order processes such as gluon radiation (QCD Compton) or quark anti-auark splitting (Boson Gluon Fusion) can be resolved with increasing Q^2.

a new boson to mediate the strong force. The color degree of freedom had been originally postulated as a solution to the apparent violation of the Pauli exclusion principle in the baryon decouplet. A gauge theory of three colored quarks which interact via the exchange of spin-one bosons called gluons was gradually developed and called Quantum Chromodynamics (QCD).

Direct experimental evidence for the existence of gluons was found in 1979 at DESY via the observation of three-jet events in e^+e^- annihilation [12]. QCD also predicted that the scaling behavior exhibited by the structure functions is only approximate as a log dependence on Q^2. Quarks can radiate gluons, which in turn can split into $q\bar{q}$ pairs. These are referred to as the "sea quarks". The number of partons increases while the average momentum per parton decreases. When probed at a scale Q, all sea quark flavors with mass $m_q \leq Q$ are active. How much of the sea structure can be resolved depends on the photon virtuality; as Q^2 increases, more and more of these fluctuations can be resolved. This is illustrated in figure 1.2. At high x, the

cross section is sensitive mainly to the valence quarks. The energy and momentum of the valence quarks will fall with increasing Q^2 due to gluon radiation, resulting in scaling violation and a decrease in cross sections. As the valence quarks carry a higher momentum fraction than the sea quarks, the structure function F_2 rises with Q^2 at low x. At low x, gluon radiation leads to more gluons and quark anti-quark pairs in the proton, so the scaling bahavior is violated and the cross sections will rise with Q^2. This can clearly be seen in fig 1.3 which shows the structure function F_2 measured as a function of Q^2 for fixed values of x [13].

The 1992 commissioning of HERA (Hadron-Elektron-Ringanlage), a lepton proton collider located at DESY in Hamburg, Germany, extended the kinematic range available for exploring deep inelastic scattering. This is illustrated in figure 1.4, which shows the kinematic (x, Q^2) plane of HERA. The fixed target experiments are typically bound below $y < 0.005$ whereas the HERA collider data can reach almost up to the physical limit of $y = 1$. HERA has extended both the x and Q^2 ranges by more than two orders of magnitude. When HERA was comissioned it ran with a proton beam energy of 820 GeV, and after an upgrade in 2000, the proton beam energy was raised to 920 GeV. With electron beam energies at $E_e = 27.5$ GeV the center of mass energy $\sqrt{s} = 318$ GeV is reached ($\sqrt{s} = 300$ GeV pre-upgrade). The HERA collider operates with either electrons or positrons brought into head-on scattering with protons. In this thesis a high liminosity positron-proton (e^+p) sample is analyzed; the term electron is used most of the time in reference to the positron unless clearly stated otherwise.
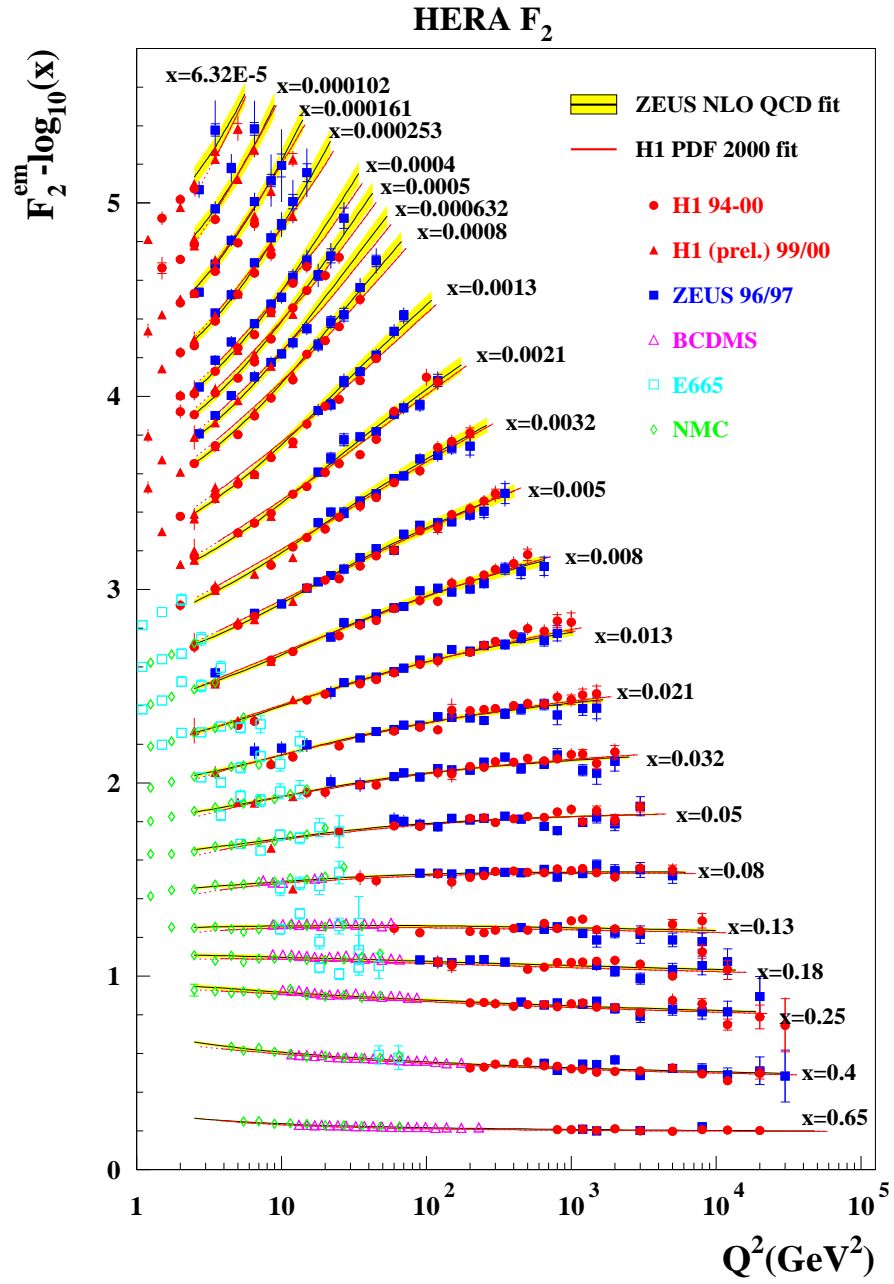
Figure 1.3: The measured scaling behavior of F_2. Scaling violation can be seen clearly at low x.
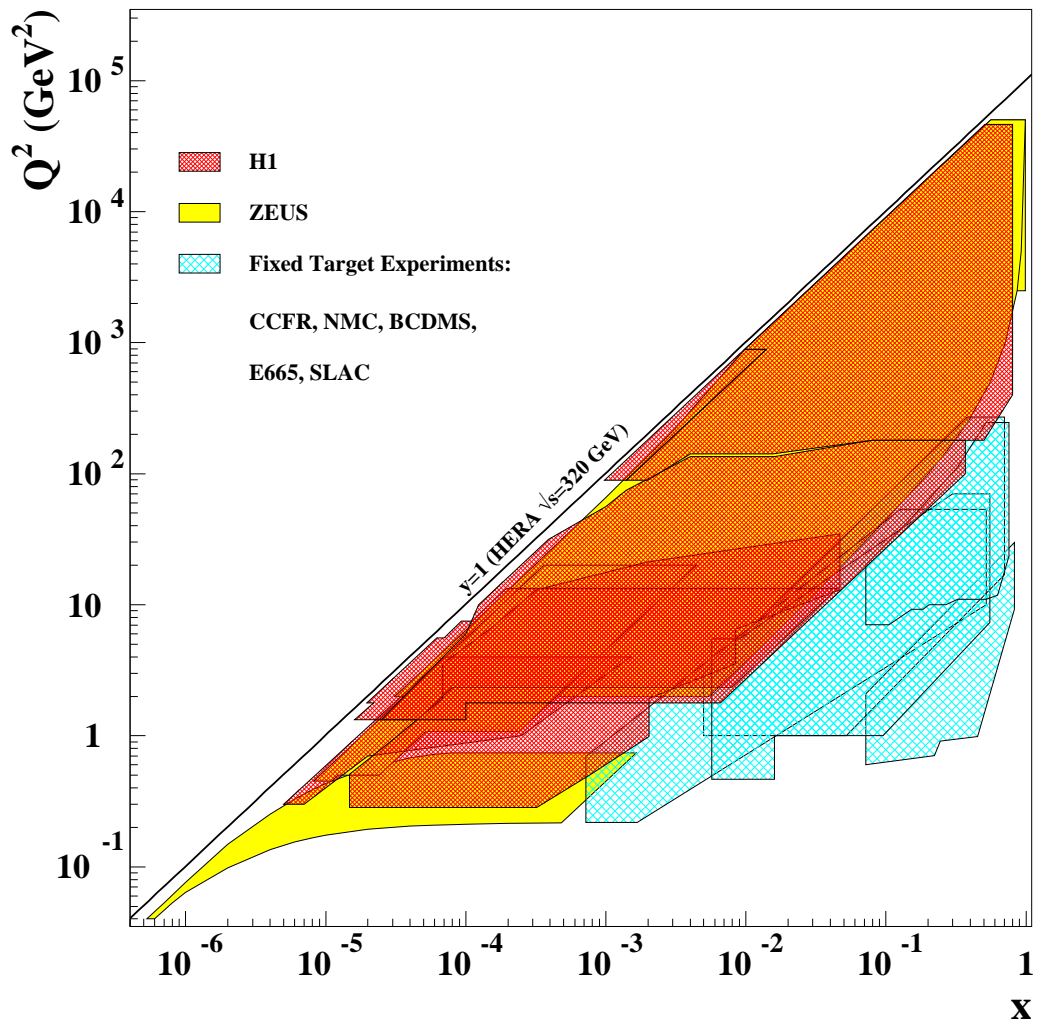
Figure 1.4: Phase space for various DIS experiments in the (x, Q^2) plane. HERA reaches almost to the kinematic limit of $y = 1$.
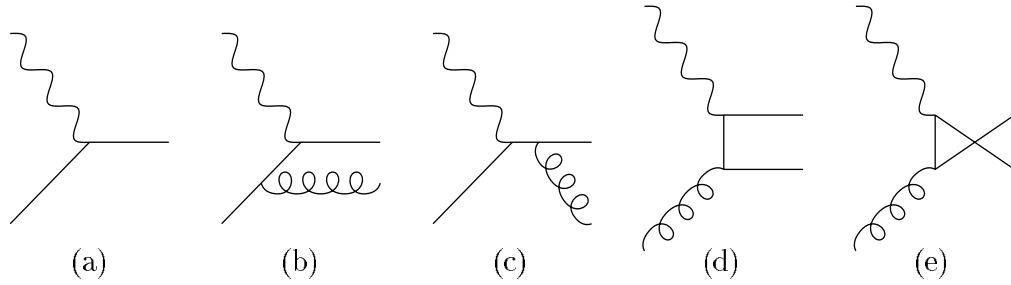
Figure 1.5: Feynman diagrams for DIS up to $\mathcal{O}(\alpha_s)$. In addition to the lowest order QPM diagram (a), the following $\mathcal{O}(\alpha_s)$ corrections are shown: (b) initial state QCD Comptopn radiation; (c) final state QCD Compton radiation; (d) and (e) the Boson Gluon Fusion (BGF) process.

1.2.4   Perturbative QCD

In order for QCD to be useful in predicting the behavior of quarks and gluons, the field equations from which the theory is comprised must be approximately solved. Traditionally this is accomplished using perturbative methods whereby the equations are broken down into individual reactions which can be solved analytically. This procedure is referred to as perturbative QCD (pQCD). In the high energy limit as α_s becomes small, quantities which do not depend on the long distance behavior of the theory are calculated as a series expansion in the strong coupling constant. Each term of the expansion consists of one or more integrals, which are each represented figuratively by a Feynman diagram. Each of the possible reactions that are allowed for the involved particles has an associated Feynman diagram and an associated integral. Each part of the integrand is associated with one interaction within the diagram. Figure 1.5 shows the Feynman diagram for the lowest order QPM interaction between a quark and a photon, as well as the $\mathcal{O}(\alpha_s)$ diagrams which represent the QCD corrections to the QPM. Higher order QCD corrections to the $\gamma^* q \rightarrow q$ process have been

carried out to $\mathcal{O}(\alpha_s^2)$ but in most Monte Carlo models used only the matrix elements up to $\mathcal{O}(\alpha_s)$ are used. The influence of these higher order diagrams is hopefully smaller and presumably safe to ignore. If the scale is large (hard) then the particles can be treated like free particles and the assumptions of perturbation theory are valid.

Chapter 2

Experimental Measurements of Charged Multiplicity

One of the most fundamental observables in any high energy collision process is the total number of particles produced in the final state. However only charged particles can be easily detected and tracked, allowing directly measured determination of their kinematics. The multiparticle final state in high energy collisions can be characterized by the charged-particle multiplicity distribution of the hadrons produced. Even though the multiplicity is only a global measure of the characteristics of the final state, it is an important parameter for understanding hadron production. Independent emission of single particles leads to a Poisson multiplicity distribution. Deviation from the Poisson shape reveal correlations [14], which are the signatures of the mechanisms involved in the evolution of the early stages of the interaction from the appearance of the primary partons to the production of the particles in the final-state. It is possible to extract information about the underlying dynamics of particle production from the shape of the charged-particle multiplicity distribution. The usual way of studying the charged-particle multiplicity distribution and its shape, is to calculate its moments.

22

General characteristics of the charged-particle multiplicity distribution are obtained using lower-order moments such as the mean. The mean charged multiplicity has been measured over a large range of energies and for the many different collision processes, from e^+e^- annihilation to proton-proton collisions. Comparisons of these types of measurements reveal the differences and simularities in the mechanisms of final state particle production on different initial state particles.

The analysis described in this thesis relies upon the use of reference frames other than the laboratory frame for the comparison of measurements of the final state multiplicity in DIS to similar measurements using different initial state particles such as e^+e^- annihilation and hadron-hadron scattering. The Breit and hadronic center of mass reference frames are introduced in sections 2.1.1 and 2.1.2, followed by descriptions of the e^+e^- annihilation and hadron-hadron multiplicity measurements and the comparisons which were made between them. Also discussed in this chapter are the results from a previous measurement of the final state multiplicity in DIS made at ZEUS, and its comparison to the e^+e^- data.

2.1   Reference Frames

The analyses undertaken this thesis are primarily devoted to studying the hadronization products of the quark in DIS. In order to study only the hadronization due to the struck quark a method of separating it from the contamination due to the proton remnant is required. This separation also allows the possibility of a comparison between the characteristics of the hadronization due to the struck quark to that due to the proton remnant. This can be accomplished by a thoughtful choice of reference frames. In addition, moving from the laboratory frame allows comparisons to be made

to experiments with different initial state particles, allowing a test of the universality of the underlying processes.

In a study of the hadronic final state, the bulk of the results available from other experiments in energy ranges comparable to that of HERA are from e^+e^- colliders. Both annihilation and DIS can be used to study the action of the QCD forces which arise as quarks are pulled apart from one another at high energies, and to gain insight into the dynamics of the underlying interaction through the observation of the mean charged multiplicity of the final state hadrons.

The similarities and differences between the two processes can be investigated by comparing measurements of the hadronic final state. It is of interest to determine whether, in the color field resulting from the splitting apart of proton constituents, (quark and diquark in the quark-parton model), the hadronization process operates in the same manner as it does in the color field formed between a newly created quark anti-quark pair.

Unlike at HERA, e^+e^- experiments are well suited to analysis in the laboratory frame, since this is also the center of mass frame. The outgoing particle and antiparticle form two distinct hemispheres and a well-defined "thrust" axis. For a given beam energy the value of $Q^2 = s = W^2$ is fixed.

At HERA events are asymmetric, and there is not an obvious choice of axis. Both Q^2 and W vary from event to event, and differ from each other. Though an obvious benefit of this is that evolution through a large range in Q^2 (or W) can be measured within a single experiment, it complicates analyses of the hadronic final state in the laboratory frame. The laboratory frame at HERA is neither the center of

mass system nor the rest frame of any of the colliding particles. Moreover, there is a large imbalance in the longitudinal momentum which typically leads to a significant amount of energy originating from the proton debris being measured in the forward direction.

Two frames widely used in HERA physics analyses are the hadronic $(\gamma^* P)$ center of mass frame (HCM) and the Breit frame, both of which are aligned along the direction of the virtual photon.

2.1.1 Hadronic Center of Mass (HCM) Frame

The HCM frame is defined by the condition $\overrightarrow{P} + \overrightarrow{q} = 0$. The positive z-axis is usually defined by the direction of the virtual photon, $\overrightarrow{q}$. Particles moving forward are said to belong to the current or photon hemisphere, while particles going backward are assigned to the target or proton remnant hemisphere. The incoming proton and photon each have energy $W/2$ and in the final state the event is symmetric with each hemisphere having energy $W/2$. The struck quark and the remnant are back to back, but the two event hemispheres bear no physical correspondence to the region associated with the struck quark and that associated with the remnant. The direction of the virtual photon is clearly defined, but the direction of QCD color flow is not.

2.1.2 The Breit Frame

In the Breit frame, or "brick wall" frame, the struck quark rebounds from the virtual photon, totally reversing its momentum, while the course of the target remnant is unaltered. The final state quark and the remnant therefore move apart in opposite directions, a configuration which permits direct comparison with the laboratory frame

final state of e^+e^- and pp annihilation experiments.

The Breit frame is defined for ep collisions by the expression: $\overrightarrow{q} + 2x\overrightarrow{P} = 0$, where $\overrightarrow{q}$ and $\overrightarrow{P}$ are the three-momenta of the colliding boson and proton respectively. The virtual photon mediating the interaction is completely space like and in a head on collision with the incoming proton. Under these two conditions, the system is unique up to a spatial rotation which is customarily chosen so that the collision axis coincides with the z-axis; the azimuthal freedom is removed by identifying the electron scattering plane with the xz plane. A more detailed discussion and derivation of the relevant formulae can be found in [15].

The Breit frame provides a good geometric separation between the outgoing struck quark (and the products of its later fragmentation) and the proton remnant since they are back to back. Hadrons observed in the final state are assigned to one of two hemispheres centered on the scattering axis based on the sign of the z component of momentum (measured in the Breit frame). The negative hemisphere, (with $p_{z,\text{Breit}} < 0$) is called the current fragmentation region and is uniquely associated with the struck quark The positive hemisphere, the target fragmentation region, is associated with the remnant, and the color string lies along the virtual photon axis. The main advantage of the Breit frame is that the current region of the Breit frame can be considered analogous to a single hemisphere of an e^+e^- annihilation event with a pair of quarks of energies $\sqrt{s}/2$ produced back to back, each of them equivalent to the struck quark of energy $Q/2$ in DIS. It should be stressed that there are important dynamical differences between the two types of hard scattering. In lepton pair annihilation, unlike DIS, there is no strongly interacting particle in the initial state. In addition, the proton remnant

Electron-positron Annihilation   DIS in the Breit Frame

(a)

(b)

(c)

CURRENT   TARGET
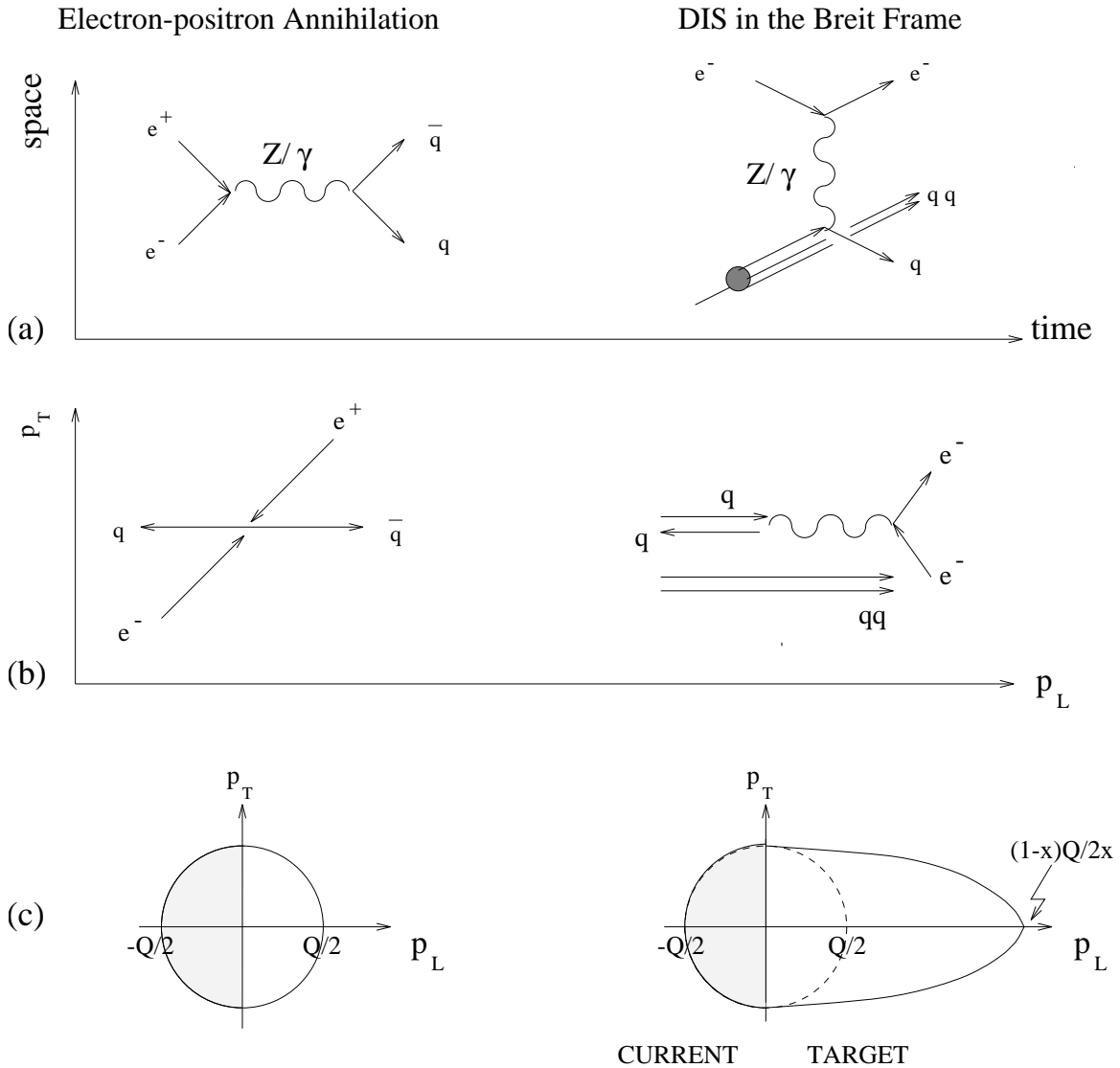
Figure 2.1: Comparison of lowest order processes in e^+e^- annihilation and Breit frame ep DIS: (a) the space-time picture; (b) the space picture and the similarity of teh current region of the Breit frame to a single hemisphere in e^+e^-; and (c) the phase space diagram for each process. Phase space for e^+e^- evolves with $Q/2 \equiv \sqrt{s}/2$. Similarly the current hemisphere in the Breit frame evolves with $Q/2$.

in the final state of DIS is not a point-like color charge but rather an object of finite size and internal structure, again a more complex situation than in e^+e^- annihilation. Hence there is no reason to expect exact equivalence between the two processes. Still, the current region of the Breit frame in DIS is analogous to a single hemisphere of e^+e^- annihilation as shown in figure 2.1 This leads to the conclusion that the evolution of soft QCD radiation from the struck quark in DIS should be identical to that from the q or $\bar{q}$ in e^+e^- [16].

In this thesis particles belonging to the hadronic final state (HFS) are investigated in terms of the mean charged multiplicity dependence on the energy available for final state hadronic production. The similarities in hadronization between processes with different initial state particles is studied by measuring the HFS in the current region of the Breit frame, the laboratory frame, and in the photon region of the HCM frame and compared to the distributions measured by e^+e^- and pp interactions. As there is only one quark jet produced in the current region of the Breit frame for DIS, compared to two quark jets in the inclusive e^+e^- process, the overall normalization of the distributions should differ by a factor of 1/2 with respect to those in e^+e^-.

2.2 Overview of Mean Charged Multiplicity Measurements

With both a lepton and a hadron in the initial state, deep inelastic scattering (DIS) is situated between e^+e^- annihilation and hadron-hadron scattering. The presence of the strongly interacting hadron makes understanding the final state in DIS much more difficult than in e^+e^- annihilation. In the purely leptonic interactions of e^+e^- annihilations, the final state contains no remnants of the initial state. The predecessor of the final state is a single quark anti-quark pair produced from the vacuum by

a virtual photon or a Z-boson. In the case of hadron-hadron scattering, the situation is more difficult since there are two hadrons in the initial state and two sets of hadron remnants in the final state. The study of hadron-hadron interactions benefits from much larger cross sections compared to DIS, and from the symmetry of the reaction which is not present in DIS. But there are advantages to studying the hadronic final state (HFS) in DIS that go beyond probing hadron inner structure at smaller and smaller scales. The high energies available at HERA lead to an enriched structure of the HFS and allow deeper insight into the nature of the strong interactions.

2.2.1   Multiplicity Measurements in e^+e^-

Unlike the other types of collisions, the e^+e^- interaction has the advantage of offering a clean framework for the study of multiplicity since all the available center-of-mass energy is used in the interaction. Electrons and positrons are point-like and massless and interact only via the electroweak interaction, which is well understood and described in the standard model. The electron-positron pair annihilates into a photon or a Z^0 boson which then decays into a quark-anti-quark pair. The $q\bar{q}$ pair then hadronizes, and the colored partons fragment into colorless hadrons forming jets. These hadrons then decay into the stable particles which constitute the final state.

Measurements of the e^+e^- multiplicity distributions have been carried out at center of mass energies below 50 GeV at PETRA and SPEAR [17]. Measurements were performed at PETRA using the PLUTO detector at center of mass energies ranging from 9.4 - 31.6 GeV, the JADE detector at center of mass energies ranging from 12.0 - 36.7 GeV, and the TASSO detector at center of mass energies of 14 - 46.8 GeV. Measurements were performed at SPEAR using the MARK-I detector at

center of mass energies between 3.4 GeVand 7.6 GeV. The mean charged multiplicity at center of mass energies above 100 GeV was measured at LEP and LEPII using the ALEPH, DELPHI, OPAL and L3 detectors [18].

The measurements of the charged-particle multiplicity distributions and their means showed that the shape of the e^+e^- multiplicity distributions was similar to those in $p\bar{p}$ and narrower than those in pp [19], and well described by a log-normal distribution [20]. The Lund parton shower model (see chapter 5 for details) was shown to describe the features of the charged particle multiplicity distributions [21]. In addition, measurements showed that the mean-charged multiplicity increases faster than $ln(s)$ as a function of the center of mass energy [19, 22]. Fragmentation models based on first order QCD were shown to give good description of the energy dependence of the $\langle n_{\mathrm{ch}} \rangle$ [22, 20].

2.2.2 Multiplicity Measurements in pp

The study of multiplicity in pp collisions is not as clean as in e^+e^- because some of the energy of the collision is carried by the proton remnant and is therefore not available for particle production. The interaction takes place between two colored objects, the quarks inside the protons.

Early measurements of multiplicity in pp collisions were preformed at the CERN Intersecting Storage Rings (ISR) with different values of the center of mass energy ranging from $\sqrt{s} = 23.6$ GeV to $\sqrt{s} = 62.8$ GeV [23]. The measurements showed that $\langle n_{\mathrm{ch}} \rangle$ had a quadratic dependence on the the log of the center of mass energy. A later analysis at the ISR measured $\langle n_{\mathrm{ch}} \rangle$ at three values of center of mass energy, $\sqrt{s} = 30$ GeV, $\sqrt{s} = 44$ GeV, and $\sqrt{s} = 62$ GeV [24]. The three data points obtained

from this measurement are compared with the e^+e^- measurements done at SPEAR and PETRA in figure 2.2. These points agree well with the previous measurements at lower pp energies. The $\langle n_{\text{ch}} \rangle$ measured in the pp interactions give values of $\langle n_{\text{ch}} \rangle$ that are in disagreement with the data obtained from the e^+e^- measurements at SPEAR and PETRA, as shown by the three open triangles in figure 2.2.

2.2.3   Comparison of pp and e^+e^-

The disagreement mentioned above was attributed to the fact that the energy available for particle production in a pp interaction is not the total center of mass energy, $\sqrt{s}$, because a large fraction of the energy can be carried away by the leading proton [25]. Therefore, in pp interactions, the $\langle n_{\text{ch}} \rangle$ should be measured as a function of the actual energy available for particle production. The energy available for particle production in pp is simply the difference between the incident proton energy and the leading proton energy.

$$\sqrt{(q_{\text{tot}}^{\text{had}})^2} = \sqrt{[(q_1^{\text{inc}} - q_1^{\text{leading}}) + (q_2^{\text{inc}} - q_2^{\text{leading}})]^2} \ . \tag{2.1}$$

Where $q_{1,2}^{\text{inc}}$ and $q_{1,2}^{\text{leading}}$ are the four-momenta of the incoming protons and leading particles that escape down the beam-pipe respectively. Thus a pp interaction with two colliding protons, each with the same incoming momentum, q, will produce a set of $\sqrt{(q_{\text{tot}}^{\text{had}})^2}$ values which will cover a wide range, depending on the amount of energy taken by the leading proton [25]. It is this quantity, $\sqrt{(q_{\text{tot}}^{\text{had}})^2}$, which was then taken as the energy scale for comparing to the e^+e^- measurements. Each of the three incident ISR proton energies mentioned above correspond to a given range of $\sqrt{(q_{\text{tot}}^{\text{had}})^2}$ values. The charged multiplicity was measured by counting the tracks in
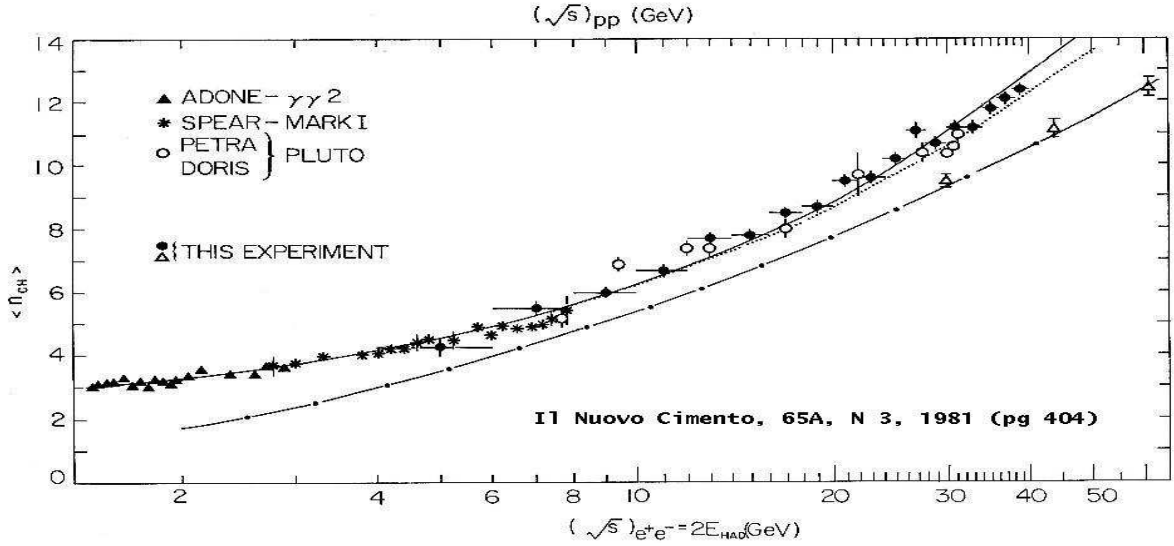
Figure 2.2: Comparison of $\langle n_{\rm ch}\rangle$ for e^+e^- and pp measurements. Shown in this figure is the $\langle n_{\rm ch}\rangle$ dependence on $(\sqrt{s})_{e^+e^-}$ in e^+e^- annhilation, compared to $\langle n_{\rm ch}\rangle$ dependence on $\sqrt{(q_{\rm tot}^{\rm had})^2}$ and on $(\sqrt{s})_{pp}$ in pp collisions. The closed circles and open triangles referred to in the plot as "this experiment", represent the pp data as measured in [25].

the same hemisphere as the leading proton. $\langle n_{\rm ch}\rangle$ and $\sqrt{(q_{\rm tot}^{\rm had})^2}$ were multiplied by 2 for comparison with the e^+e^- data which are relative to the full event. The average charged particle multiplicity measured for pp interactions is in agreement with the values measured in e^+e^- annihilations at SPEAR and PETRA [24]. The results of this comparison are shown in figure 2.2.

2.2.4 Previous Multiplicity Measurements in ep DIS and Comparison to e^+e^-

After the agreement between the dependence of the $\langle n_{\rm ch}\rangle$ for the e^+e^- and pp interactions was reported [24], it was natural to extend the investigation of the universality of fragmentation in different processes to ep interactions.

Taking advantage of the analogy between the current hemisphere of the Breit
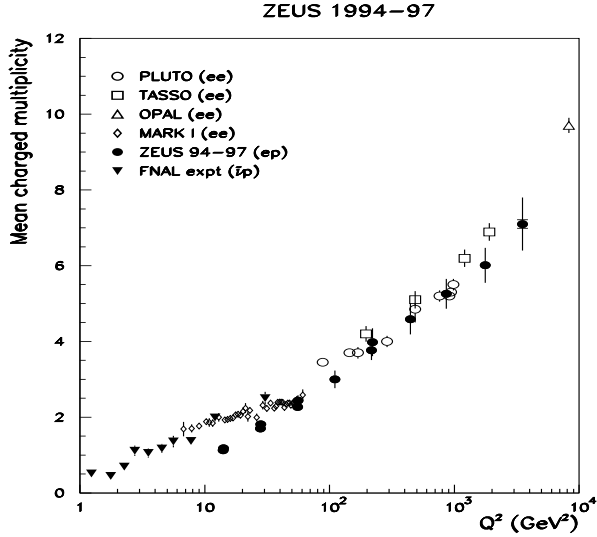
Figure 2.3: Comparison of mean multiplicity for e^+e^- and ep DIS measurements. The nch for e^+e^- is plotted as a function of $(\sqrt{s})_{e^+e^-}$, and divided by 2 for comparison to the DIS data. The ZEUS ep measurement shows the nch in the current region of the Breit frame plotted as a function of Q^2.

frame and one hemisphere of the e^+e^- annihilation, the mean charged multiplicity was measured in the current region of the Breit Frame by the ZEUS experiment. For the ep interactions, the energy available for hadron production is Q, so the dependence of $\langle n_{ch} \rangle_{ep}$ on Q was compared to the dependence of $\langle n_{ch} \rangle_{e^+e^-}$ on $\sqrt{s}$. Figure 2.3 shows good agreement of the ZEUS ep data with the e^+e^- data for Q^2 above 80 GeV. For lower Q^2 values, the e^+e^- data have higher multiplicities.

With its clean separation of the fragmentation due to the struck quark and that due to the proton remnant, the Breit frame was also used to compare the mean charged multiplicity in the current region to that in the target region. The ratio of $\langle n_{ch} \rangle_{\text{target}}$ to $\langle n_{ch} \rangle_{\text{current}}$ was measured at four values of Q^2 ranging from 14 GeV^2 to 55.3 GeV^2. The study showed that the target multiplicity was about four times higher than that in the current region [26].

The mean charged multiplicity has also been investigated for ep DIS in the laboratory frame [27]. In the pp measurement, the proton remnants were effectively removed from the sample, by using the $\sqrt{(q_{\text{tot}}^{\text{had}})^2}$ variable described in section 2.2.3. In ep DIS in the laboratory frame, if one measures the multiplicity in a pseudorapidity range far from the forward region, the proton remnant is effectively removed from the final state. For the measurement the pseudorapididty range, $|\eta| \leq 1.75$ was chosen because it is the central region of the detector, where contamination from the proton remnant is expected to be minimal, and where the detector acceptance is good. The energy available for final state hadron production is then calculated in the same η region and referred to as the effective mass, M_{eff}. The dependence of the $\langle n_{\text{ch}} \rangle$ on M_{eff} was measured and compared to the e^+e^- and pp measurements. Figure 2.4 shows that when measured versus M_{eff}, the mean charged multiplicity in ep is higher than that for e^+e^- measured as a function of $(\sqrt{s})_{e^+e^-}$.

The dependence of the mean charged multiplicity in the photon region of the $\gamma^* P$ (HCM) frame on W was investigated for ep DIS using the H1 detector [28]. These measurements were compared to fixed target lepton-nucleon data and are shown in figure 2.5. The ep data show a similar rate of increase with W to that predicted for e^+e^- annihilation.

The analysis presented in this thesis is devoted to the study of the energy dependence of the mean charged multiplicity, and was motivated by the observation that the $\langle n_{\text{ch}} \rangle$ measured in pp collisions was found to increase with energy in a similar way to the $\langle n_{\text{ch}} \rangle$ measured in e^+e^- anhillation [25].

In this thesis, new measurements of the charged multiplicity in DIS are presented.
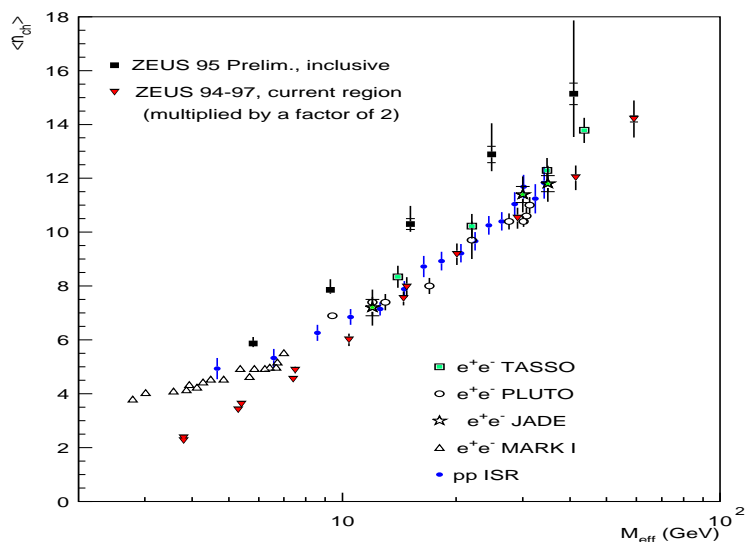
Figure 2.4: Mean multiplicity in laboratory frame compared to e^+e^- measurements. Plotted in this figure is the $\langle n_{ch} \rangle$ as a function of M_{eff} for ep in the laboratory frame (solid squares). These data are compared to $\langle n_{ch} \rangle$ for e^+e^- as a fucntion of $(\sqrt{s})_{e^+e^-}$ and $\langle n_{ch} \rangle$ for pp as a function of $\sqrt{(q_{tot}^{had})^2}$.
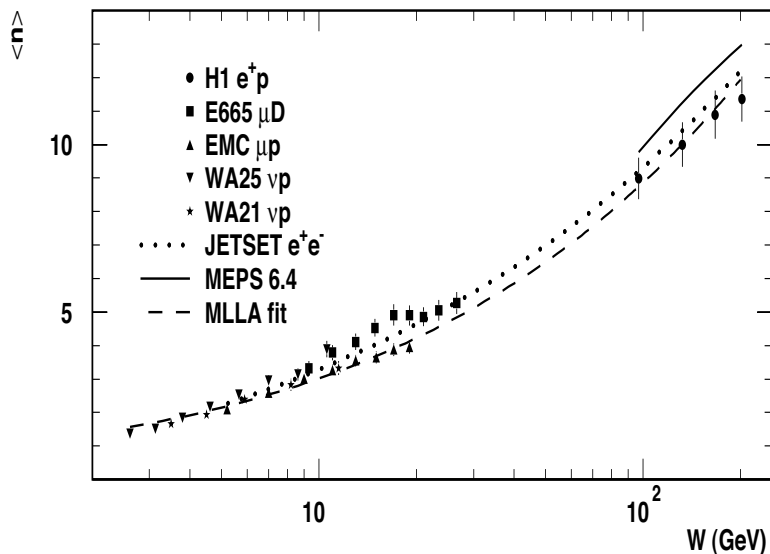
Figure 2.5: Mean multiplicity of ep DIS in HCM frame as a function of the hadronic center of mass energy, W, compared to fixed target lepton-nucleon data.

The energy dependence of the mean multiplicity is measured in the laboratory frame, the photon region of the HCM frame and the Breit frame, in both current and target regions, and the dependence on different energy scales is investigated.

The measurements done in the HCM frame are compared with those from e^+e^- and pp collisions, as well as to the previous results of DIS experiments. For the ep final state, differences are expected in the photon and proton fragmentation regions, due to the asymmetric nature of the reaction. Due to the detector acceptance, only the photon fragmentation region in ep can be measured and used for comparisons.

The charged multiplicity in the current region of the Breit frame is expected to behave similarly to one hemisphere of e^+e^-. As discussed in section 2.2.4, previous results in DIS showed a reasonable agreement with e^+e^- when Q was used as the energy scale for DIS. However, the agreement degraded at energies below $6-8$ GeV. In this analysis, the energy of the current region of the Breit frame is used as a scale for comparison with e^+e^-.

An alternative energy scale, the invariant mass of the hadronic system, M_{eff}, has been studied by comparing the $\langle n_{\mathrm{ch}} \rangle$ in different regions of the Breit and HCM frames in ep DIS.

Chapter 3

Experimental Setup

In 1959 a publicly funded national research center was founded in Hamburg, Germany with the purpose of developing, building and operating high energy particle accelerators. The center is named for the first accelerator, The Deutsches Elektronen-Synchroton (DESY), an electron synchrotron, which was built between 1960 and 1964 and was used for physics research from 1965-1976. Construction began on another accelerator in 1969. The Doppel Ring Speicher (DORIS) was designed to collide electrons and positrons against one another at high energies. The ability to accelerate particles of matter and antimatter to high energies and produce frontal collisions opened up the possibility of completely new types of experiments. DORIS has since been turned into a pure synchrotron radiation source. In 1978 a larger electron-positron storage ring, the Positron-Elektron Tandem Ring Anlage (PETRA), was commissioned. In 1979, experimentalists using PETRA were able to directly observe the gluon for the first time. In 1984, construction was begun on the Hadron-Elektron Ring Anlage (HERA). HERA began operation in 1991, and is the first and only electron-proton collider in the world; it is used exclusively for high energy physics experiments. The DESY and PETRA rings are now used as pre-accelerators for HERA. An aerial view of DESY is

Figure 3.1: An aerial view of DESY. The dashed lines show the underground locations of the PETRA and HERA ring accelerators as well as the location of the four large HERA detector halls (north, south east, west). The DESY site is encircled by the PETRA ring. The HERA facility runs under Hamburgs Volkspark as well as beneath residential and industrial areas of the city.

shown in figure 3.1. The dashed lines show the underground locations of HERA and PETRA.

3.1   The HERA Collider

HERA consists of four straight 360 m long sections connected by 90 degree arcs. An experiment is located on each of the straight segments. There are two collider experiments, H1 and ZEUS, located in the North and South Halls respectively, and two fixed-target experiments, HERMES and HERA-B, located in the East and West halls.

The HERMES experiment, commissioned in 1995, was designed to study the spin structure of the nucleon by aiming the electron beam onto a polarized gas target. HERA-B, which began operation in 1999, was used for studying CP violation in the

$b\bar{b}$ system by colliding the proton beam with a wire target.

The high energies of the particle beams in HERA are achieved in several stages. The electron beam is generated by accelerating electrons in a linear accelerator. The electrons are then transferred to the DESY and PETRA rings for further acceleration before they are injected into HERA. Protons are generated by first accelerating negative hydrogen (H^-) ions to 50 MeV in a linear accelerator. They are then transferred to DESY and further accelerated, the electrons are stripped, and the protons are injected into PETRA. Inside PETRA the protons are accelerated to 40 GeV and then injected into HERA.

Inside HERA, the electron beam is accelerated further using RF cavities until they reach 27.52 GeV. Conventional dipole magnets with a field strength of 0.165 T are used to keep the particles in orbit. The proton beam is accelerated to its final energy using superconducting dipole magnets with a field strength of 4.65 T. Before 1998, the protons were accelerated to 820 GeV. These beam energies correspond to a center of mass energy of $\sim$ 300 GeV. The proton beam energy has since been increased to 920 GeV which corresponds to an increase of the center of mass energy to $\sim$ 318 GeV.

The beams are focused using quadrapole magnets. The electrons and protons are accelerated in separate beams until they are close to the ZEUS and H1 interaction regions. Here the protons are deflected by guiding magnets until they run in the same vacuum pipe as the electrons allowing for a head-on collision. The protons are brought back to the proton ring after passing the interaction point. The HERA ring along with the associated experiments and injection facilities is shown in figure 3.2.
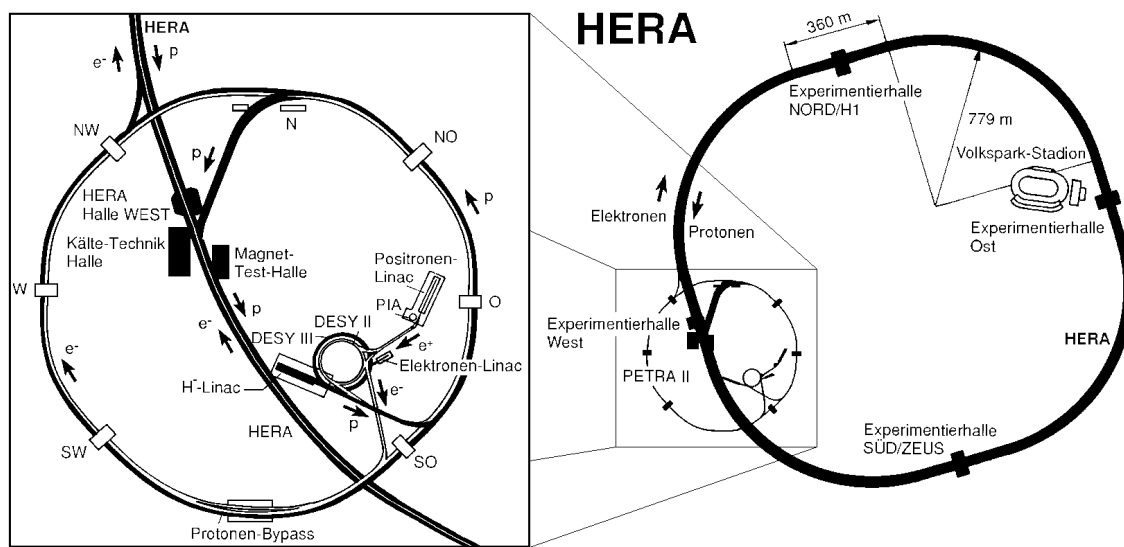
Figure 3.2: The HERA ring with associated experiments and injection facilities. The particles are accelerated in stages by the Linac, DESY, and PETRA before they are injected into HERA. The left side of the figure on the shows the detail of the PETRA ring and pre-accelerators.

The electrons and protons in the beams are organized into bunches which are separated by 96 ns. The maximum number of bunches in HERA is 220, with each bunch of electrons paired for collision with a bunch of protons. There are some bunches which are intentionally left empty. Pilot bunches, electron bunches paired with empty proton bunches, are used for background studies. A series of 10 bunches are left empty for controlled dumping of the beams.

The luminosity delivered by HERA to the experiments during the HERA I and HERA II running periods is shown in figure 3.3. The luminosity improved steadily for the years of HERA I operation.

HERA began running with with electrons but it was determined that the electron beam lifetime was limited by interactions with positively ionized dust particles originating from the vacuum pumps. In 1994, HERA switched to positrons and the luminosity increased due to the more stable positron beam. During the 1997-1998 shutdown, new pumps were installed and the proton beam energy was increased from 820 GeV to 920 GeV. For 1998 and part of 1999 HERA ran with electrons again, and then switched back to positrons.

3.2   The ZEUS Detector

The ZEUS detector is one of two general purpose detectors that were designed to study the electron-proton scattering at HERA, and is used by a large international collaboration consisting of about 300 physicists from over 50 institutes in 15 different countries. The $12 \times 11 \times 20 \, \mathrm{m}^3$, 3600 ton detector surrounds the lepton-proton interaction point and is quasi hermetic, covering 99.7% of the solid angle. Figure 3.4 shows a schematic picture of the ZEUS detector.
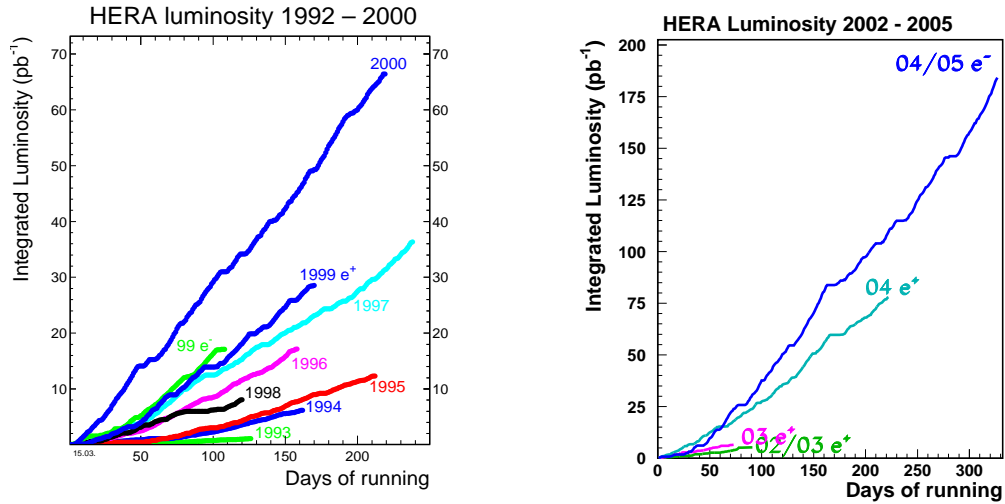
Figure 3.3: Integrated luminosity delivered by HERA for each year of running. The figure on the left is from HERA I which ran from 1992-1999, and the figure on the right is for HERA II which began in 2000.

ZEUS uses a right handed coordinate system with the nominal interaction point at the center. The incoming protons move along the positive z-axis, the positive y-axis points up, away from the earth, and the positive x-axis points toward the center of the HERA ring. In polar coordinates the polar angle, θ, is measured with respect to the z-axis, and the azimuthal angle, ϕ, with respect to the x-axis. The variable pseudorapidity, which is defined in terms of the polar angle as $\eta = -\ln\tan(\theta/2)$, is commonly used to refer to angular positions in the detector since differences in η are Lorentz invariant.

After the interaction, the final state electron moves in the backward direction, toward the rear of the detector, and the final state proton moves toward the front or forward part of the detector. Because of the asymmetry in the energies of the incoming electrons and protons, the hadronic final state particles are boosted in the forward direction. Therefore the detector was designed to be deeper in the forward

region in order to contain the more energetic hadronic final state.

Modern particle detectors are composed of components that can be classified as either tracking chambers which measure particle trajectories and momenta or calorimeters which measure energies. The ZEUS detector is composed of concentric layers of these sub-detectors around the interaction region. After an interaction, a particle first passes through the tracking chamber where the charged particles can be detected by the ionization paths that they leave. Surrounding the tracking chamber is the solenoid magnet which bends the tracks of the charged particles in the chamber so that a measurement of their momenta can be made. The tracking system is surrounded by a high precision uranium scintillator calorimeter which measures the energies of the particles.

A detailed description of all the components that make up the ZEUS detector can be found elsewhere [29]. The next sections contain a brief introduction to how particles interact within the material that makes up the detector, followed by a description of the ZEUS components that are central to this analysis.

3.2.1 Interaction of Particles with Matter

The basic idea behind particle detection devices is that a particle passing through matter will lose energy as it interacts with the atoms in that matter. The measurement of these energy deposits can be used to determine the path and identity of the particle. The interactions depend on the type of particle, its energy and the material it passes through. A calorimeter absorbs an incident particle completely and transforms a part of its energy into a measureable signal. Most particles are assumed to ionize minimally, which means that their energy loss depends only on their charge. For these types of particles, the energy loss can be used to determine the number of particles traversing

44

Overview of the ZEUS Detector
(longitudinal cut)

Overview of the ZEUS Detector
(cross section)
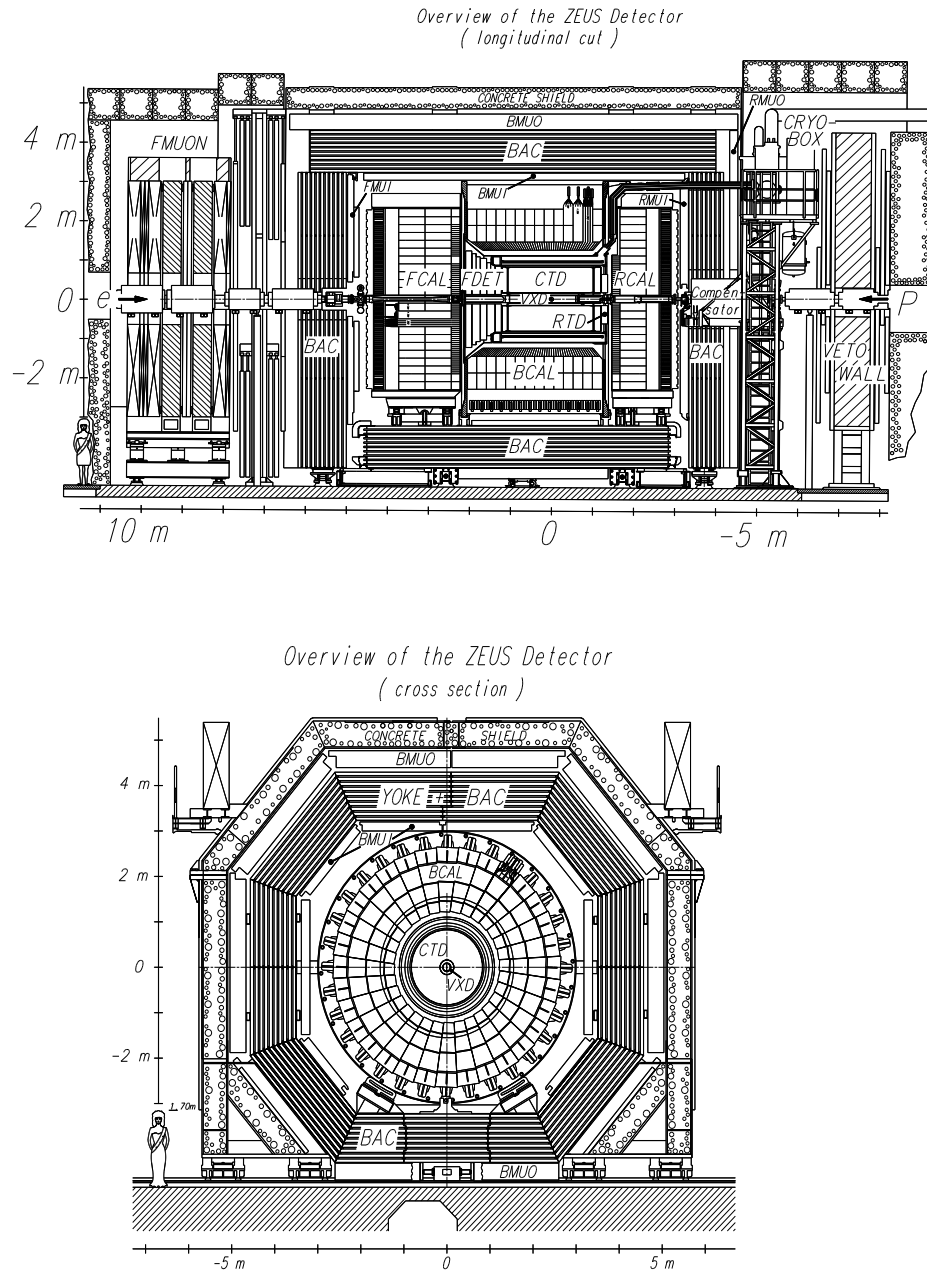
Figure 3.4: The top diagram shows a longitudinal cut of the ZEUS detector. A person is drawn in the lower-left corner of the picture for reference of the dimensions. The lower diagram shows a cross section of the ZEUS detector perpendicular to the beam direction.

the medium.

As a particle interacts with matter it is either absorbed or deflected, and in this process, several new particles are created, each carrying a fraction of the original particle's energy and momentum. An avalance of "shower" particles is created which becomes wider as it penetrates deeper into the material. Eventually, these particles become less energetic due to the conservation of energy and momentum, and as a result, new particles cease to be created and the shower becomes smaller and dissapears.

Particles react differently in matter depending on their type and energy. Electrons and photons produce a cascade of electrons and photons, called electromagnetic showers. At high particle energies, the electrons will emit bremsstrahlung photons and photons will mostly produce pairs of oppositely charged electrons. Lower energy electrons predominantly lose energy through ionization and lower energy photons through Compton scattering. Showers that are produced from hadrons are dominated by inelastic hadronic interactions. For high energies these interactions include multi-particle production and particle emission from nuclear decay and excited nuclei. Hadronic showers also have an electromagnetic component due to the fact that most of the π^0's that are produced decay electromagnetically by emitting two photons. The interactions of muons and neutrinos are also of special interest. Muons move through matter depositing minimum ionizing energy and neutrinos rarely interact with matter, and therefore leave no signature. Figure 3.5 shows typical shower profiles for different types of particles.
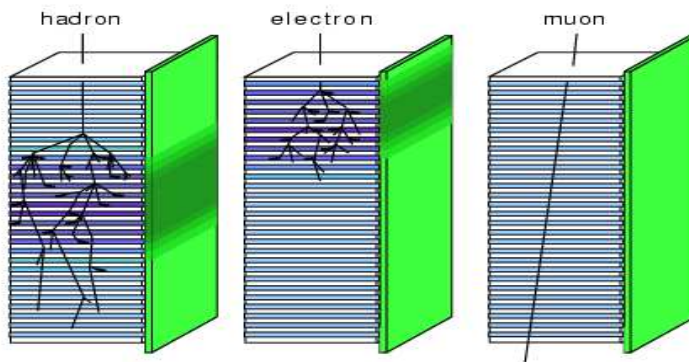
Figure 3.5: Typical shower profiles for different types of particles.

3.2.2 The Uranium Scintillator Calorimeter

A calorimeter at its most basic is just a piece of high-Z matter (an absorber) that produces a shower when hit by a particle, along with some active material to measure the shower. The energy loss deposited into the ZEUS calorimeter is then measured by a material which converts a fraction of the energy deposited into it into light (a scintillator). At ZEUS, the light generated in the scintillator is converted to an electronic signal by photomultipliers.

Calorimeters that use an absorber and a scintillator together are called sampling calorimeters because the scintillator measures only a fraction of the energy that is deposited in it by the shower. Two common calorimeter designs are spaghetti and sandwich calorimeters. In a spaghetti calorimeter scintillating fibers are placed lengthwise through the absorber material. In a sandwich calorimeter plates of scintillator material are placed between plates of absorber material.

As mentioned in the last section, electromagnetic and hadronic showers develop differently. This leads to an added complexity in measuring a particle's energy with the

calorimeter. In general, the average ratio between signals from electromagnetic and hadronic particles of the same incident energy is calorimeter and energy dependent, and there is a higher response for electromagnetic particles, typically $e/h \approx 1.1 - 1.35$. This is because, unlike electromagnetic showers, the hadronic showers lose some of their energy in nuclear processes that don't result in a measurable signal. Therefore, it is more difficult to calibrate hadronic showers. In addition, as mentioned previously, the hadronic shower has an electromagnetic component from the decay of pions, which descy into two photons. Because it is not known what fraction of the shower is hadronic or electromagnetic, is difficult to get an accurate measure of the true energy that was deposited. In order to achieve an electron/hadron signal ratio that is closer to one, several methods are used which take advantage of various phenomena in the active (scintillator) and passive (absorber) layers in sampling calorimeters. U^{238} can be used as the absorber material, making use of its fission capability for slow neutrons. The active layers can be shielded with thin sheets of low-Z material to suppress contributions from soft photons. In addition, the relative thickness of the absorber and active layers can be adjusted [30]. A calorimeter that has an electron/hadron signal ratio close to one is referred to as compensating, and have better resolution due to the equal energy response from hadronic and electromagnetic showers.

The most important property of a calorimeter is the energy resolution. The energy resolution of a sampling calorimeter is influenced mainly by its sampling fluctuations, but can also be effected by statistical effects, noise, mis-calibrations, non-uniformities, and leakage of the shower out of the detector. There are several other factors which can affect the ability of a calorimeter to measure the energy of a particle

accurately. If the calibration is off by a factor, there will be a shift in the energy reconstruction which is hard to detect from calorimeter signals alone. The calorimeter may have non-uniformities which can cause position-dependent variations in the signal response.

The goals of the ZEUS calorimeter (CAL) design were to achieve full solid-angle coverage, a good energy resolution, good calibration of the absolute energy scale and of the individual calorimeter sections with respect to each other and a good angular resolution.

The ZEUS CAL [31] is a sandwich type calorimeter composed of absorber plates of depleted uranium and plastic scintillator as active material. The ratio of the thickness of absorber (3.3mm) to scintillator (2.6 mm) has been tuned to achieve compensation. It has 99.7% solid angle coverage. The energy resolution under test-beam conditions for electrons is $\sigma(E)/E = 18\%/\sqrt{(E)}$ and hadrons is $\sigma(E)/E = 35\%/\sqrt{(E)}$, with E in GeV, and the absolute energy scale is known to 1% [32].

The CAL completely encloses the solenoid and tracking chambers except in the region around the beam-pipe. It is constructed in three main parts, the central part, a hollow cylindrical section called the barrel (BCAL) and the flat forward and rear sections (FCAL and RCAL), situated on the two ends of the barrel. These three sections are further subdivided into modules. These modules are further segmented into towers with a front surface dimension of 20 cm × 20 cm. The towers for the FCAL and RCAL are rectangular and the towers for BCAL are wedge shaped and projective in η. In order to differentiate between the electromagnetic and hadronic showers, the towers are segmented into three longitudinal sections. The EMC, HAC1,
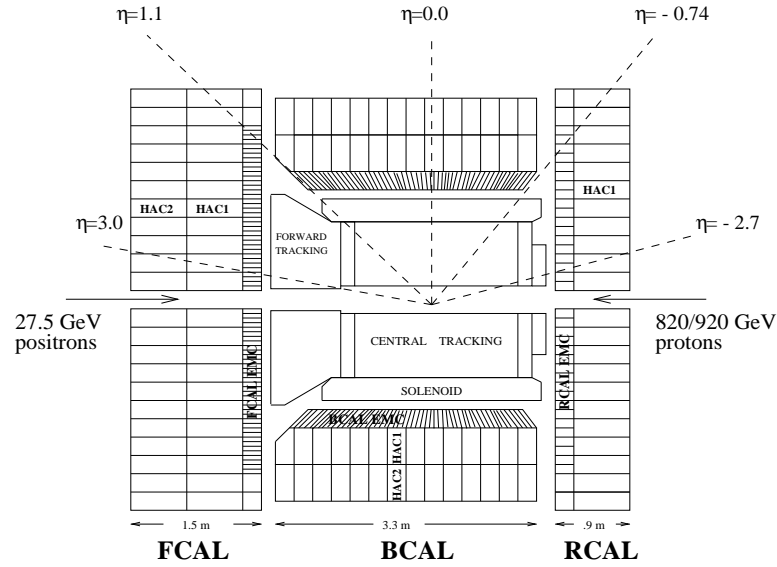
Figure 3.6: A diagram of the x-y cross section of the ZEUS calorimeter showing the three sections of the CAL and the polar-angle acceptance of each section.

and HAC2. The showers produced from electrons are typically contained in the EMC sections, while hadronic showers extend into the HAC1 and HAC2 regions. RCAL towers contain only one HAC section, due to the forward boost of the hadronic final state. A diagram of an x-y slice of the calorimeter is shown in figure 3.6.

The longitudinal extent of each EMC section is typically 25 radiation lengths, where one radiation length, X_0, is the thickness of a material which reduces the mean energy of an electron by a factor of e. The HAC1 and HAC2 sections are longer, typically 2 nuclear interaction lengths thick, where one nuclear interaction length, λ is the mean distance travelled before a nuclear interaction with the material. The sections are made up of cells which consist of alternating plates of absorber and active material. Each HAC section is made from one such cell, while the EMC sections are transversely divided into four cells. Figure 3.7 shows a schematic of the EMC and HAC sections of a typical tower in BCAL. A summary of the angular acceptance and
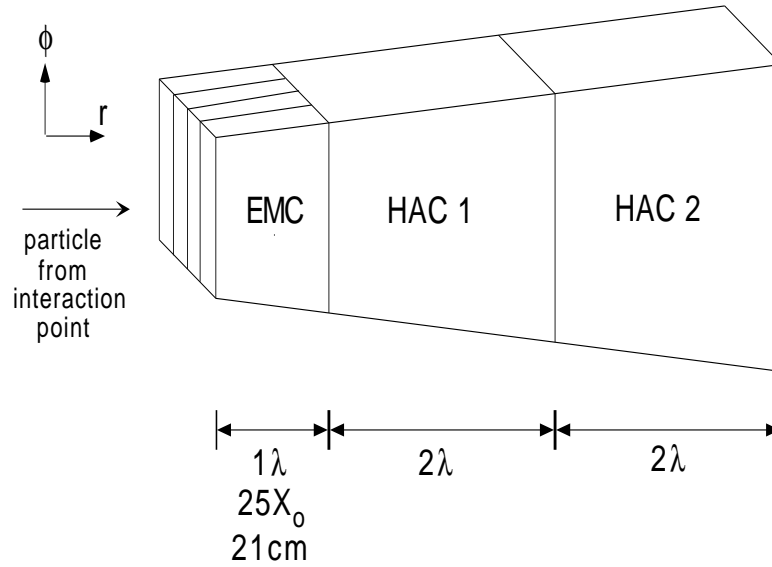
Figure 3.7: Diagram of typical BCAL tower.

	FCAL	**BCAL**	**RCAL**
η range	$3.95 - 1.01$	$1.10 - (-0.74)$	$-0.72 - (-3.49)$
θ range	$2.2^\circ - 39.9^\circ$	$36.7^\circ - 129.1^\circ$	$128.1^\circ - 176.5^\circ$
EMC radiation length (X_0)	181.0	129.0	103.0
absorption length (λ)	7.1	5.1	4.0

Table 3.1: Angular acceptance and longitudinal depth of the CAL sections.

longitudinal depth of the CAL is given in table 3.1

The scintillator light from each of the 6000 cells of the CAL is read out on both sides of each cell. Then, wavelength shifters convert the light to a longer wavelength and transport it to the back of the tower where it is read out by two photomultiplier tubes (PMT). The wavelength is shifted in order to ensure optimal performance of the PMTs. All cells are read out by two (right and left) PMTs simultaneously for several reasons.

- The redundancy of the PMTs can prevent dead spots in the detector since hard-

ware failures typically affect only one side.

- If a PMT or its infrastructure occasionaly become noisy, the noise can be differentiated from a signal by checking for a signal in the complementary PMT.

- Averaging the signal from both sides gives a more uniform detector response.

- The ratio of the response from the left and right PMTs can be used to get an approximation of the transverse location of a shower.

The calorimeter has a very good timing resolution of the order of 1-2 nanoseconds. The good timing resolution also allows the CAL to be used to reject non ep background events. Figure 3.8 shows a schematic of the how the CAL timing can distinguish non ep background events. Particles resulting from an ep DIS event which takes place at the nominal interaction point, arrive at the FCAL and RCAL simultaneously, as shown on the left of figure 3.8. If a non ep background event occurs, such as an interaction with the beam gas, which takes place upstream, the resulting particles will arrive at the RCAL roughly 10 nsearlier than activity measured in the FCAL, shown on the right of figure 3.8. A time difference between the upper and lower parts of the detector indicates a cosmic ray passing through the detector.

For calibration, the calorimeter takes advantage of the constant signal resulting from the natural radioactivity of the U^{238} which has a half-life of 4.5×10^9 years. This radiation is referred to as uranium noise (UNO) and provides a low background current in the PMTs. This current is statistically very stable and the deviations from the expected value allow the detection of problems in the operation of the PMTs. The PMTs and the readout electronics are calibrated using charge, LED, LASER
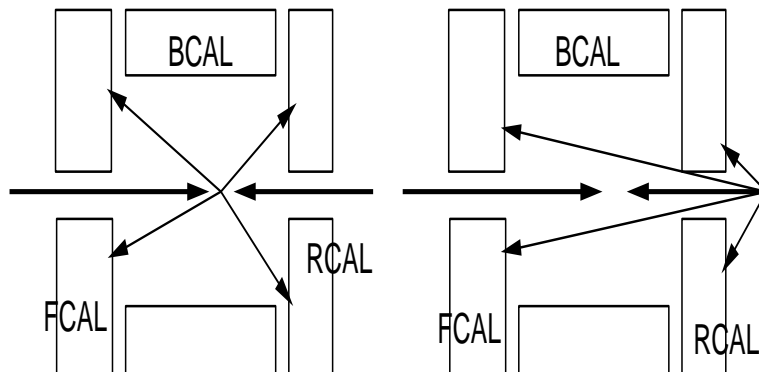
Figure 3.8: The calorimeter timing. Particles originating from a collision at the nominal interaction point hit the FCAL and RCAL at the same time, while particles from beam-gas interaction that take place upstream will reach the RCAL first.

and test pulses. Injections of charge (or light in the case of the LED or LASER) are used to simulate the signal coming from the PMT. Since the quantity of charge is known, the returned value given by the complete readout system is used to calibrate the effects of the electronics, after subtraction of the UNO noise contribution. A full calibration, which includes calibration of front-end electronics, trimming of the high-voltage settings for the PMTs, and generation of a list of read-out channels to be excluded from physics analysis, is done approximately weekly, when there is no beam in the HERA machine. The CAL is monitored and the excluded-cell list is updated daily.

3.2.3   The Central Tracking Detector

The tracking system is made up of the Central Tracking Detector (CTD) and a solenoid. The CTD [33] is a cylindrical wire drift chamber which surrounds the beam pipe. The solenoid surrounds the CTD and provides a 1.4 T magnetic field inside the CTD. The CTD detects the tracks left by charged particles and these tracks are

used to determine the momentum of the particle and the event vertex. When charged particles pass through the CTD, the magnetic field causes their trajectories to become curved. The radius of the curvature of the tracks is used to determine the transverse momentum of the particle from the cyclotron formula: $p_T = qBr$. The direction of the curvature is used to determine the sign of the charge. When used in combination with the electron finder algortithm described in section 4.3, the CTD also plays a role in identifying the scattered electron in DIS events, by matching a reconstructed track to the energy deposit in the CAL associated with the scattered electron.

The CTD chamber is filled with a gas mixture of argon, carbon dioxide, and ethane. Running through the gas filled chamber are groups of wires organized into layers. In order to detect particles a high voltage is applied to the wires. Each group contains positively charged sense wires and negatively charged field wires. A charged particle traversing the drift cell ionizes the gas of the chamber releasing atomic electrons. These drift at known speed to the positively charged sense wires. The positively charged ions move more slowly to the field wires. By measuring the arrival time of the electrons, the position in the cell is obtained. The trail of ions produced by the traversing particle creates a series of hits which are then reconstructed as tracks.

The CTD is 241 cm long with and inner radius of 16.2 cm and outer radius of 85.0 cm. Running through the gas chamber are 72 radial layers of wires which are divided in groups of eighth into nine superlayers. The odd numbered superlayers have wires that are parallel to the CTD axis (axial wires). The wires in the even numbered superlayers are inclined at angles of around ±5° with respect to the z axis (stereo wires) in order to more accurately determine the z coordinate of a hit. The angular
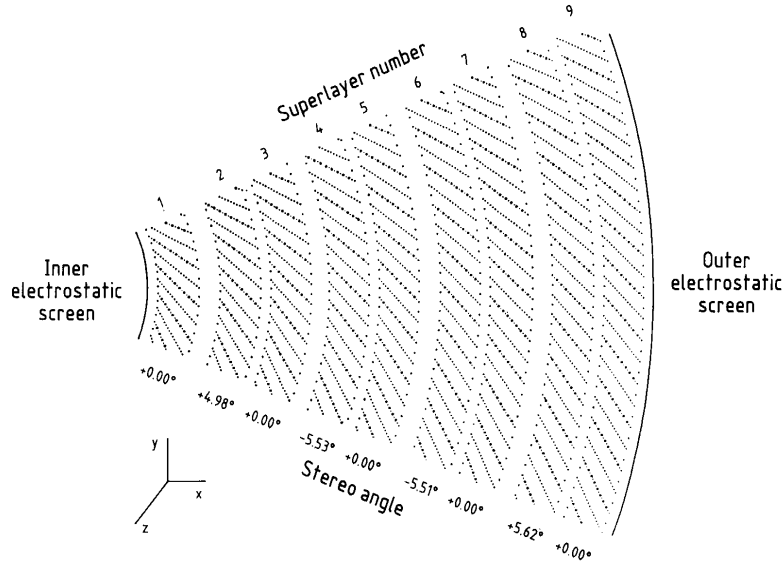
Figure 3.9: Diagram of one octant of CTD.

coverage of the CTD in terms of the polar angle is $15° < \theta < 164°$. The angular acceptance can be extended in the forward using the FTD and in the rear using the RTD. One octant of the CTD is shown in figure 3.9

In order to accurately measure the physical properties of a track it should pass through three of the CTD superlayers. The spatial resolution of the CTD is 120 - 130 μm in the plane perpendicular to the beam. The resolution for good tracks with $p_T > 150$ MeV is $\sigma(p_T)/p_T = \sqrt{(0.0058\dot{p}_T)^2 + 0.0065^2 + (0.0014/p_T)^2}$ [34]. The first term gives the resolution of the hit position, and the second and third terms depend on the multiple scattering inside and before the volume of the chamber respectively. The three inner superlayers have a z-by-timing system which uses the axial wires to make a fast determination of the event vertex z-position [33]. This is used for background rejection at the SLT (see section 6.1.2). The vertex resolution is 4 mm in

the z-direction.

3.2.4   The Trigger System

The purpose of the ZEUS trigger system is to select a small fraction of events which are of interest for physics analysis from an overwhelmingly large background. Every 96 ns, which corresponds to a rate of 10 MHz, a bunch of protons crosses a bunch of electrons in the interaction region of the ZEUS detector. Each crossing has the potential to produce an event which is interesting for physics analysis. But the writing speed of the ZEUS data acquisition system (DAQ) to tape is limited to a few events per second. The job of the trigger to select the interesting events from the background and reduce the rate to acceptable levels for the DAQ. The background rate is around 50 kHz while the rate of ep events is less than 500Hz. The main sources of background arise from interactions of the proton beam with residual gas molecules in the vacuum, proton beam halo events, and cosmic ray induced events. Due to the extremely limited time available for determining if an event should be accepted or rejected, the trigger system is organized into three levels as seen in figure 3.10. The task of each level is to reduce the input rate such that its output rate is below the rate required for the next level.

3.2.4.1   First Level Trigger (FLT)

The First Level Trigger (FLT) is a hardware based trigger that makes a fast decision as to whether the event could be from an *ep* collision or not. It takes the FLT 4.4μ sec to process an event. Because this is considerablly longer than the 96 ns interval between bunch crossings, the data is transferred to a 5μ sec buffer, known as a pipline, to await

56
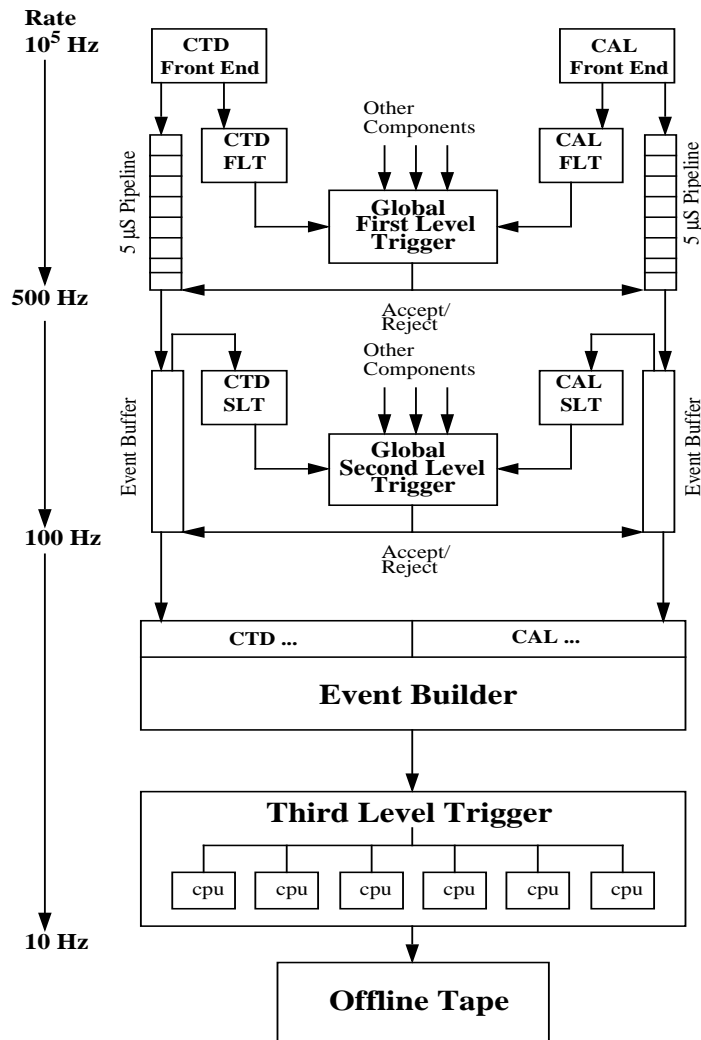
Figure 3.10: ZEUS trigger and Data Aquisition system.

a FLT decision.

Most of the detector components have their own FLT which consists of dedicated hardware that operates on a subset of the full data. The FLT relies on the Calorimeter first Level Trigger (CFLT) [35] and the CTD FLT [36]. The FLT bases its decision on a limited amount of component data, such as simple energy sums, the number of isolated electrons, and number of CTD tracks. The component FLTs transfer this information to the global first Level Trigger (GFLT) approximately $2\mu\,sec$ after the bunch crossing. The GFLT is designed to reduce the rate to 500 Hz. If the GFLT decision is positive, a signal is sent to read out the detector, the data stored in the pipline are transferred to the Second Level Trigger (SLT).

3.2.4.2 Second Level Trigger (SLT)

Compared to the FLT, the Second Level Trigger (SLT) is able to use more complicated and detailed calculations on a larger range of data variables, enabling rejection of a greater proportion of background events and refinement of the sample of physics candidate events. Similarly to the FLT, each component has its own SLT which analyzes the data and sends the processed information to the Global Second Level Trigger (GSLT). The SLT is software based and uses parallel processing on a network of transputers distributed over the components of the detector [37]. The SLT reduces the rate to below 100 Hz, typically around 35 Hz. Upon GSLT accept, data are sent to the event builder (EVB). The EVB collects and puts the data in standard ZEUS format before sending it to the Third Level Trigger (TLT).

3.2.4.3   Third Level Trigger (TLT)

The job of the Third Level Trigger (TLT) is to reduce the rate to the level that allows writing the events to tape. The TLT is software based and runs a slightly reduced version of offline reconstruction code on a processor farm built from commodity computers. The TLT analyzes the event as a whole, and calcualtes kinematic properties such as Q^2, x, y, and E_T. It performs a final rejection of non ep background and classifies events into physics categories according to filters set by various physics analysis groups. The TLT reduces the rate to $1\,\mathrm{Hz}$, with accepted events being written to mass storage (tape) for later processing.

3.2.5   The Luminosity Measurement System

The precise measurement of the luminosity is essential in order to obtain the correct absolute normalization of all measured cross sections. The definition of a cross section is the number of events per luminosity, corrected for acceptance, $\sigma = N/\mathcal{L}$. One can get a precise measure of the luminosity by counting the rate at which a well understood process takes place. At HERA the luminosity is measured from the Bethe-Heitler process $(ep \rightarrow e'\gamma p)$ [38] where the electron and photon are scattered at very small angles. The rate of hard bremsstrahlung photons is measured, N_γ, and the well-known (up to an accuracy of 0.05%) theoretical cross section of this process is used to determine the ep luminosity, $\mathcal{L} = N_\gamma/\sigma$.

N_γ is measured by the luminosity monitor system shown in figure 3.11. it consists of two lead scintillator calorimeters which detect the outgoing electron and photon in coincidence [39]. The photon calorimeter is protected from synchrotron radiation by a thin carbon-lead filter. The electron calorimeter can also be used to tag electrons
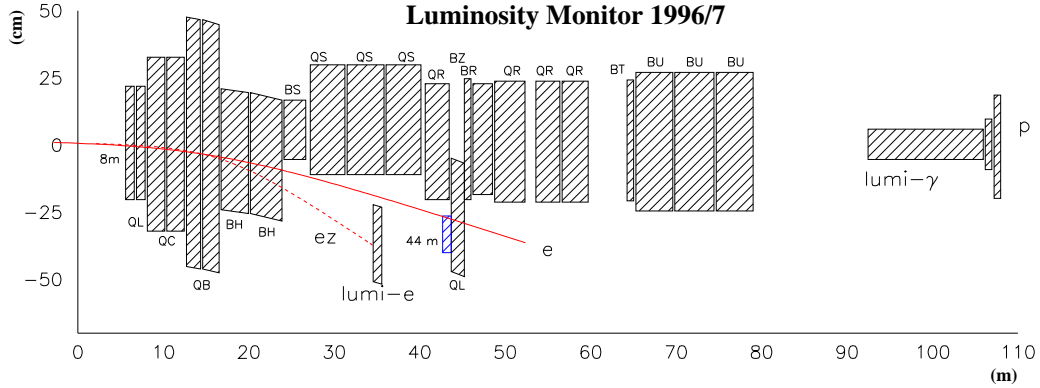
Figure 3.11: The layout of the ZEUS luminosity monitoring system for 1996-97. The nominal interaction point is at (0,0).

from photoproduction events.

3.2.6   Components for Correcting Scattered Electron Measurements

The identification of the scattered electron and the accurate measurement of its physical properties is essential for any neutral current DIS analysis. Measurements of the energy and position of the scattered electron are made by the main calorimeter and the CTD. However the scattered electrons lose some energy by showering in the so-called dead material that they pass through before entering the calorimeter. The Presampler (PRES) and Small Rear Tracking Detector (SRTD) are pre-shower detectors used to measure this energy loss. The Hadron-Electron Seperator (HES) is used to increase the precision of the position measurement.

3.2.6.1   The Hadron-Electron Separator

The HES consists of an array of 3×3 cm silicon diodes which are located at a depth of 3 radiation lengths into the EMC sections of the FCAL and RCAL [40]. The HES was designed to distinguish between electromagnetic and hadronic showers. Because

it has a finer granularity than the CAL and lies at a fixed depth, the HES can be used to increase the precision of the scattered electron position measurements made by the calorimeter.

3.2.6.2 The Presampler and Small Rear Tracking Detector

After the scattered electron leaves the interaction point it passes through the CTD and on into the CAL. But along the way it also passes through the beam pipe, the solenoid magnet, support structures, cooling systems, cables and electronics. These are all examples of inactive material that is not designed to sample the energy absorbed. The energy the electron loses from interacting with this dead material is therefore not measured. The scattered electron produces a shower of charged particles (positrons and electrons) and photons, which ionize in the dead material, and results in an energy loss with respect to the original scattered electron that is proportional to the number of particles prodced in the shower. The RPRES and SRTD can be used to determine how much energy has been lost by counting the number of minimum ionizing particles (MIPS) on the face of the RCAL. The energy measured by the calorimeter is scaled up by a factor proportional to the number of MIPS measured in the SRTD or RPRES to correct for the energy loss due to dead material.

The RPRES consists of 20×20 cm scintillator tiles placed directly in front of RCAL with an angular coverage of $128° < \theta < 176°$. The SRTD consists of 4 sections of 24×44 cm scintillating strips surrounding the beam pipe hole on the RCAL. It has a maximum angular coverage of $159° < \theta < 178°$. The SRTD is useful for correcting low Q^2 DIS electrons, where the electron scatters at small angles.

Chapter 4

Event Reconstruction

The trigger, described in section 3.2.4, selects events based on the information gathered from the various components. From this information a precise reconstruction of the event kinematics must be made offline. The event data are also corrected to ensure that the fundamental measurements (i.e. the energies measured in the CAL cells) are accurate and reliable. The most important event quantities for this analysis are the total number of charged tracks that were measured by the CTD and the amount of energy deposited into the calorimeter. Other important variables that must be reconstructed from the event data are the kinematic variables, Q^2, W, and x since the measurements are binned in these variables. It is also important that the scattered electron is properly reconstructed since it is used to distinguish a neutral current DIS event. This chapter describes the techniques used to convert the output from the detector components into a fully reconstructed data set.

4.1 Track and Event Vertex Reconstruction

The analysis presented in this thesis relies heavily on the CTD for measurements of the track and vertex properties which are used to determine the number of charged

tracks that come from the primary event vertex.

The track and vertex finding for ZEUS is performed by a pattern recognition software package called VCTRACK [41] The main function of the VCTRACK software is to recognize trajectories in the CTD, fit them and then estimate the primary and secondary verticies.

The trail of ions produced by the charged particle traversing the CTD creates a series of hits on the wires in the drift chamber which are then reconstructed as tracks. The VCTRAK software groups the individual hits into track candidates, which are then fit with a five-parameter curve. The tracks can be connected to the primary vertex (the interaction vertex) or a secondary vertex (a vertex originating from particle decays or interactions with the beam pipe). The connection of tracks to a vertex further constrains the tracks and helps to reconstruct the position of the vertex.

4.1.1 Track finding

Each track candidate begins as a track "seed" which consists of three adjacent hits in the outer axial superlayers in the CTD. The software connects the hits found in each superlayer to form complete tracks. The reconstruction begins from the outermost superlayer and is extrapolated inward guided by a "virtual hit" which is added at the beam line ($x = y = 0$). This virtual hit is retained throughout the pattern recognition and subsequent trajectory fit. As the seed is extrapolated inward, additional hits are gathered with increasing precision; trajectory parameters are updated, and a circular arc is formed in the xy plane. In order to construct the z coordinate of the trajectory, information from both axial and stereo superlayers is needed. Initially a z-by-timing measurement is used (section 3.2.3), yielding a coarse first estimate of the trajectory

in 3D and thereby limiting the region which has to be searched for hits on the stereo wires. The stereo hits are then used to provide more accurate information on the z position.[1]

4.1.2 Track Fitting

Because the magnetic field from the solenoid is parallel to the axis of the CTD, the track path can be represented by an axial helix. Each track candidate is fitted to a five parameter helix model with the fit beginning with the innermost tracks. The trajectory fit begins with an estimation of the momentum based on the slope and curvature provided by the pattern recognition. A trajectory is established by starting from the innermost measured hit and proceeding outward. Finally, the trajectory is transported inward to coincide with the z axis at $x = y = 0$. Magnetic field effects are corrected for, and allowance is made for multiple Coulomb scattering inside the beam pipe and the inner wall of the CTD. The resulting information is then ready for use by the vertex reconstruction.

4.1.3 Event Vertex Reconstruction

The determination of the event vertex is integrated into the track reconstruction procedure. The event vertex is the collision point of the initial positron and proton and all particle angles are measured with respect to it. The positron and proton do not always collide at the nominal interaction point (0,0,0) in the ZEUS coordinate system. The spread of the vertex in the longitudinal direction is determined by the proton bunch

---

[1]As mentioned in section 3.2.3, the stereowires are inclined at angles of around $\pm 5°$ with respect to the z axis in order to more accurately determine the z coordinate of a hit.

length which is about 8mm. The transverse size is less than 0.07mm.

All tracks passing through the innermost superlayer are included in a minimization fit procedure to determine the event vertex. The tracks that are assigned to the vertex by the minimization procedure are refitted using the event vertex as an additional constraint.

4.2   Global Calorimeter Quantities

Accurate information about the energy deposits in the CAL is crucial for the precise reconstruction of the hadronic final state. The calorimeter is one of the main components used in this and in most ZEUS analyses. In this analysis, the quantities reconstructed from the information measured by the CAL are used to calculate M_{inv}. The necessary quantities are the total deposition of energy in the CAL, E_{tot}, and its projections along the space coordinates, which are defined as:

$$E_{\text{tot}} = \sum_i E_i \ , \tag{4.1}$$

$$p_{\text{x}} = \sum_i E_i \sin \theta_i \cos \phi_i \ , \tag{4.2}$$

$$p_{\text{y}} = \sum_i E_i \sin \theta_i \sin \phi_i \ , \tag{4.3}$$

$$p_{\text{z}} = \sum_i E_i \cos \phi_i \ . \tag{4.4}$$

The summation runs over all CAL cells and E_i, θ_i, and ϕ_i are the energy, polar and azimuthal angles of the i-th CAL cell respectively. The angles are calculated from the z coordinate of the reconstructed event vertex and the center of each CAL cell.

In all processes four-momentum is assumed to be conserved, and therefore the difference between the energy and the longitudinal component of the momentum is

conserved. $E - p_\mathrm{z}$ is defined as follows:

$$(E - p_\mathrm{z})_\mathrm{beam} = E_\mathrm{tot} - p_\mathrm{z} = \sum_i E_i(1 - \cos\theta_i) \; . \tag{4.5}$$

Because of the definition of the ZEUS coordinate system, the energy and momentum of the proton cancel. But for the electron, they add up to twice the electron beam energy, 55 GeV. The energy and momentum associated with the proton remnant escapes undetected down the beam pipe, but the $E - p_\mathrm{z}$ for the remnant is small.

4.2.1   Calorimeter Cells and Energy Flow Objects (EFOs)

In this analysis it is especially important that the hadronic mass be precisely determined from the energy measured in the CAL cells. The measurement of the hadronic mass is sensitive to noise in the CAL cells. To ensure that the energy measured in the calorimeter is not due to noise, cells that are determined to be noisy are excluded from further reconstruction [42]. A CAL cell is assumed to be noisy if it is isolated and has low energy, if one of its photomultiplier tubes shows a larger signal than the other, or if it appears on a list of known bad cells that is updated for each running period. The calorimeter is then calibrated so that the energy response is the same in Monte Carlo simulations and data [43].

The tracking system has a much better angular resolution and a better energy resolution at lower energies than the CAL, therefore an improved measurement of the energy deposits can be made by combining CAL and tracking information into energy flow objects (EFOs) [44]. At ZEUS, these EFOs are referred to as "ZUFOs". The energy of the ZUFOs is set equal to the momentum so that they are massless.

All CAL cells (except those associated with the scattered electron) and all good

tracks[2] are used to construct the ZUFOs. The ZUFOs are built by combining the calorimeter cells belonging to the same shower into an "island" which are then matched to a track. The cells are combined using a next-neighbor algorithm which doesn't connect cells diagonally. It is not required that each ZUFO have exactly one island and one track; a ZUFO can have more than one track or island, and may or may not have both a track and an island. The procedure for assigning position and energy to each ZUFO consists of the following steps [44]:

- Islands or tracks which are unmatched are counted singly. Tracks which are not matched to islands are considered to be ions for the purposes of calculating their energy.

- Islands with more then three associated tracks are measured with the calorimeter.

- The calorimeter measurement is used when the energy measured in the calorimeter is much higher for an island than the energy of the associated tracks. In this case, it is assumed that neutral particles hit the calorimeter in the same position as the charged ones.

- At low energies, the tracking system has better resolution than the calorimeter, so when a ZUFO is determined to have a low energy then the measurement is taken from the tracking system.

- When a match consists of more than one island the information from the islands

---

[2]Tracks which pass through at least three CTD superlayers, have p_T above 150 MeV, and come from the primary vertex are considered to be "good tracks".

is combined and used for this algorithm, similarly, if the match has more than one track, the information from the tracks are combined for use with this algorithm.

- When a single track is matched to one or two islands, the positional information is taken from the tracking system.

The result is that ZUFOs provide improved resolution in E_t and η over CAL cells alone [44].

In this analysis, ZUFOs are used to calculate the inariant mass of the hadronic system, $E - p_z$, and the kinematic variables for the DA and JB methods described below.

4.3 Electron Reconstruction

A scattered positron in the final state is the primary signature of neutral current DIS events, therefore the correct identification of the positron, and the precise reconstruction of its energy and position are vital to any analysis of neutral current DIS events.

For the analysis described in this thesis, the positrons are identified using the SINISTRA95 [45] electron finder. SINISTRA uses a neural network approach for particle identification based on the showering properties of the particles in the calorimeter. SINISTRA uses the electromagnetic and hadronic shower topologies to differentiate between the two. The shower associated with an electron generally is short and narrow, whereas the hadronic showers are deeper and more laterally spread. The aim of the software is to best identify the electromagnetic particles from the information measured in the CAL.

SINISTRA takes all CAL cells after noise suppression and groups them into islands. Islands within CTD acceptance but without an associated track are not considered. The longitudinal and transverse energy profiles of the corresponding CAL cells of the islands are input into the neural network. Each island is a potential electron candidate. The output of the SINISTRA neural network is a probability that the energy deposit is of an electromagnetic origin. Efficiency and purity studies have shown that a good selection of candidates is made by considering candidates with probabilities greater than 0.9 [46]. The candidate with the highest probability is identified as the electron.

Once the electron is identified, the energy is calculated from the sum of the energies of the cells that make up the island. SINISTRA can reliably assign probabilities to islands with energies larger than 10 GeV [46]. The energy of the electron is then corrected for different shower developments using the preshower detectors (see section 3.2.6). The energy is also corrected for energy loss in the dead material in front of the CAL using dead material maps (see section 3.2.6.2).

The position of the final electron candidate is determined from weighting the positions of the cells of the island by their energy. From the energy and position measurements the four-momentum of the island is reconstructed and associated with the final electron candidate.

The main SINISTRA algorithm which is based solely on CAL data has been supplememnted with an electron candidate matched to a reconstructed track using CTD data. This feature has been used in the present analysis in order to remove the electron track from the pool of hadron candidates.

4.4 Kinematic Reconstruction

The precise reconstruction of the variables x, y and Q^2 (introduced in section **??**) from the final states is of vital importance for the description of DIS events. The kinematic reconstruction of these variables based on quantities measurable in the ZEUS detector can be done using several methods which are described in this section.

To first order, the final state in a neutral current DIS event consists of a scattered lepton and a scattered quark as shown in the following diagram; where E_e, E', and θ
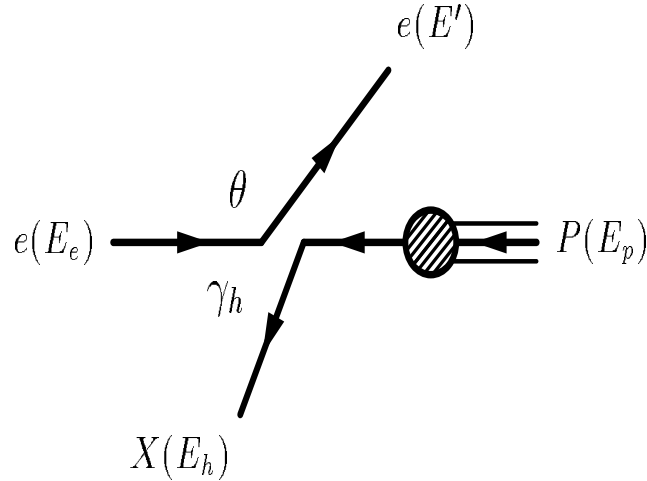
are the initial energy, final energy and scattering angle of the lepton, respectively. E_p, E_h, and γ_h are the beam proton energy, the final hadronic energy and the polar angle of the final hadronic system, respectively.

In general, eight variables are necessary to describe the final state of particles in DIS: the four-momentum of the hadronic system, $X(E_h)$, and the four momentum of the scattered positron, $e(E')$. These variables are constrained by the fixed mass of the lepton and the conservation of energy and momentum. These constraints result in the

need for only three independent variables to describe the final state, typically chosen
to be the Lorentz invariant quantities, Q^2, x, and y. A final constraint, $Q^2 = sxy$,
imposed by the fixed center of mass energy at HERA reduces the number of variables
needed to describe the interaction to two. Q^2, x, and y must be reconstructed from
the following four quantities which are measurable in the detector: the energy and
polar angle of the scattered lepton, E' and θ, and the energy and polar angle of the
hadronic final state, E_h and γ_h. Because only two of these variables are needed to
fully constrain the kinematics, we have a choice of which variables to use, and the pair
that provides the most accurate reconstruction can be chosen.

4.4.1 Electron Method (el)

The electron method uses only the scattered electron variables for kinematic recon-
structions, making it conceptually the simplest reconstruction method. Using the
definitions of the kinematic variables given in section 1.2.1, the following expressions
are obtained:

$$Q_{\text{el}}^2 = 2E_e E'(1 + \cos\theta) \ ;$$
$$y_{\text{el}} = 1 - \frac{E'}{2E_e}(1 - \cos\theta) \ ; \tag{4.6}$$
$$x_{\text{el}} = \frac{Q_{\text{el}}^2}{s \ y_{\text{el}}} \ .$$

4.4.2 Jacquet-Blondel Method (JB)

One can reconstruct the kinematics using the hadronic system only. This method
is entirely independent of the electron. Some of the particles that make up the hadronic
final state belong to the proton remnant and escape down the beam pipe. A kinematic
reconstruction procedure was proposed by Jacquet and Blondel [47] for which the four

momentum is summed up for all the particles in the hadronic final state. To avoid biases from the particles lost through the beam pipe, one looks only at the transverse momentum, $p_{\mathrm{T,had}}$, and the difference between energy and longitudinal momentum, $(E - p_z)_{\mathrm{had}}$. As mentioned above, both of these variables are close to zero for remnant particles going down the beam pipe. The resulting formulas for the kinematic variables are:

$$y_{\mathrm{JB}} = \frac{1}{2E_e} \sum_i (E_i - p_{\mathrm{z,i}}) \ ;$$

$$Q_{\mathrm{JB}}^2 = \frac{1}{1 - y_{\mathrm{JB}}} [(\sum_i p_{\mathrm{x,i}})^2 + (\sum_i p_{\mathrm{y,i}})^2] \ ; \tag{4.7}$$

$$x_{\mathrm{JB}} = \frac{Q_{\mathrm{JB}}^2}{s \ y_{\mathrm{JB}}} \ .$$

4.4.3 Double Angle Method (DA)

The double angle method [48] uses the polar angle of the electron and the angle of the hadronic system. For Quark-Parton Model events (section 1.2.4), the angle of the hadronic system is aligned with the polar angle of the scattered quark. The double angle method yields the following formulae for the kinematics:

$$y_{\mathrm{DA}} = \frac{\sin\theta(1 - \cos\gamma_h)}{sin\gamma_h + sin\theta - sin(\gamma_h - \theta)} \ ;$$

$$Q_{\mathrm{DA}}^2 = 4E_e^2 \frac{sin\gamma_h(1 + cos\theta)}{sin\gamma_h + sin\theta - sin(\gamma_h + \theta)} \ ; \tag{4.8}$$

$$x_{\mathrm{DA}} = \frac{Q_{\mathrm{DA}}^2}{sy_{\mathrm{DA}}} = \frac{E_e}{E_p} \frac{sin\gamma_h + sin\theta + sin(\gamma_h + \theta)}{sin\gamma_h + sin\theta - sin(\gamma_h + \theta)} \ .$$

Since the angle, γ_h, of the struck quark can not be measured directly, it must be calculated from hadronic variables using the Jacquet-Blondel Method:

$$cos\gamma_h = \frac{(\sum_h p_{xh})^2 + (\sum_h p_{yh})^2 - (\sum_h E_h - p_{zh})^2}{(\sum_h p_{xh})^2 + (\sum_h p_{yh})^2 + (\sum_h E_h - p_{zh})^2} \ . \tag{4.9}$$

The advantage of the double angle method is that in certain kinematic regions, the angular resolution is normally better than energy resolution, giving a more precise measurement.

4.4.4 Summary of Kinematic Reconstruction

The accuracy of each reconstruction method varies depending on the kinematic region of interest. The double angle method has a good resolution at high values of Q^2 and x, but as x and Q^2 decrease, the resolution of the electron method becomes better. In the analysis described in this thesis, for the reconstruction of the photon virtuality, Q^2, Bjorken x, and the γ^*P centre-of-mass energy, W, the double angle method (DA) was chosen. Variables calculated by electron method and by the Jacquet-Blondel method were used only in the event selection.

Chapter 5

Monte Carlo Simulations

The reconstruction of the DIS events as decribed in chapter 4, yields measurements which are biased by the effects of particular characteristics of the ZEUS detetector. The detector is a highly complex device, so the measurement of observables requires correction to account for finite detector efficiency, resolutions and acceptances. In order to correct for these effects or even to accurately estimate the related experimental uncertainties they need to be well understood. Measured results which are not corrected for these effects would not address universal physics but rather specifics of the detector itself.

Because the ZEUS detector is a complicated and extensive arrangement of sub-components, it is difficult to find expressions for the performance parameters such as resolutions and acceptances from knowlegde of its geometry and internal structure alone. In high energy experimental physics, a well-established probabilistic Monte Carlo method produces a large sample of simulated data using programs which generate events. This method is based on the assumption that a good understanding of local properties can be carried through to the macroscopic level using statistical analysis of simulated data. In this way, Monte Carlo simulations are used to correct

for limited geometrical acceptance of the detectors and to understand the effects of the measurement resolution on kinematical variables. In addition, the systematic effects introduced by the detector can be estimated by averaging the calculated detector response over large samples of simulated events and comparing it to the known input. In order for this approach to work, the studied Monte Carlo sample must be representative of the actual collected data set so that the treatment of the Monte Carlo sample in the detector is similar to that of the data.

In order correct the data for detector effects using a Monte Carlo, the Monte Carlo sample itself need not contain any physics-related input. It is more practical, however, to base the Monte Carlo event generators on the actual physics processes which are being studied using the detector. In this way, experimentalists can use the Monte Carlo simulations to evaluate the underlying physics assumptions that are made in the algorithms of the event generator. Hence, a comparison can be made and the Monte Carlo can be tuned or revised using feedback from the experimental data.

In this chapter the method for simulating the physics processes using Monte Carlos will be examined. Information about the specific Monte Carlos used to simulate the data for the analysis presented in this thesis is also included in this chapter.

5.1 Event Generators

A Monte Carlo event generator simulates physics processes by selecting the event type and computing its relavant subprocesses according to probability distributions from the cross-sections predicted by a given theoretical model. There are a number of Monte Carlo programs that can be used to generate events for neutral current ep DIS interactions at ZEUS. Events are randomly generated using algorithms based on

the rules of QCD and phenomenological models. These algorithms are separated into distinct steps, whereby the perturbatively calculable hard processes at the partonic level are separated from the hadronic structure in the initial state and the hadronization in the final state, which are not calculable from first principles. The first part of the algorithm simulates the perturbative leading order matrix element and leading log initial and final state parton showers; the second part includes the non perturbative hadronization via phenomenological models. Some experimentally determined parameterizations for the parton densities are also used as input to the event generators. These are described in the next section. The QCD factorization theorem justifies the separation of hard scattering processes from the subsequent soft QCD cascades and hadronization [49]. The event generator algorithms are made up from the following steps:

- The leading order matrix elements from the hard subprocess (the interaction between a parton in the proton and the exchanged photon) are calculated using perturbative QCD. At the end of this stage there are the final state partons and the proton remnant.

- The partons emitted from the hard scatter produce a shower called the parton cascade which generates additional partons. A model is applied which compensates for these higher order effects whereby the radiation is simulated by an arbitrary number of branchings of one parton into two. The shower evolution stops at some fixed scale, μ_0, typically of the order of 1 GeV. At the end of this stage there are a rather large number of partons and the proton remnant which evolve according to phenomenological models.

- The partons from this last stage carry color charge that connects them. A phenomenological model is applied for the non-perturbative hadronization, where the colored partons (and the remnant) are grouped into the colorless hadrons of the final state. The hadron level is defineds the stage where all particles present are stable hadrons.

The result is a complete set of four-vectors of the final state particles, which are then fed into a simulation of the detector where they decay further or interact with the detector.

5.2   Parameterizations

The distributions of partons in hadrons can not be calculated using perturbation theory. However, as mentioned above, the QCD factorization thoerem [50] states that for hard scattering reactions the cross section can be decomposed into the parton densities of incoming particles and the cross section from the hard process which are calculable in pQCD. The hadronic structure is parameterized in terms of parton distribution functions (PDFs). The PDFs provide the probability of finding a parton with an arbitrary momentum fraction, x, inside a hadron moving fast with respect to the probe. In order to separate the long range and the short range processes, a cut off parameter, the factorization scale, μ_f, is introduced. All effects that are considered soft effects inside the proton are absorbed into a PDF. The structure of the hadron is dependent on the four-momentum transfer, Q^2, at which the hadron is being resolved into partons.

The PDFs themselves must be determined by global fits to experimentally mea-

sured data sets. Typically one assumes a reasonable functional form of the x dependence at the starting scale Q_0^2 and applies perturbative evolution DGLAP equations [51] to obtain predictions at higher scales. These predictions are constrained by measured values of the PDFs at a given scale, allowing for a fit to a few unknown parameters and predictions of their evolutions to some new scale.

The knowledge of the evolution of the PDFs can be exploited to determine them experimentally. If the perturbative part is calculated and the cross section of a certain process is measured, the PDF can be extracted from the data. The factorization theorem of QCD states that the PDFs are process independent. Once determined for a given process, they can be used to make predictions for another proces. For the small x region with a finite Q^2, another scheme called BFKL [52] can be used for parton evolution.

The hard process is short ranged and can be perturbatively calculated. In order to calculate self energy diagrams which yield divergent integrals, a renormalization scale, μ_r, is introduced, and the divergences are absorbed into the definition of the PDFs.

The parameterization which is used in this analysis is CTEQ4D [53] which includes data from HERA [54] and provides a good description of cross sections observed at ZEUS.

5.3 Hard Subprocess

In the case of DIS, the hard scattering is an electromagnetic interaction between the virtual photon and a quark originating from the proton. It is typically calculated to first order in the electromagnetic coupling constant, $\mathcal{O}(\alpha_{\rm em})$ The leading order includes

QCDC

BGF
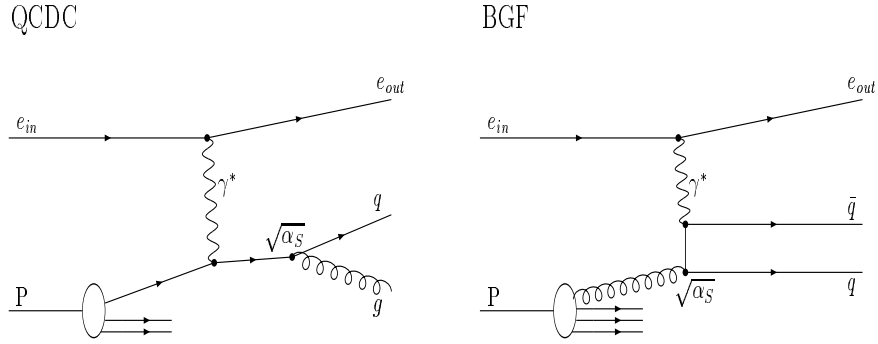
Figure 5.1: Feynman diagrams for the $O(\alpha_s)$ processes in DIS.

no QCD vertices but additional diagrams of order $\mathcal{O}(\alpha_s)$ are taken into account. These are the QCD-Compton (QCDC) and Boson-Gluon Fusion (BGF) diagrams shown in figure 5.1. The QCDC diagram differs from the leading order QPM diagram only by the gluon radiation in the final state.

The event generators used in this thesis are LEPTO, HERWIG and ARIADNE. LEPTO and ARIADNE support exact matrix element calculation for DIS to order $\mathcal{O}(\alpha_{\mathrm{em}}, \alpha_s)$. HERWIG, does not explicitly add contributions from the BGF and QCDC processes, and therefore supports exact matrix element calculation to $\mathcal{O}(\alpha_{\mathrm{em}})$. The other two have the additional functionality of excluding individually QCDC and/or BGF contributions to facilitate interfacing to other generators.

5.4   Parton Cascade Models

The particles involved in the hard scattering need to be "dressed up" with a shower of low virtuality partons. Multiple parton branchings are needed to build up the shower and therefore, unlike the hard matrix element calculation, this process is no longer of fixed order in the strong coupling constant. There are several models for the

parton cascades. The parton cascade is modeled by the generation of additional partons from splitting a gluon into a $q\bar{q}$ pair or by generating additional gluon radiation. A cascade is created through iterations of this procedure. The splitting continues until the particle's virtuality approaches a low momentum transfer cut-off below which the non-perturbative hadronization must take over. The Monte Carlo programs referred to in this thesis employ two different methods of modeling the parton showers. The Matrix Element/Parton Shower (MEPS) approach is used by LEPTO and HERWIG and the Color Dipole Model (CDM) is used by ARIADNE.

5.4.1   Matrix Element Parton Showers

In DIS, QCD (gluon) radiation can occur both before and after the hard interaction as shown in figure 5.2. In the MEPS scheme showers that originate before and after the hard interaction are treated differently although they are both based on splitting functions which describe the dynamics of the branching of $q \rightarrow qg$, $g \rightarrow gg$ and $g \rightarrow q\bar{q}$. The DGLAP evolution equations describe the changing or evolution of the splitting functions with Q^2 by taking into account the leading-logarithmic terms, resummed to all orders, of the matrix element. In the leading-logarithmic picture, a shower may be viewed as a sequence of branchings of the form $a \rightarrow bc$, where a is called the mother parton and b and c, the two daughter partons. Each daughter is free to branch in its turn, so that a tree-like structure can evolve.

The final state radiation is analogous to parton radiation in $e^+e^- \rightarrow q\bar{q}$ which has been tested extensively against the data. The evolution is based on the Sudakov form factor, which expresses the probability that a parton does not branch between some initial maximum virtuality and some minimun value [55]. The virtuality of the

partons control the showers, by separating on-shell ($m^2 \approx 0$) partons and off-shell partons which are either space-like ($m^2 < 0$) or time-like ($m^2 > 0$). If a parton splits up, the sum of virtualities of the two daughter partons is less than the virtuality of the original parton. Therefore, a shower starts with a parton and generates a cascade of partons with decreasing virtuality by iterating the branching process until all the partons are on-shell, i.e. all parton virtualities are below some cutoff, typically ~ 1 GeV.

The initial state radiation is reconstructed from the hard interaction backwards, with decreasing virtuality at each splitting, to the on shell parton from the incoming nucleon. This is a more compliciated process since the parton density function must be taken into account, which reduces the amount of radiation.

By requiring that multiparticle emissions are in decreasing order in the relative angle between the two produced particles, effects due to the coherence are explicitly incorporated. However, interference terms between the initial and final state showers are neglected. The initial and final state radiation are combined with the matrix element calculation. The MEPS approach does not take into account QCD emissions from the proton remnant.

5.4.2   Color Dipole Model

An alternative approach inspired by classic dipole radiation is implemented in ARIADNE. The struck quark and the proton remnant carry color and anti-color charge, and therefore they can be interpreted as a dipole. The algorithm of the Color Dipole Model (CDM) [56] relies on the assumption that gluon radiation can be calculated in a dipole approximation. In contrast to the MEPS approach, here the inital and
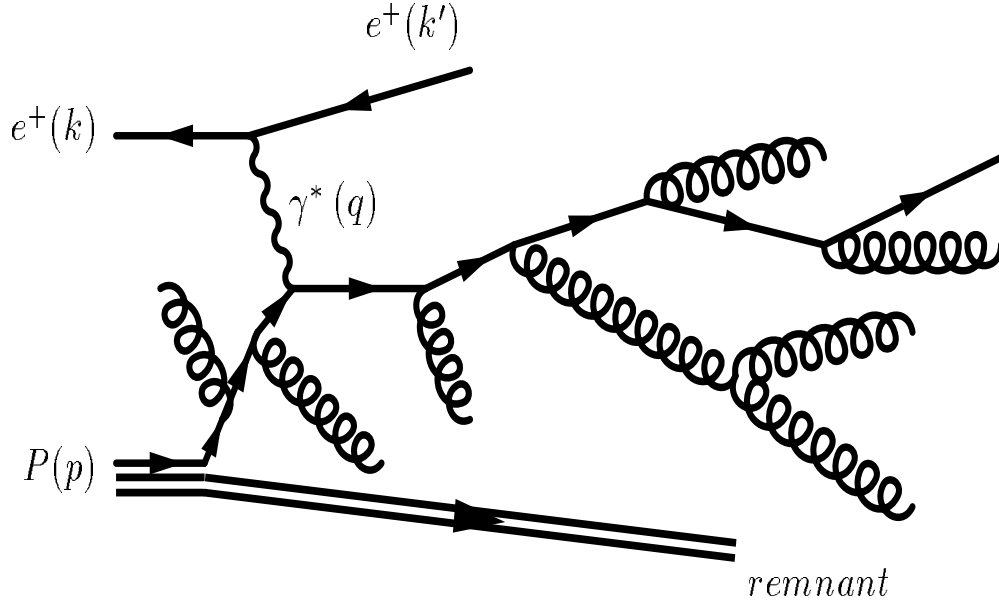
Figure 5.2: Matrix-Element/Parton Shower (MEPS) approach to parton cascade. The parton cascade is treated as successive branching sof partons with decreasing virtuality.

final state radition are modeled in the same manner. The radiation process can be seen as a modified e^+e^- reaction with one of the quarks from the hard interaction substituted for the proton remnant as shown in figure 5.3. Because the radiated gluon itself carries color, two new dipoles are created; one between the struck quark and the gluon and one between the proton remnant and the gluon. The process is repeated, as softer gluon emission can be treated as radiation from these two independent dipoles. To allow for the creation of quarks, an additional process is introduced that splits up a gluon into a $q\bar{q}$ pair.

Because this model is based on the e^+e^- interaction where BGF processes do not occur, the matrix elements for this process are not explicitly included in the CDM and must be added in by hand. This is done by allowing the first dipole to emit the anti-partner of the struck quark so that two color dipoles are created which continue to radiate independently according to the model. These two dipoles are meant to mimic
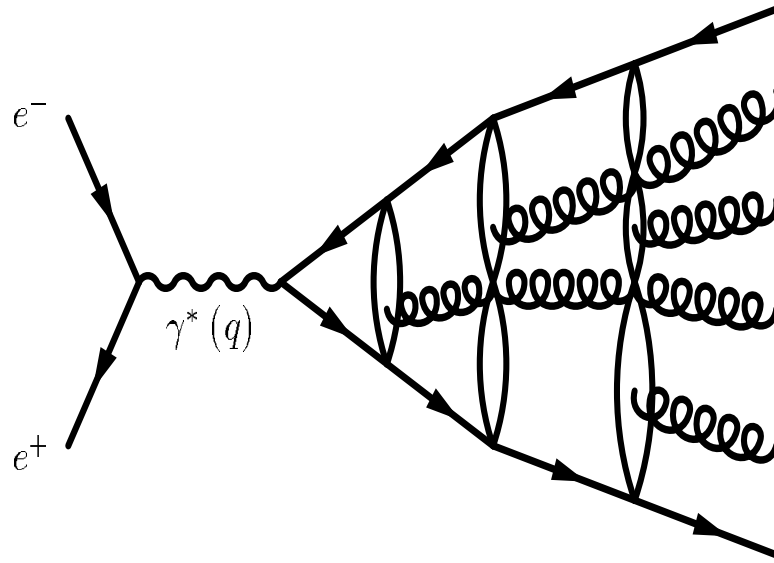
Figure 5.3: Color Dipole Model approach to parton showers. The cascade is treated as a formation of color dipoles, each of which may produce one or more softer emissions.

the color connection between each of the final state quarks with the proton remnant of a BGF process.

5.5 Hadronization

The colored partons which are the final result of the parton showers are not observable as free particles. The colored partons must be grouped into color singlet states of confined quarks and gluons called hadrons. Hadronization refers to the mechanism by which quarks and gluons produced in the hard process form the hadrons that are observed in the final state. This is an intrinsically non-perturbative process and therefore not calculable in pQCD. At present, the description of this transition of quarks and gluons to hadrons is done via phenomenological models only. Hence the measurement of the mean charged multiplicity in high-energy scattering experiments represents a test of the hadronization models. Two such models are the Lund string

model which is used by Ariadne and Lepto and the cluster fragmentation model used by Herwig.

5.5.1   Lund String Model

The Lund string model of hadronization [57], used by the Ariadne and Lepto Monte Carlos, is based on the assumption that the confinement potential between two color charges at large distances is linear. When two quarks, $q\bar{q}$, move apart from their common production point, a color field is produced between them and referred to as a color flux tube, or string. This tube or string is considered to be one-dimensional and contains energy proportional to its length, representing the force of the color connection between the partons. The string stores energy in the same way that a stretched spring does; as the $q\bar{q}$ pair continues to separate after their production, the string stretches between them, and the more it stretches, the more work is done against the recoil force of the spring, adding energy to the system. Eventually enough energy will be stored in the string to facilitate the creation of another $q\bar{q}$ pair which forms when the string breaks. The breaking of the original string results in two new strings with a quark and anti-quark on each end, which begin to evolve independently and stretch strings between them. The process is shown schematically in figures 5.4 and 5.5. The process continues until the invariant mass of any string segment is below a threshold value. When the splitting ceases, hadrons are formed from the colorless stable objects spanned by the string below the mass threshold.
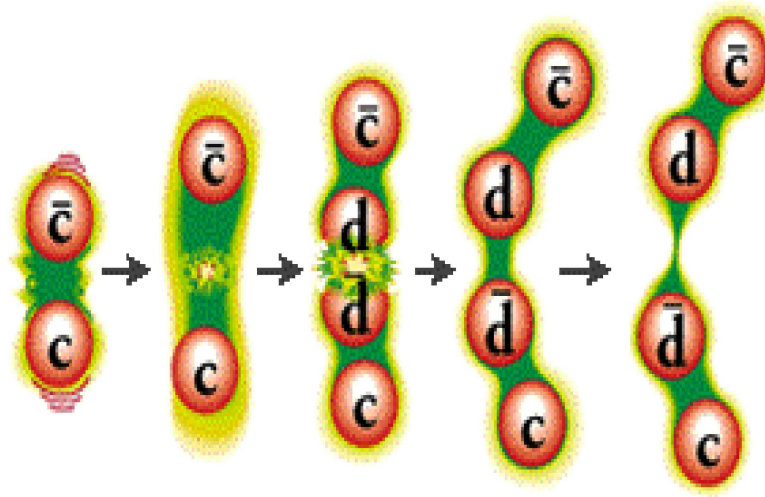
Figure 5.4: Schematic of hadronization via string breaking in the Lund String Model.

5.5.2 Cluster Fragmentation Model

A schematic of the cluster fragmentation model [58], used by the HERWIG Monte Carlo is shown in figure 5.5. After the parton shower has terminated, the outgoing gluons are non-perturbatively split into light quark anti-quark pairs, $g \rightarrow q\bar{q}$. Neighboring quarks and anti-quarks are grouped into color-singlet combinations. These color singlet combinations are assumed to form clusters, which mostly undergo simple isotropic decay into pairs of observable hadrons according to their masses. The cluster masses peak at low values due to the preconfinement property of the QCD parton shower. If a cluster is too light to form two hadrons, it is presumed to be the lightest hadron of its flavor and its mass is shifted to the correct value via the exchange of momentum with the neighboring cluster.
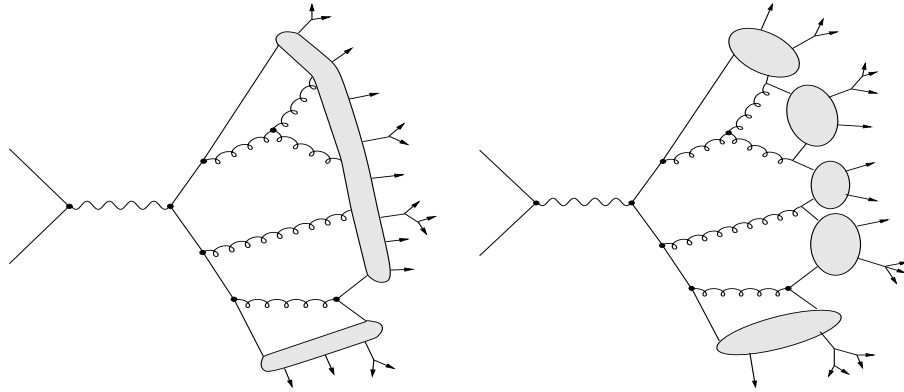
Figure 5.5: Diagrams of the hadronization schemes according to the Lund string model (left) and the Cluster Fragmentation Model (right). The shaded regions of each drawing represent the strings and clusters, and the outgoing arrows represent hadrons [59].

5.6 Detector Simulation

The hadrons that emerge from the hadronization process are then fed into a simulation of the complete ZEUS detector. The program performing this task, MOZART [29] is based on the GEANT package [60] and incorporates our best knowledge of the detector material composition and geometry, supported by the test beam data as well as experience gained through previous data collection. Four-vectors from the event generator are tracked through the detector, fully simulating interactions with material in the detector, acceptance and detector response and signal quality. Decisions of the ZEUS trigger are calculated separately by a program called ZGANA [61]. Both simulation utilities are updated according to the detector configuration and therefore exist in versions valid for specific running periods. The resulting information about the simulated events is stored in a format identical to those originating from the readout electronics of the ZEUS detector, which allows analysis in the same way. The fully simulated events are passed through the reconstruction procedure in a manner identical to that applied to real data described in chapter 4 and then they

are subject to the data selection criteria to be discussed in chapter 6.

5.7   Monte Carlo used in this Analysis

Samples of neutral current DIS events were generated using the Heracles 4.6.1 [62] MC program with the Djangoh 1.1 [63] interface to the hadronisation programs. The QCD cascade is simulated using the colour dipole model as implemented in Ariadne 4.08 [64] or with the MEPS model of Lepto 6.5 [65]. Both Ariadne and Lepto use the Lund string model for the hadronisation. A special high Q^2 treatment for Ariadne discussed in [66] has been turned on and off to check the effect on the results. The high Q^2 treatment is a tuning of the Monte Carlo designed to describe the high energy data. All event samples were generated using the CTEQ4D [53] parameterization of the parton distribution functions in the proton. The MC program Herwig 6.100 [67] with cluster hadronization model has been used to check the effect of the different hadronisation scheme on the unfolding procedure. The generated hadron distributions do not include charged particles produced from weak decays with lifetimes below $3 \cdot 10^{-10}$ seconds. The charged-particle decay products of K_S^0 and Λ were excluded. This was done in order to ensure the uniformity of the definition of the final state in all the experiments that are compared in this analysis.

Chapter 6

Event Selection

An inclusive sample of neutral current DIS events was selected from HERA I data taken with the ZEUS detector during the years 1996 and 1997. The final sample of events that was used for this measurement were selected in two stages, online and offline. The cuts applied by the three level trigger system system (described in section 3.2.4) constitute the first (online) selection. The events passing the online selection have met certain trigger criteria which are designed to meet the bandwidth and storage limitations of the ZEUS data acquisition system, and to minimize the loss of events relevant to the measurement in the kinematic range of interest. After the data are selected by the trigger and the events are fully reconstructed as described in chapter 4, the data undergoes an offline selection where the specific events to be analyzed are chosen. These offline cuts are designed to further reduce background and to select the pertinent kinematic region for analysis. This chapter outlines the event selection procedure for this analysis and explains the trigger conditions and offline cuts.

6.1   Online Event Selection

Online event selection is made at all three levels of the ZEUS trigger system, FLT, SLT and TLT. Because the defining characteristic of a neutral current DIS event is the presence of a scattered electron in the final state, the trigger is designed to efficiently detect the presence of a scattered electron. The accuracy of the information available from the CAL and CTD improves at each subsequent trigger level due to the larger amount of information and increased calculation time available. The requirements for an event to pass become increasingly more strict as the event moves through each trigger level. The online requirements made in the trigger are much less restrictive than the final requirements made in the offline selection.

Each trigger level is decomposed into sets of requirements and associated logic which are grouped together into trigger "slots". The trigger slots provide a binary decision on whether a given event is preserved or rejected and these decisions for a trigger level are grouped into trigger words, made up of bits which store the logical decision for each requirement. This provides a rapid mechanism for filtering events based on small trigger words stored with the event. In this way the trigger is able to produce an event sample for many types of physics events, depending on the trigger slots chosen at each level. The various trigger slots that are chosen at each level for a particular analysis are referred to as the trigger chain.

In general, when choosing a particular trigger chain the following should be considered:

- The trigger cuts a certain number of physics events along with the background. This can cause some regions of phase space to have an acceptance that is difficult

to determine. Therefore, the trigger chain chosen should consist of a small number of trigger slots which have a good acceptance in the pertinent region of phase space.

- Some events which are rejected by the trigger correspond to an event simulated in the Monte Carlo which passes all cuts and ends up in the final sample. To avoid a discrepancy between data and Monte Carlo, the simulated events should be filtered through the same trigger chain as the data.

- Certain trigger slots are prescaled, i.e. they take only every Nth event of all those they trigger on, where N is the prescale value. The effective luminosity for prescaled slots is different from non-prescaled slots and dealt with by giving different weights for these events. These events should be given a weight based on the effective luminosity for the prescale slots. The statistical error can become larger if a large fraction of events comes from prescaled triggers since the error corresponds to the effective luminosity. The trigger chain used in this analysis contains no prescaled slots.

The trigger chain used for this analysis is a combination of FLT, SLT and TLT slots which are well understood and simulated for Monte Carlo events. For the selection of DIS events, the TLT slot used is the so-called "medium Q^2" DIS trigger (DIS03). Before passing the DIS03 TLT slot, it is necessary that one of the corresponding FLT and SLT slots took the event. The DIS03 trigger slot has a particular configuration of FLT and SLT slots for which it works reliably. These are described below.

6.1.1 First Level Trigger (FLT)

Possible DIS candidates are loosely identified and selected at the first stage of triggering from information taken from the CFLT and CTD FLT. The CFLT provides locally identified electron candidates and global sums such as the total energy or total transverse energy deposited in the CAL. The CTD FLT uses loose tracking requirements to select events with "good tracks". In order for a track in the CTD to be considered a "good track" at the level of the CTD FLT, it must have a z-position in the first superlayer between -50 cm and 80 cm and point to the reconstructed vertex. Other CTD tracks are considered for triggering if they pass some minimal quality cuts. The information from the CFLT and CTD FLT is used in combination to distinguish classes of real physics events which may contain an electron in the final state.

The FLT provides several logic bits dealing with energy deposits in the electromagnetic section of the CAL. The bits are set when a deposit exists greater than some tunable threshold. The relevant bits for selecting DIS events for 1996-97 are:

- The **RCAL-IsoE** bit selects events with isolated electromagnetic deposits in the RCAL. The towers are summed in groups of 4; a group with an electromagnetic deposit must be surrounded by quiet towers.

- The **REMCth** bit requires the total energy in the electromagnetic section of the RCAL to be greater than 3.75 GeV

- The **REMC** bit is set for events with a total energy in the electromagnetic section of the RCAL to be greater than 3.4 GeV (excluding towers next to the

RCAL beam-pipe hole).

- The **BEMC** bit selects events with a total energy in the electromagnetic section of the BCAL to be greater than 4.8 GeV.

- The **SRTDgood** veto requires a detected signal in SRTD with acceptable timing.

- The **anyTRK** veto requires at least one good track found by the CTD FLT.

For the analysis described in this thesis, the GFLT selects events based on the following two slots, which are logical combinations of the bits described above.

- Slot 30 = **RCAL-IsoE** .and. (**SRTDgood** .or. **REMCth**)

- Slot 44 = (**BEMC** .and. **anyTRK**) .or. **REMC**

The efficiency of these slots has been measured as a function of Q^2, [68] and is high for Q^2 above 4 GeV. Based on the data collected in 1993, the efficiency of the slots was estimated to be around 98% [35].

6.1.2 Second Level Trigger (SLT)

Unlike the FLT which is hardware based, the SLT is software based, running on dedicated commercial processor hardware. This allows the SLT to calculate more sophisticated quantities and create a more accurate overview of the event. Information about the global timing, the total energy and total momentum in the CAL, and energy imbalances in the CAL cells is used to "veto" events to reject the most severe backgrounds.

Cuts on the timing in the CAL are effective for reducing beam-gas events. These types of events can be identified by differences in the arrival times of particles in the RCAL and FCAL, as described in section 3.2.2. Beam-gas background can also be rejected by vetoing events where the total $E - p_z$ in the CAL is above 75 GeV, where E is the total energy and p_z is the total longitudinal momentum of the event. This requirement is well above the kinematic bound of twice the electron beam energy, $2 \cdot E_e = 55$ GeV, for DIS events. The calculation of $E - p_z$ is described below, and in equation 4.5. The global timing information is also used to veto the relatively small cosmic ray background. The signature of these events is no energy in the FCAL or RCAL, and a difference in the up-down timing of the energy deposits in the BCAL. CAL cell imbalance information is used to remove fake scattered electrons. These fakes can appear when random discharges of static energy occur between a PMT base and its shielding causing a large and isolated energy deposit in the CAL which can mimic a high energy electron. These occurrences are characterized by a large energy imbalance in the cell, and are easily identified and removed. These vetoes are essentially independent of the physics analysis filtering.

If an event survives the SLT vetoes, it must be accepted by the DIS filter. This requires the event to have an $E - p_z$ that is sufficiently high.

$$\delta = E - P_z = \sum_i E_i - P_{z,i} = \sum_i \delta_i \tag{6.1}$$

The sum is over all final state particles. In the ZEUS coordinate system, this quantity is small for very forward particles. It is therefore dominated by the energy of the positron since, for the initial state $E_e = -P_{z,e}$, and $\delta \simeq 2 \cdot E_e = 55$ GeV. δ is a conserved quantity, so we can infer the existence of a final state positron in the CAL

by a value of δ close to 55 GeV.

At the trigger level, an approximation is made, and δ is calculated from the CAL info:

$$\delta = \sum_i E_i(1 - \cos\theta_i) \tag{6.2}$$

where the sum runs over the CAL cells, and θ_i is the polar angle of each cell. The requirement made at the SLT is:

$$\delta' = \delta + 2E_\gamma^{LUMI} > 29 \text{ GeV} \tag{6.3}$$

The energy of the LUMI photon tagger (section 3.2.5), E_γ^{LUMI}, has been included to keep events with tagged initial state radiation.

In addition to the $E - p_z$ requirement, there are various DIS filters available at the second level. The data sample for this analysis was expected to satisfy each of the following conditions which comprise the DIS01 filter:

- the event must have passed at least one of the DIS triggers at the FLT, or must have a high total $E_t > 25$ GeV,

- the total deposits in the electromagnetic sections of either RCAL, BCAL or FCAL are required to have energy greater than 2.5 GeV, or the energy in the hadronic sections of FCAL exceeds 2.5 GeV.

The first requirement of the DIS01 filter increases the acceptance for high Q^2 events, and the second requirement was designed to reject events that are basically empty from the CAL point of view.

The logic and cuts were stable throughout the 1996-97 running period covered by this analysis.

6.1.3   Third Level trigger (TLT)

The third level trigger concludes the online selection. Like the SLT, the TLT is software based, but run on commodity processors, and here, all the data pertaining to the considered events is available. Each event is almost completely analyzed at this stage and nearly all event quantities have been calculated.

Of the multiple DIS filters at the TLT, the so-called "medium Q^2" filter (DIS03) was chosen for this analysis. The DIS03 filter requires that events meet all of the following criteria:

- the event has passed any DIS bit at FLT,

- the $E - p_z + 2 \cdot E_\gamma$ is required to be above 30 GeV,

- a redundant demand of $E - p_z < 100$ GeV,

- a scattered electron candidate identified by SINISTRA (described in section 4.3) with an energy greater than 4 GeV,

- the impact position of the scattered positron on the face of the RCAL outside a circle with a radius of 25 cm centered on the beam-pipe.

The events that satisfy these criteria are then made available to the offline analysis.

6.2   Offline Preselection

After the data have passed all the requirements of the trigger chain, it is analyzed using the full offline reconstruction software package. At this point, the final

calibration for all components is available, and any miscellaneous information such as bad running periods or bad channel lists is incorporated. A reduced event record, which contains enough information to determine the event kinematics is written to Data Summary Tables (DSTs). It is from the DSTs that the final event selection is made.

Various selection algorithms are run on the DSTs in a manner analogous to a fourth level of triggering. These decisions are also stored in bits for economy of storage. The events chosen for this analysis required that DST bit 9 is true. Bit 9 is a logical .OR. of four positron finders (of which SINISTRA [45] is one) and is true if any one of them found a positron with $E_{e'} > 4$ GeV.

Records of runs affected by detector malfunctions and other problems than can affect data quality are kept in a centrally maintained database accessed through a routine called EVTAKE. Only data satisfying the following minimum requirements on the detector condition are accepted:

- the LUMI monitor was fully functional,

- the magnetic field was on,

- the CTD was operating at full high voltage with no large dead regions,

- the CAL was operational with an insignificant number of dead channels,

- the interaction vertex was not shifted[1].

After EVTAKE selection, the integrated luminosity is $38.2pb^{-1}$.

---

[1]Occasionaly runs are taken with an intentionally shifted vertex and these runs are excluded

6.3 Track Selection

This analysis used a set of tracks reconstructed by the VCTRACK package as described in section 4.1. The online track selection criteria are mainly governed by the acceptance of the CTD and the limitations of the reconstruction algorithm. As a result they have a lot in common with the cuts used in earlier analyses of charged particles [69] although some differences are present. Tracks were selected for analysis if they

- were assigned to the primary vertex,

- were not matched to the SINISTRA electron,

- had a transverse momentum $p_t > 0.15$ GeV,

- had a pseudorapidity as measured in the lab frame $|\eta_{\mathrm{lab}}| < 1.75$,

- had hits in the three innermost superlayers of the CTD,

In addition to the criteria listed above, the tracks were required to be in the current region of the Breit frame or the photon region of the HCM frame (described in sections 2.1.1 and 2.1.2) for the measurements done in these reference frames.

6.4 Identification of Scattered Positron

As previously mentioned, the presence of a scattered positron is the primary signature that distinguishes NC DIS from other processes. As described in section 4.3, good quality positrons are found by the SINISTRA electron finder which is run over all energy deposits in the CAL. If a positron candidate has been found (with a probability

of at least 0.9) the event is accepted and the energy deposits belonging to that electron are removed from the further analysis. The track associated with the positron is identified and removed from the list of accepted tracks for the event. A cut on the energy of the scattered positron of $E_{e'} > 12$ GeV is made to ensure a high purity and efficiency of the electron finder. This cut is made on the positron energy after the corrections for energy losses in the dead material (described in section 3.2.6) have been applied. The reconstruction of the positron is difficult near the beam pipe region therefore the impact position of the scattered positron on the face of the RCAL is required to be outside of a circle of radius 25 cm centered around the beam pipe. As mentioned earlier, this cut also reduces beam-gas background events which leave signatures in the electromagnetic section of the inner part of the RCAL.

6.5 Kinematic Selection

The cuts described in this section are applied to define the kinematic range to be analyzed. The variables that define the phase space are reconstructed using the various reconstruction methods described in section 4.4. The phase space is also defined by the same requirements for the Monte Carlo simulated events. The phase space is defined by the following requirements on Q^2, W, and y:

- $Q^2_{\mathrm{DA}} > 25 \; Gev^2$

- $70 < W_{\mathrm{DA}} < 225$ GeV

- $y_{\mathrm{el}} < 0.95$

- $y_{\mathrm{JB}} > 0.04$

For small values of y, a significant fraction of the energy may escape down the beam pipe in the forward direction, and escape detection. For these types of events, the reconstruction of the Breit frame is difficult due to the fact that an accurate determination of the kinematics is not possible. Also, for events with low values of y, there is not sufficient energy in the hadronic system to use the double angle method for reconstructing Q^2 and W. These effects may be minimized by cutting on y reconstructed using the JB method: $y_{\mathrm{JB}} > 0.04$.

Events with a misidentified electron can be identified by a characteristically high value of y obtained from the electron method. An electron can be produced in a hadronic shower with a small polar angle in the FCAL region around the beam pipe, where typically the majority of the hadronic activity is usually observed. Some of this activity includes neutral pions which can mimic electrons. Due to the kinematics, the DIS electron is bound to have an extremely high energy if detected in the FCAL, especially in the vicinity of the beam-pipe. The pion is not subject to such kinematic restrictions and, if taken as an electron candidate, leads to high values of y. These events are rejected if $y_{\mathrm{el}} > 0.95$.

6.6   Cuts on Global Quantities

DIS events are relatively rare compared to photoproduction and contribute only a small fraction of the total ep scattering cross section. The ep interaction is dominated by photoproduction where $Q^2 \approx 0$. The remaining offline cuts described in this section are placed on the event sample to further suppress the contamination of the event sample due to interactions other than DIS. As previously discussed, momentum conservation requires that the total $E - p_{\mathrm{Z}} = 2E_e = 55$ GeV for a fully contained

event. Requirements on this quantity are made from the second level trigger onwards and the final offline cut is $40 < E - p_Z < 60$ GeV with the quantities summed over the hadronic system plus electron contribution calculated after energy corrections. This range excludes both events from photoproduction as well as beam-gas events. Photo-produced events where the electron is not detected will typically have values of $E - p_Z$ which fall outside the lower range of this cut, whereas beam-gas interactions which deposit energy into the RCAL populate the high $E - p_Z$ tail. This cut also supresses radiative events with an energetic initial state photon.

In the determination of the number of charged tracks, which is one of the main measurements in this analysis, it is important to consider only those tracks which come from the hadrons produced in the hard interaction. This can be ensured by requiring that an event vertex be found. A cut on the longitudinal position of -50 cm $<$ $Z_{\mathrm{vtx}} < 50$ cm, not only requires that a vertex be found, but also ensures that the emanating tracks can be safely measured in the CTD. This cut also removes beam-gas background events which typically have vertices outside this range. Muons of any kind transversing the detector at random locations will also be cut by this requirement, as long as they do not pass through the vertex.

Along with photoproduction and DIS events, there is a contribution to the ep cross section from diffractive events. These events are not simulated by the Monte Carlo used for this analysis and therefore must be removed. These events are characterized by the lack of particles between the proton remnant and hadronic systems, a so-called rapidity gap. A distinguishing feature of an event with a rapidity gap is that the most forward energy deposit in the CAL will occur at smaller values of η, i.e

farther away from the proton direction, leaving a gap between the beam-pipe and the most forward energy deposit. Therefore, to remove these events, the pseudorapidity of the most forward energy deposit, η_{max}, as measured in the laboratory frame, is required to be greater than 3.2.

6.6.1 Binning

In each reference frame studied in this thesis, the dependence of $\langle n_{\mathrm{ch}} \rangle$ on M_{eff} or $2 \cdot E_{\mathrm{Breit}}^{\mathrm{current}}$ or W was measured. The measurements were made in bins of the energy variables. The same binning was used for the M_{eff} and $2 \cdot E_{\mathrm{Breit}}^{\mathrm{current}}$ energy scales. The bin ranges for these are shown in table 6.6.1. The measurement of $\langle n_{\mathrm{ch}} \rangle$ as a function of $2 \cdot E_{\mathrm{Breit}}^{\mathrm{current}}$ in the current region of the Breit frame was done in all seven bins, whereas in the target region of the Breit frame and in the photon region of the HCM frame, the measurement of $\langle n_{\mathrm{ch}} \rangle$ versus M_{eff} was done in the lowest 6 bins due to limited statistics in the highest energy bin. The statistics for events with $M_{\mathrm{eff}} > 10$ GeV in the current region of the Breit frame are very limited, so this measurement was done in only the first five bins of M_{eff}. The bin ranges for W are shown in table 6.6.1. The laboratory frame analysis versus M_{eff} presented in this thesis was split into kinematic bins of x and Q^2. These kinematic bins must be consistent with the resolutions in the reconstructed x and Q^2. At the same time, the size of a bin is limited by the statistics needed for a measurement of a reasonable accuracy. The x and Q^2 bins used in this analysis (for the lab frame versus M_{eff} analysis) have been based on previous multiplicity analyses where the efficiencies, purities and acceptances were studied extensively [69]. Tables 6.6.1 and 6.6.1 provide the kinematic ranges of the x and Q^2 bins.

bin	range of M_{eff} and $2 \cdot E_{\text{Breit}}^{\text{current}}$ (GeV)
1	1.5 - 4
2	4 - 8
3	8 - 12
4	12 - 20
5	20 - 30
6	30 - 45
7	45 - 100

Table 6.1: Bin ranges for M_{eff} and $2 \cdot E_{\text{Breit}}^{\text{current}}$.

bin	range of W (GeV)
1	70 - 100
2	100 - 150
3	150 - 225

Table 6.2: Bin ranges for W.

bin	range of x_{DA}
1	$6.0 - 12.0 \times 10^{-4}$
2	$1.2 - 2.4 \times 10^{-3}$
3	$2.4 - 10.0 \times 10^{-3}$
4	$1.0 - 10.0 \times 10^{-2}$

Table 6.3: Bin ranges for x_{DA}.

bin	range of Q_{DA}^2(GeV^2)
1	25 - 50
2	50 - 150
3	150 - 1200

Table 6.4: Bin ranges for Q_{DA}^2.

Chapter 7

Analysis Method

In the multiplicity analyses of e^+e^- and pp interactions, the dependence of the mean charged multiplicities on the respective center-of-mass energy has been studied. For these interactions, the center of mass energy is also the invariant mass of the produced hadrons. Recall from section 2.2.2 that in the case of the pp studies the effect of the leading particles (proton remnants) had to be properly taken out in order to compare to e^+e^-.

In our analysis of ep interactions, we also chose to measure the mean charged particle multiplicity versus the respective effective mass, M_{inv}, with the aim of comparing to the e^+e^- and pp experimetnts. For a group of N particles, the invariant mass is defined as

$$M_{\mathrm{inv}}^2 = \sum_{i=1}^{N}(E_i)^2 - \sum_{i=1}^{N}(\vec{p_i})^2 \,, \tag{7.1}$$

where E_i and $\vec{p_i}$ are the energy and (three)momentum of the i-th particle.

At the HERA ep collider, because of the large asymmetry between the e-beam and the p-beam momenta, a large part of the final hadronic system is produced near the proton and falls outside the region of acceptance of the detector. Therefore, to compare to e^+e^- and pp only hadrons belonging to the photon fragmentation region of

the hadronic center-of-mass frame (HCM)(section 2.1.1) and the current region of the Breit frame (section 2.1.2 were used. These frames are chosen because of similarities between the current (photon) region of the Breit (HCM) frame and half hemispheres of e^+e^- and pp. In addition, the hadronization of the proton remnant happens outside of these regions. Measurements were performed also in the laboratory frame and in the target region of the Breit frame, but these are not directly comparable to the e^+e^- and pp measurements. This will be discussed in more detail in chapter 9. The current chapter outlines general similarities and differences between particle production in ep and e^+e^- interactions as well as details of the analysis methods used in the Breit, HCM, and Laboratory frame and the reconstruction of the invariant mass in each case. In the last section **??** comparisons between the data and Monte Carlo predictions are shown and discussed.

7.1   Comparisons of particle production in ep and e^+e^- collisions

As explained in section 2.1.2, the current region of the Breit frame for DIS is analogous to one hemisphere of the e^+e^- interaction. But this analogy is not perfect and there are some important differences. Figure 7.1 displays two diagrams of interaction and hadron production for e^+e^- and ep. The diagram for e^+e^- (top) shows the annihilation of the electron and positron into a photon producing a $q\bar{q}$ pair which hadronizes. The time axis is from left to right and the number of particles produced, N, depends on the center of mass energy, $\sqrt{s}$. Because the hemispheres are symmetric, the number of particles produced in each hemisphere is $N/2$. The diagram
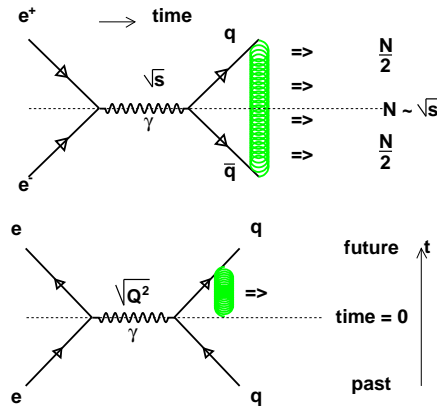
Figure 7.1: The diagram for e^+e^- (top) where electron and positron collide with energy $\sqrt{s}$ producing two quarks is compared to the diagram for ep (bottom) where the energy transferred to the struck quark is $\sqrt{Q^2}$. The upper halves of these two diagrams are identical, and therefore one hemisphere of e^+e^- is analogous to the current region of the Breit frame for ep.

for ep (bottom) shows the incoming electron scattering off a quark from the proton via the exchange of a photon with momentum $\sqrt{Q^2}$. This one hemisphere is similar to one-half hemisphere of e^+e^- where here we have $\sqrt{Q^2}$ instead of $\sqrt{s}$. The outgoing particles are the electron and the scattered quark, with the hadronization taking place between the scattered quark and the proton remnant. The time axis for this diagram is from bottom to top, and the string of hadronization coming from the struck quark is shown as a partial string and not connected to the other quark. The other quark, in this case, is the incoming quark and lies in the past section of the diagram. In Fig. 7.2 the diagrams are shown for e^+e^- (left) and ep (right) using the same time axis. One can see from this figure that the e^+e^- interaction is symmetric with two identical hemispheres. Each hemisphere of the e^+e^- interaction contains an outgoing quark and an equal portion of the hadronizing string. The current and target regions of the Breit frame for ep contain an unequal portion of the hadronizing string and
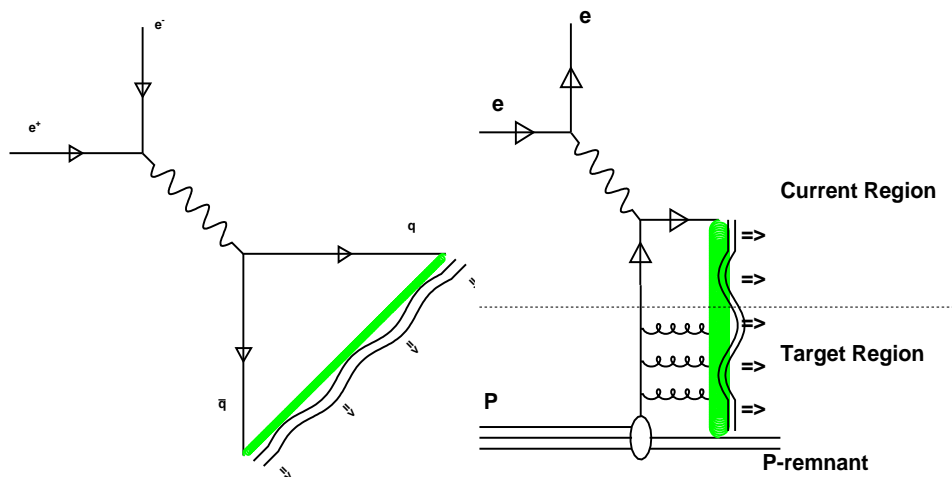
Figure 7.2: The diagram for e^+e^- (left) compared to the diagram for ep (right) shown on the same time axis, where time flows from left to right. The horizontal line divides the Breit frame into the current and target regions.

therefore a different amount of particle production occurs in each hemisphere. The target region contains the proton remnant and gluon ladder with some portion of the hadronizing string, and the current region contains the rest of the string and the struck quark. The asymmetry between the current and target regions of the Breit frame is evident in Fig 7.3. This figure shows the ep interaction in the Breit frame (compare to figure 2.1), along with the hadronization string connecting the struck quark and the proton remnant. The vertical line separates the current region and the target region. In the current region the incoming quark (as part of the proton) interacts with the virtual photon and scatters back along the same axis. The hadronizing string stretches between the struck quark and the proton remnant, crossing the boundary between the current and target regions. The proton remnant hadronizes in the target region.
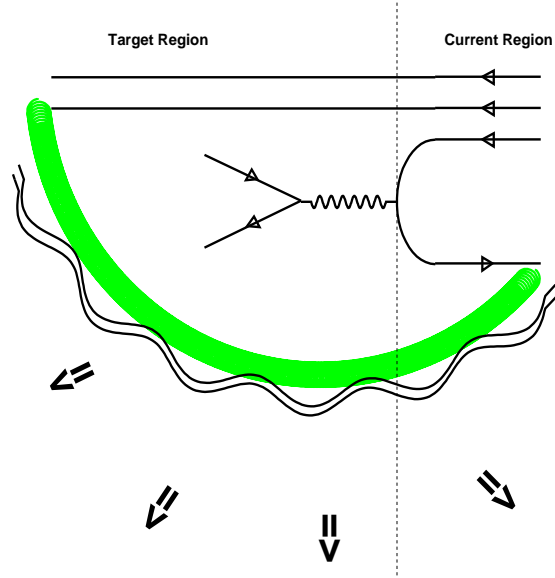
Figure 7.3: The typical diagram of an ep interaction in the Breit frame, but shown with the hadronizing string between the struck quark and the proton remnant. The vertical line divides the current region from the target region. This diagram emphasizes the asymmetry in terms of hadronization for the two regions of the Breit frame.

7.2   Current Region of the Breit Frame

The similarities between the current region of the Breit frame in DIS and one hemisphere in e^+e^-, which was introduced in 2.1.2 and illustrated in figure 2.1, have been previously exploited by ZEUS (see section 2.2.4) for comparing multiplicity measurements for the two interactions. In the analysis presented in this thesis, we also use the current region fo the Breit frame to compare the $\langle n_{\mathrm{ch}} \rangle$ in ep to that in e^+e^-. As stated in section 2.2.4 and shown in figure 2.3, the previous ZEUS measurement found reasonable agreement between e^+e^- and ep when comparing the $\langle n_{\mathrm{ch}} \rangle$ in the current region of the Breit frame as a function of Q^2 in ep with $\langle n_{\mathrm{ch}} \rangle/2$ as a function of $\sqrt{s}$ in e^+e^-, for the region above 8 GeV, while the region below 6-8 GeV shows some disagreement.
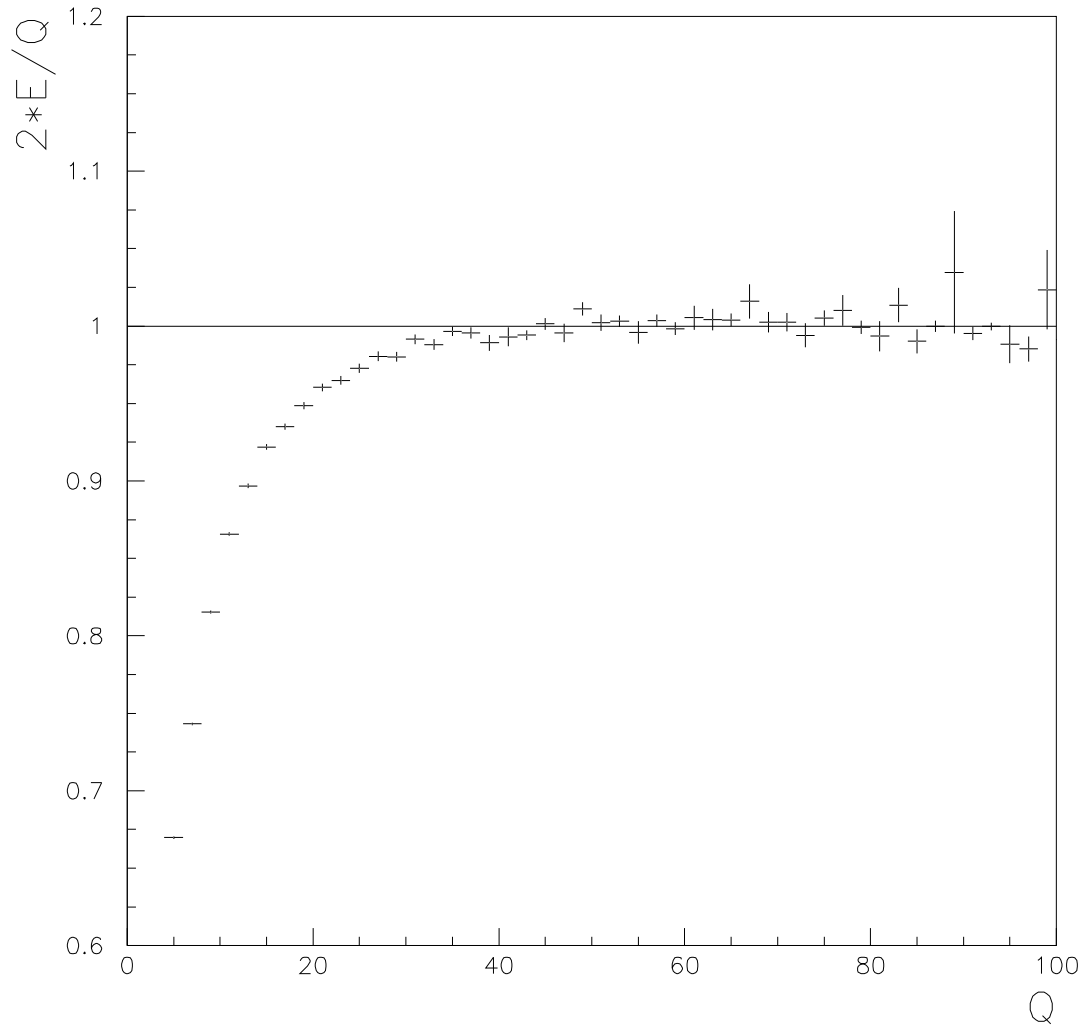
Figure 7.4: Ratio of twice the total energy in the current hemisphere of the Breit frame, $2 \cdot E_{\mathrm{current}}$ to Q as a function of Q as predicted by ARIADNE. The discrepancy between the actual energy in the current region and $Q/2$ is more pronounced at lower values of Q because migrations from the current region into the target region of the Breit frame are more likely at lower energies.

The reason of disagreement can be understood as follows. For the quark-parton model (QPM) type of events, where the struck quark moves backwards in the current region of the Breit frame, carrying a momentum of $Q/2$, twice the energy in the current region, $2 \cdot E_{\text{Breit}}^{\text{current}}$, is equal to Q. It is the same as for the e^+e^- case, where the total energy of the collision, $\sqrt{s}$, is equally divided between two hemispheres. Allowing for gluon radiation changes the picture [70]. In e^+e^- particles will migrate within the total sphere, such that the total energy will stay the same, but in the ep case they can escape the current region into the target region. The available energy in the current region is no longer $Q/2$ and, therefore, measuring $\langle n_{\text{ch}} \rangle$ as a function of Q overestimates the real energy available in the current region. In order to compensate for these migrations, we measure $\langle n_{\text{ch}} \rangle$ as a function of the actual energy measured in the Breit frame, multiplied by two (for the two hemispheres of an e^+e^- interaction). Using $M_{\text{inv}} = 2 \cdot E_{\text{Breit}}^{\text{current}}$ as a scale properly compensates for migrating particles and their corresponding energy. Figure 7.4 shows the ratio of twice the total energy in the current hemisphere of the Breit frame, $2 \cdot E_{\text{Breit}}^{\text{current}}$, to Q as a function of Q as predicted by ARIADNE. The discrepancy between the actual energy in the current region and Q/2 is more pronounced at lower values of Q as expected since migrations from the current region into the target region of the Breit frame are more likely at lower energies. One can see from this plot that $Q/2$ is accurate as measure of the energy in the current region of the Breit frame only at larger energies. Using the $2 \cdot E_{\text{Breit}}^{\text{current}}$ as the energy scale for comapring the nch of ep to thatin e^+e^- is a method to compensate for migrating particles and their corresponding energy.

The hadronic system of the current region used in this analysis is almost fully

(about 95%) contained within the acceptance of the CTD. The acceptance for the target region of the Breit frame is only about 30%, making measurement of the target charged multiplicity strongly biased by the corrections for the invisible part.

7.3   Photon Hemisphere of the HCM Frame

In an analogous method to the one used in the Breit frame in the photon hemisphere of the HCM frame, we measured the $\langle n_{\mathrm{ch}} \rangle$ as a function of twice the energy in the photon region fo the HCM frame, $2 \cdot E_{\mathrm{HCM}}^{\mathrm{photon}}$. By construction of the HCM frame, the energy that goes into each hemisphere is $W/2$. This frame is also called the $\gamma^* P$ center of mass frame. The multiplicity in the DIS HCM frame is usually studied as a function of W [71, 72, 73, 74]. It has been found that in the HERA kinematic region the $E_{\mathrm{HCM}}^{\mathrm{photon}}$ coincides with $W/2$ within $0.3 - 0.4\%$. Figure 7.5 shows the ratio of twice the total energy in the photon hemisphere of the HCM frame to W as a function of W as predicted by Ariadne. This ratio has been fit to a line with a negative slope of the order $\sim 10^{-4}$ GeV^{-1}. The difference between $2 \cdot E_{\mathrm{HCM}}^{\mathrm{photon}}$ and W is negligible, migrations between hemispheres are small, and $2 \cdot E_{\mathrm{HCM}}^{\mathrm{photon}} = W$. Therefore, because we want to measure the dependence of $\langle n_{\mathrm{ch}} \rangle$ on the M_{inv} as we did in the Breit frame, we take $M_{\mathrm{inv}} = W$. As before, the $\langle n_{\mathrm{ch}} \rangle$ must be multiplied by two when comparing to $e^+ e^-$.

The advantage of moving to the HCM frame is multifold. All particles visible in the detector are contained in the photon region of the HCM frame. The part of the fianl state that is invisible due to detector acceptence is comprised of not more than $20 - 40\%$ making the corrections reasonably small. The particles from the proton
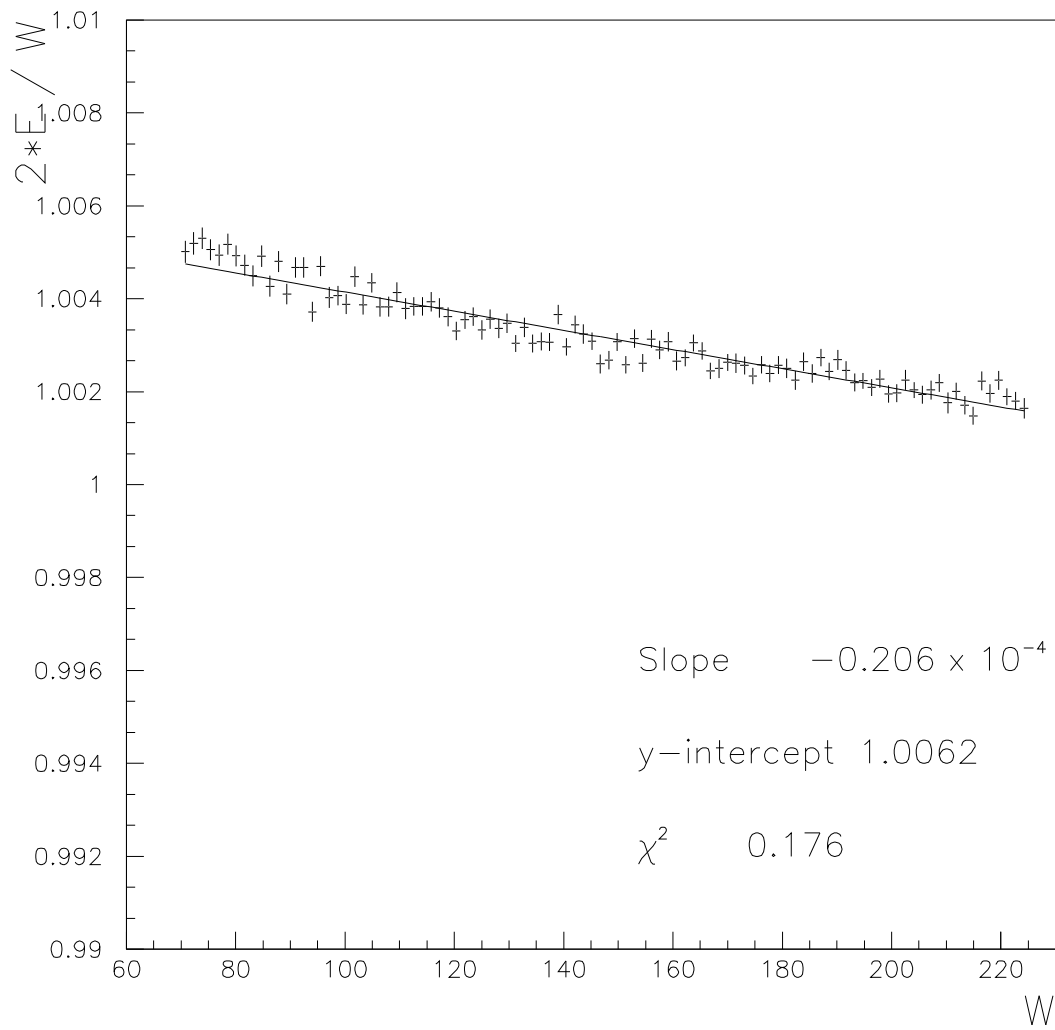
Figure 7.5: Ratio of twice the total energy in the photon hemisphere of the HCM frame, $2 \cdot E_{\mathrm{HCM}}^{\mathrm{photon}}$ to W as a function of W as predicted by ARIADNE. A linear fit to the data is shown with the slope and y-intercept. The difference between the energy measured in the photon hemisphere and $W/2$ is negligible.

remnants go only into the proton fragmentation region and can be easily separated.

7.4   Invariant Mass of the Hadronic System

Following the idea of using the energy available for hadronisation used by the pp experiments to study the dependence of the $\langle n_{\mathrm{ch}} \rangle$ [25], the charged multiplicities for ep DIS in the current and target regions of the Breit frame, and the photon region of the HCM frame can be compared as a function of the invariant mass of the corresponding hadronic system.

Previous studies at ZEUS have measured the hadronic system in the laboratory frame using the invariant mass of the corresponding hadronic system [27]. ZEUS ep DIS measurements of $\langle n_{\mathrm{ch}} \rangle$ in the current region of the Breit frame have also been compared to ep measurements of $\langle n_{\mathrm{ch}} \rangle$ in the target region of the Breit frame [75], though these measurements used Q as a scale rather than the invariant mass of the hadronic system as a scale.

In this analysis the invariant mass of the final state hadronic system is reconstructed from the energy and momenta of the hadrons as:

$$M_{\mathrm{eff}}^2 = \left(\sum_i E_i\right)^2 - \left(\sum_i P_{X_i}\right)^2 - \left(\sum_i P_{Y_i}\right)^2 - \left(\sum_i P_{Z_i}\right)^2 , \qquad (7.2)$$

where the sum runs over the calorimeter ZUFOs or hadrons of the system, in the case of the hadron level MC.

It is important to note, that the sum runs over all particles, charged and neutral. For all particles in e^+e^- or pp, $M_{\mathrm{eff}} = \sqrt{s}_{ee,pp}$ and if the leading particles are excluded in the pp case, $M_{\mathrm{eff}} = \sqrt{(q_{\mathrm{tot}}^{\mathrm{had}})^2}$ (see equation 2.1).

Analysis	Invariant Mass Reconstruction
e^+e^-	$M_{\mathrm{inv}} = \sqrt{s}$
pp	$M_{\mathrm{inv}} = \sqrt{(q_{\mathrm{tot}}^{\mathrm{had}})^2}$
ep current reg. Breit frame	$M_{\mathrm{inv}} = 2 \cdot E_{\mathrm{Breit}}^{\mathrm{current}}$
ep γ reg. HCM frame	$M_{\mathrm{inv}} = 2 \cdot E_{\mathrm{HCM}}^{\mathrm{photon}}$
ep Breit, HCM and Lab	$M_{\mathrm{inv}} = (\sum_i E_i)^2 - (\sum_i P_{X_i})^2 - (\sum_i P_{Y_i})^2 - (\sum_i P_{Z_i})^2$

Table 7.1: A summary of the various methods for reconstructing the invariant mass for e^+e^-, pp and e^+e^-.

For each measurement the sums run only over the portion of the hadrons that are visible in the detector. The visible part of the detector is defined as the range of pseudorapidity where the accaptance in the CTD is good. This corresponds to a range of $-1.75 < \eta_{\mathrm{lab}} < 1.75$, where η_{lab} is the pseudorapisity measured in the laboratory frame. For these measurements the charged multiplicity is measured in the visible region and the M_{eff} is measured in the corresponding range of η_{lab}. In addition, for the $\langle n_{\mathrm{ch}} \rangle$ measurements in the non-laboratory reference frames, the sums run only over part of the hadronic system, e.g. the current region of the Breit frame, the target region of the Breit frame or the photon region of the HCM frame.

7.5 Summary of the Invariant Mass Reconstruction

The different methods for the reconstruction of the invariant mass are summarized in table 7.5.

7.6 Comparison of Monte Carlo and Data

In order to reliably unfold the data to the hadron level, the detector level Monte Carlo predictions must reasonably describe the data distributions of the various kine-

matic variables. Both ARIADNE and LEPTO were used to unfold the data and therefore comparisons between the data and detector level were made for both Monte Carlos and are shown in Figs. 7.6 through 7.10.

Shown in Figs. 7.6 and 7.7 are the kinematic variables associated with the scattered positron: energy ($E_{e'}$), angle ($\theta_{e'}$), and the x and y position. A good description of the positron variables is necessary for accurate selection of DIS events and assures the accuracy of the Lorentz boost between the laboratory and the Breit or HCM frame. Fig. 7.8 shows the variables associated with the energy scale of the interaction, Q^2 and W, which were reconstructed using the Double-Angle method described in section 4.4.3. Both ARIADNE and LEPTO agree well with the data for the positron and energy scale variables.

Figure 7.9 shows the comparisons for the number of reconstructed tracks in the CTD, N_{tracks}, and the effective mass, M_{eff}, reconstructed from the ZUFOs [44]. Both N_{tracks} and M_{eff} are reasonably described by both Monte Carlos, with ARIADNE giving a better description of N_{tracks} and LEPTO giving a better description of M_{eff}.

Figure 7.10 shows the distributions for the total $E - p_{\text{z}}$ and y_{Bj}, which was reconstructed using both Jacquet Blondel (y_{JB}) and electron methods (y_{el}) as described in sections 4.4.2 and 4.4.1. The $E - p_{\text{z}}$ distribution is generally described allthough the Monte Carlo has a small shift with respect to the data. This results in a systematic error for the measurement, however this systematic effect was found to be very small, as shown in section 9.6. Both LEPTO and ARIADNE describe the reconstructed y_{JB} and y_{el}.

Figure 7.11 shows the longitudinal component of the event vertex, Z_{vtx}. The
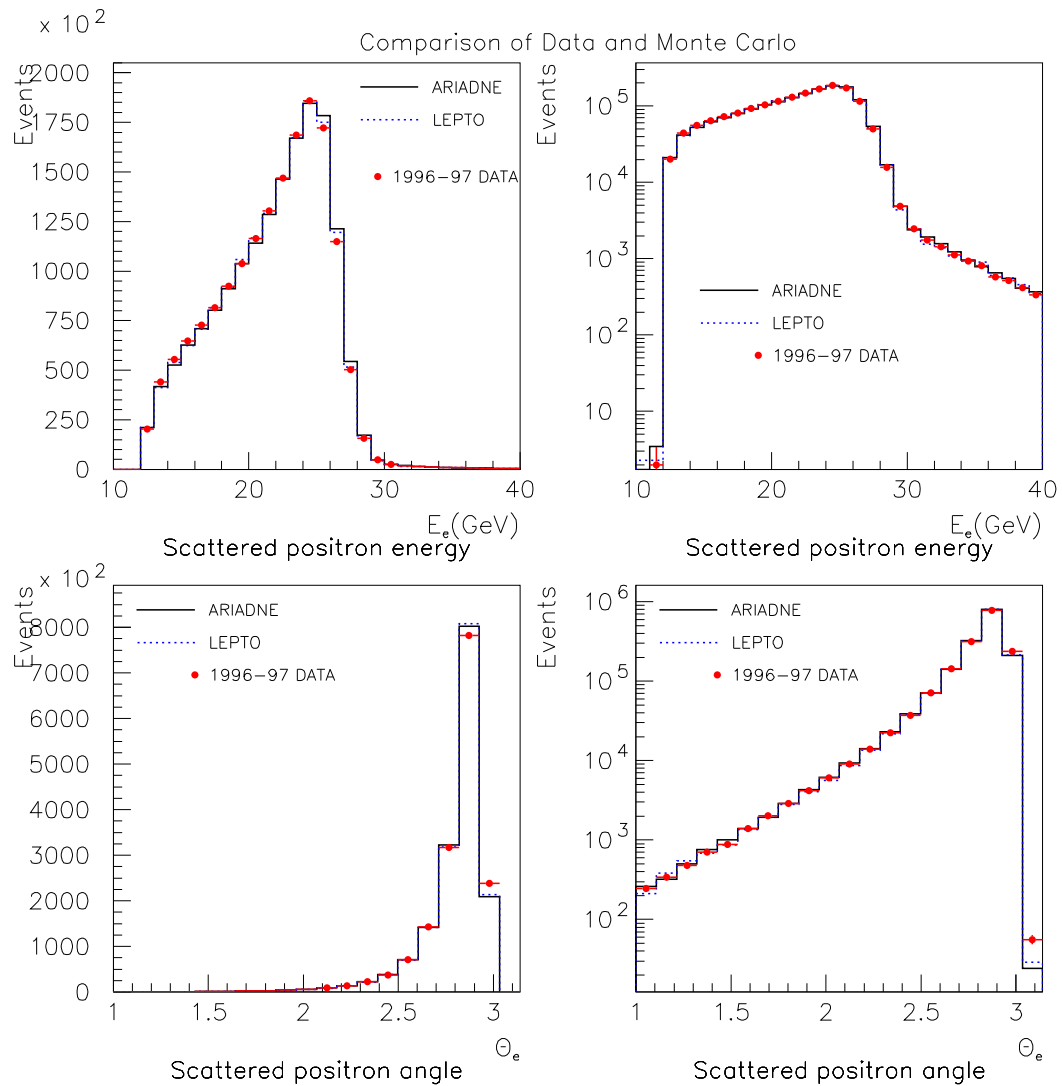
Figure 7.6: Comparison of the data and MC for the energy and angle of the scattered positron. The data are compared to ARIADNE and LEPTO, both of which are generated with $Q^2 > 20$ GeV^2. The MC distributions are normalized to the number of events in the data. The plots are shown in linear scale on the left and log scale on the right.
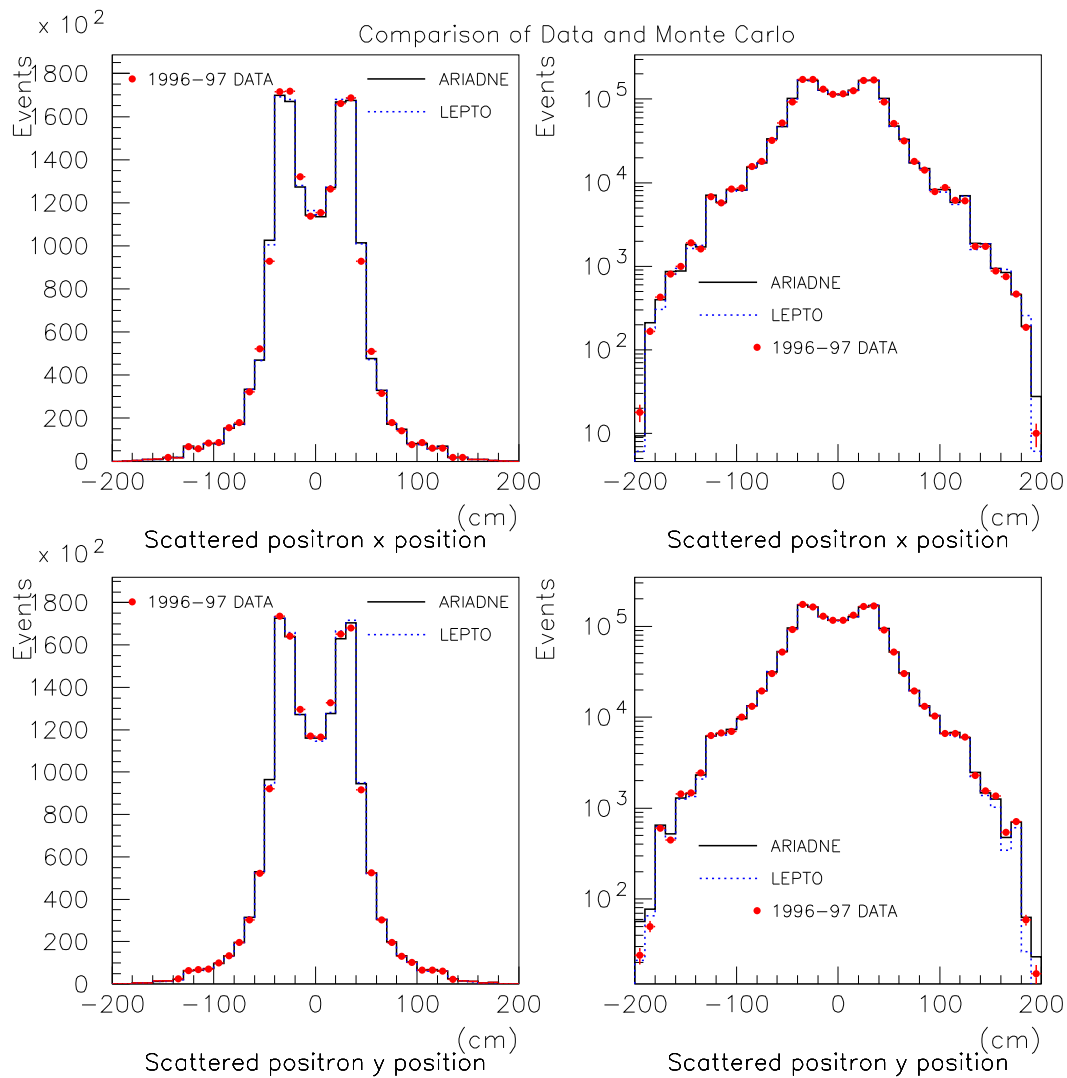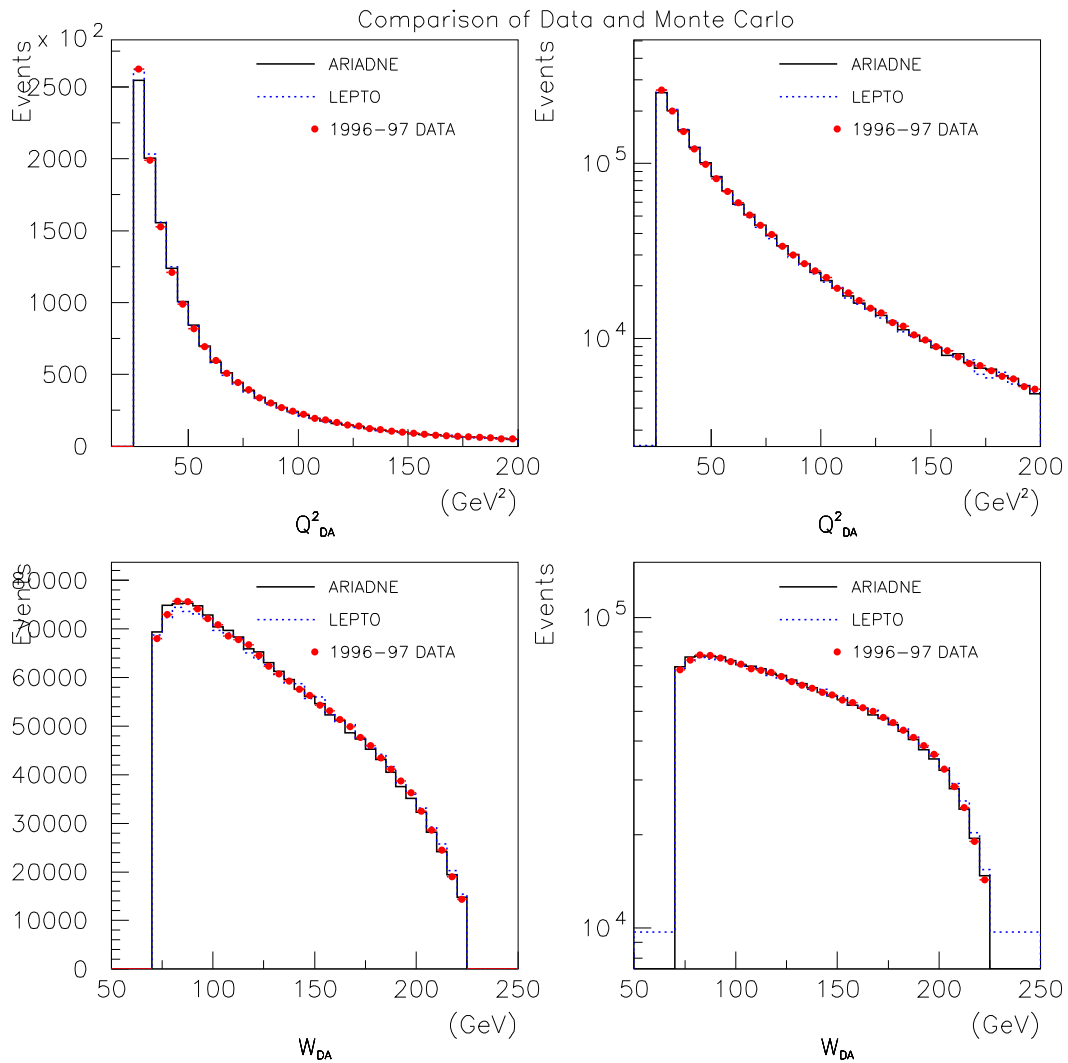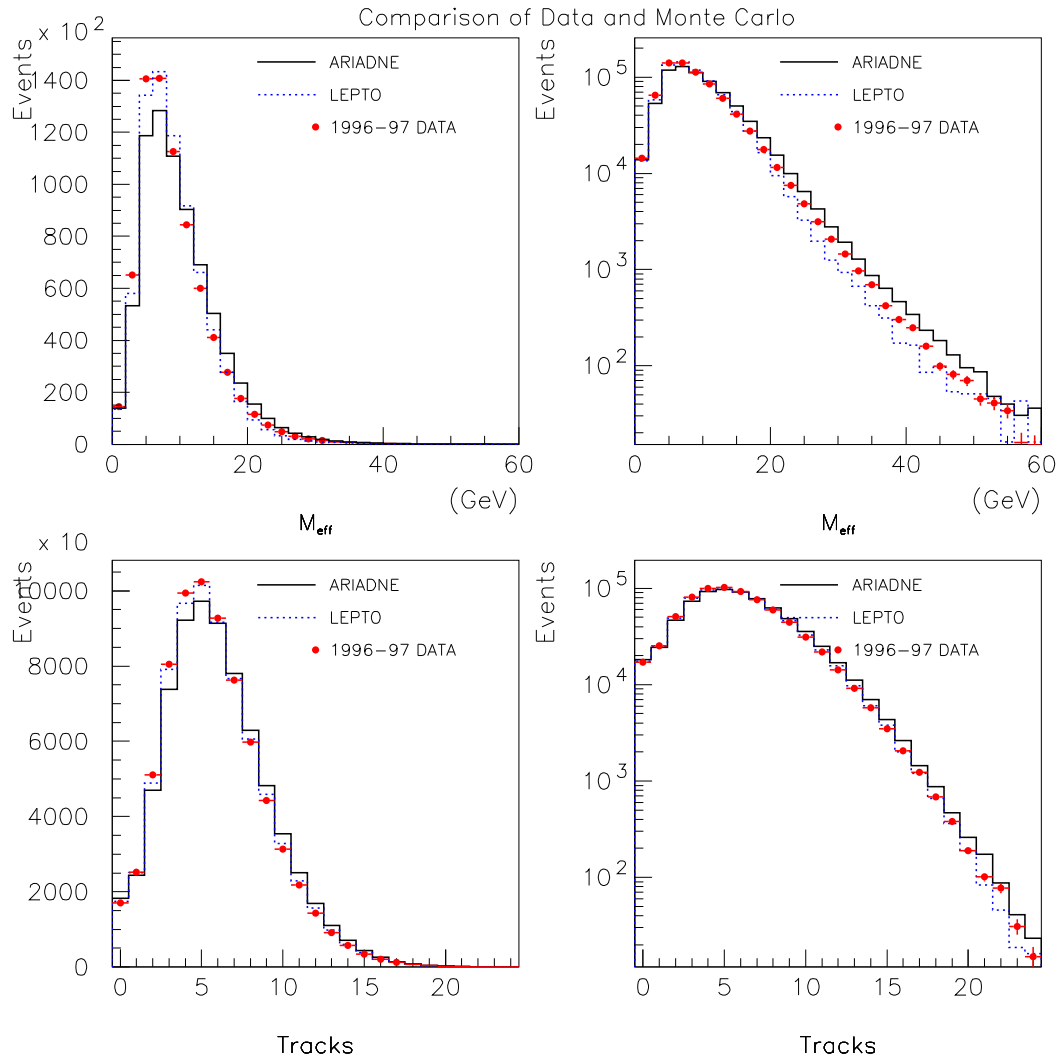
Figure 7.7: Comparison of the data and MC for the x and y position of the scattered positron. The data are compared to ARIADNE and LEPTO, both of which are generated with $Q^2 > 20$ GeV^2. The MC distributions are normalized to the number of events in the data. The plots are shown in linear scale on the left and log scale on the right.
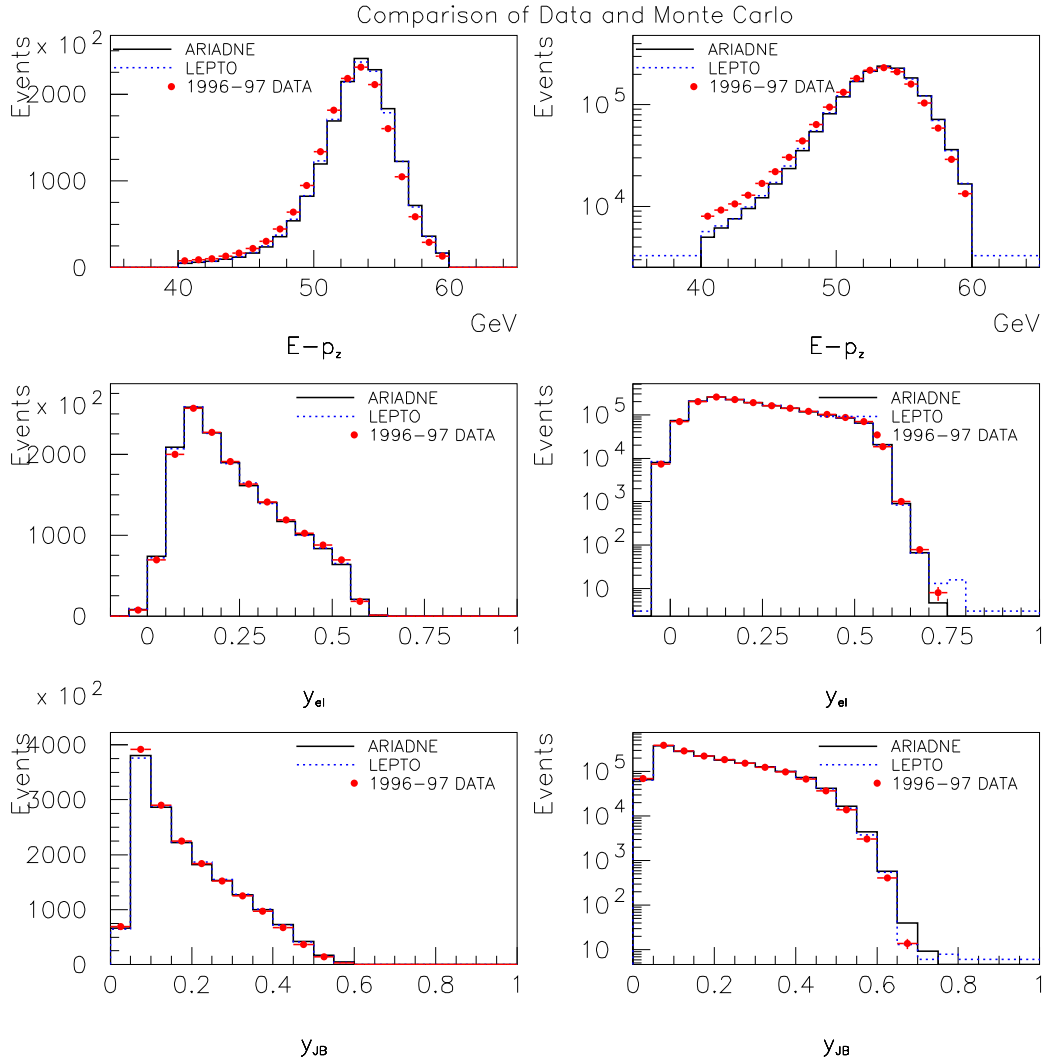
Figure 7.8: Comparison of the data and MC for Q^2 and W reconstructed using the double angle method. The data are compared to ARIADNE and LEPTO, both of which are generated with $Q^2 > 20$ GeV^2. The MC distributions are normalized to the number of events in the data. The plots are shown in linear scale on the left and log scale on the right.

Figure 7.9: Comparison of the data and MC for M_{eff} and the number of tracks, $N_{t}racks$. The data are compared to ARIADNE and LEPTO, both of which are generated with $Q^2 > 20$ GeV^2. The MC distributions are normalized to the number of events in the data. The plots are shown in linear scale on the left and log scale on the right.

Figure 7.10: Comparison of the data and MC for the total $E-p_z$ and y reconstructed using both the electron (y_{el}) and double angle (y_{DA}) methods. The data are compared to ARIADNE and LEPTO, both of which are generated with $Q^2 > 20$ GeV^2. The MC distributions are normalized to the number of events in the data. The plots are shown in linear scale on the left and log scale on the right.

detector level event vertex distribution was determined from the measured vertex distribution of the full inclusive NC DIS sample and was used as an input to the MC generators. Also shown in this figure is the pseudorapidity of the most forward energy deposit in the detector, $\eta_{\max}$, which was reconstructed using the ZUFOs.

Both the ARIADNE and LEPTO samples used for the above comparisons were generated with $Q^2 > 20$ GeV^2. ARIADNE was generated with $Q^2 > 80$ GeV^2 using the high Q^2 treatment described in citeproc:MC:1999:47 and compared to the data as a check, and found to describe the data with a similar level of agreement to the ARIADNE without the high Q^2 treatment.

7.6.1 Resolutions

When measuring a variable X in the ZEUS detector, the measured value X^{det} is different from the actual value the variable had in the underlying process, X^{gen}. The measured values of X will be distributed around the actual value in a Gaussian. The mean of the Gaussian is shifted from the true value of the variable and this shift is referred to as bias, and the width of the Gaussian is the resolution of the measurement. In a perfect detector, the measured value would always equal the actual value of the variable, and there would be no shift and no resolution effects. In a good detector the shift and the resolutions are small. The resolution determines the quality of the measurement, small resolutions indicate that X is accurately measured. Determining the resolution in a variable is useful when binning a measurement in X and for evaluating the systematic errors introduced in a measurement from cuts made on that variable. For example, when binning a measurement in X, the events can fall into different bins at the hadron level than at the detector level. This so-called bin
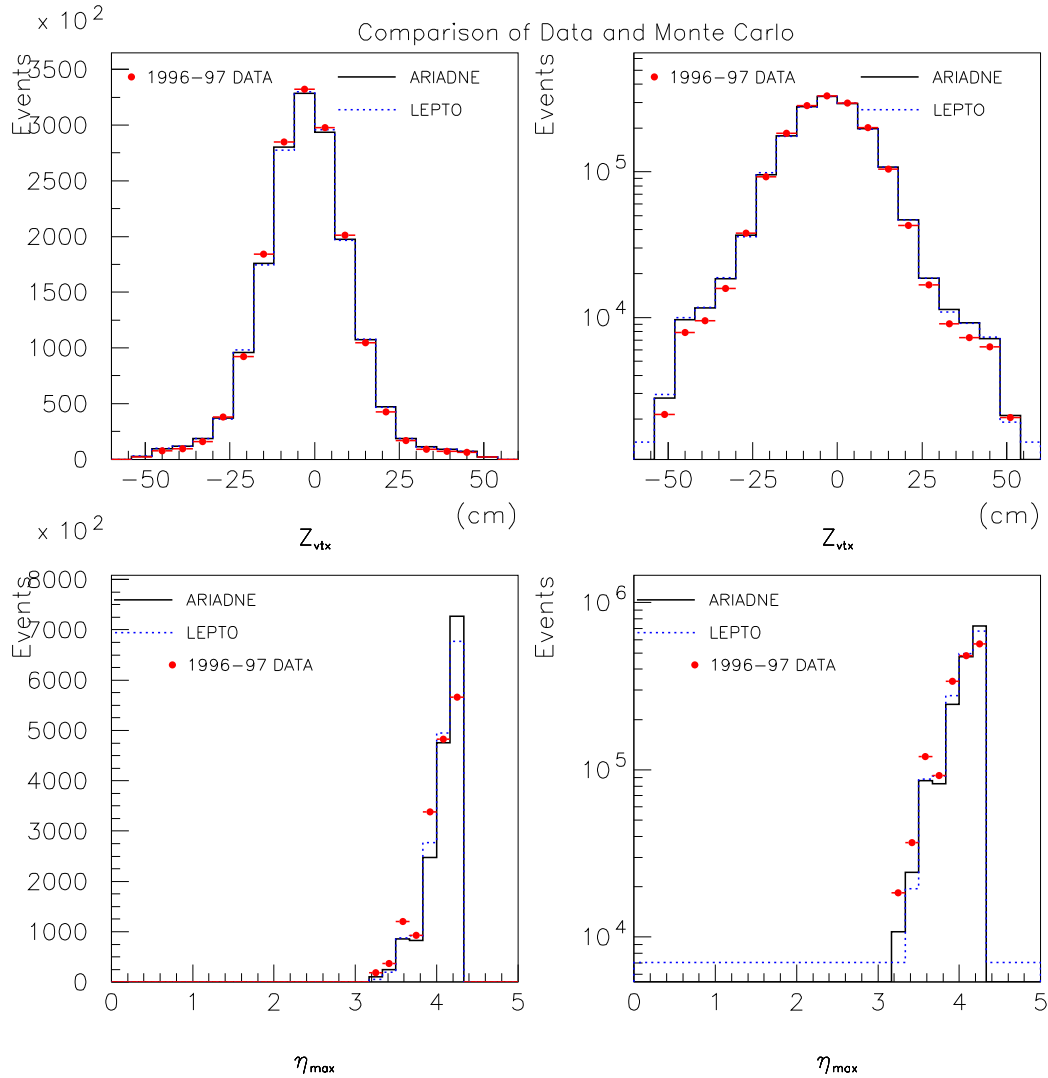
Figure 7.11: Comparison of the data and MC for the Z_{vtx} and η_{max}. The data are compared to ARIADNE and LEPTO, both of which are generated with $Q^2 > 20$ GeV^2. The MC distributions are normalized to the number of events in the data. The plots are shown in linear scale on the left and log scale on the right.

migration leads to impurities and inefficiencies in the measurement. The migrations and therefore the impurities and inefficiencies can be minimized by making the bins three to four times wider than the resolution of X. Making selection cuts on X^{det} can also introduce impurities and inefficiencies into the measurement because events with X^{gen} values close to the cut will have X^{det} values that are randomly above or below the cut causing events to be randomly accepted or rejected. The systematic error due to these selection cuts is determined by changing the value of the cut by the resolution of X^{det}. To determine the resolution of a variable X one uses a Monte Carlo simulation to calculate the distribution of the difference between the measured values and the true value of the variable and then fits a Gaussian to that distribution. Both the relative and the absolute resolutions can be measured. For a variable with dimension the relative resolution is determined by:

$$\delta_X = \frac{X^{det} - X^{gen}}{X^{gen}} .$$

(7.3)

The distribution, δ_X, is fit to a Gaussian and the width is taken as the resolution of X. Here the resolution is determined as a percent. For a dimensionless variable it is more appropriate to use

$$\delta_X = X^{det} - X^{gen}$$

(7.4)

to determine δ_X. Here the resolution is determined in absolute values, and in both cases the resolution itself is dimensionless.

The resolution of the most important variables that are used in selection cuts are shown in figure 7.12. For these variables the relative resolution is shown, except for Z_{vtx} where the absolute resolution is shown. There are two measurements for the resolution of W because we make a cut on two values of W, and the resolution is W

dependent.

Figure 7.13 and 7.14 show the resolution of the track variables p_T and η. For these variables the detector level tracks and generator level hadrons were matched. For a track to be matched to a hadron, it must be closer than 0.1 in η-ϕ-space. The resolution is then determined for all matched pairs of tracks and hadrons. The track p_T was calculated in three different regions of hadron level p_T, as well as for all hadrons. The upper left plot of figure 7.13 shows the distribution when no cut is applied on the p_T of the charged hadrons. The other plots show the distribution for three different regions of p_T of the charged hadrons; $p_T < 0.5$ GeV (upper right), 0.5 GeV $< p_T < 1.5$ GeV (lower left), and $p_T > 1.5$ GeV (lower right).

For the variables that were used to bin the measurements, W and M_{eff}, the resolutions are shown in figure 7.15 plotted as a function of the variables. The points are placed at the mean of the Gaussian fit and show the shift or bias in the measurement, and the error bars are the 1σ value extracted from the fit, or the resolution in that variable. One can see from these types of plots the dependence of the bias and resolution on the variable itself. The upper figure shows a small systematic shift in M_{eff}. All M_{eff} bins used in the analysis are sufficiently larger than the resolution. The W plot shows sizable shifts in the mean of the distributions, and therefore the analysis was restricted to the region between 70 GeV and 225 GeV where there is little bias. The resolution in this region is sufficiently small for the size of the W bins chosen in the analysis.

For some measurements in the analysis, the data were also binned in x and Q^2. The resolution of x_{DA} is shown in figure 7.16. The resolutions for x were determined
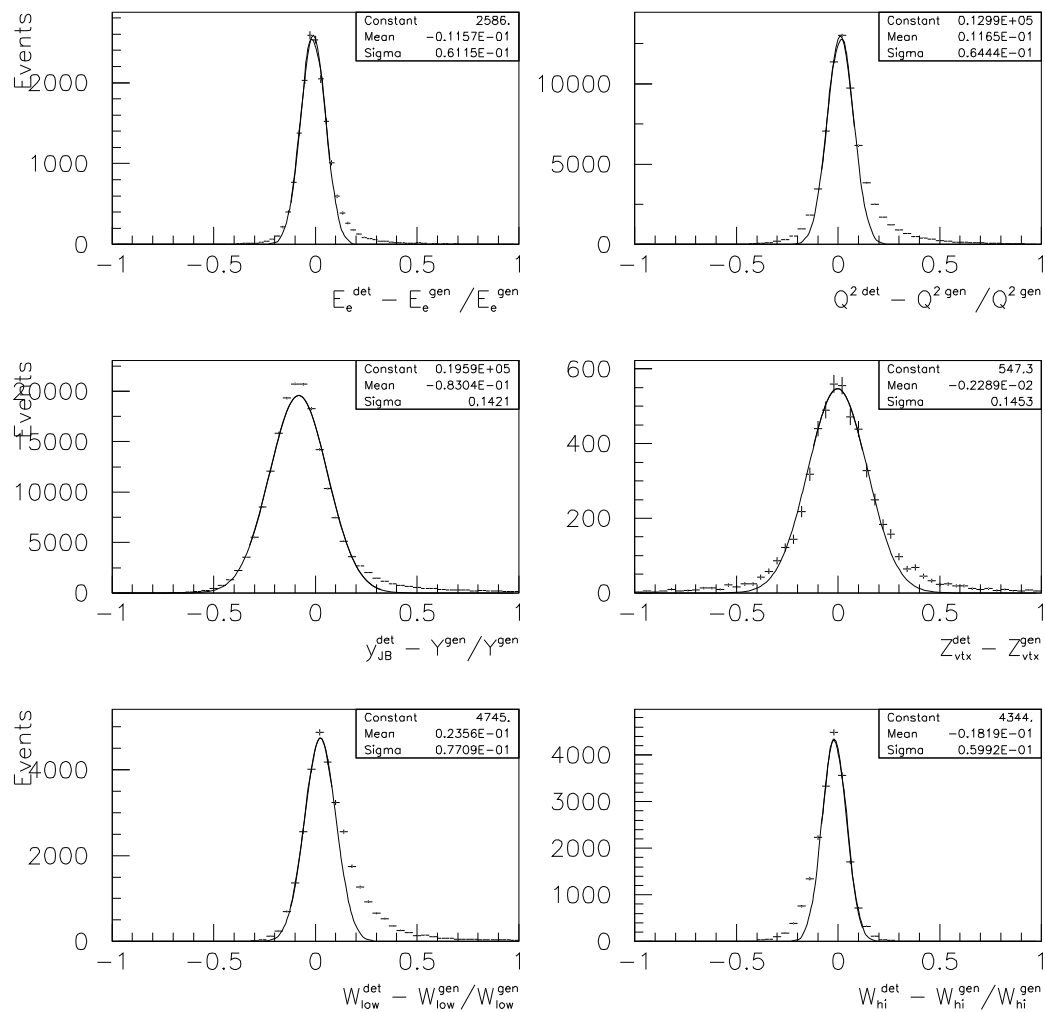
Figure 7.12: Resolutions of kinematic variables. Relative resolutions are shown for the energy of the scattered positron $E_{e'}$, (upper left), Q^2 (upper right), y (middle left), and W (lower two). The absolute resolution is shown for the Z_{vtx} (middle right). Each distribution is fit to a Gaussian, and labeled with the sigma of the Gaussian fit which is the resolution of the variable.
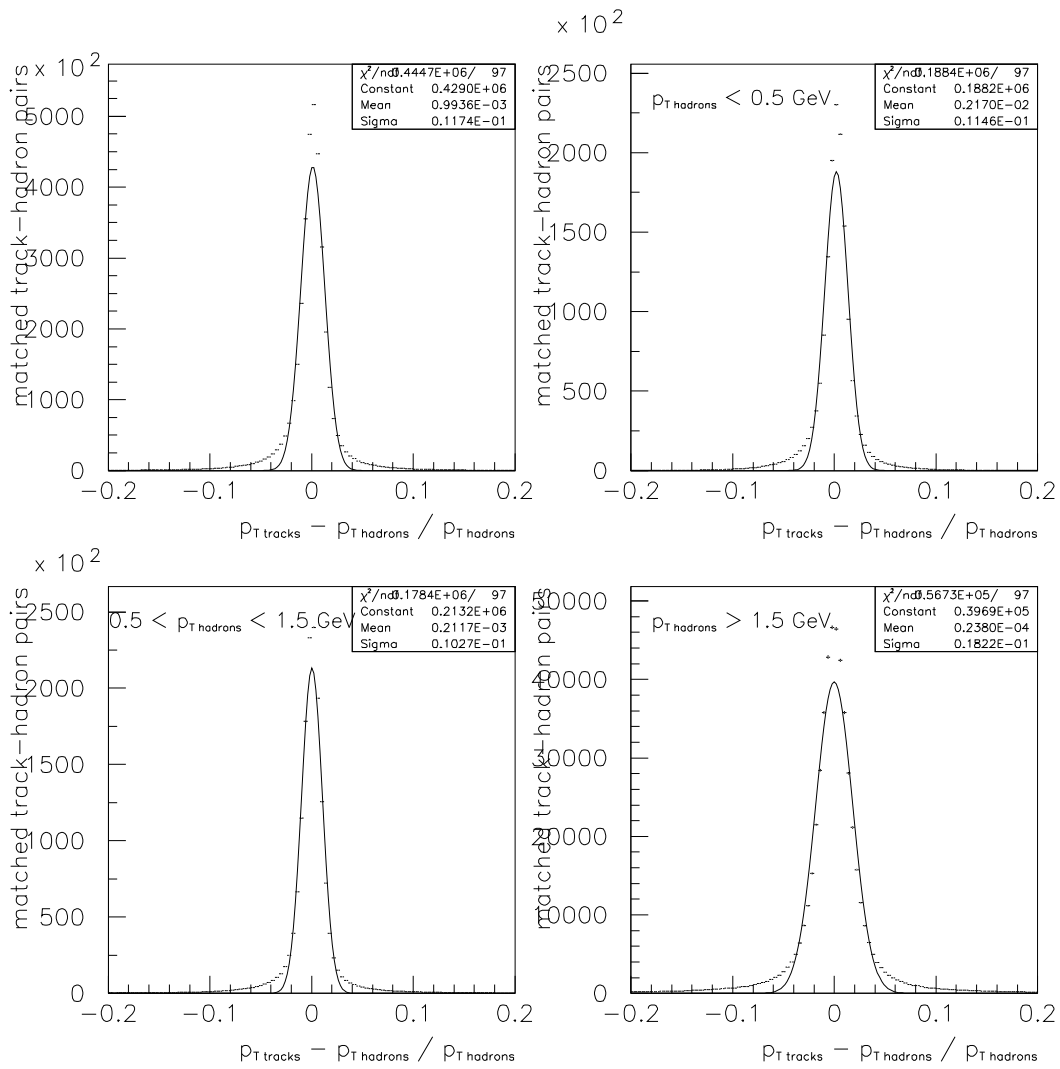
Figure 7.13: Track p_T resolution plots for different regions of hadron p_T with ARIADNE.
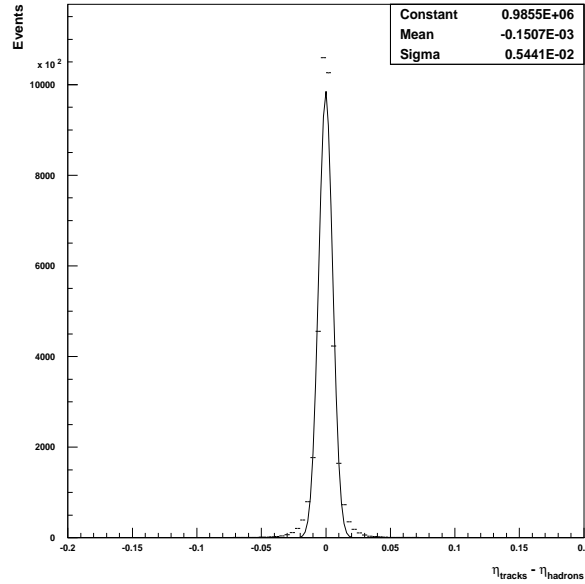
Figure 7.14: Absolute resolution of the pseudorapidity of the tracks.

in each of the four x bins of the analysis which are given in section 6.6.1. The double-angle reconstruction method produced overall better resolutions and therefore was chosen over the Jacquet Blondel method to use for the binning.

The resolution of Q^2_{DA} is shown in figure 7.17. The resolutions of Q^2 were determined in each of the three Q^2 bins used in the analysis, and described in section 6.6.1. The resolution is similar in each of the Q^2 bins. The resolutions are better for Q^2_{DA} so it was chosen over Q^2_{el} to use for the binning.

The resolution of the multiplicity was determined and plotted as a function of the multipliticy, in the same way as for the W and M_{eff} and is shown in figure 7.18. The bias decreases and the resolution improves as multiplicity increases.
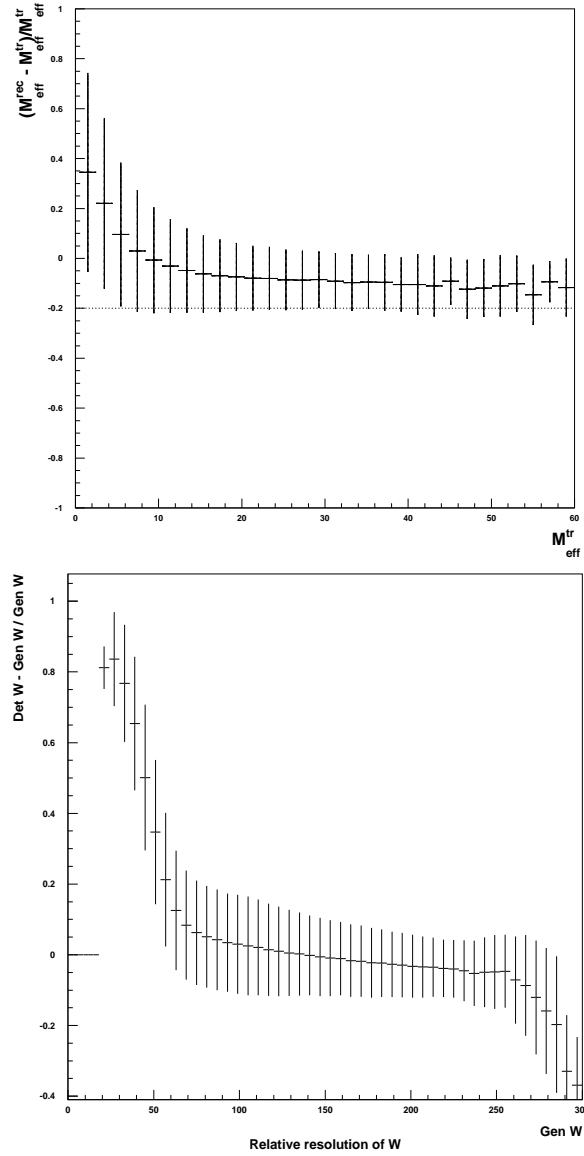
Figure 7.15: Profile histograms showing the bias and the relative resolutions of M_{eff} (top) and W (lower) as a function of each variable.

128
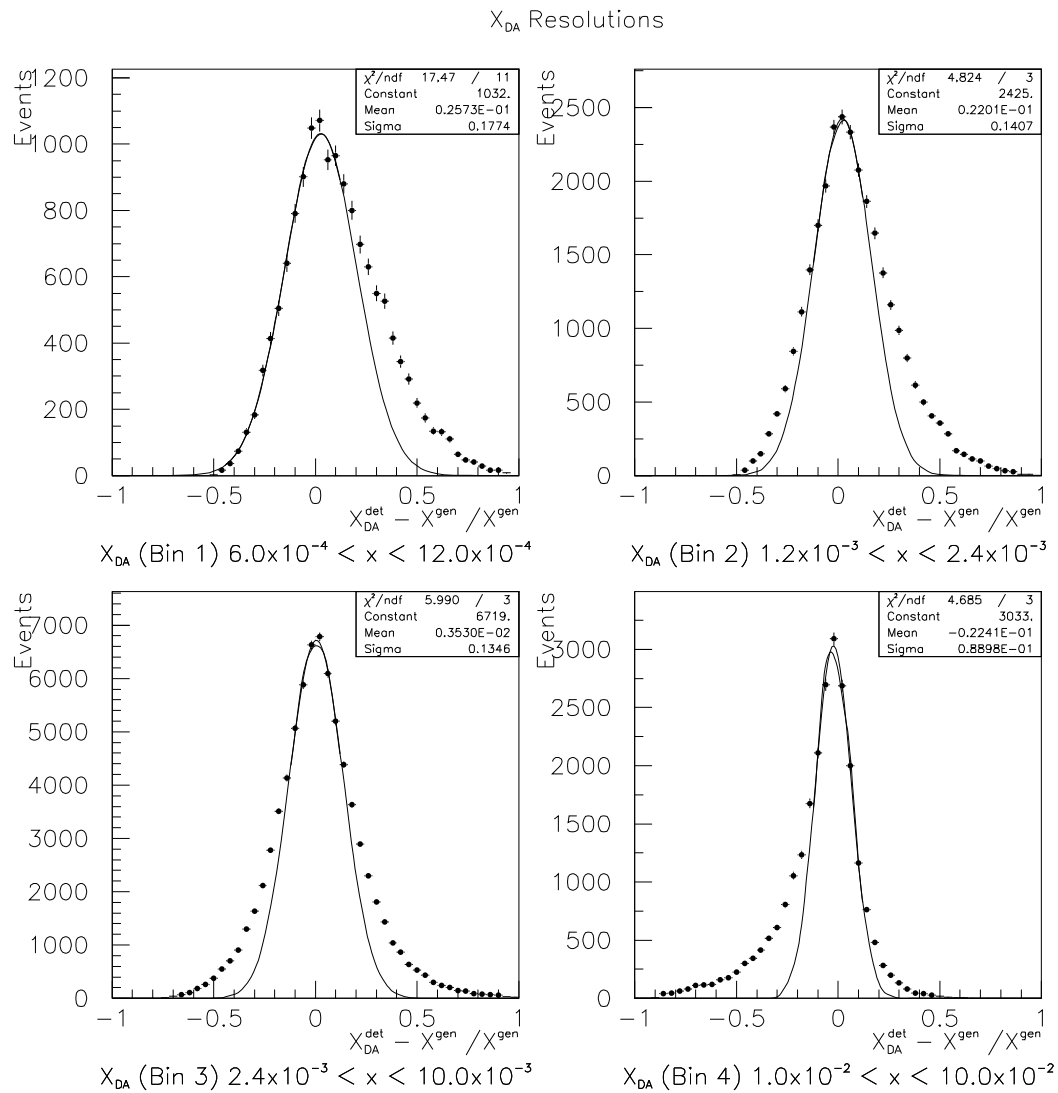
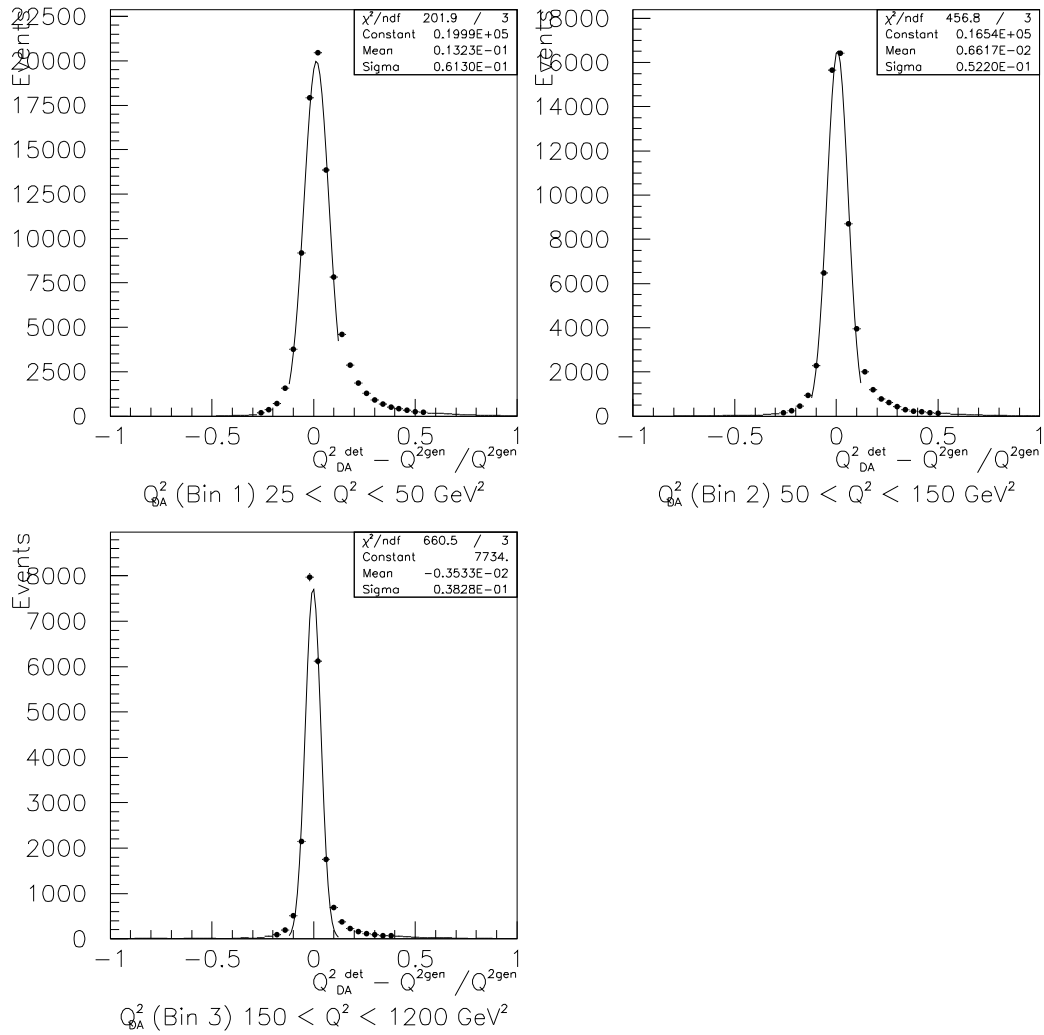**Figure 7.16:** Relative resolutions of x_{DA} in each of the x bins.

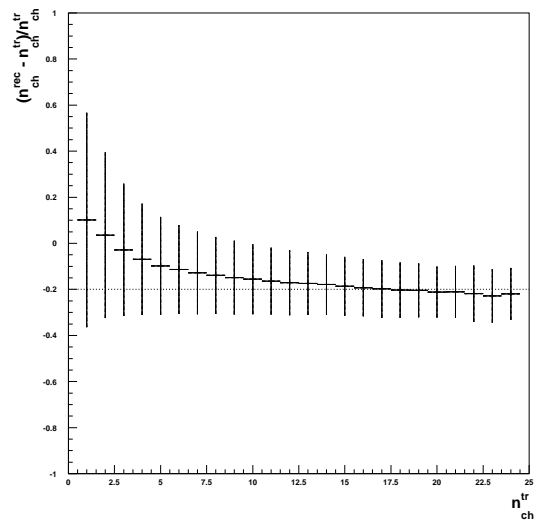**Figure 7.17:** Resolution of Q^2_{DA} in each of the Q^2 bins used in this analysis.

Figure 7.18: Profile histogram showing the bias and resolution of the charged multiplicity as a function of the charged multiplicity.

Chapter 8

Correction of Data to Hadron Level

8.1 Introduction

The data measured in the ZEUS detector are a convolution of the real physical quantities and effects from the interaction of the particles with the detector. In order to study the underlying physics of the event, we must remove the effects that are specific to the ZEUS detector. This is done using Monte Carlo simulated events. The detector effects are related to the acceptance and resolution of the detector, event selection cuts, QED-radiative effects, track reconstruction, track selection cuts, the decay products of K_S^0 and Λ assigned to the primary vertex, and energy losses in the inactive material in front of the calorimeter in the case of the energy measurement. If the Monte Carlo simulation describes the data as measured in the detector, then it can be used to correct for the detector effects, with the assumption that both the physics simulation and the detector simulation are accurate. As shown in section 7.6 both the ARIADNE and LEPTO samples give a reasonable decription of the data at the detector level and we have chosen to use both ARIADNE and LEPTO for the corrections, and their difference is taken into account in the systematic uncertainties

of the measurement. For cross section measurements the usual method for correcting

the data to the hadron level is the so called bin-by-bin method, where the correction

factors are calculated as ratios of generated events to detected events in each bin of

the analysis. For the analysis presented in this thesis, the bin-by-bin method must

be modified to account for hadrons with p_T less than 0.15 GeV which are not seen as

tracks in the detector. For multiplicity analyses the usual method of correcting the

data is the matrix unfolding method [75]. In addition to using the matrix unfolding

method, as a cross check we also use a modified bin-by-bin method. Both methods

are described in detail in the following two sections.

8.2 Matrix Method

The matrix correction procedure for the multiplicity distributions has been used

in previous multiplicity studies by ZEUS [75] and is performed in two stages.

In the first step, in each bin of the analysis, a comparison was made between the

observed number of charged tracks at the detector level, n_{ch}^{DET}, after all the cuts, and

the number of hadrons generated, n_{ch}^{GEN}, for the same events. This comparison yields

the correction matrix, $M_{n_{\mathrm{GEN}},\ n_{\mathrm{DET}}}$, with elements defined by

$$M_{n_{\mathrm{GEN}},n_{\mathrm{DET}}} = \frac{No.\ of\ events\ with\ n_{\mathrm{ch}}^{\mathrm{GEN}}\ hadrons\ generated\ and\ n_{\mathrm{ch}}^{\mathrm{DET}}\ tracks\ observed}{No.\ of\ events\ with\ n_{\mathrm{ch}}^{\mathrm{DET}}\ tracks\ observed}\ .$$

$$(8.1)$$

Both n_{DET} and n_{GEN} are started from 0 and run through all possible n combinations.

This matrix relates the observed to the generated distributions by

$$P_{n_{\mathrm{GEN}}} = \sum_{n_{\mathrm{DET}}} M_{n_{\mathrm{GEN}},n_{\mathrm{DET}}} \cdot P_{n_{\mathrm{DET}}}\ . \qquad (8.2)$$

Using this matrix the number of hadrons can be calculated. The first step of the

method only corrects for the events selected at the detector level.

The second step corrects for migrations and for the acceptance of the event selection cuts using correction factors that are defined in each bin of the analysis as:

$$C = \frac{\rho_{\text{gen}}}{\rho_{\text{det}}},\qquad(8.3)$$

where ρ_{gen} is the normalized generator level multiplicity distribution with only generator level cuts applied, and ρ_{det} is the normalized generator level multiplicity distribution with the detector level cuts applied.

The fully corrected multiplicity distribution is then calculated according to the formula

$$P_{n_{\text{corrected}}} = C \cdot \sum_{n_{\text{data}}} M_{n_{\text{GEN}},n_{\text{data}}} \cdot P_{n_{\text{data}}}\ .\qquad(8.4)$$

The uncorrected track distribution, the matrix, and the corrected track distribution for each bin of each analysis are shown in appendix A. These plots for a particular energy bin (12 - 20 GeV) for the current region of the Breit Frame anaysis versus $2 \cdot E_{\text{Breit}}^{\text{current}}$ are shown in figure 8.1 as an example.

In order to give an idea of the size of the first part of the matrix correction, the ratio of the means of the data histograms before and after correction by the matrix are shown in the upper plot of figure 8.2. The lower plot shows the correction factors from the second part of the matrix correction. Again, this plot is just an example from the analysis versus $2 \cdot E_{\text{Breit}}^{\text{current}}$ in the current region of the Breit frame, the complete set of these plots for all the analysis are also in appendix A.
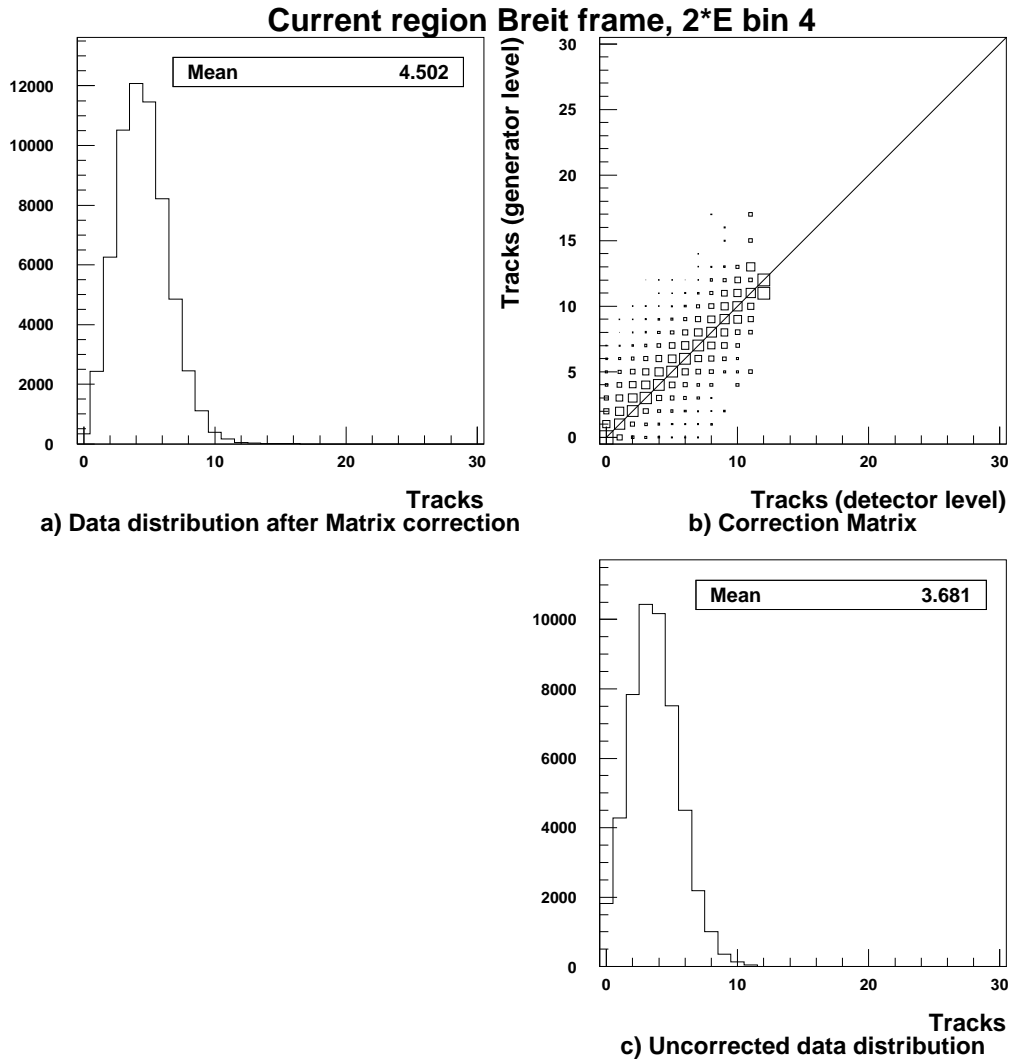
.

134

Current region Breit frame, 2*E bin 4

a) Data distribution after Matrix correction

b) Correction Matrix

c) Uncorrected data distribution

Figure 8.1: The matrix correction for $\langle n_{\mathrm{ch}} \rangle$ in the 4th bin (12 - 20 GeV) of $2 \cdot E_{\mathrm{Breit}}^{\mathrm{current}}$ in the current region of the Breit frame. The uncorrected number of tracks in the data (C) is multiplied by the normalized matrix (B) and the result is shown in (A). Similar plots for the other bins of this anaysis, as well as plots in each bin for the other analyses are found in appendix A.
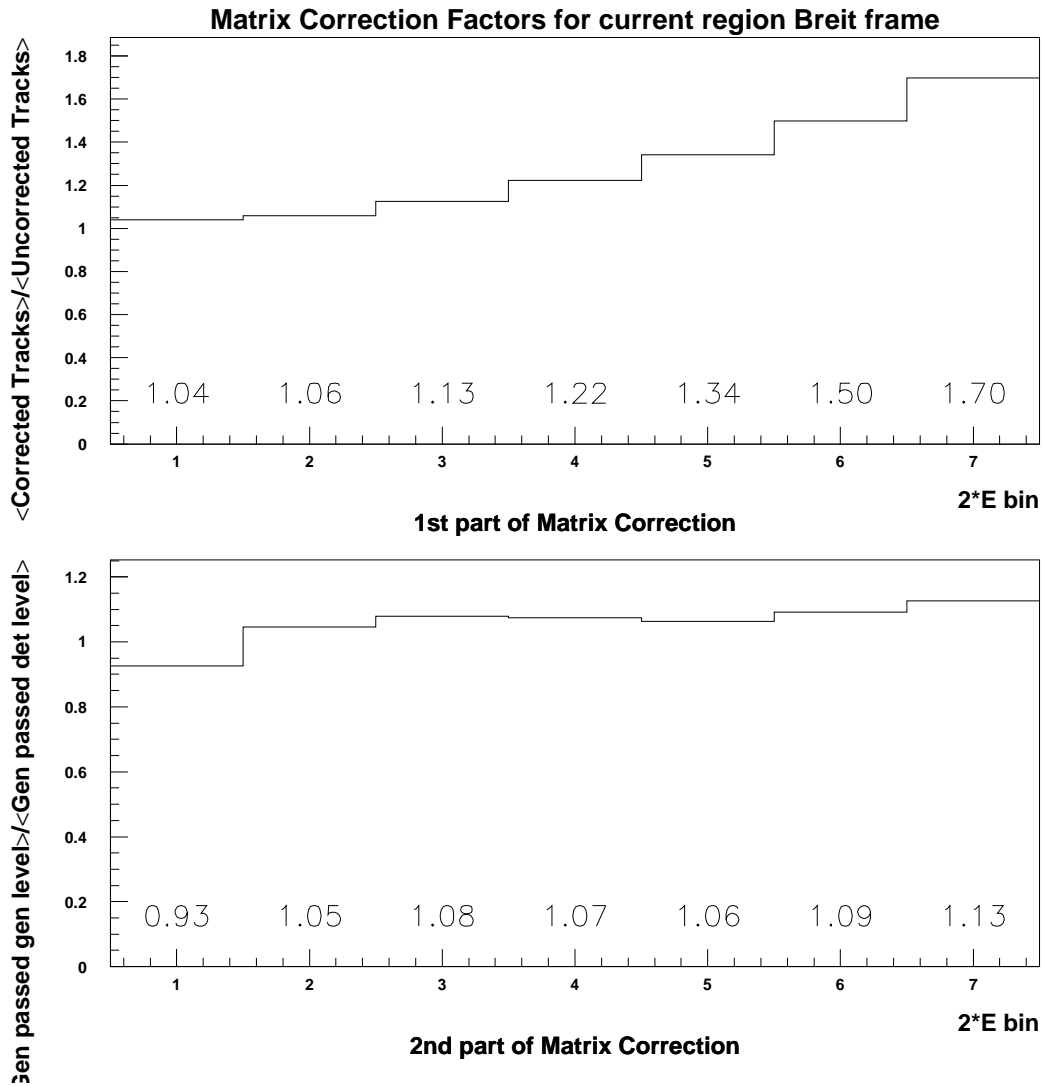
Figure 8.2: Matrix correction factors for $\langle n_{\mathrm{ch}} \rangle$ in the current region of the Breit frame in bins of $2 \cdot E_{\mathrm{Breit}}^{\mathrm{current}}$. The bin ranges are given in table 6.6.1. Shown in the upper plot is the average matrix correction factor, a ratio of the mean of the corrected track ditribution to the mean uncorrected track distribution in each bin of $2 \cdot E_{\mathrm{Breit}}^{\mathrm{current}}$. Shown in the bottom plot is the mean of the histograms of the correction factor, $C = \rho_{\mathrm{gen}}/\rho_{\mathrm{det}}$, for the second part of the matrix correction. Similar plots which show the correction factors for the other analyses are found in appendix A.

8.3 Modified Bin-by-bin Method

The bin-by-bin correction is also done in two steps, which are different from the ones for the matrix correction method described above.

In the first step a correction is made using only the tracks and hadrons with $p_{\mathrm{T}} > 150\,\mathrm{MeV}$. Let $n_{\mathrm{ch,\,i}}^{\mathrm{DET}}$ be the charged particle multiplicity distribution at the detector level in bin i with all the detector level cuts applied and $n_{\mathrm{ch,\,i}}^{\mathrm{GEN,\,0.15}}$ be the charged hadron multiplicity distribution in bin i with all generator level cuts applied and the additional requirement that $p_{\mathrm{T}} > 150\,\mathrm{MeV}$ for each generated hadron. The distributions of correction factors for each bin i, are then defined as in the standard bin-by-bin method:

$$C_{1,\,i} = \frac{n_{\mathrm{ch,\,i}}^{GEN,\,0.15}}{n_{\mathrm{ch,\,i}}^{DET}} \; . \tag{8.5}$$

The p_{T} distributions of the tracks and hadrons are shown in figure 8.3.
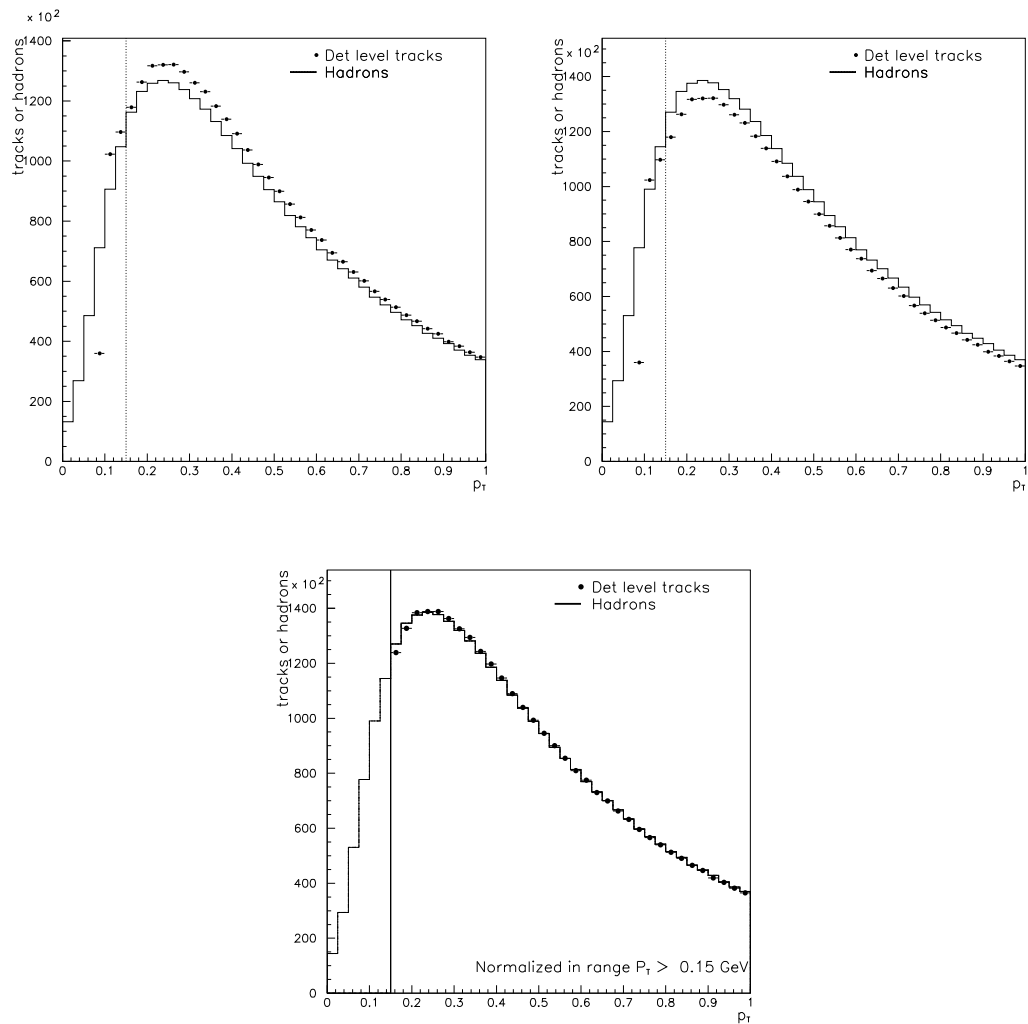
Figure 8.3: Comparison of p_T for detector level tracks and generator level charged hadrons for ARIADNE. The vertical dashed lines are $p_T = 0.15$ GeV, which is the minimum p_T for tracks used in this analysis. The plot on the upper left is not normalized, the upper right is area normalized. The lower plot is area normalized above $p_T = 0.15$ GeV.

The effect of this first correction is shown by plotting the means of the C_1 distributions. The upper plot of figure 8.4 shows this correction for the analysis done versus $2 \cdot E_{\text{Breit}}^{\text{current}}$ in the current region of the Breit frame. For the complete set of plots of the bin-by-bin correction factors calculated for the other analysis, see appendix B

The second step is to correct for the hadrons generated with $p_{\text{T}} < 150\,\text{MeV}$ that are not detected. This is done by calculating in each bin i the ratio of the mean of the distribution of all charged hadrons generated in that bin, $n_{\text{ch, i}}^{GEN}$, to the mean of the distribution of charged hadrons generated in that bin with $p_{\text{T}} > 150\,\text{MeV}$, $n_{\text{ch, i}}^{GEN,\,0.15}$. The second part of the correction is then:

$$C_{2,\,i} = \frac{\langle n_{\text{ch, i}}^{GEN} \rangle}{\langle n_{\text{ch, i}}^{GEN,\,0.15} \rangle}. \tag{8.6}$$

This ratio is shown in the lower plot of figure B.4 for the analysis versus $2 \cdot E_{\text{Breit}}^{\text{current}}$ in the current region fo the Breit frame. These ratios are presented in appendix B for the other analyses. Note that the C_1's are distributions and the C_2's are numbers.

In each bin, i, the uncorrected charged track distributions, $n_{\text{ch, i}}^{DATA}$, are multiplied by the $C_{1,\,i}$ distributions. The mean of the resulting distribution is then multiplied by the corresponding C_2. In this way the corrected mean charged multiplicity in each bin is calculated as:

$$\langle n_{\text{ch, i}}^{corrected} \rangle = \langle n_{\text{ch, i}}^{DATA} \cdot C_{1,\,i} \rangle \cdot \frac{\langle n_{\text{ch, i}}^{GEN} \rangle}{\langle n_{\text{ch, i}}^{GEN,\,0.15} \rangle}. \tag{8.7}$$

8.4   Correction of Invariant Mass

The invariant mass, M_{inv}, is corrected from detector level to hadron level using a ratio of the means of the M_{inv} distributions. In each bin the $\langle M_{\text{inv}}^{\text{DET}} \rangle$ with the detector
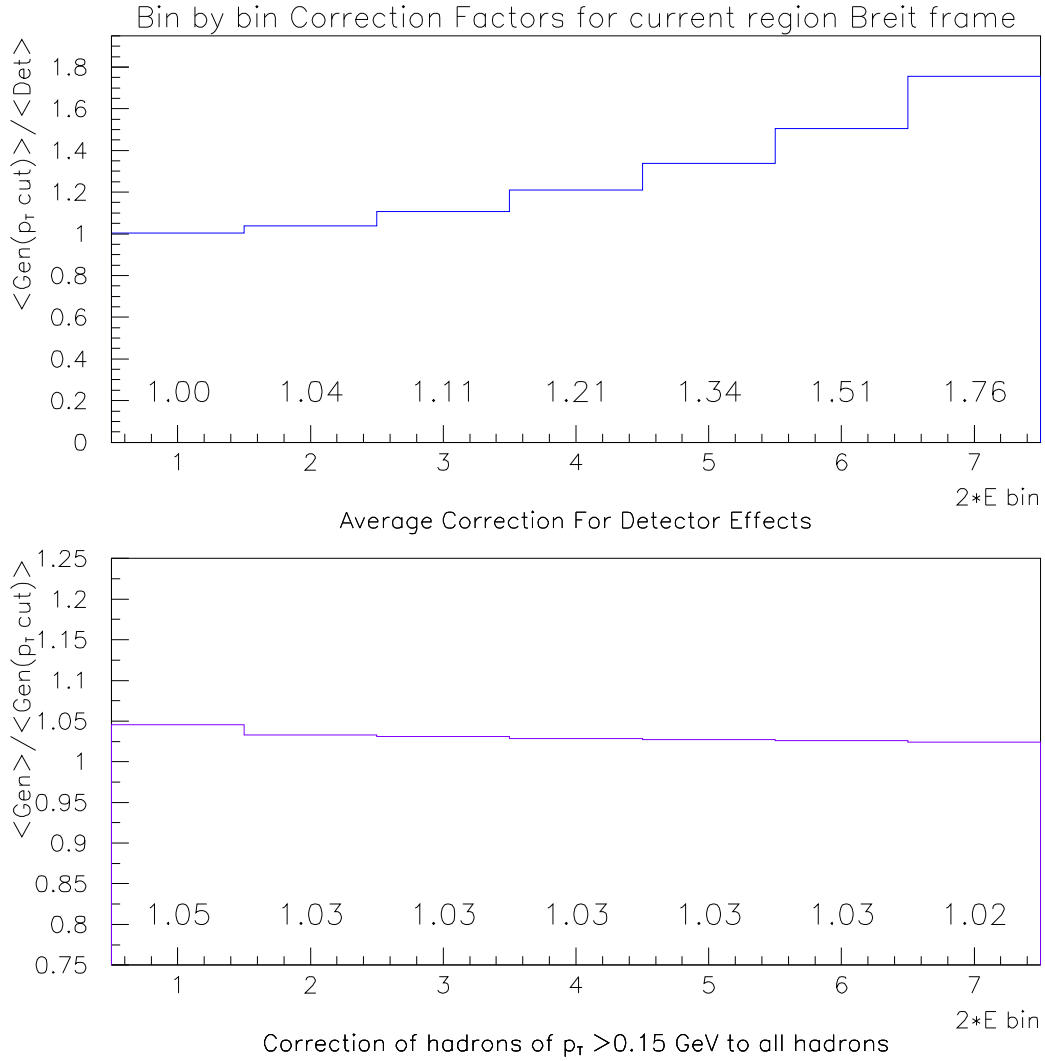
Figure 8.4: Bin-by-bin correction factors for $\langle n_{\mathrm{ch}} \rangle$ in the current region of the Breit frame in bins of $2 \cdot E_{\mathrm{Breit}}^{\mathrm{current}}$. The bin ranges are given in table 6.6.1. Shown in the upper plot is the average correction factor for detector effects, $\langle C_1 \rangle$ from equation 8.5. Shown in the bottom plot is the correction factor, C_2 from equation 8.6, for the hadrons with $p_{\mathrm{T}} < 150\,\mathrm{MeV}$.

level cuts and $\langle M_{\text{inv}}^{\text{GEN}} \rangle$ with generator level cuts are calculated independently. The M_{inv} in each bin is then calculated as:

$$M_{\text{inv}} = \langle M_{\text{inv}}^{\text{DATA}} \rangle \frac{\langle M_{\text{inv}}^{\text{GEN}} \rangle}{\langle M_{\text{inv}}^{\text{DET}} \rangle} \; . \tag{8.8}$$

This is done for M_{eff}, $2 \cdot E_{\text{Breit}}^{\text{current}}$, and W. These energy scale correction factors, $\langle M_{\text{inv}}^{\text{GEN}} \rangle / \langle M_{\text{inv}}^{\text{DET}} \rangle$, are shown in figure 8.5.

8.5 Pseudorapidity Acceptance Correction

For the measurements in the current region of the Breit frame and in the photon region of the HCM frame an additional correction for the invisible part of the charged hadrons is required. This corrects for those charged hadrons that fall outside the good acceptance region of the CTD ($|\eta^{\text{LAB}}| < 1.75$).

Figure 8.6 shows the pseudorapidity distribution of all the hadrons in the laboratory frame, with the vertical lines corresponding the $|\eta^{\text{LAB}}| = 1.75$. The shaded histogram represents the hadrons belonging to the current region of the Breit frame. About 95% of the hadrons in the current region of the Breit frame are contained in the visible pseudorapidity region of the detector. The corrections are calculated in bins of M_{inv} at the generator level as

$$C_\eta^{hadrons} = \langle n_{\text{ch}}^{hadrons} \rangle / \langle n_{\text{ch}}^{hadrons,visible} \rangle \; , \tag{8.9}$$

where $n_{\text{ch}}^{hadrons,visible}$ refers to the charged hadron multiplicity in the current region of the Breit frame generated in the visible part of the detector and $n_{\text{ch}}^{hadrons}$ to the full charged hadron multiplicity in the current region of the Breit frame. The data are multiplied with the correction factors, $C_\eta^{hadrons}$. The sizes of the corrections are shown

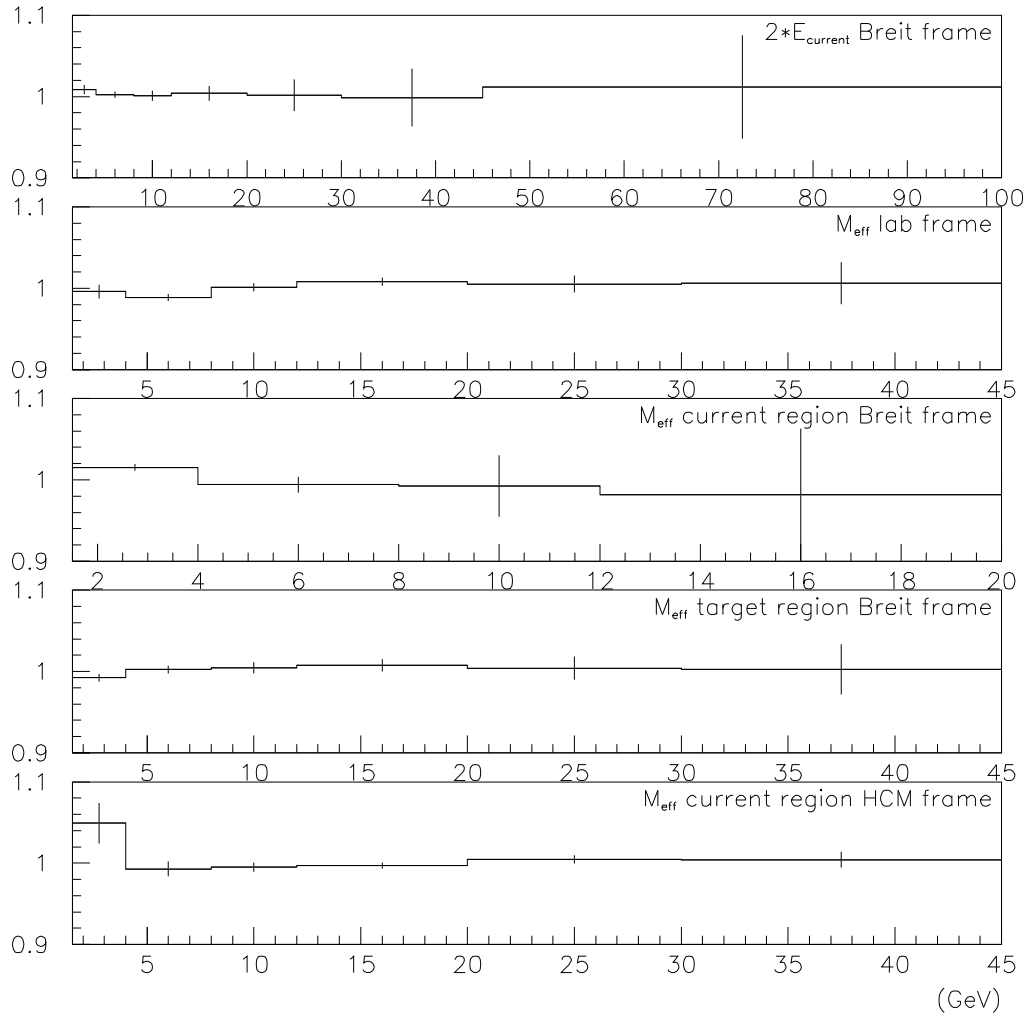**Figure 8.5:** Energy scale correction factors for M_{eff} and $2 \cdot E_{\text{Breit}}^{\text{current}}$ in bins of M_{eff} and $2 \cdot E_{\text{Breit}}^{\text{current}}$ for laboratory, current and target regions of Breit frame, and for the photon region of the hadronic center of mass frame.
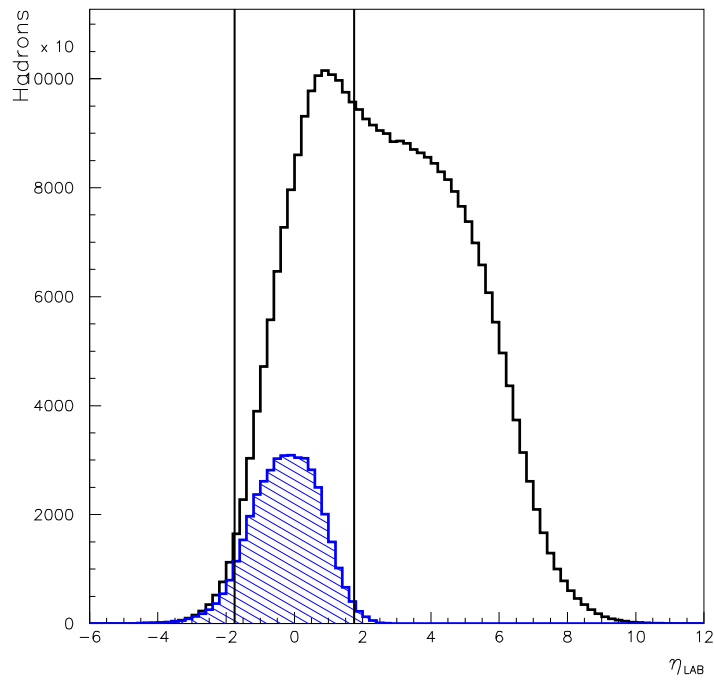
Figure 8.6: Laboratory frame pseudorapidity distribution of the charged hadrons gerner-ated with ARIADNE. The hadrons belonging to the current region of the Breit frame are shown as the shaded histogram. The vertical lines indicate the region of visible pseudora-pidity.

in figures 8.7 and 8.8 for both of the M_{inv} variables, M_{eff} and $2 \cdot E_{\mathrm{Breit}}^{\mathrm{current}}$, that were used in the current region of the Breit frame measurement.

For the measurements in the photon hemisphere of the HCM frame, the pseudo-rapidity acceptance corrections are calculated in the same way as in the Breit frame, but the corrections are larger. This is because only about 60-80% of the charged hadrons in the photon hemisphere of the HCM frame are contained in the visible pseudorapidity region of the detector. Figure 8.9 shows the pseudorapidity distribution of all the charged hadrons in the laboratory frame. The shaded histograms are the hadrons which are found in the photon hemisphere (left histogram) and the proton hemisphere (right histogram) of the HCM frame. The verticle lines indicate the region visible in the detector. The hadrons belonging to the proton hemisphere of the HCM frame lie completely outside the visible region of the detector. In Figure 8.10 the correction factors for the photon region of the HCM frame are shown. Unlike the correction factors for the Breit frame measurements which are uniform with respect to the bins of M_{inv}, the correction factors for the photon region of the HCM frame are W dependent. For the measurement of $\langle n_{\mathrm{ch}} \rangle$ versus W in the HCM frame, the corrected mean charges multiplitity is simply multiplied by the correction factor, $C_{\eta}^{hadrons}$. For the measurement of $\langle n_{\mathrm{ch}} \rangle$ versus M_{eff} in the HCM frame, however, the number of tracks are corrected on an event by event basis, with the number of track for each event multiplied by a different factor, $C_{\eta}^{hadrons}$, depending on the value of W for that event.

For the measurement versus M_{eff}, in the HCM frame, in addition to correcting for the tracks which lie outside the visible region of the detector, it is necessary to
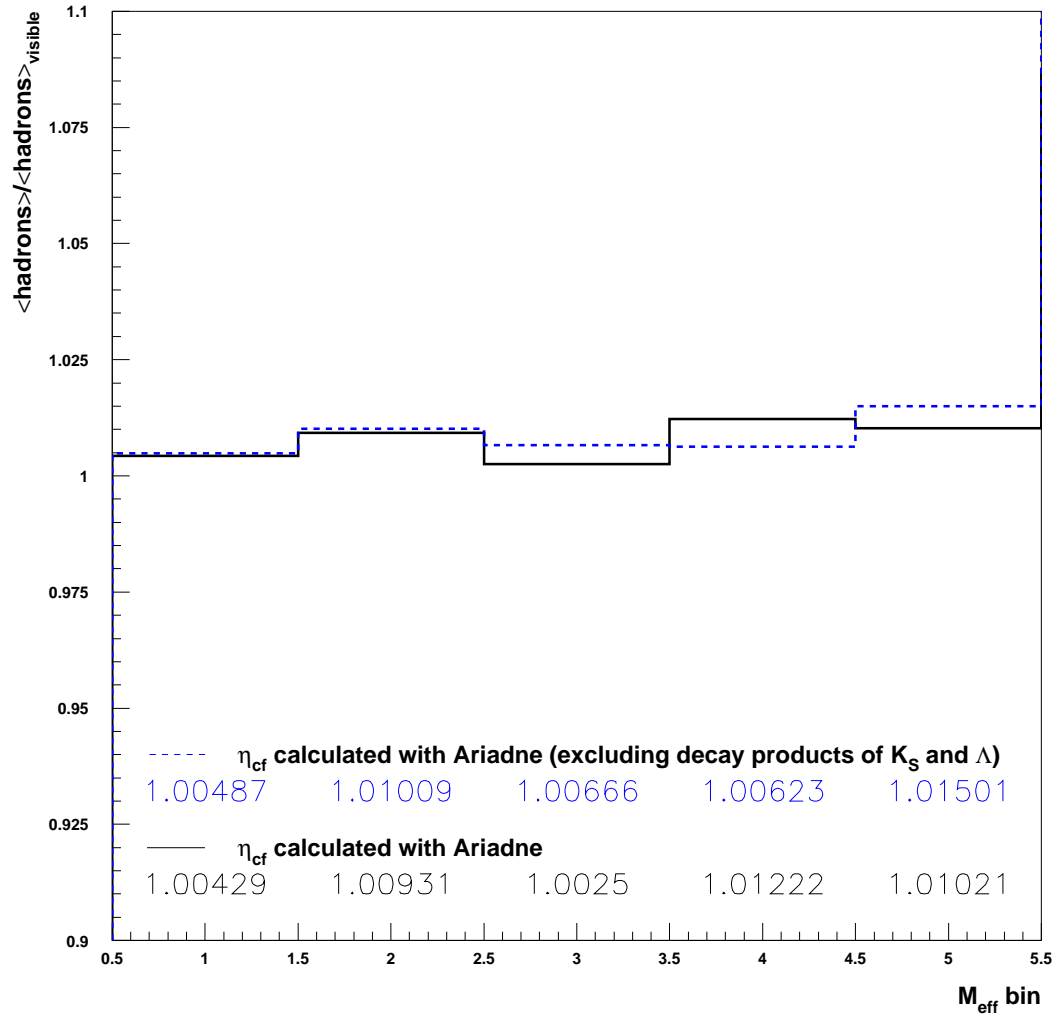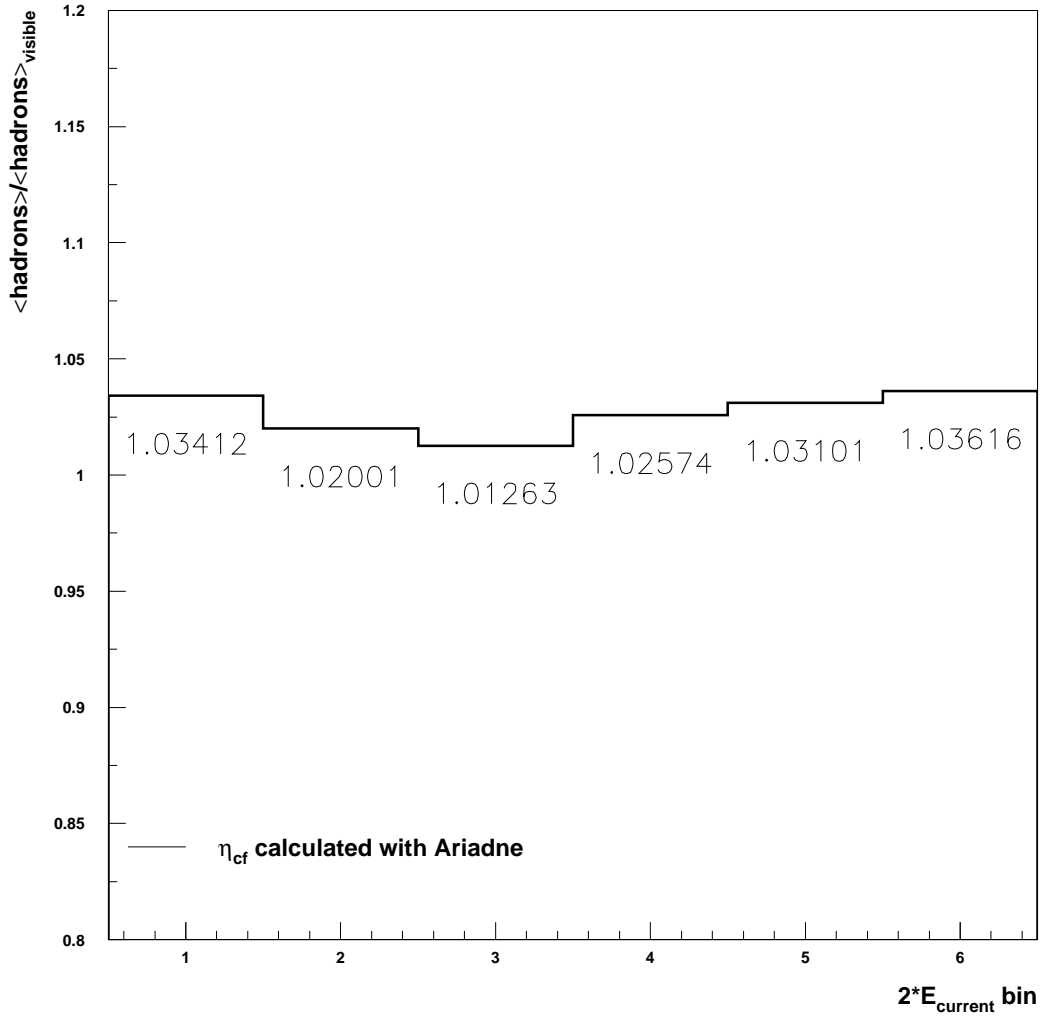
Figure 8.7: Correction factors, $C_\eta^{hadrons}$ (equation 8.9), for the part of the multiplicity falling outside the η acceptance of the detector in bins of M_{eff} for the current region of the Breit frame. The bin ranges for M_{eff} are given in table 6.6.1.

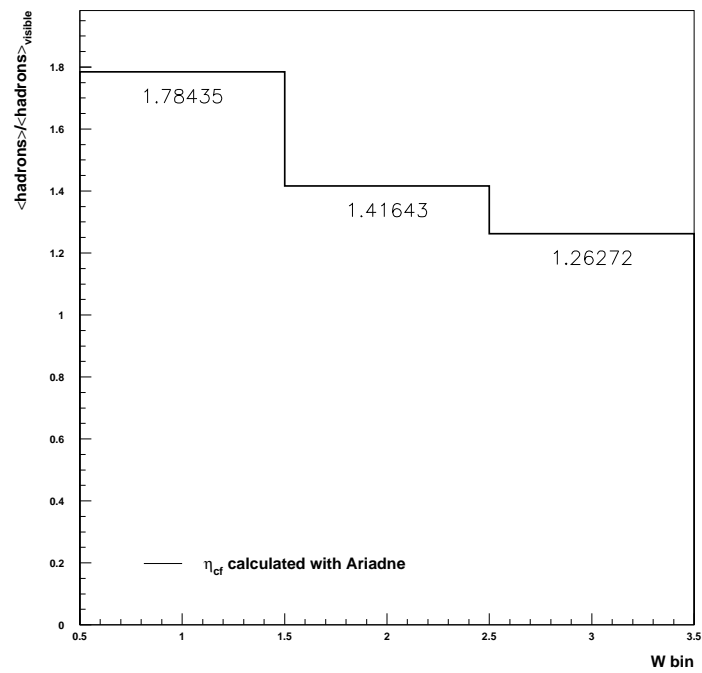**Figure 8.8:** Correction factors, $C_\eta^{hadrons}$ (equation 8.9), for the part of the multiplicity falling outside the η acceptance of the detector in bins of $2 \cdot E_{\mathrm{Breit}}^{\mathrm{current}}$ for the current region of the Breit frame. The bin ranges for $2 \cdot E_{\mathrm{Breit}}^{\mathrm{current}}$ are given in table 6.6.1.

146
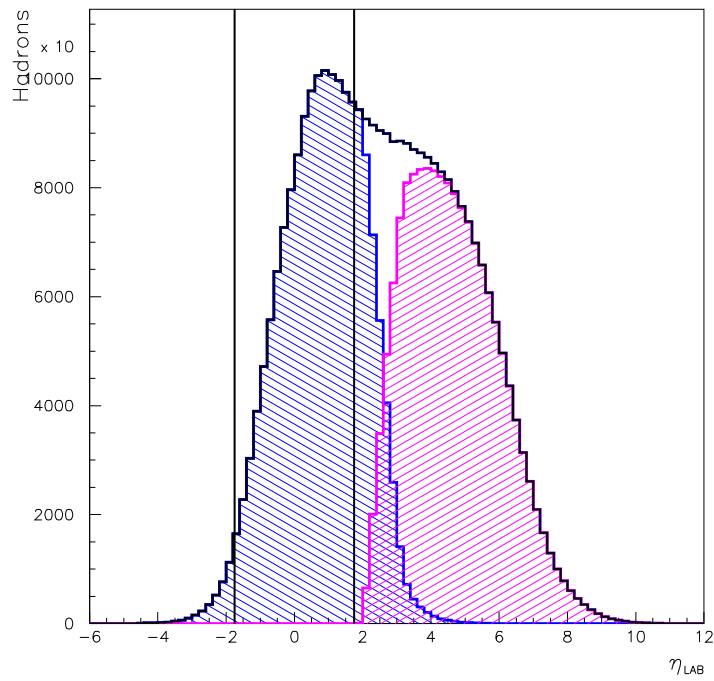
Figure 8.9: Lab-frame pseudorapidity distribution of the charged hadrons generated usin ARIADNE. The shaded histograms are the hadrons belonging to the photon hemisphere (left) and the proton hemisphere (right) of the HCM frame. The vertical lines indicate the region of visible pseudorapidity.

Figure 8.10: Correction factors, $C_\eta^{hadrons}$ (equation 8.9), for the part of the multiplicity outside the η acceptance of the detector in bins of W for the photon region of the hadronic center of mass frame.
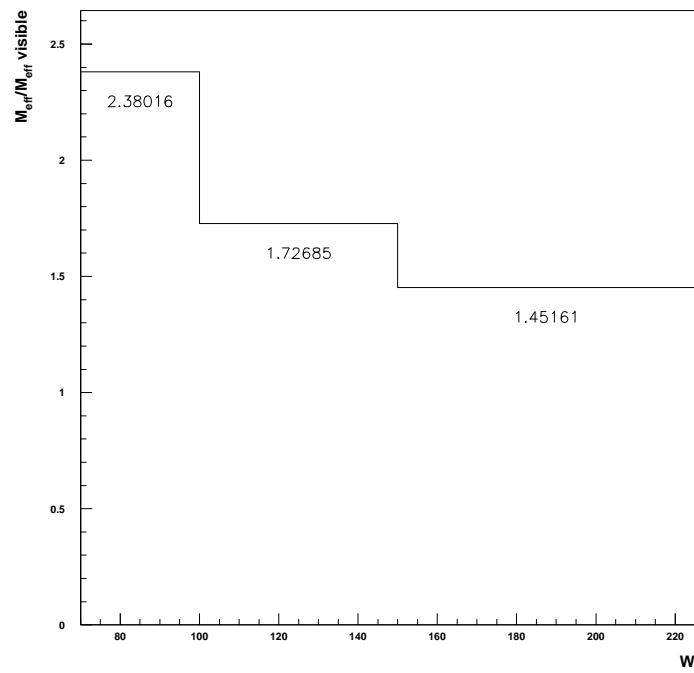
Figure 8.11: Correction factors, $C_\eta^{M_{\text{inv}}}$ (equation 8.10), for the part of the energy that falls outside the η acceptance of the detector for the photon region of the hadronic center of mass frame in bins of W.

correct for the energy that lies outside the visible region of the detector. This pseudorapidity correction is calculated in a similar way as the corrections for the hadrons in equation 8.9. The pseudorapidity correction factors for the M_{eff} are calculated at the generator level as

$$C_\eta^{M_{\text{inv}}} = \langle M_{\text{eff}}^{hadrons} \rangle / \langle M_{\text{eff}}^{hadrons,visible} \rangle \, , \tag{8.10}$$

where $\langle M_{\text{eff}}^{hadrons,visible} \rangle$ is calculated from the four momentum of the hadrons generated in the visible range of the detector. These corrections are done in 3 bins of W and are presented in figure 8.11. Like the pseudorapidity corrections for the tracks shown in figure **??**, these corrections are also W dependent.

For the measurement of $\langle n_{\text{ch}} \rangle$ vs. M_{eff} in the HCM frame, both correction factors, $C_\eta^{hadrons}$ and $C_\eta^{M_{\text{inv}}}$, are applied on an event by event basis to the tracks in the photon region before correction to the hadron level using the matrix or the modified bin-by-bin method. This results in each event having a non-integer number of tracks. Because of this, it is necessary to make the binning in the track distributions much finer. The number of bins for the track distributions is increased by a factor of 20.

No pseudorapidity acceptance correction for the invariant mass $(C_\eta^{M_{\text{inv}}})$ is applied to the measurement of the multiplicity versus $2 \cdot E_{\text{Breit}}^{\text{current}}$ in the current region of the Breit frame, since that is taken to be equal to W.

Chapter 9

Results

In this chapter the results obtained from the measurements in the Breit frame, the HCM frame and the laboratory frame are presented. For clarity they will be presented in the following order. The measurements in the current region of the Breit frame versus $2 \cdot E_{\mathrm{Breit}}^{\mathrm{current}}$ and in the photon region of the HCM frame versus W will be discusssed in sections 9.1 and 9.2. The comparison of these measurements with previous results from HERA is presented in section 9.3 and with results from other experiments in section 9.4. Section 9.5 will discuss the measured dependence of the mean charged multiplicity on M_{eff}, which was measured for the current and target regions of the Breit frame and for the photon region of the HCM frame. In the photon region of the HCM frame, the dependence of the multiplicity on M_{eff} is also studied in bins of x and Q^2 and the results of these measurements are also presented in section 9.5. In the final section of this chapter the method of determining the systematic errors for each of the above measurements is explained.

9.1 Mean Number of Charged Hadrons in the Breit Frame

The upper plot in figure 9.1 shows $\langle n_{\mathrm{ch}} \rangle$, measured in the current region of the Breit frame as a function of $2 \cdot E_{\mathrm{Breit}}^{\mathrm{current}}$, compared with predictions of ARIADNE with and without the high Q^2 treatment described in [66]. At energies below 20 GeV, the data are reasonably described by ARIADNE both with and without the high Q^2 treatment reasonably described. Within the large systematic uncertainties for the energy bins above 20 GeV, the data are reasonably described by ARIADNE both with and without the high Q^2 treatment. In the lower bins of $2 \cdot E_{\mathrm{Breit}}^{\mathrm{current}}$. ARIADNE with the high Q^2 treatment does a better job of describing the data in the highest bins of $2 \cdot E_{\mathrm{Breit}}^{\mathrm{current}}$.

9.2 Mean Number of Charged Hadrons in the HCM Frame

The lower plot in figure 9.1 shows the measured mean charged multiplicity, in the photon region of the HCM frame as a function of W. The measurement as a function of W can be only performed at high W, because of the acceptance of the ZEUS detector. The same predictions as in the upper plot of figure 9.1 are shown. Both ARIADNE samples describe the data well. The measurements of both plots in figure 9.1 are also shown in table 9.1

9.3 Comparison to Previous ep Measurements

Figure 9.2 shows the measured mean charged multiplicity, $\langle n_{\mathrm{ch}} \rangle$, in the photon region of the HCM frame as a function of W and the mean charged multiplicity, measured in the current region of the Breit frame as a function of $2 \cdot E_{\mathrm{Breit}}^{\mathrm{current}}$, compared with results of the previous measurements at HERA [71, 76, 75] and with predictions
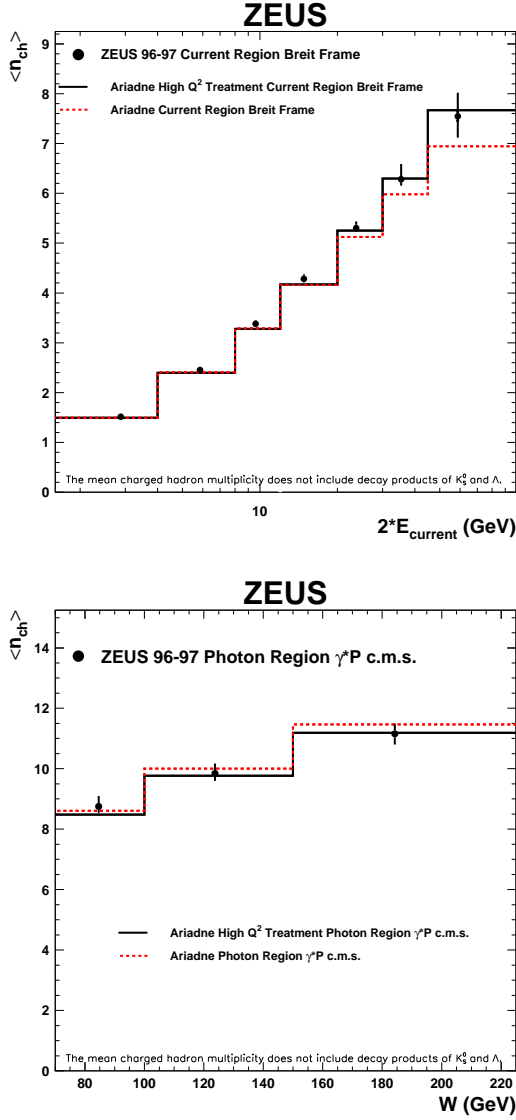
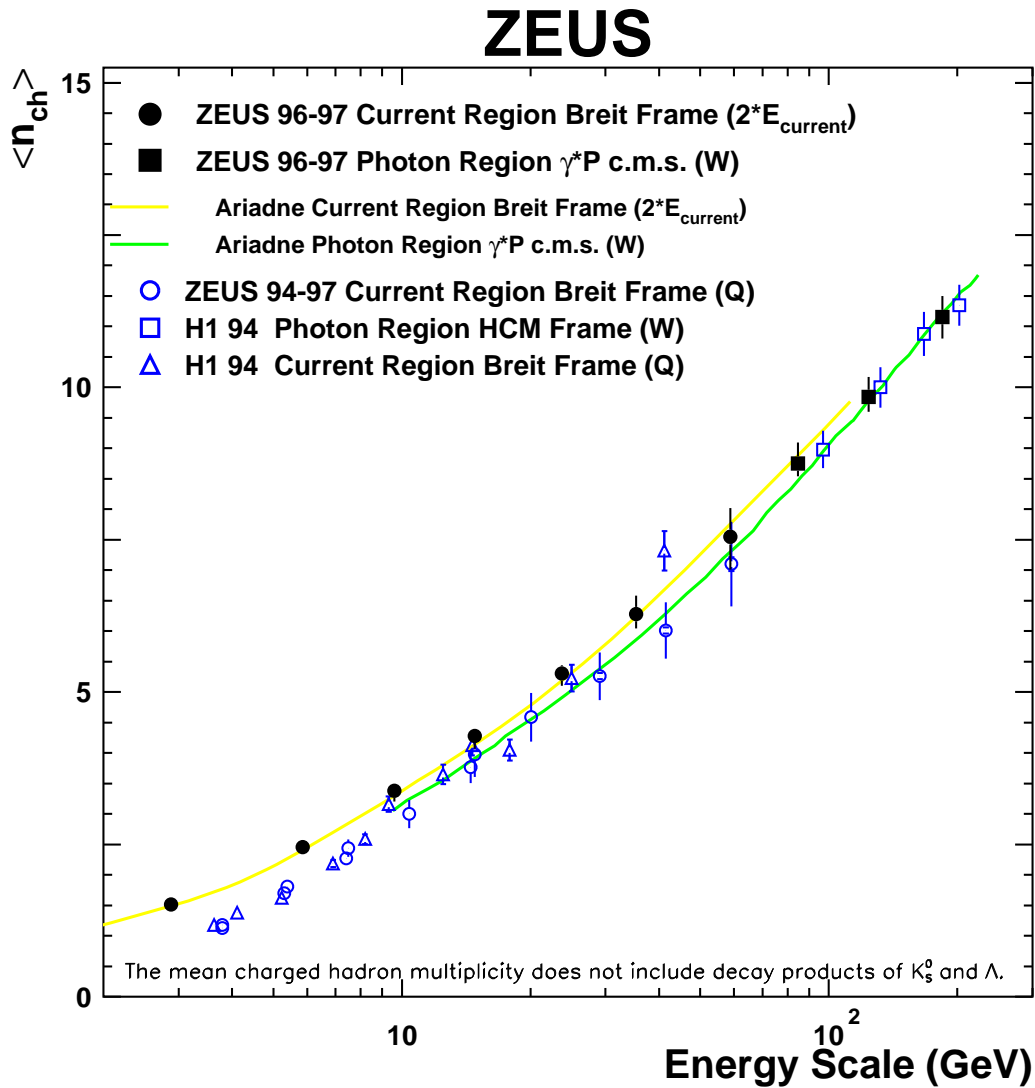**Figure 9.1:** (top) Mean charged multiplicity, $\langle n_{ch} \rangle$, in the current region of the Breit frame as a function of $2 \cdot E_{\text{Breit}}^{\text{current}}$. (bottom) Mean charged multiplicity, $\langle n_{ch} \rangle$, in the photon fragmentation region of the HCM as a function of W. The inner error bars represent the statistical uncertainties. The outer error bars represent the quadratic sum of statistical and systematic uncertainties. Also shown are the predictions from ARIADNE and LEPTO.

of ARIADNE. As discussed in section 2.2.4, at low energies, the $\langle n_{\mathrm{ch}} \rangle$ measurement as a function of $2 \cdot E_{\mathrm{Breit}}^{\mathrm{current}}$ presented in this thesis disagrees with the previous measurements of $\langle n_{\mathrm{ch}} \rangle$ as a function of Q. At higher energies, as a function of W, the data agree within the experimental uncertainties with the H1 measurement. ARIADNE MC decribes the data well. If compared at the same energies, the predictions for the $\langle n_{\mathrm{ch}} \rangle$ in the current region of the Breit frame are slightly higher than that for the photon region of HCM frame. Similar differences can be observed by comparing the results of fixed target DIS experiments to e^+e^-, but it cannot be confirmed experimentally at HERA, because of high systematic uncertainties and low statistics in the region of energies where the Breit frame and HCM measurements may overlap.

9.4   Comparison to Other Experiments

To compare the results of the measurements in the Breit and HCM frames with results of e^+e^- and pp experiments the mean charge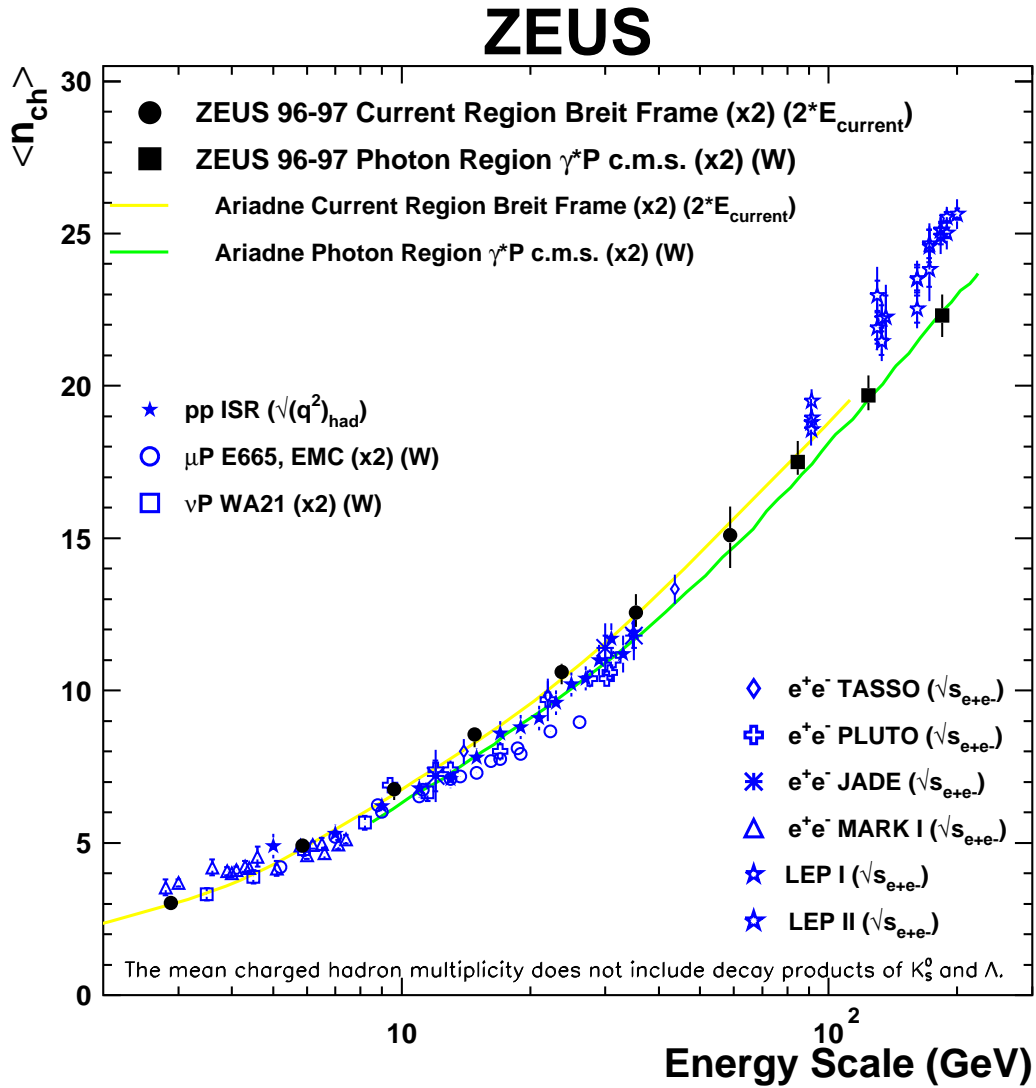d multiplicity is multiplied by 2. Figure 9.3 shows twice the measured mean charged multiplicity, $2 \cdot \langle n_{\mathrm{ch}} \rangle$, in the current region of the Breit frame plotted versus $2 \cdot E_{\mathrm{Breit}}^{\mathrm{current}}$ and twice the measured mean charged multiplicity in the photon region of the HCM frame plotted versus W. Also shown are the predictions of ARIADNE and the measurements from e^+e^- [17, 18], pp [25] and fixed target DIS experiments [72, 73, 74]. The measurements presented in this paper agree overall with the results of e^+e^- and pp measurements. It is noteworthy that at low values of energy, where the agreement with DIS measurements as a function of Q is degraded, the measurement as a function of $2 \cdot E_{\mathrm{Breit}}^{\mathrm{current}}$ agrees well with e^+e^- results. This can be explained by the fact that the migrations of final state particles out of the current region are compensated for in $E_{\mathrm{Breit}}^{\mathrm{current}}$.

ZEUS

Figure 9.2: Mean charged multiplicity, $\langle n_{\mathrm{ch}} \rangle$, in the current region of the Breit frame as a function of $2 \cdot E_{\mathrm{Breit}}^{\mathrm{current}}$ and in the photon fragmentation region of the HCM as a function of W. The inner error bars represent the statistical uncertainties. The outer error bars represent the quadratic sum of statistical and systematic uncertainties. Also shown are the results of previous HERA measurements [71, 76, 75] and predictions from ARIADNE.

Figure 9.3: Mean charged multiplicity, $\langle n_{ch} \rangle$, in the current region of the Breit frame multiplied by 2 plotted versus $2 \cdot E_{\mathrm{Breit}}^{\mathrm{current}}$ and in the photon region of the HCM frame multiplied by 2 plotted versus W. The results of e^+e^- [17, 18], pp [25] and fixed target DIS experiments [72, 73, 74], as well as prediction of the ARIADNE are also shown.

Starting at about 20 GeV, the results of fixed target DIS measurements demonstrate slightly different energy dependence, than that expected from the ARIADNE ep MC.

9.5   Dependence of Mean Charged Multiplicity on M_{eff}

As discussed in section 7.4 the charged multiplicities in the different regions can be also compared as a function of the invariant mass of the correspondent hadronic system, M_{eff}.

To confirm that the comparison of charged multiplicity as a function of M_{eff} is not biased by the choice of the phase space the x and Q^2 dependences were studied. Figure 9.4 presents the mean charged multiplicity in the photon region of HCM as a function of the correspondent M_{eff} in four x regions. From this plot one can observe that $\langle n_{\mathrm{ch}} \rangle$ is independent of x for events with lower M_{eff}, but for events with larger M_{eff}, the multiplicity increases by about 10 % as x decreases. As x decreases the phase space available for gluonic radiation inside the proton increases, which could explain the increase in multiplicity. This x dependence is predicted by ARIADNE as shown on this plot. The ARIADNE predictions agree well with the measured multiplicity in all the x regions. Figure 9.5 presents the same results in bins of x and Q^2, along with the Monte Carlo predictions from ARIADNE. The solid black line in each of the x-Q^2 bins is the ARIADNE prediction in the full phase space, i.e. over all x and Q^2. This line is therefore identical in all x and Q^2 bins, and has been plotted to guide the eye when looking at differences in the bins. The dashed lines are the ARIADNE predictions for each particular x and Q^2 bin. The charged multiplicities are described by ARIADNE. In figure 9.5 the x dependence that was shown figure 9.4 is observed, and does not
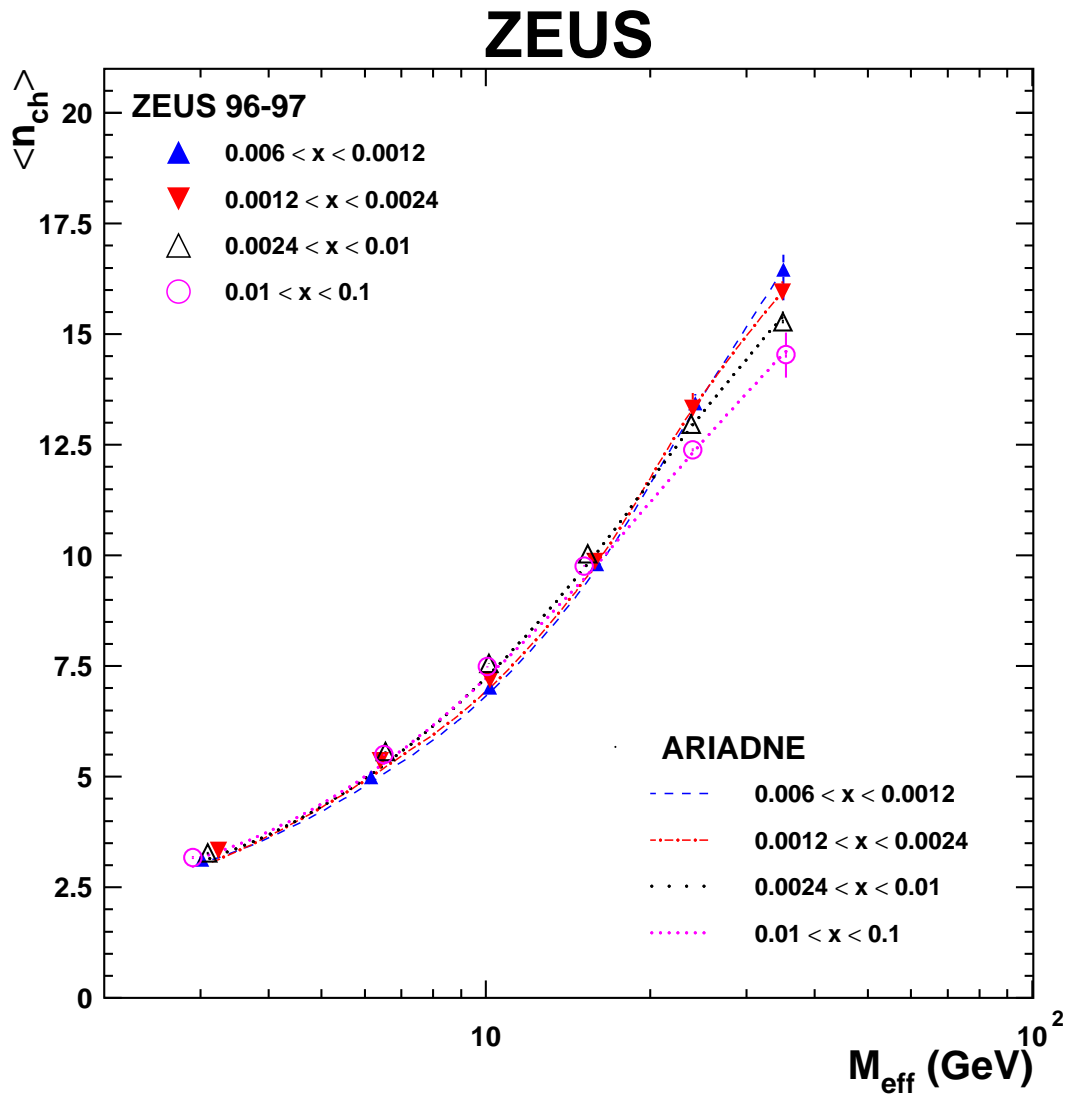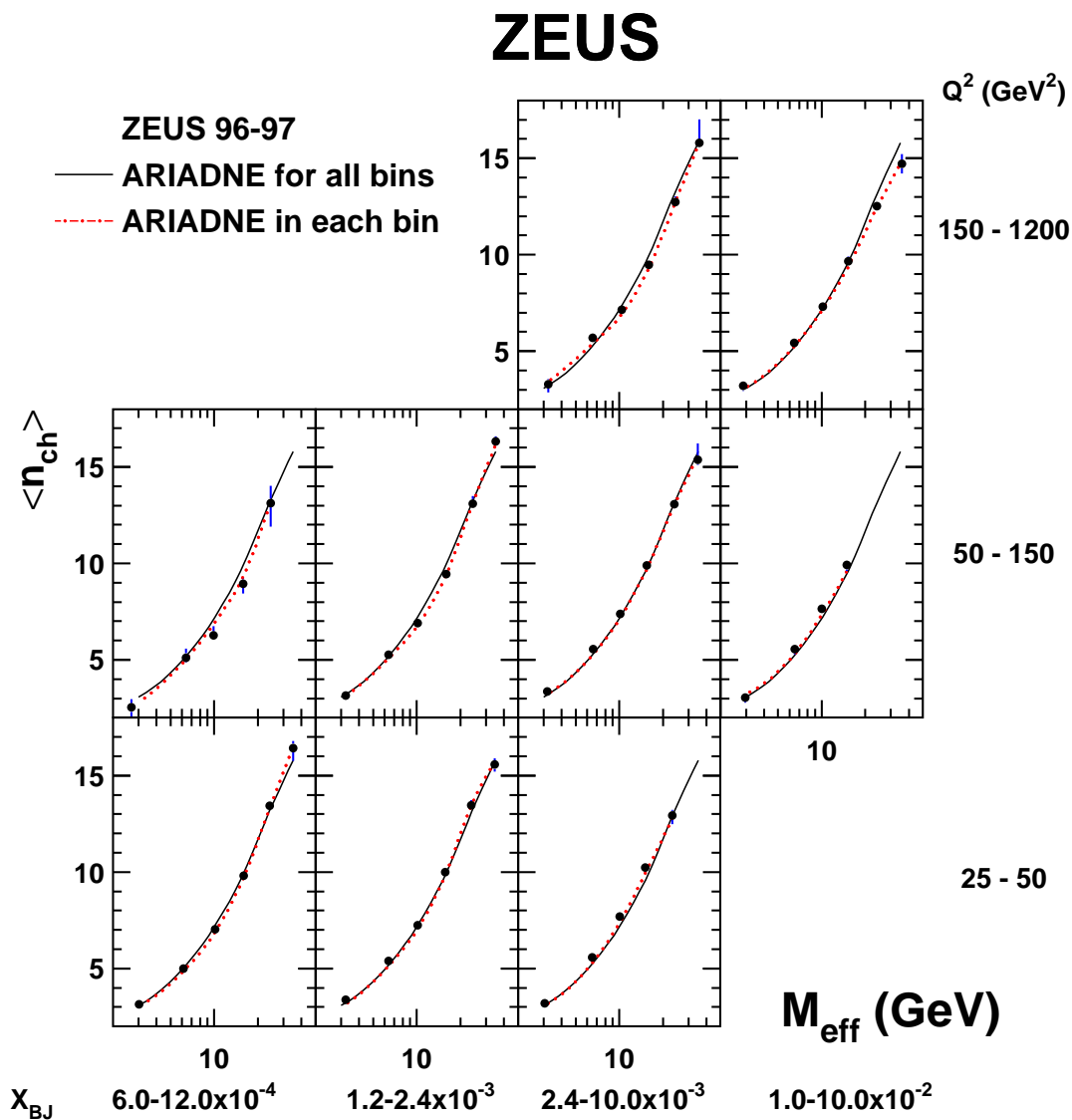
Figure 9.4: Mean charged multiplicity, $\langle n_{ch} \rangle$, in the photon region of the HCM frame for different x regions together with predictions from ARIADNE.

seem to be dependent on Q^2. The results are correlated since $Q^2 = sxy$ and so some Q^2 dependence is expected. As Q^2 increases, the multiplicity can be seen to slightly decrease. The data are described reasonably well by ARIADNE.

In the upper plot of figure 9.6 the current multiplicity is compared to the target multiplicity in the Breit frame. To avoid large MC-dependent correction factors, see section 7.2, the target multiplicity is only measured in the angular region defined by the acceptance of the detector. This comparison was performed in the previous ZEUS analysis as a function of Q^2, where it was found that the visible target multiplicity is about four times higher than the current one for the same Q^2 [75]. As a function of the M_{eff} the target multiplicity is slightly above the current one for the same values of the M_{eff} indicating that it has a bigger contribution of soft particles. The current region of the Breit frame and photon region of the HCM frame are compared in the lower plot of figure 9.6 and in table 9.2. Although for the low values of M_{eff} the number of charged hadrons scales similar for both regions, starting at about 10 GeV the number of charged particles increases faster with the M_{eff} in the photon region of HCM than in the current region of the Breit frame.

Comparing figures 9.2, 9.3 and the lower plot of 9.6 and the corresponding tables one can conclude also, that the $\langle n_{\text{ch}} \rangle$ as a function of M_{eff} for the current region of the Breit frame exhibits similar behavior to $2 \cdot \langle n_{\text{ch}} \rangle$ as a function of $2 \cdot E_{\text{Breit}}^{\text{current}}$ and, therefore, the same one as $\langle n_{\text{ch}} \rangle$ as a function of $\sqrt{s}_{ee}$ in $e^+ e^-$. This scaling obviously does not hold in the HCM frame case.

$2 \cdot E_{\text{Breit}}^{\text{current}}$	$\langle n_{\text{ch}} \rangle$	δ_{stat}	δ_{sys}
2.88	1.516	0.003	+0.089/-0.027
5.85	2.452	0.002	+0.080/-0.020
9.61	3.38	0.01	+0.08/-0.18
14.8	4.28	0.01	+0.10/-0.21
23.7	5.30	0.02	+0.13/-0.20
35.4	6.28	0.04	+0.30/-0.23
58.7	7.55	0.09	+0.46/-0.53
W	$\langle n_{\text{ch}} \rangle$	δ_{stat}	δ_{sys}
84.6	8.75	0.01	+0.35/-0.21
124	9.84	0.01	+0.33/-0.24
184	11.16	0.01	+0.35/-0.35

Table 9.1: Mean charged multiplicity, $\langle n_{\text{ch}} \rangle$, measured in the current region of the Breit frame as a function of $2 \cdot E_{\text{Breit}}^{\text{current}}$ and in the photon fragmentation region of the HCM frame as a function of W.

M_{eff}	$\langle n_{\text{ch}} \rangle$ (Breit, Current)	δ_{stat}	δ_{sys}
2.4	2.979	0.002	+0.016/-0.067
5.08	4.95	0.01	+0.02/-0.16
9.32	6.92	0.04	+0.04/-0.08
14.2	8.67	0.09	+0.13/-0.89
23	9.72	0.02	+0.99/-2.33
M_{eff}	$\langle n_{\text{ch}} \rangle$ (HCM, Photon)	δ_{stat}	δ_{sys}
3.03	3.21	0.01	+0.01/-0.10
6.47	5.45	0.01	+0.05/-0.09
10.1	7.44	0.01	+0.04/-0.08
15.5	9.92	0.01	+0.09/-0.07
23.9	13.12	0.01	+0.21/-0.11
35	15.71	0.02	+0.33/-0.06

Table 9.2: Mean charged multiplicity, $\langle n_{\text{ch}} \rangle$, measured in the current region of the Breit frame and in the photon fragmentation region of the HCM frame as a function of M_{eff}.

ZEUS

ZEUS 96-97
— ARIADNE for all bins
—·— ARIADNE in each bin

Q^2 (GeV^2)

$\langle n_{ch} \rangle$

150 - 1200

50 - 150

10

25 - 50

M_{eff} (GeV)

X_{BJ} 6.0-12.0x10^{-4} 1.2-2.4x10^{-3} 2.4-10.0x10^{-3} 1.0-10.0x10^{-2}

Figure 9.5: Mean charged multiplicity, $\langle n_{ch} \rangle$, in the photon region of the HCM frame as a function of M_{eff} for different Q^2 and x regions together with ARIADNE predictions. The prediction of ARIADNE for the total phase space (solid line) is shown in each (x, Q^2) region for comparison.
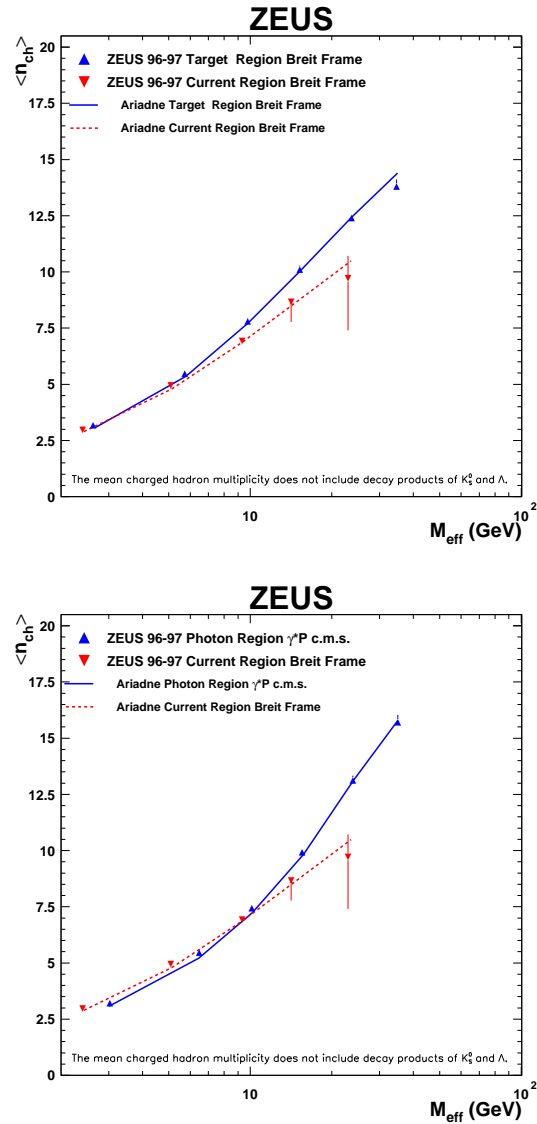
Figure 9.6: (top) Comparison of the mean charged multiplicity in the current and target regions of the Breit frame as a function of M_{eff}. The target region points shown are for the part of the target region that is visible in the detector. (bottom) Mean charged multiplicity, $\langle n_{\mathrm{ch}} \rangle$, in the photon fragmentation region of the HCM frame and in the current region of the Breit frame as a function of M_{eff}. Predictions from ARIADNE are also shown.

9.6 Systematic Uncertainties

The statistical errors for this measurement are small and cannot be seen in the plots because they are smaller than the size of the markers. Systematic errors make up almost the entire uncertainty of the measurements presented in this thesis. In the final plots of the measurements, only the uncorrelated systematic error is shown .

9.6.1 Correlated Systematic Uncertainties

In this analysis the main source of correlated systematic error is the uncertainty in the energy scale of the calorimeter. The calorimeter energy scale uncertainty was studied for singe-jet events and was determined to be within ± 3 % [77]. The effect of this uncertainty on each of the measurements is determined by varying the energy measured from ZUFO's by ± 3 % and evaluating the difference this causes in the resulting measurement. For each measurement in this analysis, the systematic error in percentage coming from the calorimeter energy scale uncertainty is shown in figure 9.7. The error is less than 2 % in all bins, for all measurements, and tends to decrease as the energy scale increases. For the measurement of $\langle n_{\mathrm{ch}} \rangle$ vs. W in the photon region of the HCM frame, which reaches much higher energies than the other measurements, the error due to the calorimeter energy scale uncertainty is less than 0.5 % in all three W bins.

9.6.2 Uncorrelated Systematic Uncertainties

Uncorrelated systematic uncertainties arise from imperfections in the Monte Carlo model used for acceptance corrections. Most of these errors come from applying a cut on a variable with a distribution that is not fully reproduced by the Monte Carlo.

164
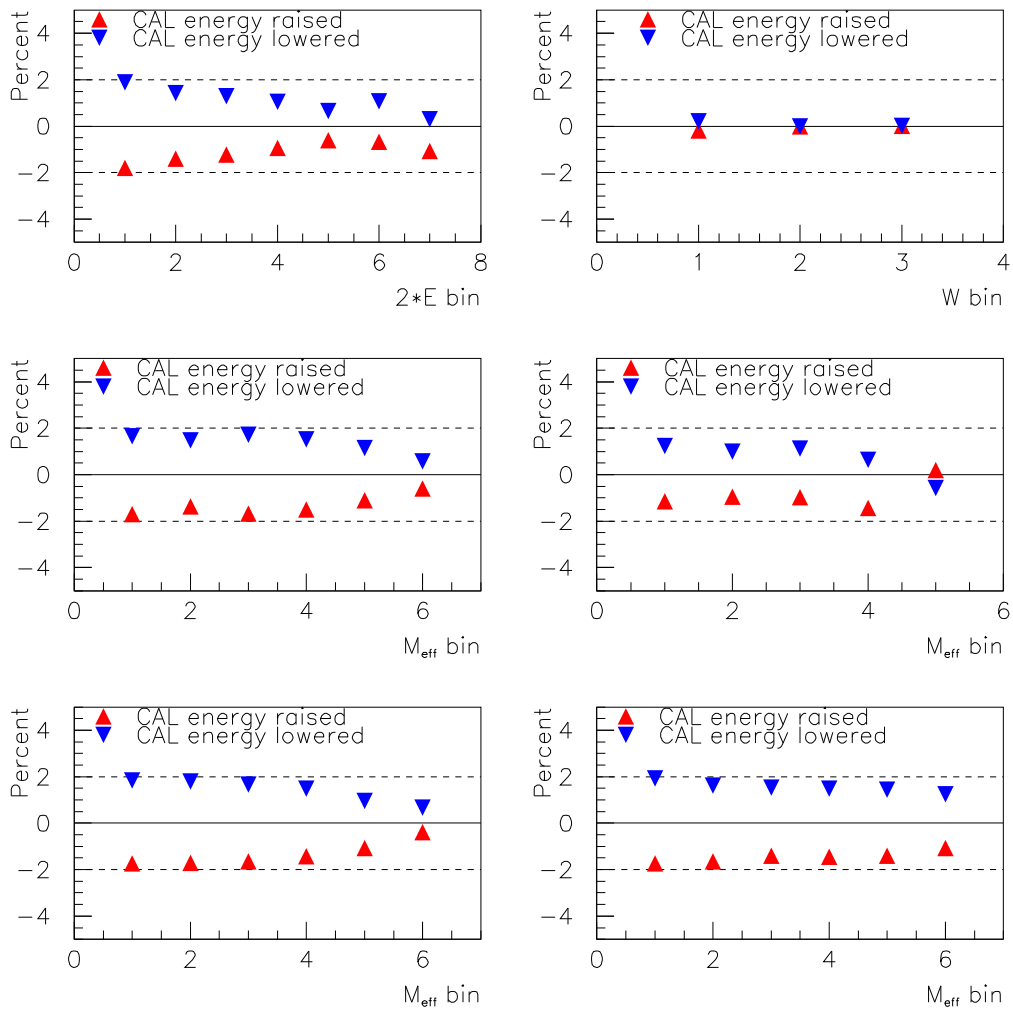
Figure 9.7: Percent of systematic error caused by the calorimeter energy scale uncertainty for each measurement. The ranges for the W, $2 \cdot E_{\mathrm{Breit}}^{\mathrm{current}}$ and M_{eff} bins are given in section 6.6.1.

Each selection cut made on the data introduces a systematic error because there are events that migrate over the cut boundary. If the Monte Carlo described the data in the distribution perfectly, and therefore described perfectly these migrations, then there would be no systematic error. In order to estimate the size of this effect, the cuts used in the analysis are varied by one standard deviation of the resolution (at the cut boundary) of the variable in consideration, keeping all other cuts at their nominal value. The difference in the resulting measurement is the systematic uncertainty. The systematic uncertainties from each of these excursions are then added in quadrature to get the total uncorrelated systematic error. This procedure has been followed for the following cuts, while the original cut values are described in chapter 6:

- Track p_{T}, raised by 50 MeV

- $E_{e'}$, variation by ± 1 GeV

- Q^2_{DA}, variation by ± 1.6 GeV^2

- Z_{vtx}, variation by $\pm 5 cm$

- $E - p_{\mathrm{z}}$, both lower and upper cut variation by ± 5 GeV

- radius cut, variation by $\pm 1 cm$

- y_{JB}, variation by ± 0.006

- y_{el}, variation by ± 0.05

- W, lower cut variation by 5.6 GeV and upper cut variation by 13.5 GeV

The following additional sources of uncorrelated systematic error were also included:

- using the bin-by-bin method instead of the matrix method to correct $\langle n_{ch} \rangle$ for detector acceptance.

- using LEPTO instead of ARIADNE

- removing the η_{max} cut

The variations in percentage from each of these excursions is shown for each measurement in figures 9.8 through 9.13. In general the errors coming from the cuts are small, typically less then 0.5 % for all the measurements, but can reach $1.5 - 2.5$ % for isolated bins. The main source of uncorrelated systematic error for all the measurements comes from the choice of method used to correct the data to the hadron level and the choice of Monte Carlo.

The dependence on the choice of Monte Carlo is pronounced for the measurement in the photon region of the HCM frame versus W, shown in Figure 9.9. Using LEPTO instead of ARIADNE introduces a systematic error that increases up to 6% in the highest W bin, with LEPTO predicting increasingly higher multiplicities than ARIADNE.

Figure 9.11 shows the variations for the measurement in the current region of the Breit Frame versus M_{eff}. The largest M_{eff} bin has a systematic uncertainty that is significantly larger than for the other M_{eff} bins caused by the lower statistics in this bin. This bin is most sensitive to variations in the track p_T, W, choice of Monte Carlo and method of correction.

The total systematic error is shown as a percentage for each measurement in figure 9.14.
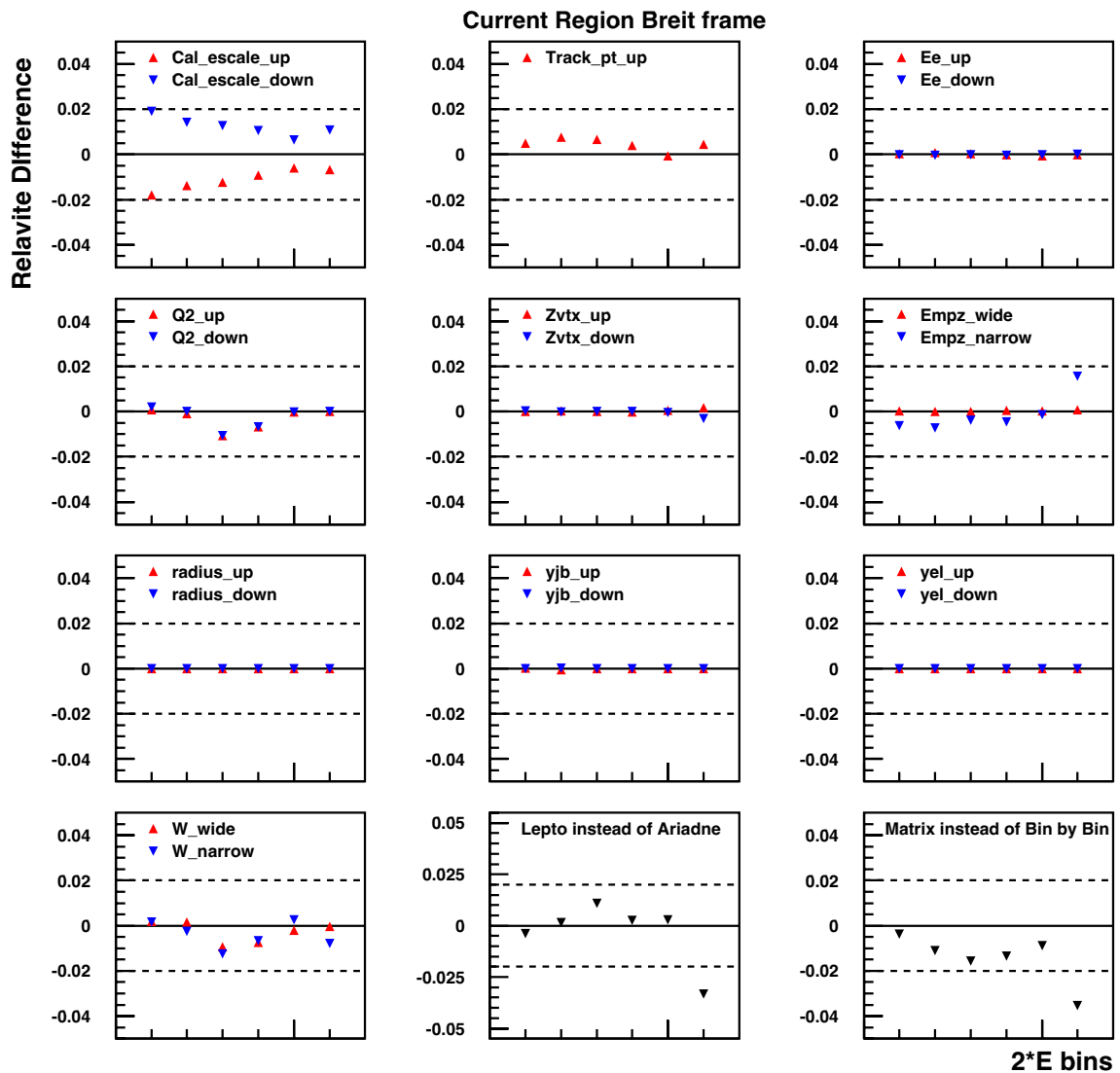
Figure 9.8: Percent of each systematic for each $2 \cdot E_{\mathrm{Breit}}^{\mathrm{current}}$ bin in current region of Breit frame. The horizontal dashed lines indicate $\pm 2\%$.

Photon Region Hadronic Center of Mass Frame
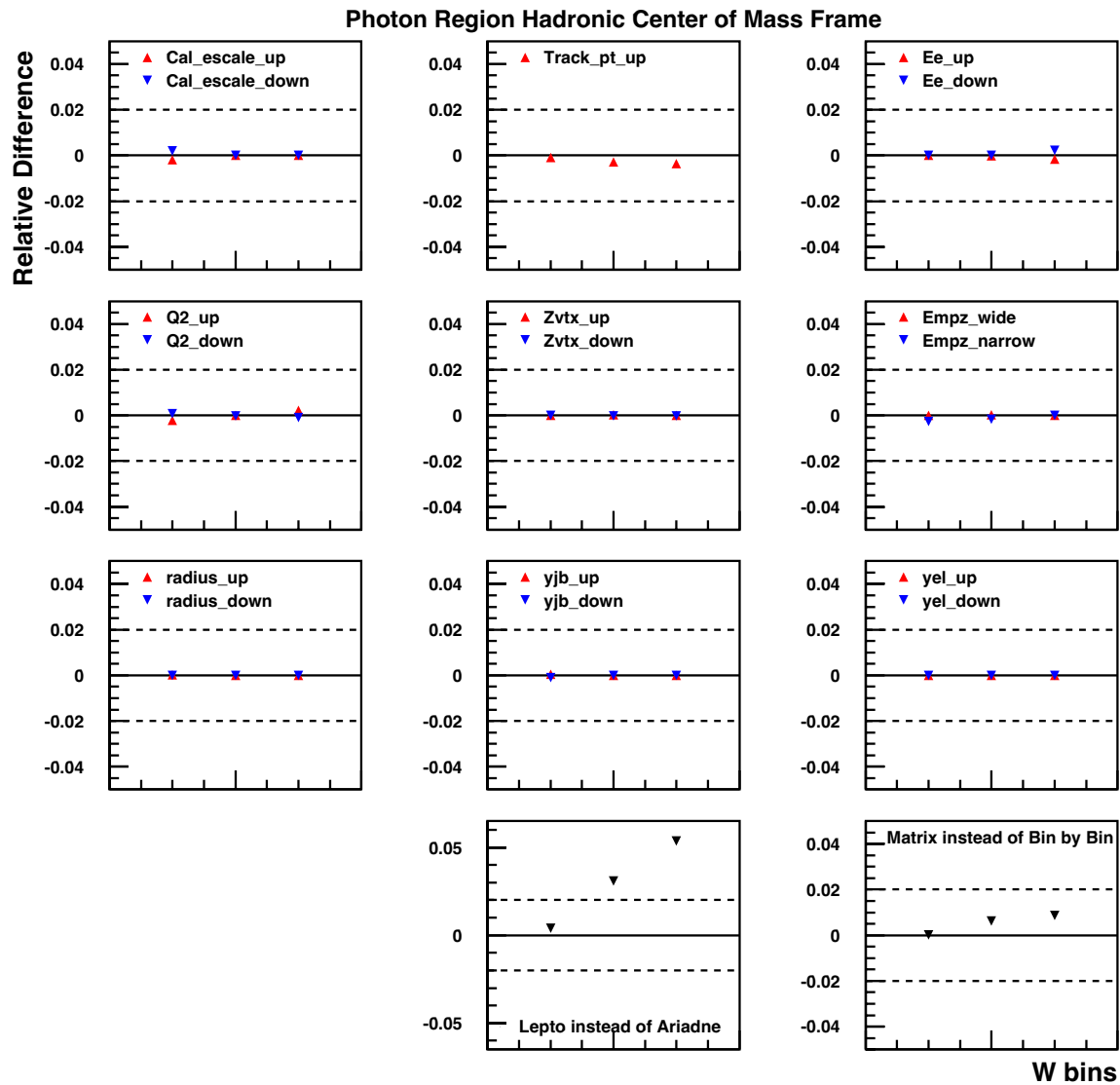
Figure 9.9: Percent of each systematic for each W bin in current region of hadronic center of mass frame. The horizontal dashed lines indicate $\pm 2\%$.

169
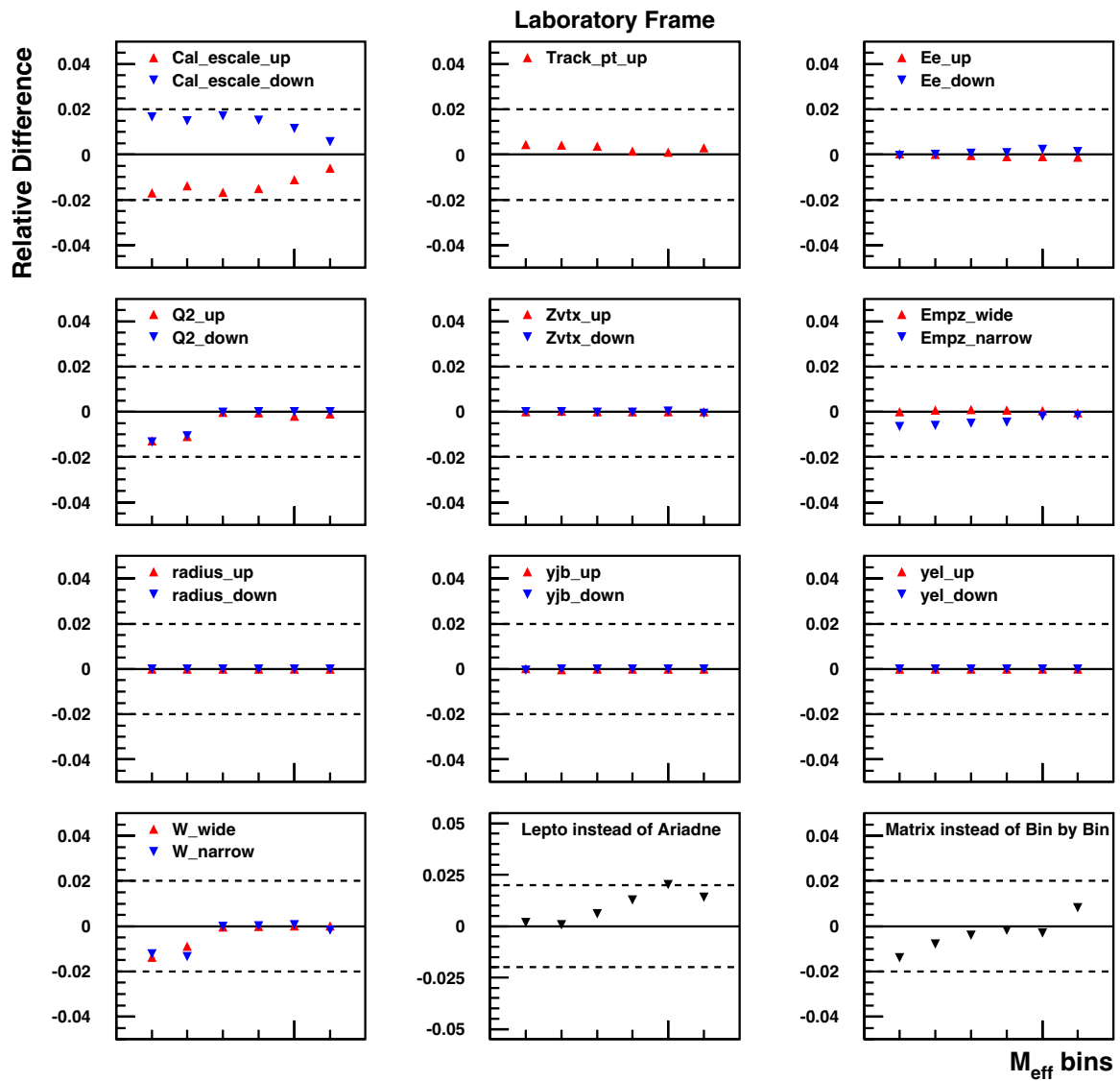
Figure 9.10: Percent of each systematic for each M_{eff} bin in the laboratory frame. The horizontal dashed lines indicate $\pm 2\%$.

170
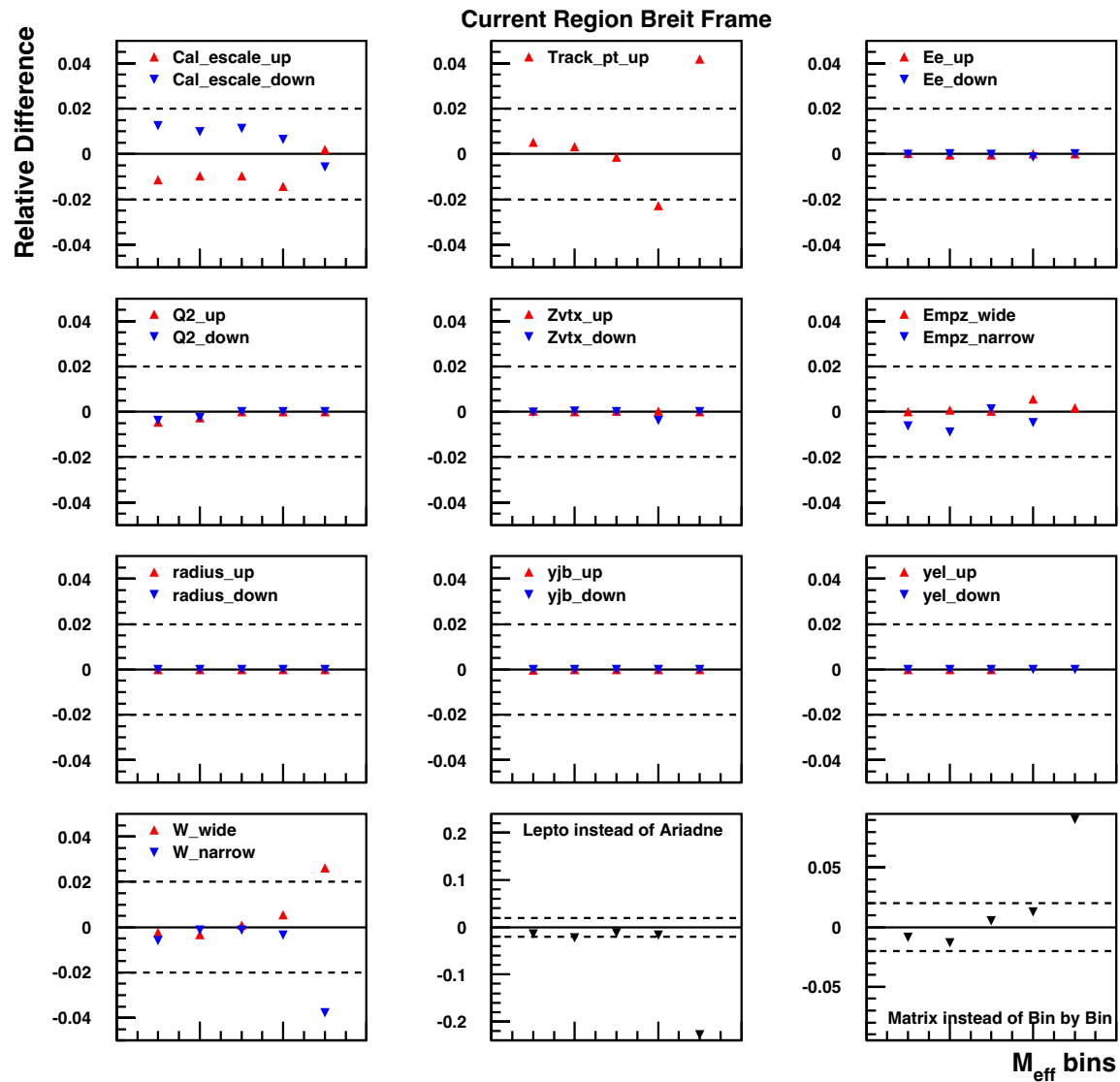
Figure 9.11: Percent of each systematic for each M_{eff} bin in the current region of the Breit frame. The horizontal dashed lines indicate $\pm 2\%$.
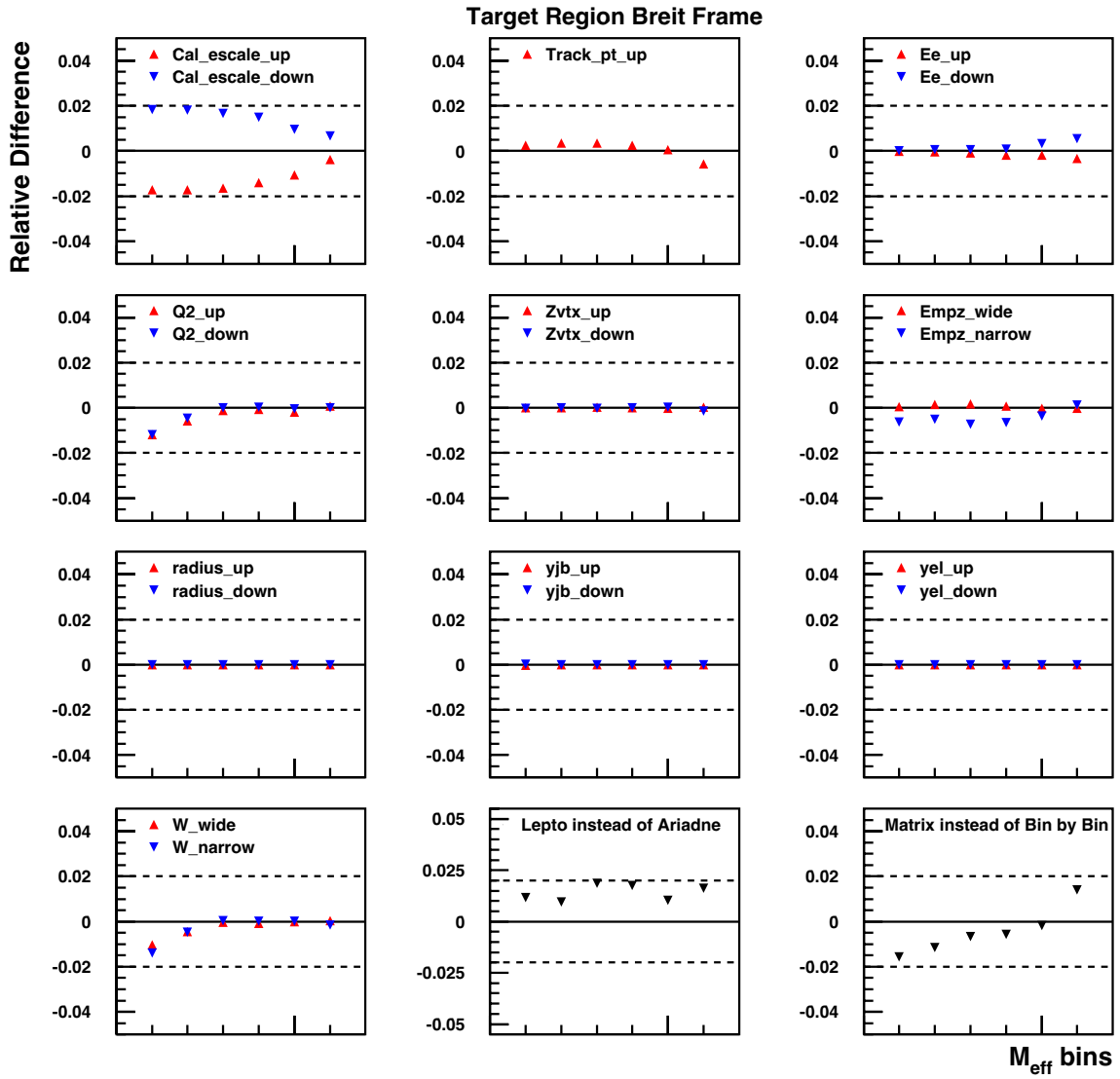
Figure 9.12: Percent of each systematic for each M_{eff} bin in the target region of the Breit frame. The horizontal dashed lines indicate $\pm 2\%$.

172
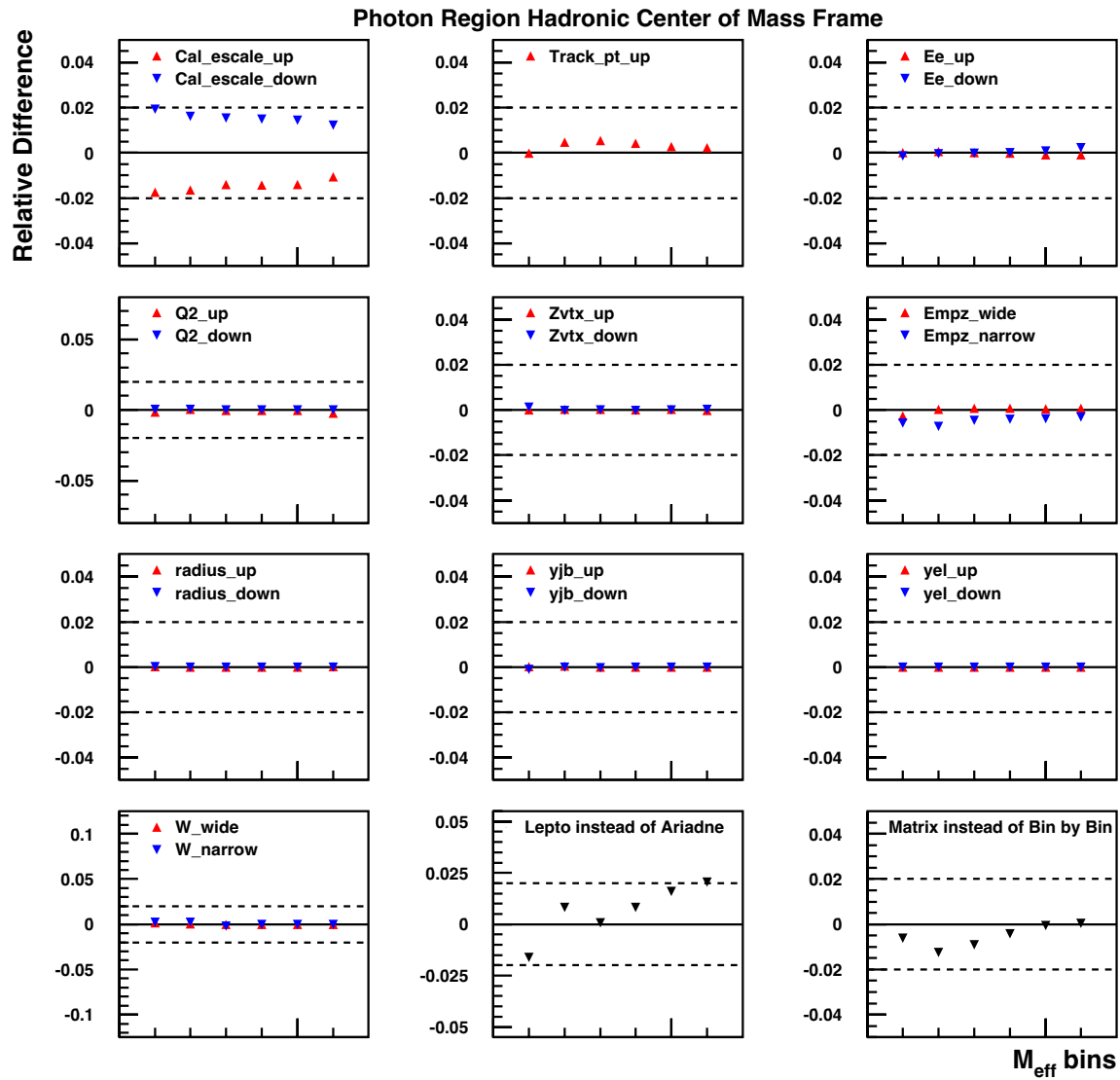
Figure 9.13: Percent of each systematic for each M_{eff} bin in current region of hadronic center of mass frame. The horizontal dashed lines indicate $\pm2\%$. (Multiply y-axis by 100 to get percent.
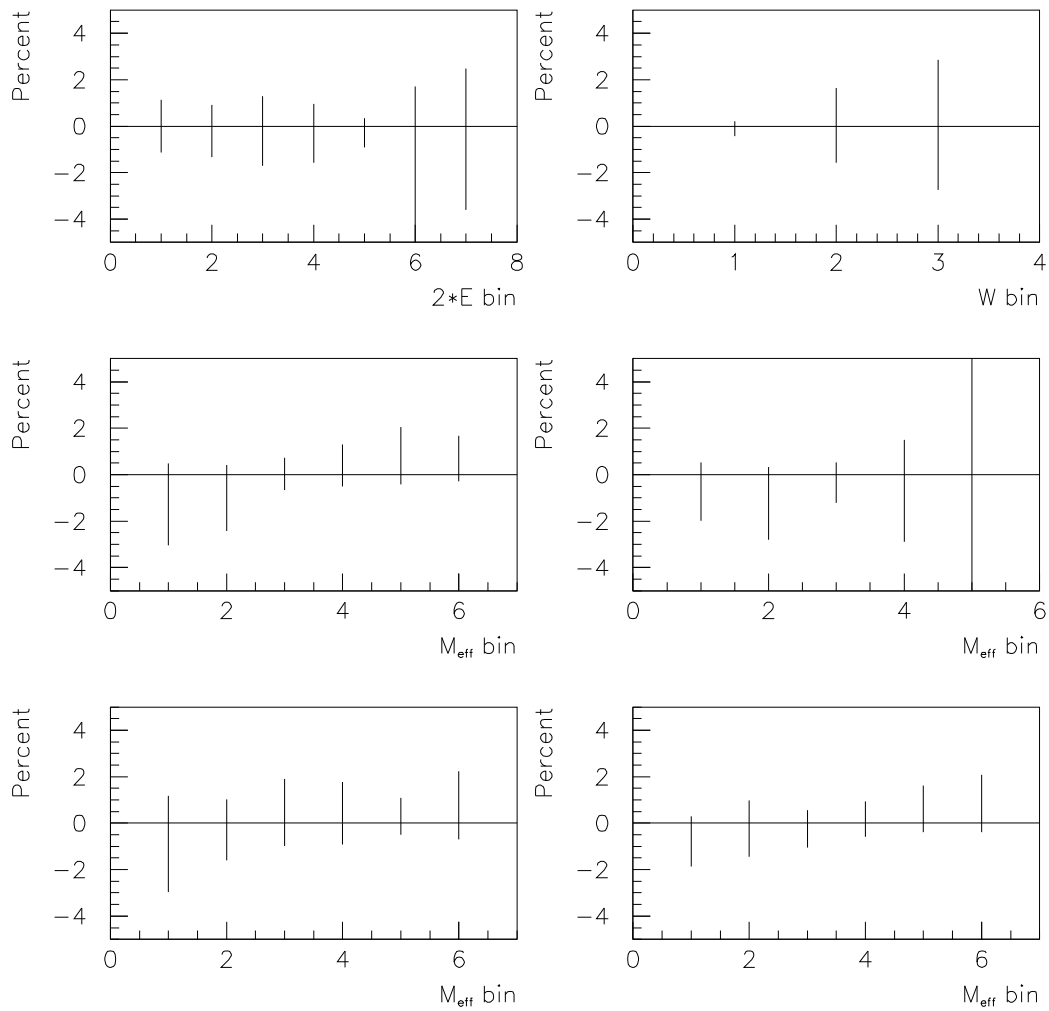
Figure 9.14: Total systematic error for each measurement in percentage, calculated by adding the uncorrelated systematic errors in quadrature. The definition of the bins is given in section 6.6.1.

The systematic error was also determined in the laboratory frame in four bins of x versus M_{eff}. The x bin ranges are given in section 6.6.1. The main sources of systematic error are shown in figures 9.15 through 9.20 and as one might expect, are the same as for the measurement in the total phase space. For that measurement, shown in figure 9.10, the variations in Q^2 and W show a systematic shift of about 1.5% in the negative direction for the first two bins of M_{eff}, and almost no variation in the other bins. Figures 9.17 and 9.18 show that when this measurement is divided into x bins, the sensitivity of the lowest two M_{eff} bins to the Q^2 and W cuts comes mainly from the highest two x bins. The total systematics added in quadrature are shown in bins of x in figure 9.21.
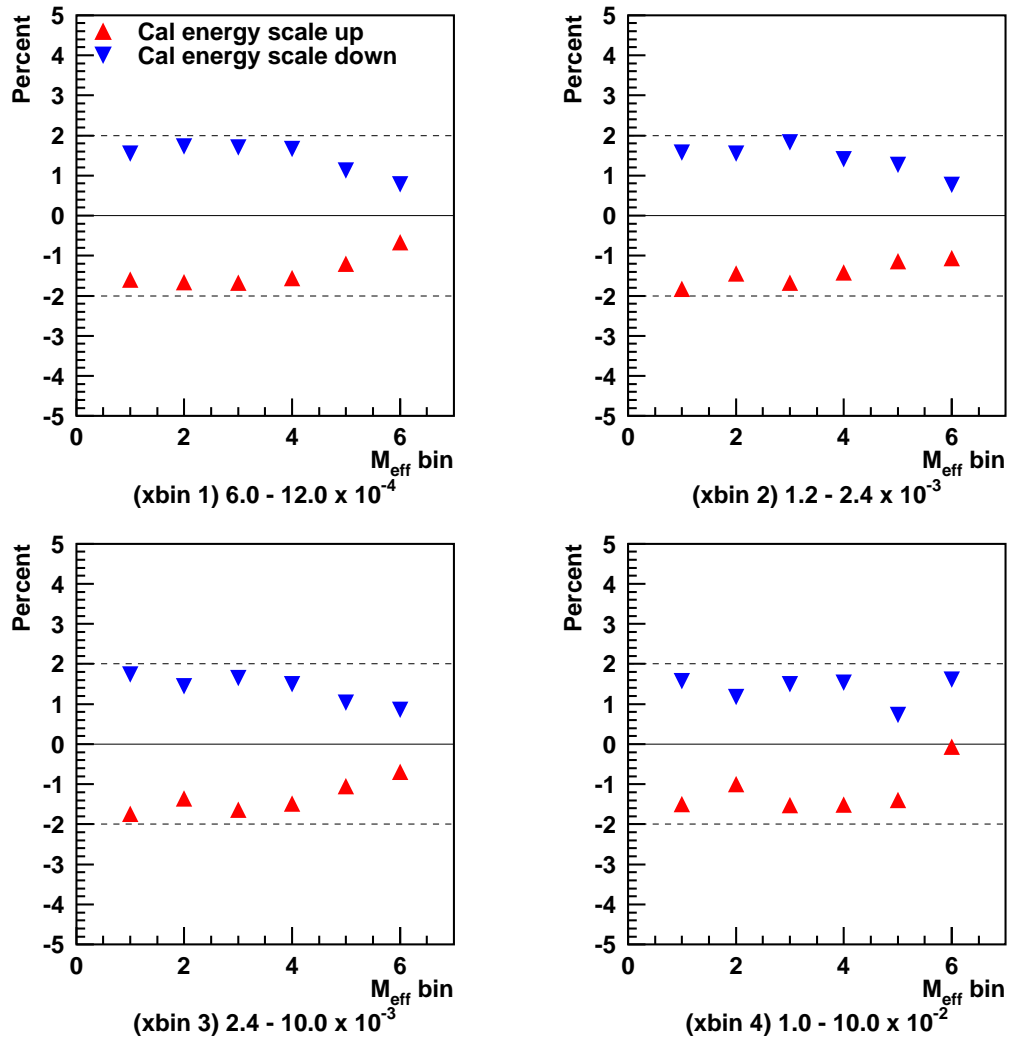
Figure 9.15: Percent of systematic error caused by the calorimeter energy scale uncertainty for the laboratory frame measurement of $\langle n_{\mathrm{ch}} \rangle$ versus M_{eff} in four bins of x. The range of the x bins is given in section 6.6.1. The horizontal dashed lines indicate $\pm 2\%$.
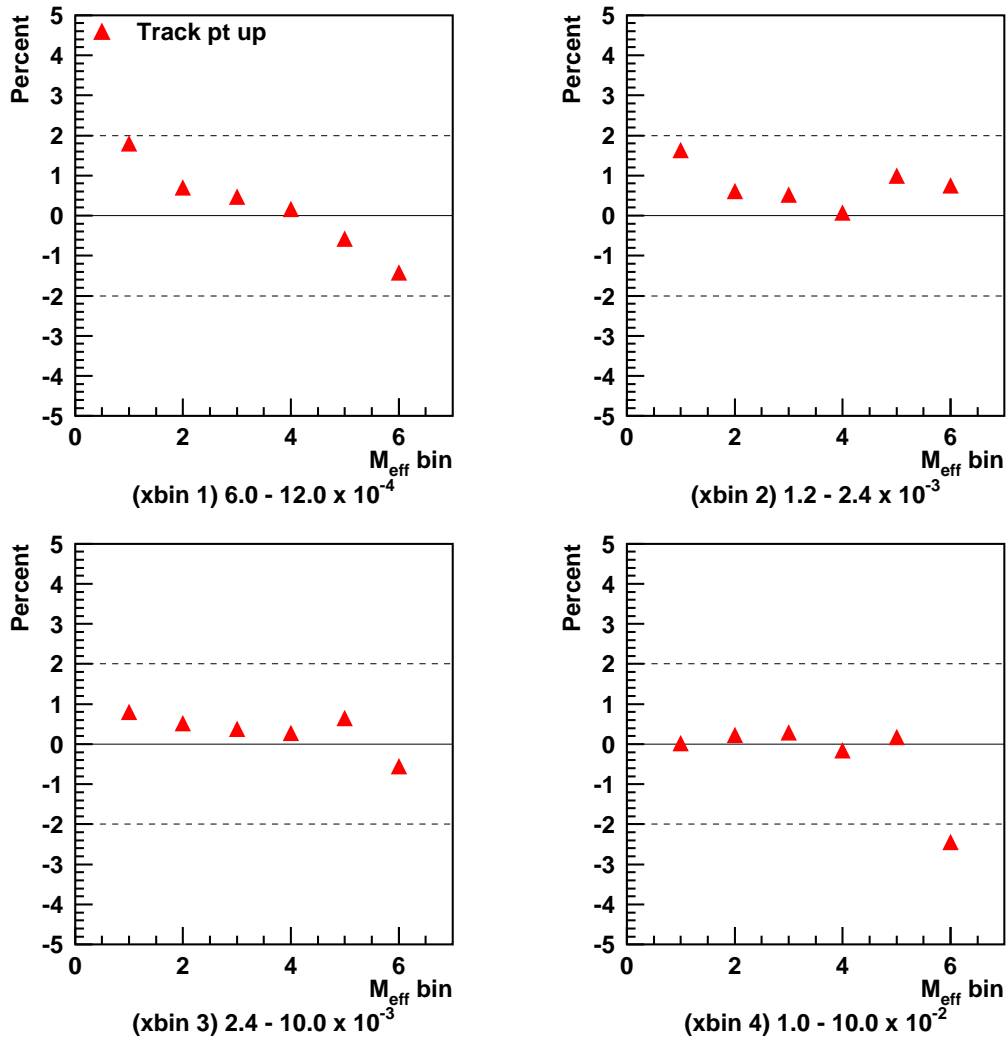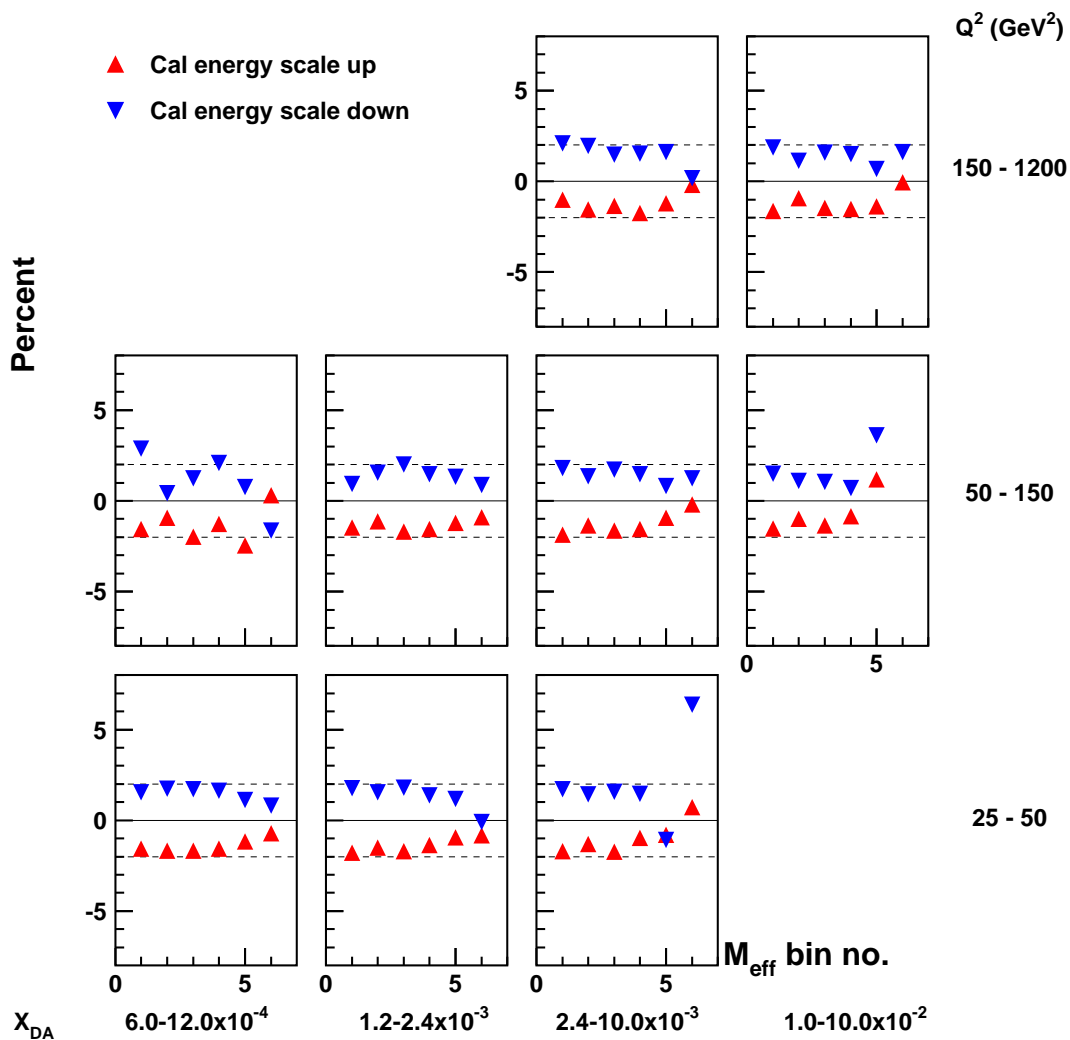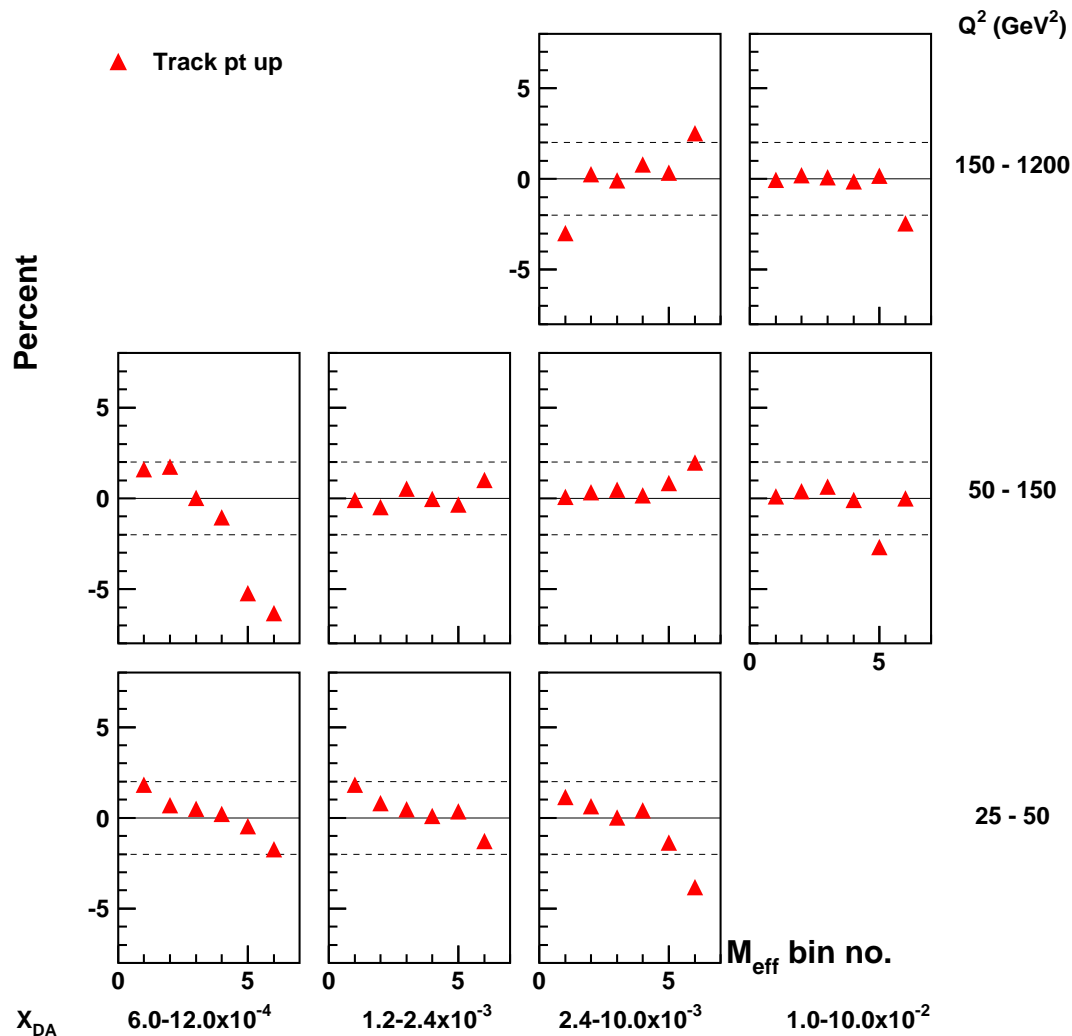
Figure 9.16: Percent of systematic error caused by raising the p_T of the tracks for the laboratory frame measurement of $\langle n_{\mathrm{ch}} \rangle$ versus M_{eff} in four bins of x. The range of the M_{eff} bins is given in section 6.6.1. The horizontal dashed lines indicate $\pm 2\%$.
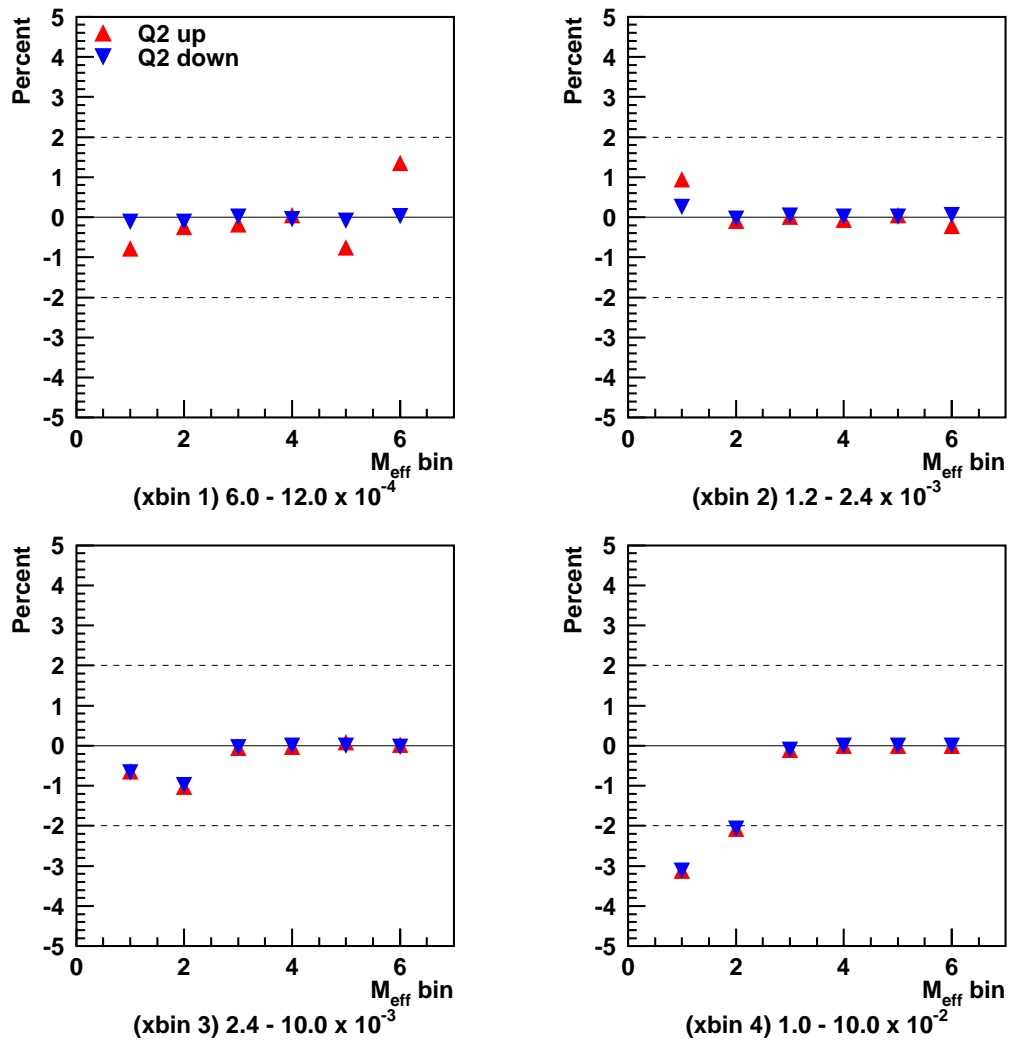
Figure 9.17: Percent of systematic error caused by varying the Q^2 cut for the laboratory frame measurement of $\langle n_{\mathrm{ch}} \rangle$ versus M_{eff} in four bins of x. The range of the M_{eff} bins is given in section 6.6.1. The horizontal dashed lines indicate $\pm 2\%$.

178
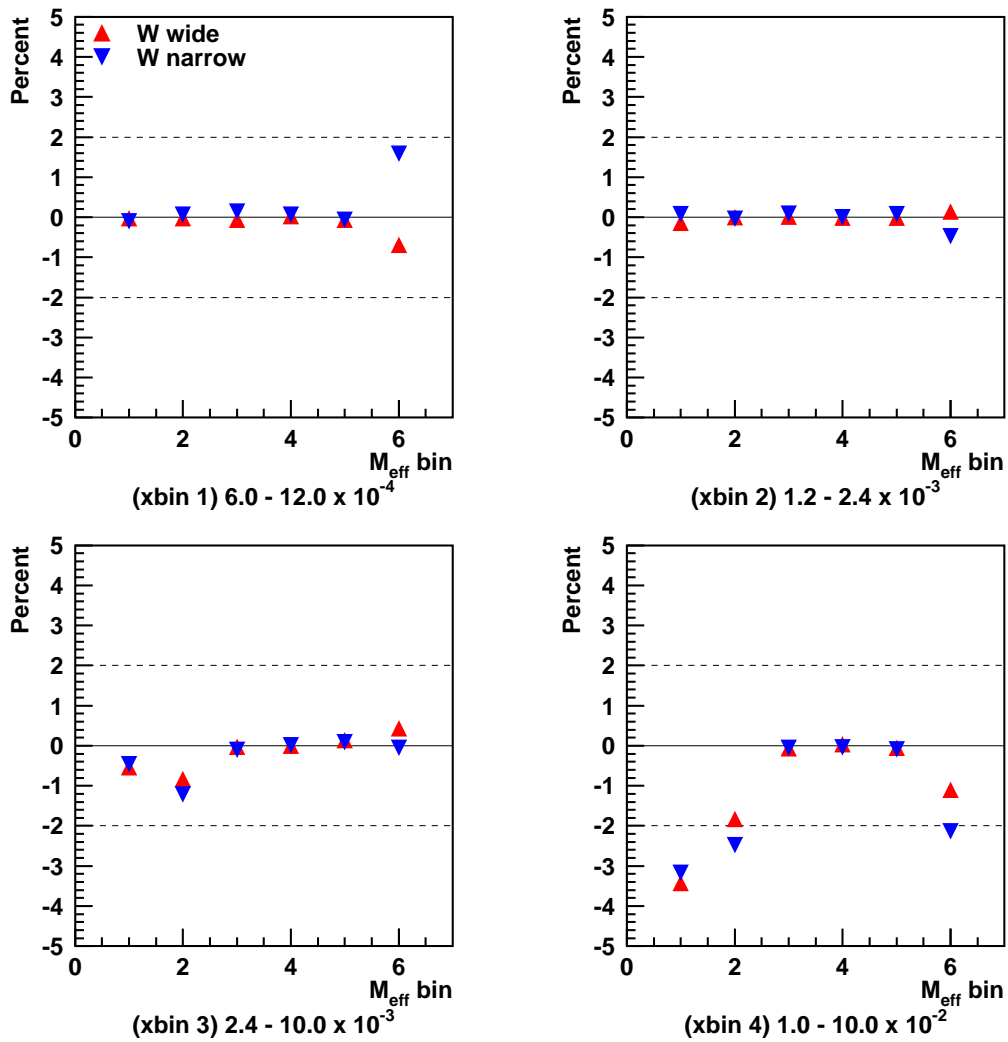
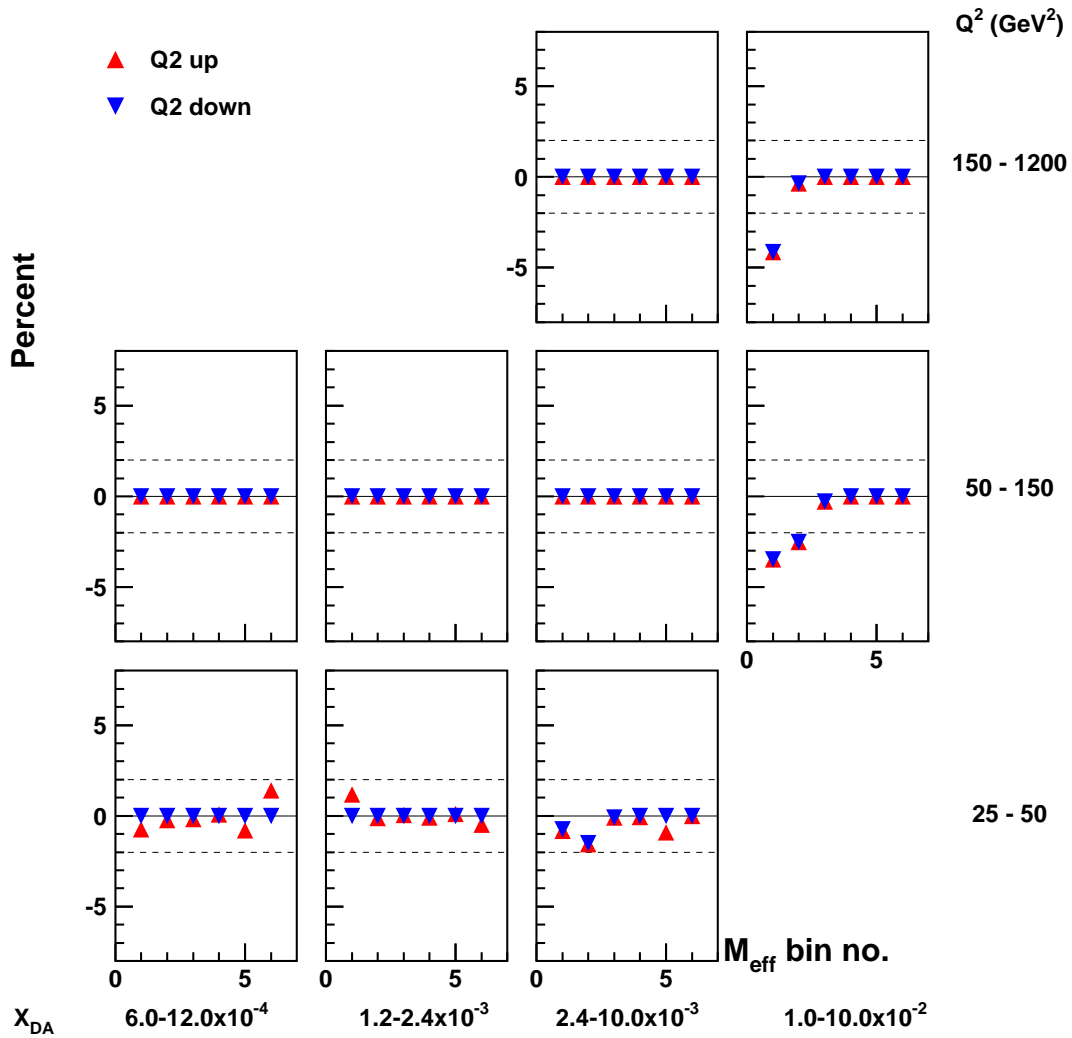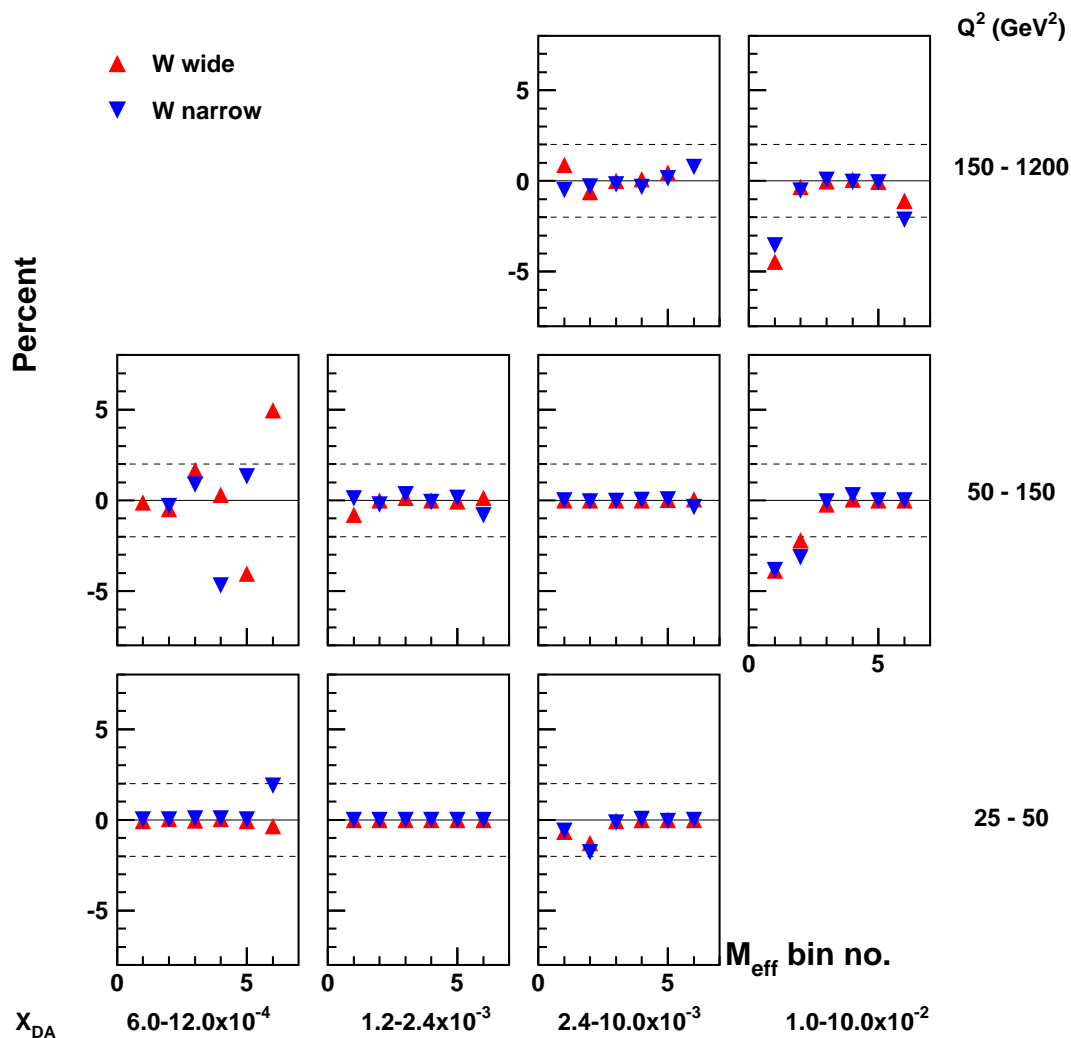**Figure 9.18:** Percent of systematic error caused by varying the W cut for the laboratory frame measurement of $\langle n_{ch} \rangle$ versus M_{eff} in four bins of x. The range of the M_{eff} bins is given in section 6.6.1. The horizontal dashed lines indicate $\pm 2\%$.

Matrix instead of Bin-by-bin

(xbin 1) 6.0 - 12.0 x 10^{-4}

(xbin 2) 1.2 - 2.4 x 10^{-3}

(xbin 3) 2.4 - 10.0 x 10^{-3}

(xbin 4) 1.0 - 10.0 x 10^{-2}
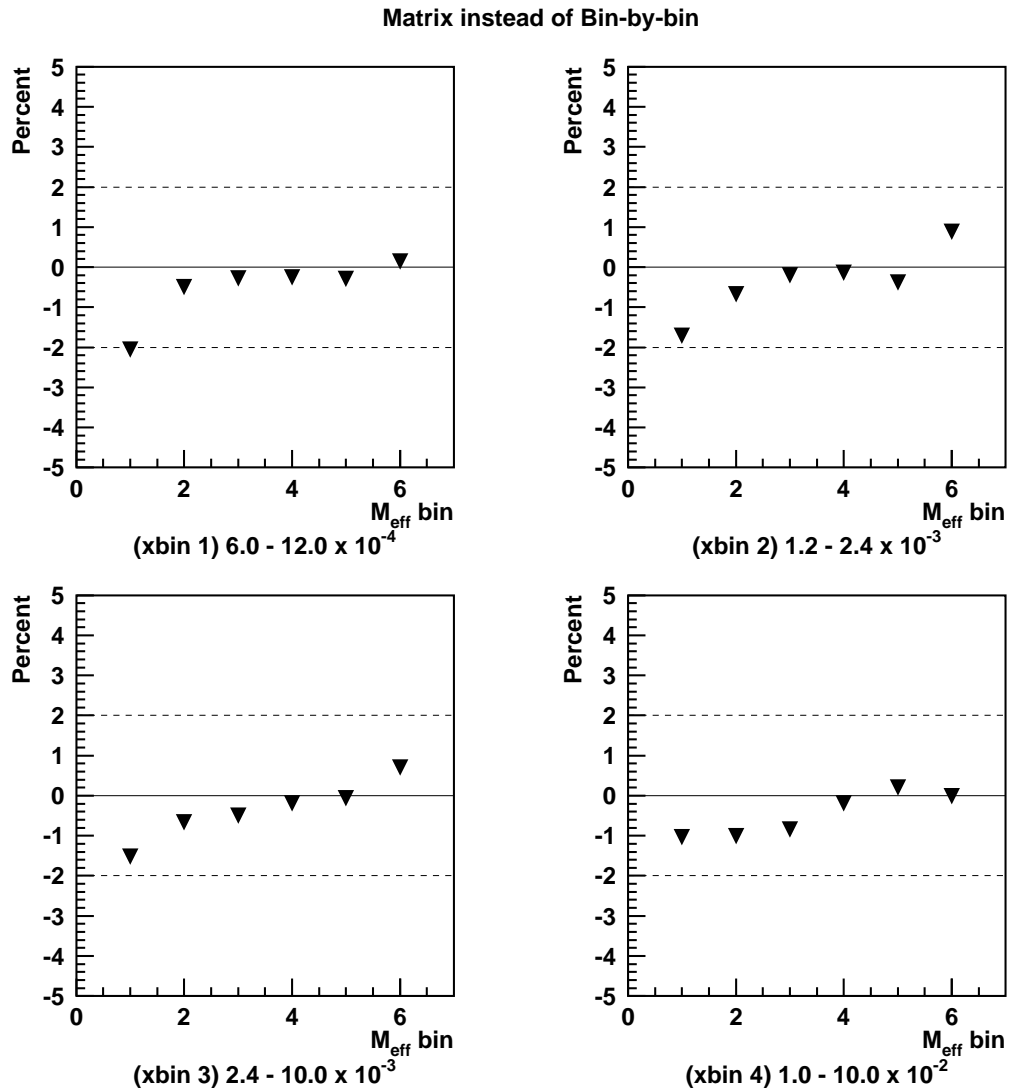
Figure 9.19: Percent of systematic error caused by using the bin-by-bin method instead of the matrix method for correcting the $\langle n_{\mathrm{ch}} \rangle$ to the hadron level (see section 8.3) for the laboratory frame measurement of $\langle n_{\mathrm{ch}} \rangle$ versus M_{eff} in four bins of x. The range of the M_{eff} bins is given in section 6.6.1. The horizontal dashed lines indicate $\pm 2\%$.
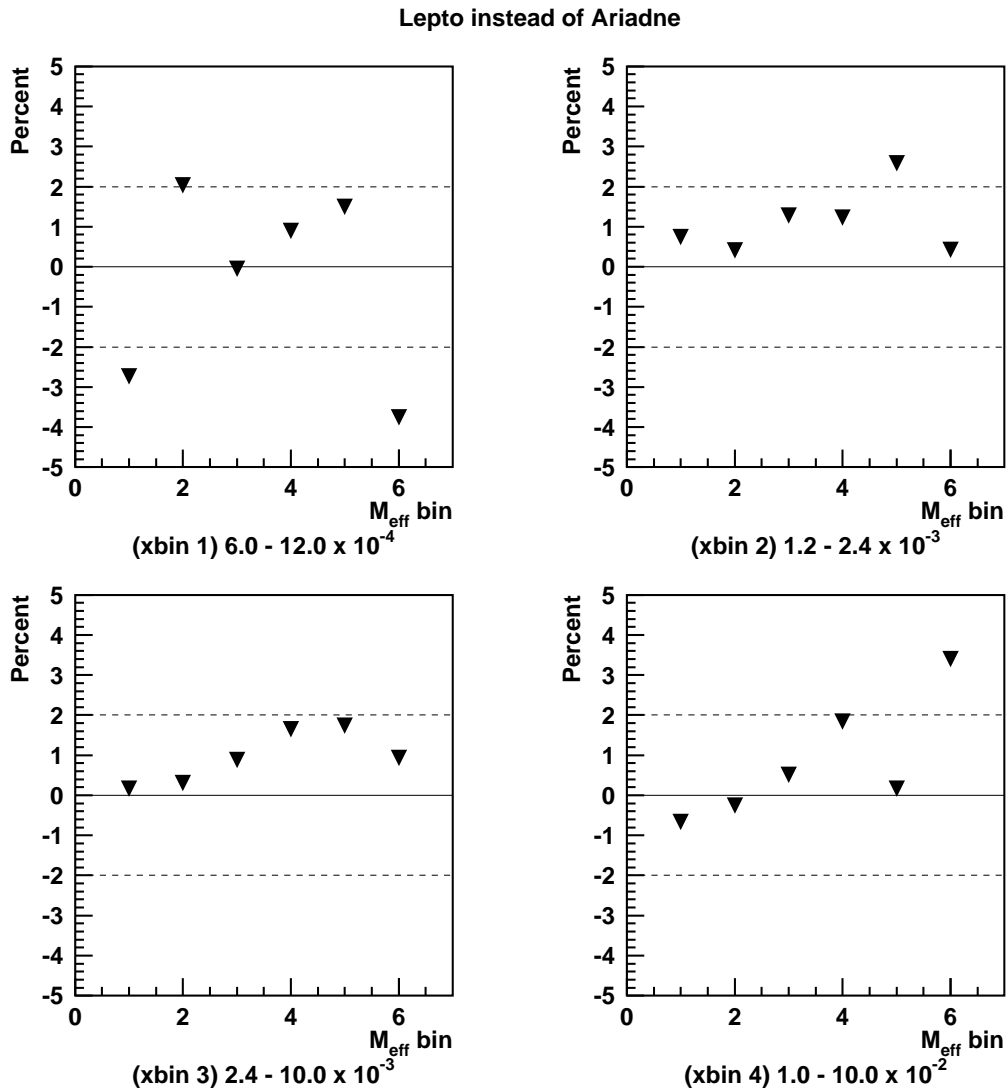
Figure 9.20: Percent of systematic error caused by using LEPTO instead of ARIADNE to calculate the acceptance corrections for the laboratory frame measurement of $\langle n_{\text{ch}} \rangle$ versus M_{eff} in four bins of x. The range of the M_{eff} bins is given in section 6.6.1. The horizontal dashed lines indicate $\pm 2\%$.
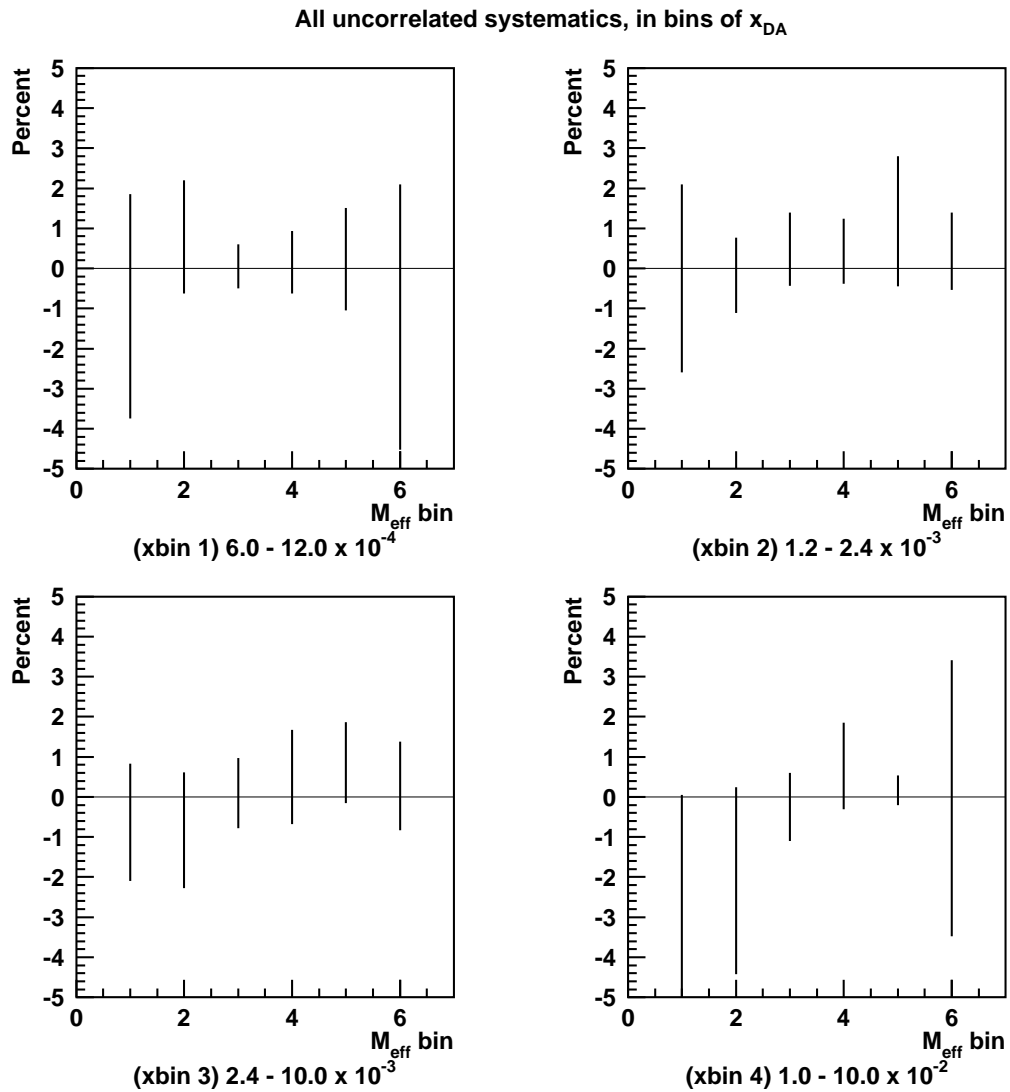
Figure 9.21: Percent of all uncorrelated systematic errors added in quadrature for each bin of M_{eff}, in each x bin in the laboratory frame. The range of the M_{eff} bins is given in section 6.6.1.

The measurement in the laboratory frame versus M_{eff} was also studied in bins of both x and Q^2. The range of the x and Q^2 bins is given in section 6.6.1. The systematics are presented in the same order as for the x binning alone. The first plots (figures 9.22 through 9.27) show the most significant sources of systematic error as a separate plot for each variation, followed by figure 9.28 of the total systematic error in percentage for each x and Q^2 bin. This figure shows that the majority of the systematics are less than 2 % with some isolated (and mostly low statistic) M_{eff} bins showing errors of 10 % or more.

Figure 9.22: Percent of systematic error caused by the calorimeter energy scale uncertainty for the laboratory frame measurement of $\langle n_{\mathrm{ch}} \rangle$ versus M_{eff} in four bins of x and Q^2. The horizontal dashed lines indicate $\pm 2\%$. The range of the M_{eff} bins is given in section 6.6.1.

Figure 9.23: Percent of systematic error caused by raising the p_T of the tracks for the laboratory frame measurement of $\langle n_{ch} \rangle$ versus M_{eff} in four bins of x and Q^2, where the x and Q^2 bin ranges are given in section 6.6.1. The horizontal dashed lines indicate $\pm 2\%$. The range of the M_{eff} bins is given in section 6.6.1
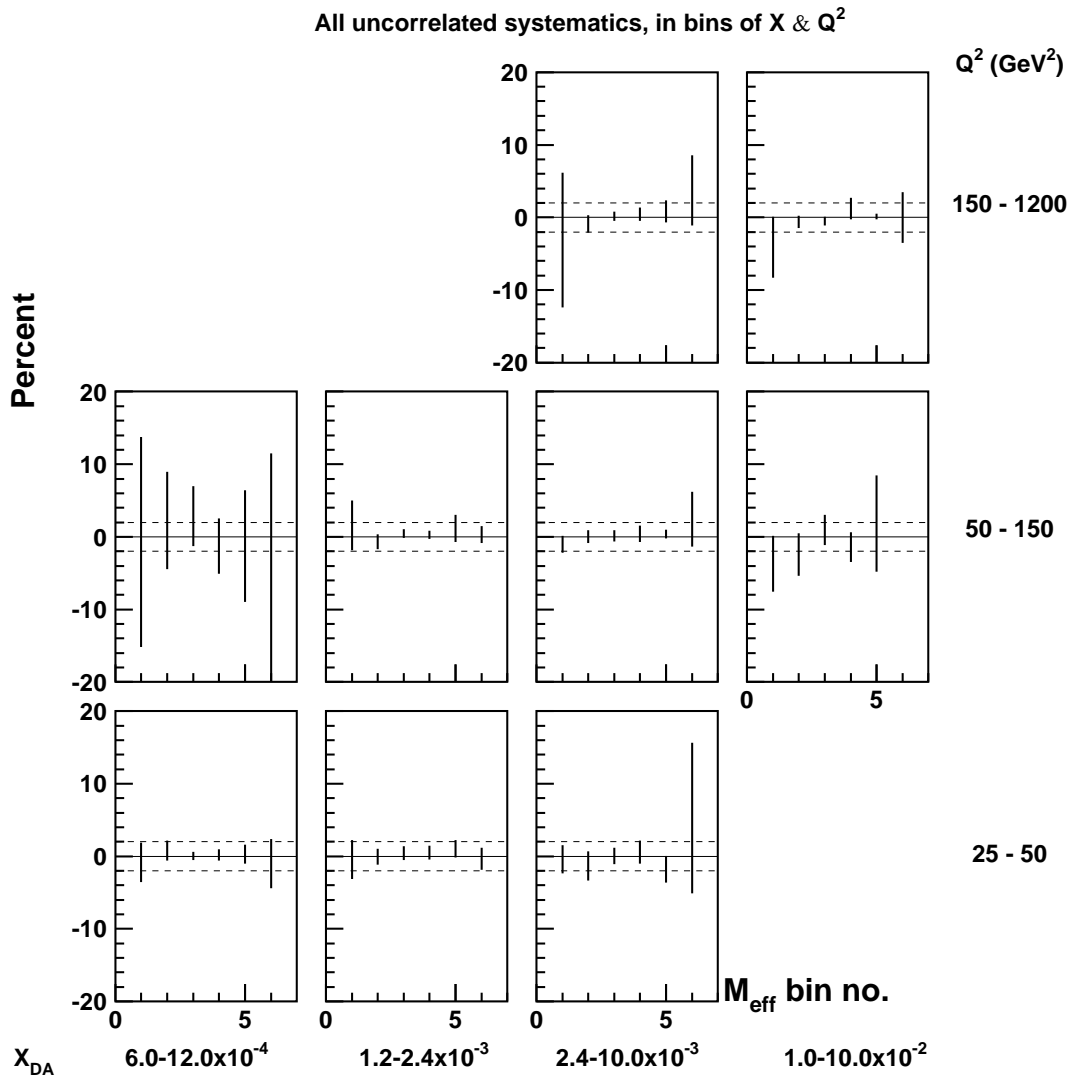
Figure 9.24: Percent of systematic error caused by varying the Q^2 cut for the laboratory frame measurement of $\langle n_{\mathrm{ch}} \rangle$ versus M_{eff} in four bins of x and Q^2, where the x and Q^2 bin ranges are given in section 6.6.1. The horizontal dashed lines indicate $\pm 2\%$. The range of the M_{eff} bins is given in section 6.6.1.

Figure 9.25: Percent of systematic error caused by varying the W cut for the laboratory frame measurement of $\langle n_{\mathrm{ch}} \rangle$ versus M_{eff} in four bins of x and Q^2, where the x and Q^2 bin ranges are given in section 6.6.1. The horizontal dashed lines indicate $\pm 2\%$. The range of the M_{eff} bins is given in section 6.6.1.
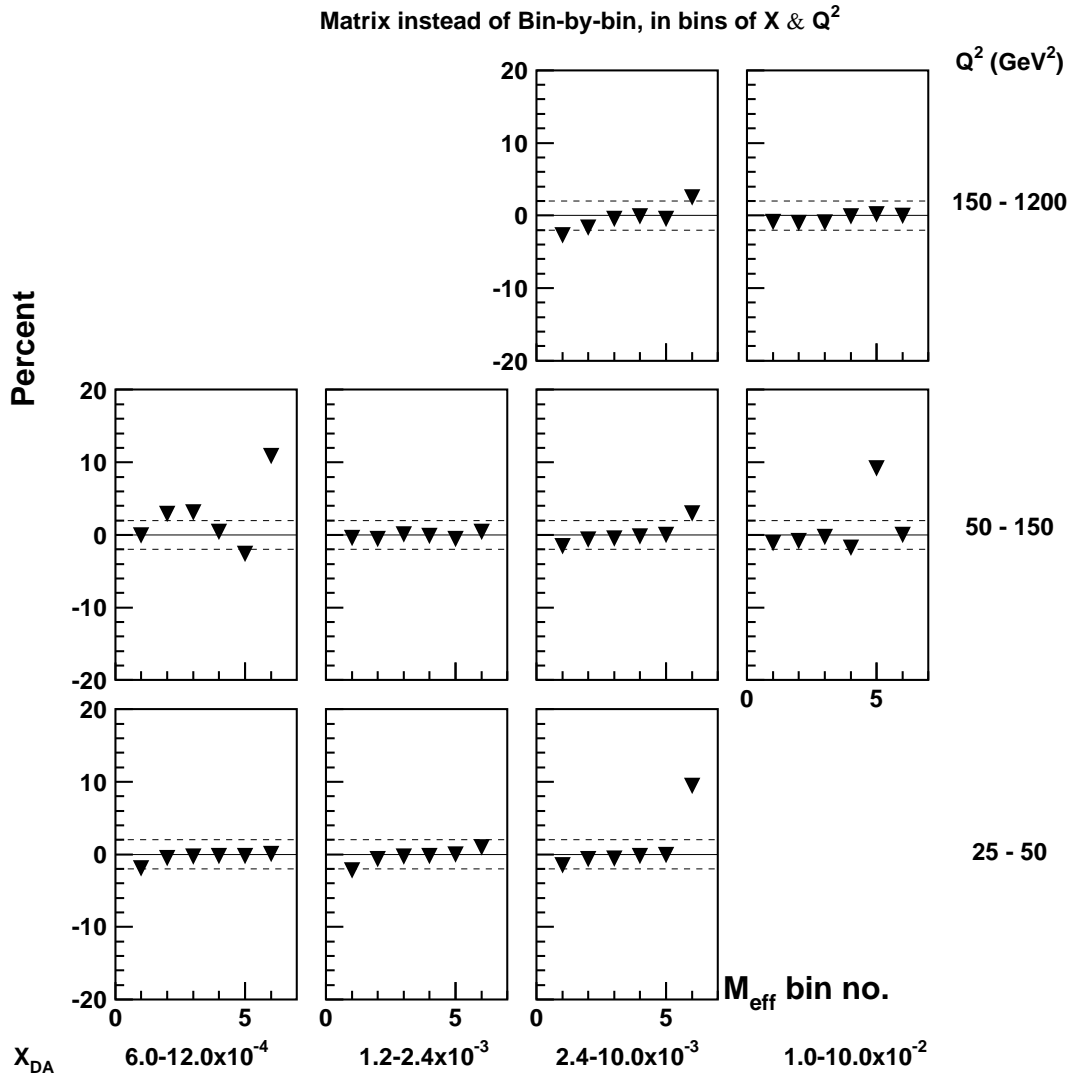
Figure 9.26: Percent of systematic error caused by using the bin-by-bin method instead of the matrix method for correcting the $\langle n_{\mathrm{ch}} \rangle$ to the hadron level (see section 8.3) for the laboratory frame measurement of $\langle n_{\mathrm{ch}} \rangle$ versus M_{eff} in four bins of x and Q^2, where the x and Q^2 bin ranges are given in section 6.6.1. The horizontal dashed lines indicate $\pm 2\%$. The range of the M_{eff} bins is given in section 6.6.1.

188
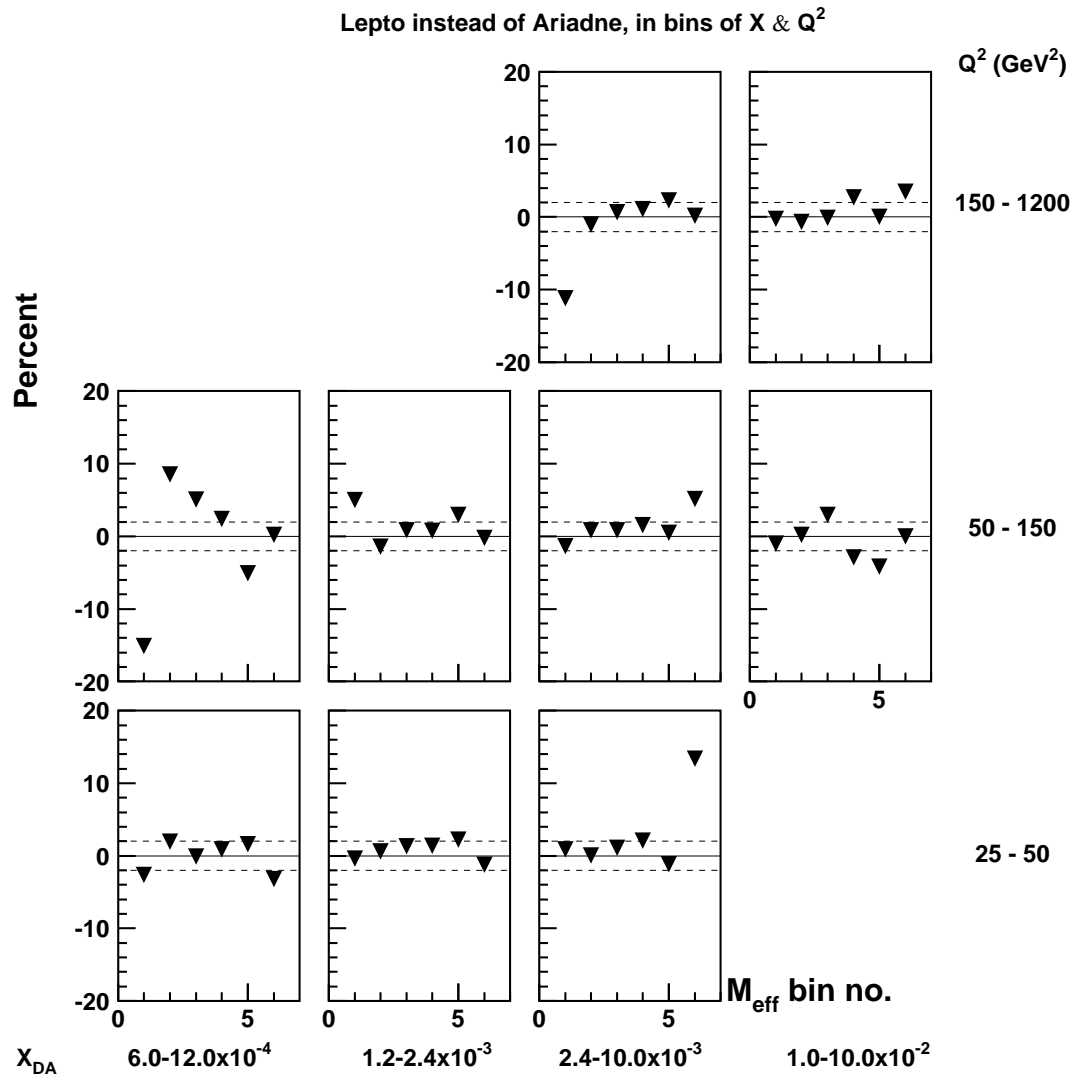
Figure 9.27: Percent of systematic error caused by using LEPTO instead of ARIADNE to calculate the acceptance corrections for the laboratory frame measurement of $\langle n_{ch} \rangle$ versus M_{eff} in four bins of x and Q^2, where the x and Q^2 bin ranges are given in section 6.6.1. The horizontal dashed lines indicate $\pm 2\%$. The range of the M_{eff} bins is given in section 6.6.1.

Figure 9.28: Percent of all uncorrelated systematic errors added in quadrature for each bin of M_{eff}, in each x and Q^2 bin in the laboratory frame. The x and Q^2 bin ranges are given in section 6.6.1 The range of the M_{eff} bins is given in section 6.6.1.

Chapter 10

Summary and Conclusions

The hadronic final state has been investigated in inclusive neutral current deep inelastic ep scattering in the kinematic range $Q^2 > 25$ GeV^2 and $70 < W < 225$ GeV in terms of the mean charged multiplicity, the centre-of-mass energy and the respective invariant mass of the charged and neutral particles, M_{eff}.

For the first time the lowest energy data of the current region of the Breit frame are shown to agree with the measurements of e^+e^- and pp by using the effective energy scale, $2 \cdot E_{\mathrm{Breit}}^{\mathrm{current}}$. The mean charged multiplicity in the photon region of the ep HCM frame has been compared to the results of e^+e^- and shown to agree within the uncertainties of the data. The total energy region examined in this analysis covers the range of energies from 2 to 200 GeV.

A new energy variable, M_{eff}, has been used for comparison between different regions of the ep hadronic final state, as well as for comparison with other experiments. The mean charged multiplicity in the current region of the Breit frame scales with the corresponding M_{eff} in the same way as $2 \cdot \langle n_{\mathrm{ch}} \rangle$ with $2 \cdot E_{\mathrm{Breit}}^{\mathrm{current}}$, and, therefore, as $\langle n_{\mathrm{ch}} \rangle$ with $\sqrt{s_{ee}}$ in e^+e^-. The $\langle n_{\mathrm{ch}} \rangle$ in the photon region of HCM rises faster, as a function of M_{eff}, than the $\langle n_{\mathrm{ch}} \rangle$ in the current region of the Breit frame.

The measurement of the multiplicity in the photon region of the HCM frame as a function of M_{eff} showed almost no dependence on x and Q^2.

Appendix A

Matrix Correction Plots

Plots which show the magnitude of the matrix correction as described in section 8.2 are presented in this section. The uncorrected track distributions, the matrix, and the corrected track distributions for each bin of each analysis are shown in figures A.1 through A.33. In order to give an idea of the size of the first part of the correction, the ratio of the means of the track distributions before and after correction by the matrix procedure as shown in the upper plots of figures A.34 through A.39. The lower plots in these figures show the correction factors from the second part of the matrix correction.

194
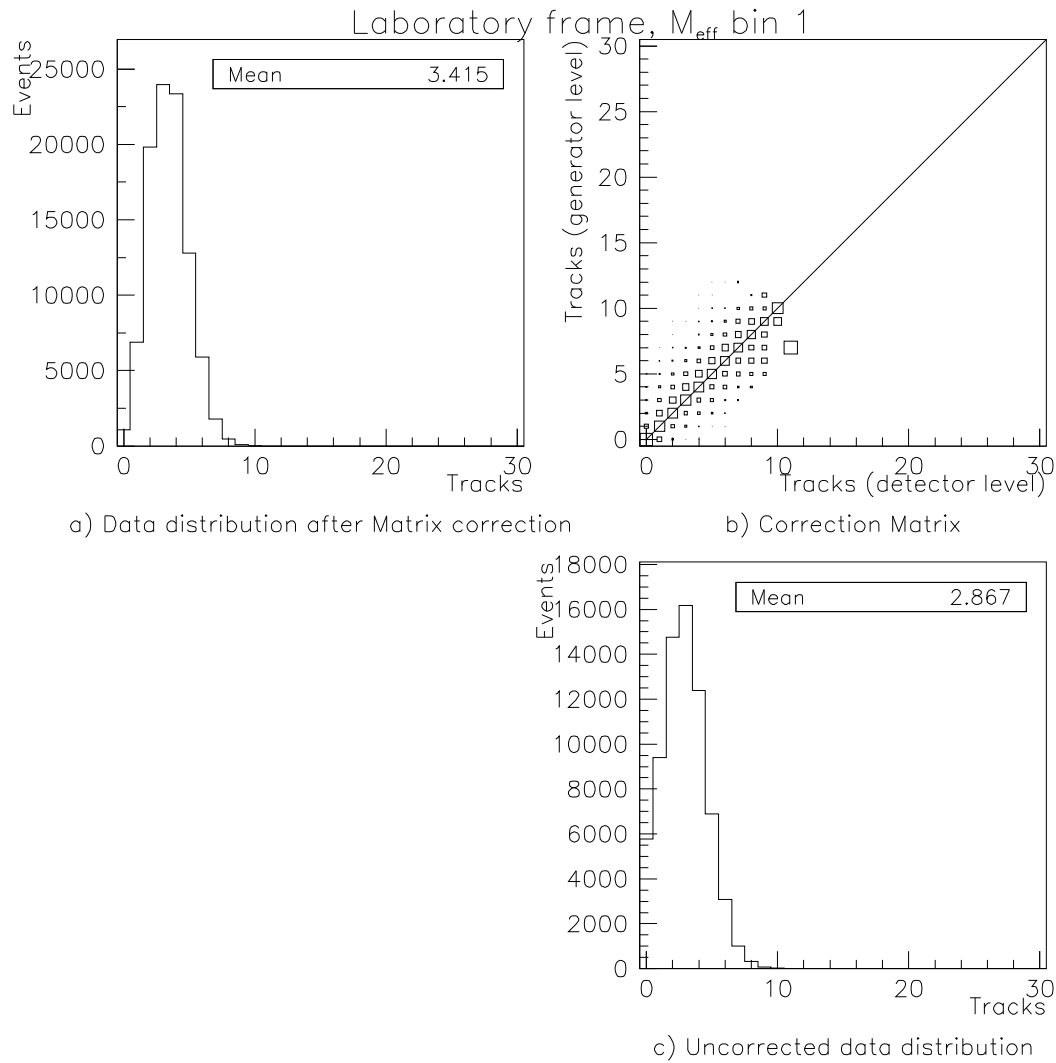
Figure A.1: Matrix correction for $\langle n_{\rm ch} \rangle$ in the 1st bin of $M_{\rm eff}$ in the lab frame (1.5 GeV < $M_{\rm eff}$ < 4 GeV). The uncorrected number of tracks in the data (C) is multiplied by the normalized matrix (B) and the result is shown in (A).
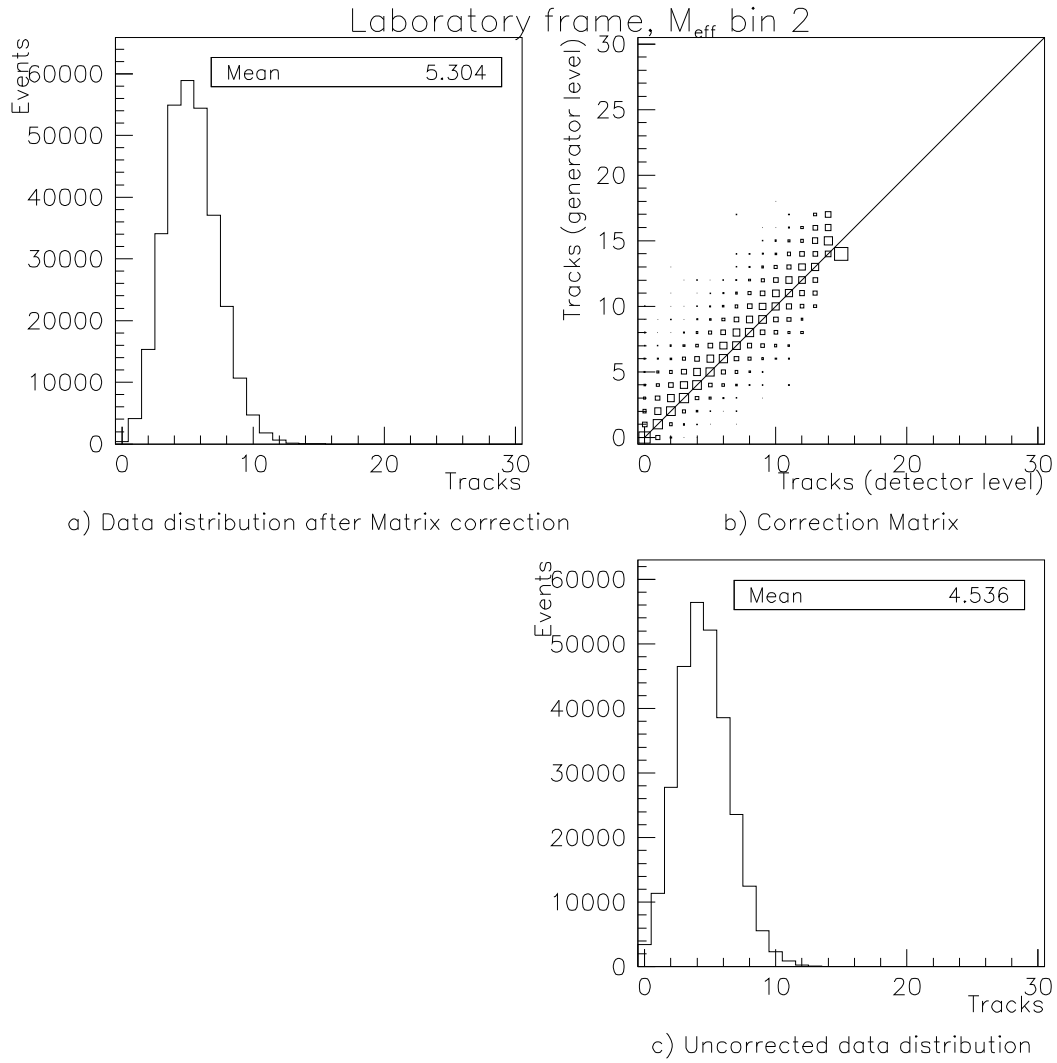
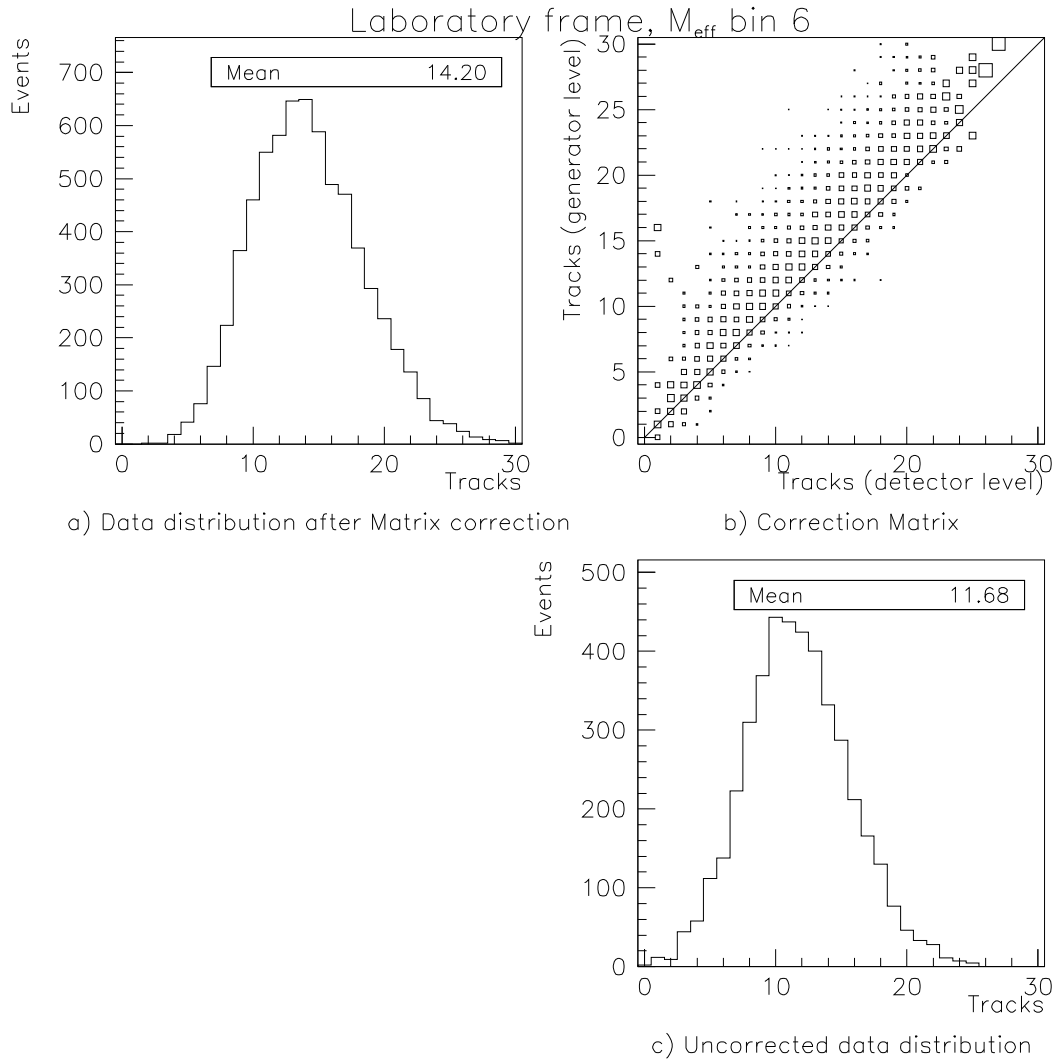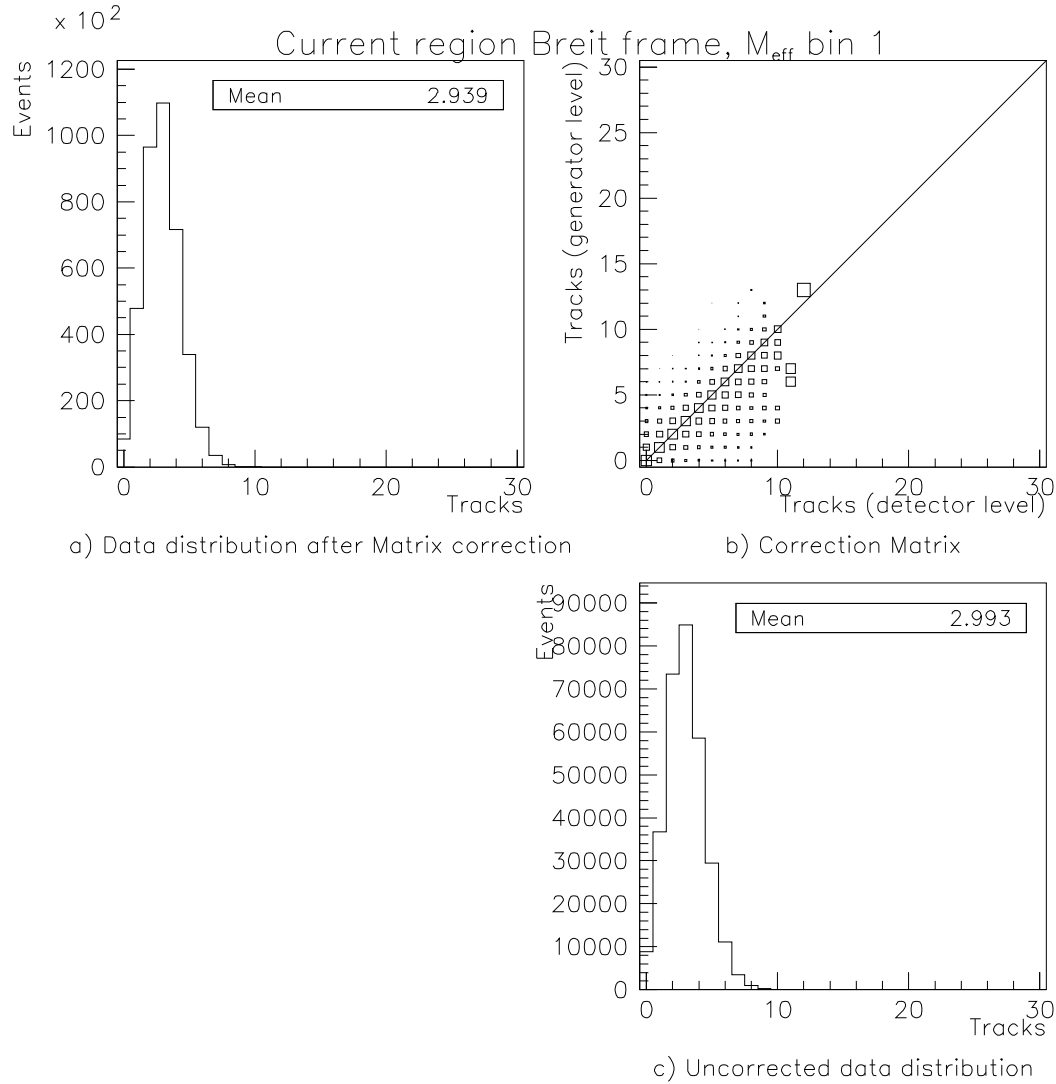**Figure A.2:** Matrix correction for $\langle n_{\mathrm{ch}} \rangle$ in the 2nd bin of M_{eff} in the lab frame (4 GeV < M_{eff} < 8 GeV). The uncorrected number of tracks in the data (C) is multiplied by the normalized matrix (B) and the result is shown in (A).
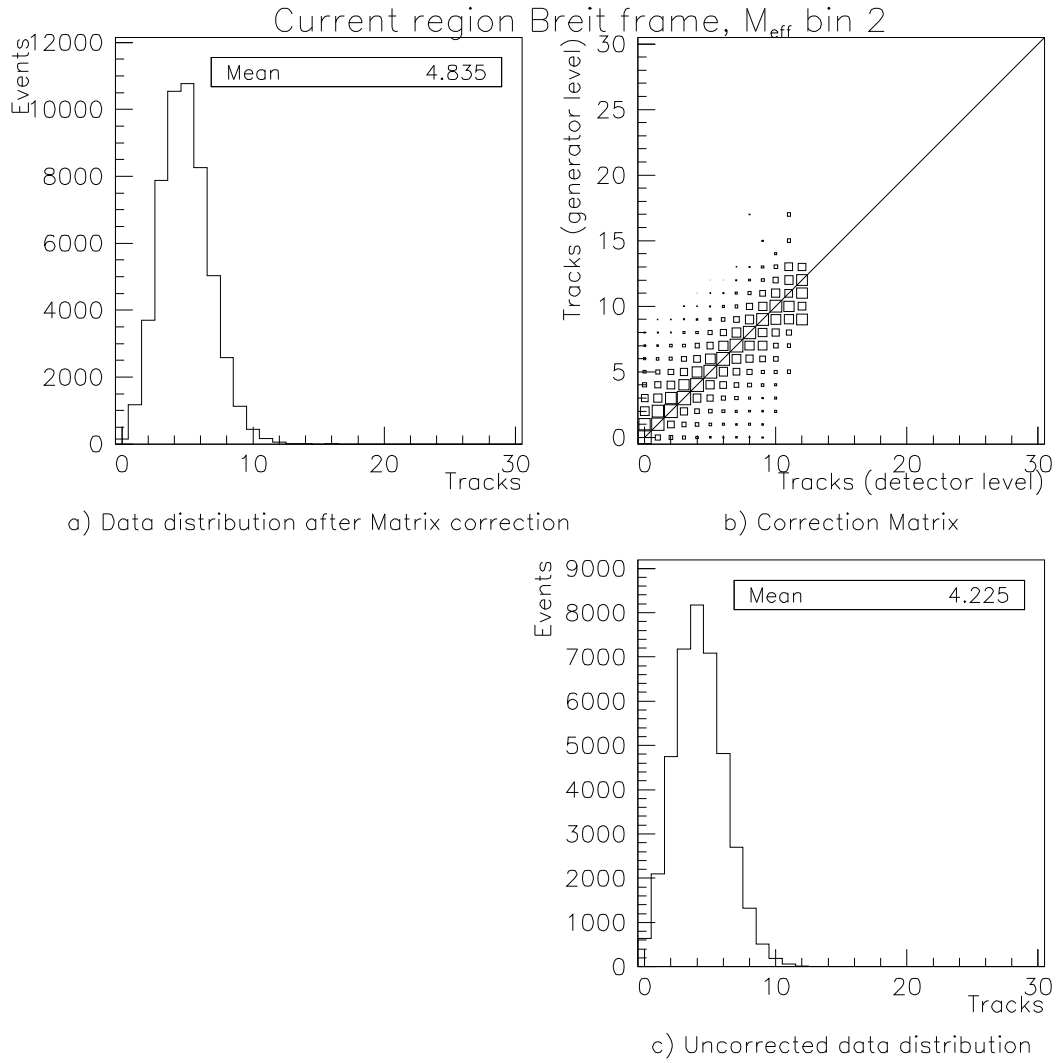
196
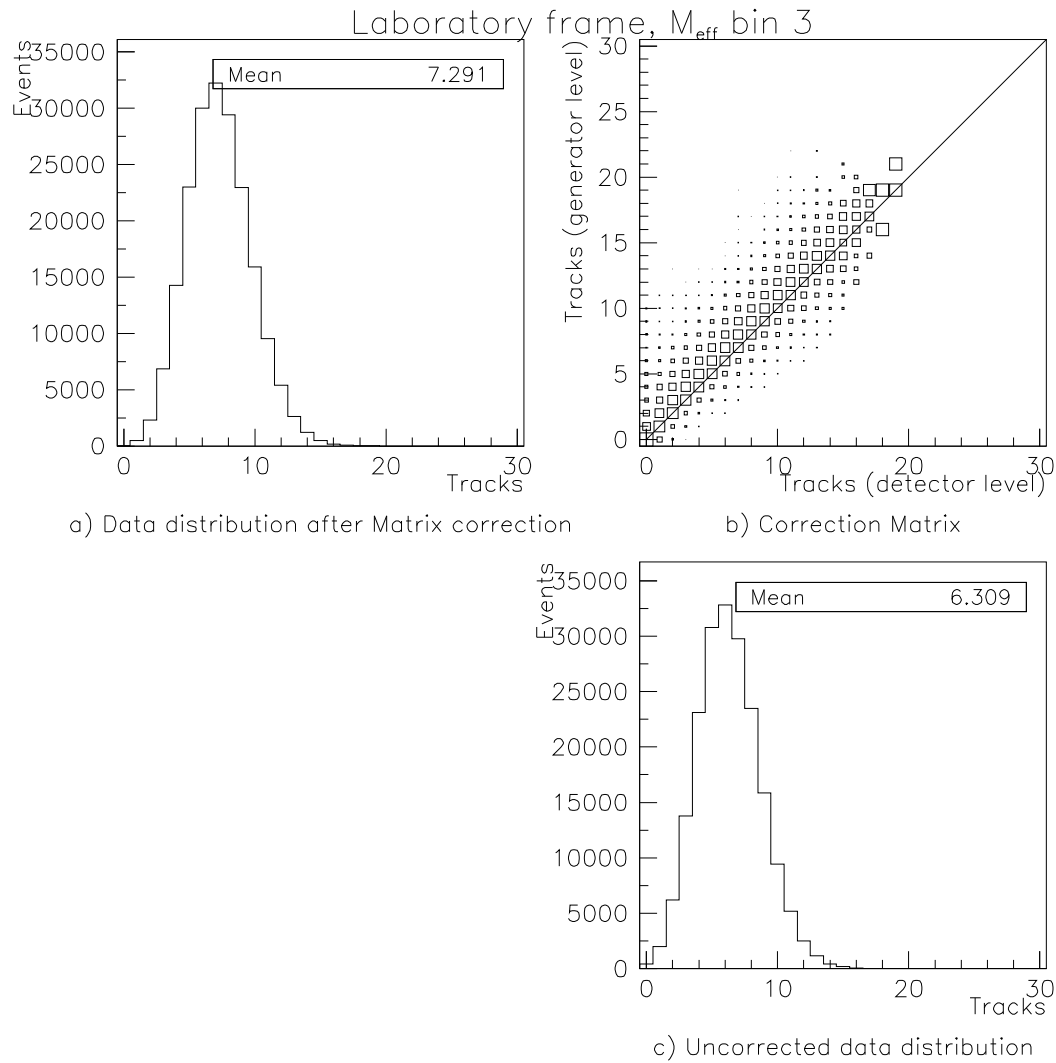
Figure A.3: Matrix correction for $\langle n_{\mathrm{ch}} \rangle$ in the 3rd bin of M_{eff} in the lab frame (8 GeV < M_{eff} < 12 GeV). The uncorrected number of tracks in the data (C) is multiplied by the normalized matrix (B) and the result is shown in (A).
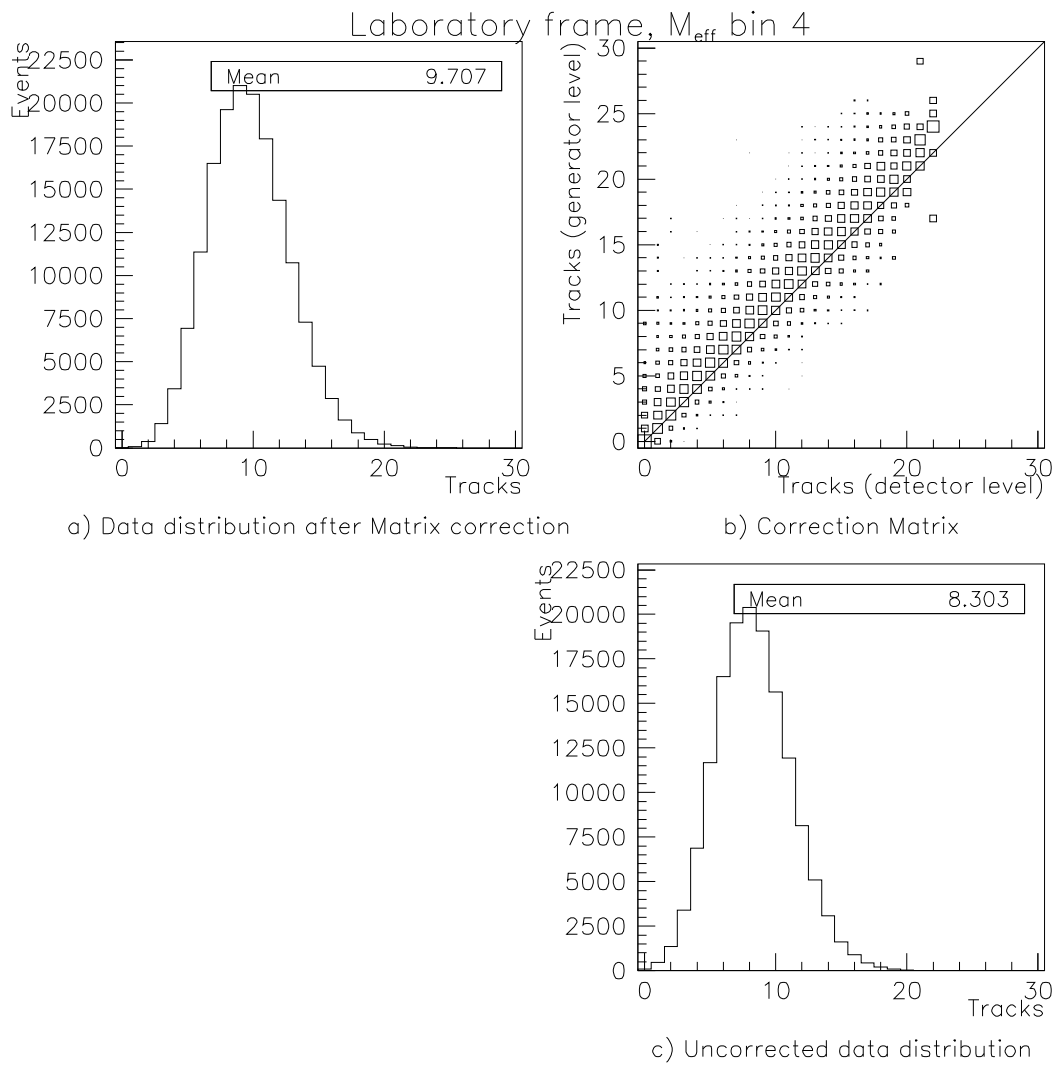
Figure A.4: Matrix correction for $\langle n_{\mathrm{ch}} \rangle$ in the 4th bin of M_{eff} in the lab frame (12 GeV $<$ $M_{\mathrm{eff}} <$ 20 GeV). The uncorrected number of tracks in the data (C) is multiplied by the normalized matrix (B) and the result is shown in (A).

198

a) Data distribution after Matrix correction

b) Correction Matrix

c) Uncorrected data distribution
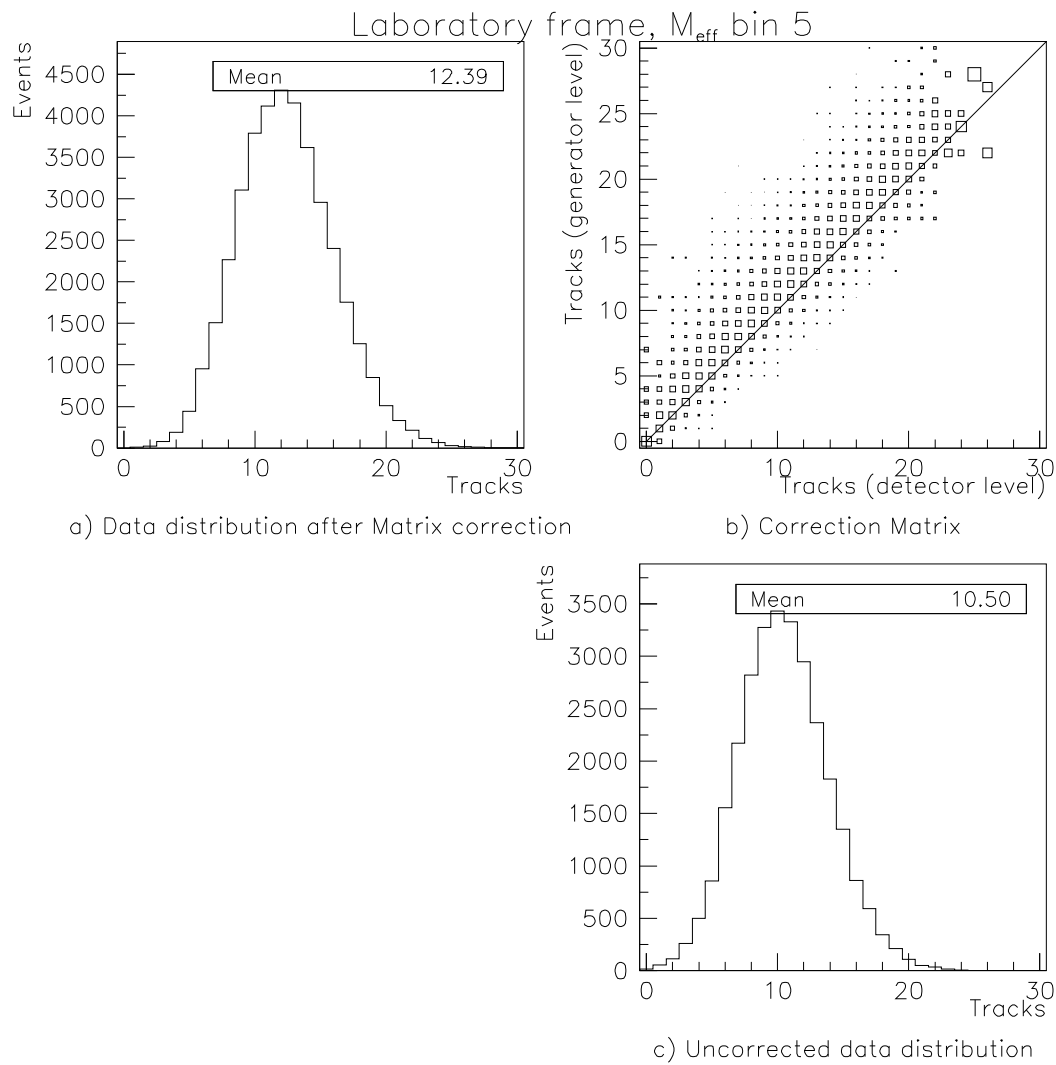
Figure A.5: Matrix correction for $\langle n_{\text{ch}} \rangle$ in the 5th bin of M_{eff} in the lab frame (20 GeV < M_{eff} < 30 GeV). The uncorrected number of tracks in the data (C) is multiplied by the normalized matrix (B) and the result is shown in (A).
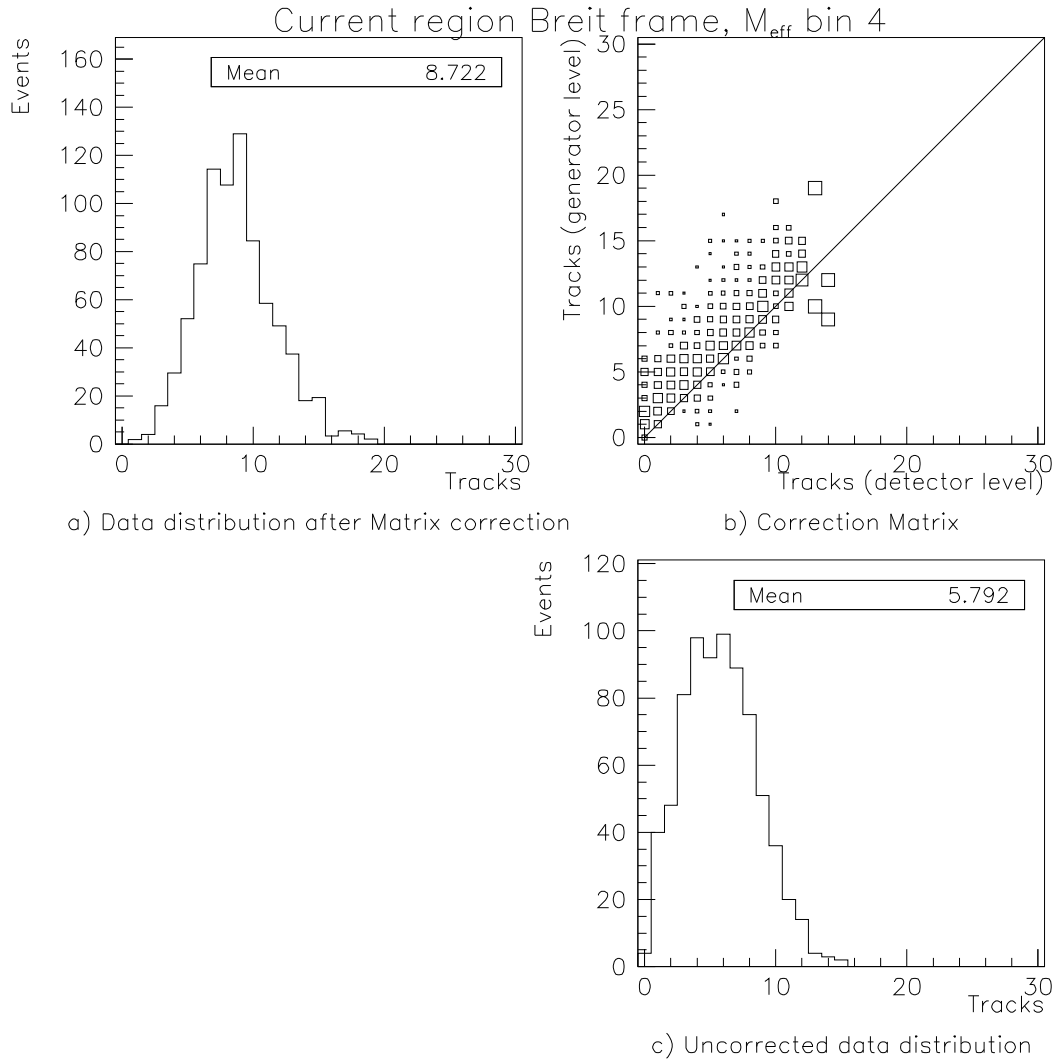
Figure A.6: Matrix correction for $\langle n_{\mathrm{ch}} \rangle$ in the 6th bin of M_{eff} in the lab frame (30 GeV < M_{eff} < 45 GeV). The uncorrected number of tracks in the data (C) is multiplied by the normalized matrix (B) and the result is shown in (A).

200

a) Data distribution after Matrix correction

b) Correction Matrix

c) Uncorrected data distribution

Figure A.7: Matrix correction for $\langle n_{\mathrm{ch}} \rangle$ in the 1st bin of M_{eff} in the current region of the Breit frame (1.5 GeV $< M_{\mathrm{eff}} <$ 4 GeV). The uncorrected number of tracks in the data (C) is multiplied by the normalized matrix (B) and the result is shown in (A).
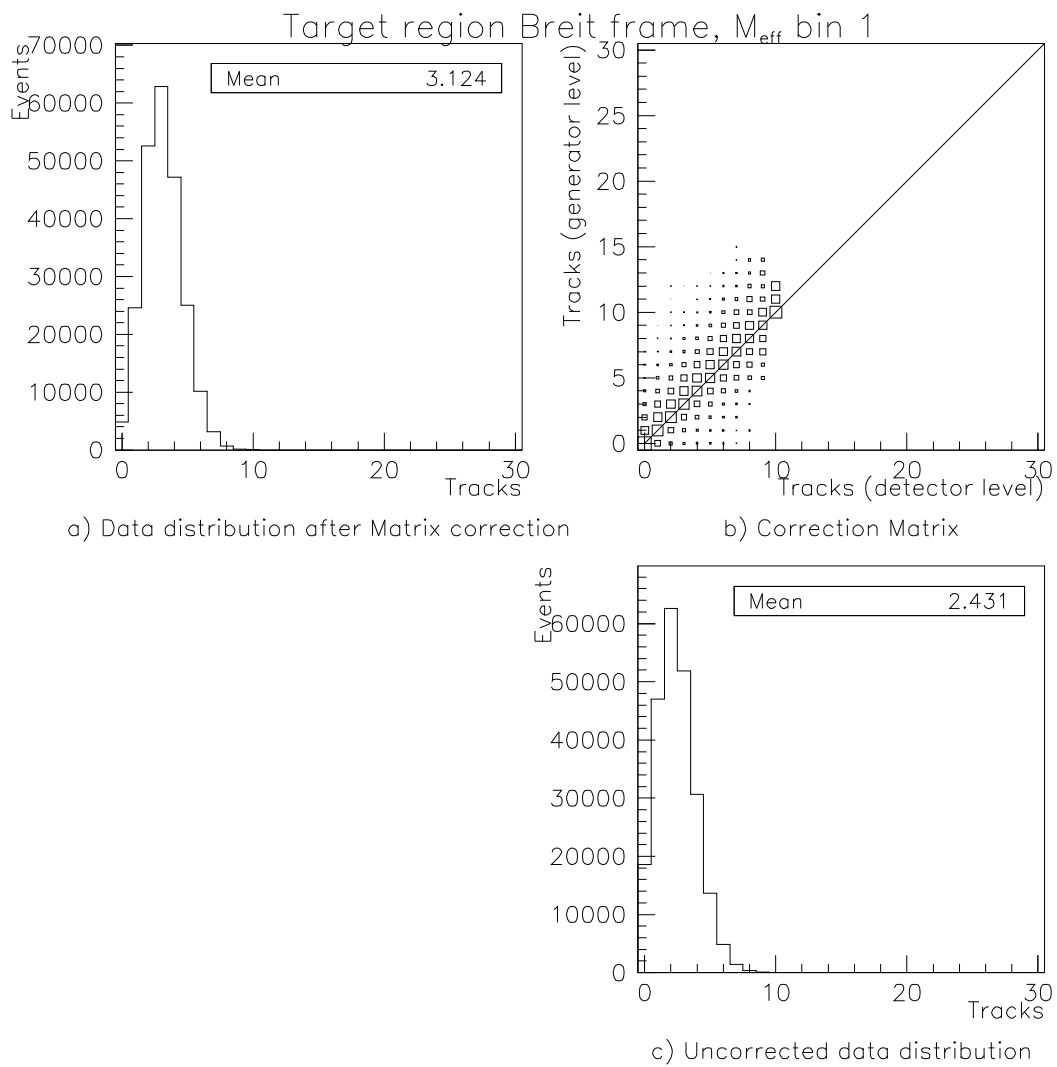
Figure A.8: Matrix correction for $\langle n_{\mathrm{ch}} \rangle$ in the 2nd bin of M_{eff} in the current region of the Breit frame (4 GeV $< M_{\mathrm{eff}} <$ 8 GeV). The uncorrected number of tracks in the data (C) is multiplied by the normalized matrix (B) and the result is shown in (A).
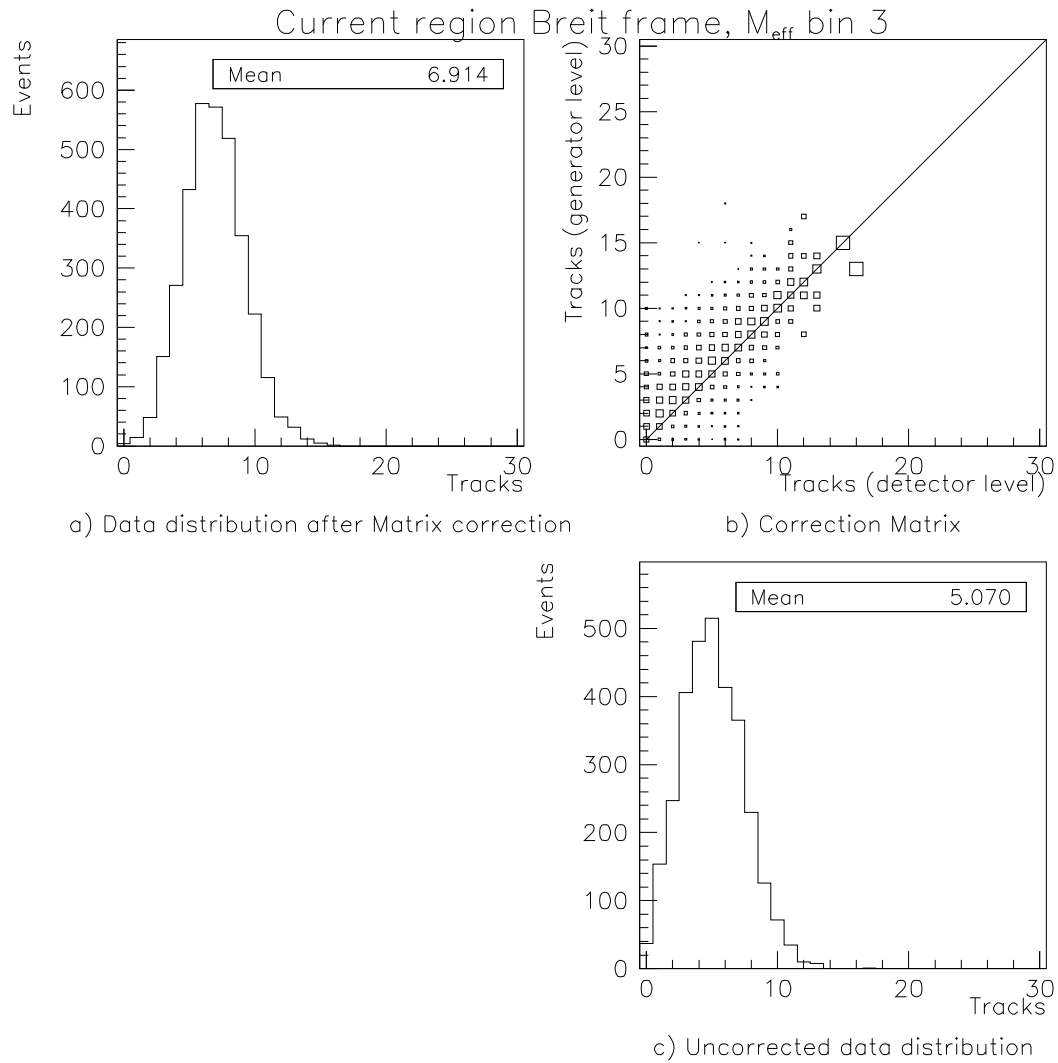
Figure A.9: Matrix correction for $\langle n_{\mathrm{ch}} \rangle$ in the 3rd bin of M_{eff} in the current region of the Breit frame (8 GeV $< M_{\mathrm{eff}} < 12$ GeV). The uncorrected number of tracks in the data (C) is multiplied by the normalized matrix (B) and the result is shown in (A).
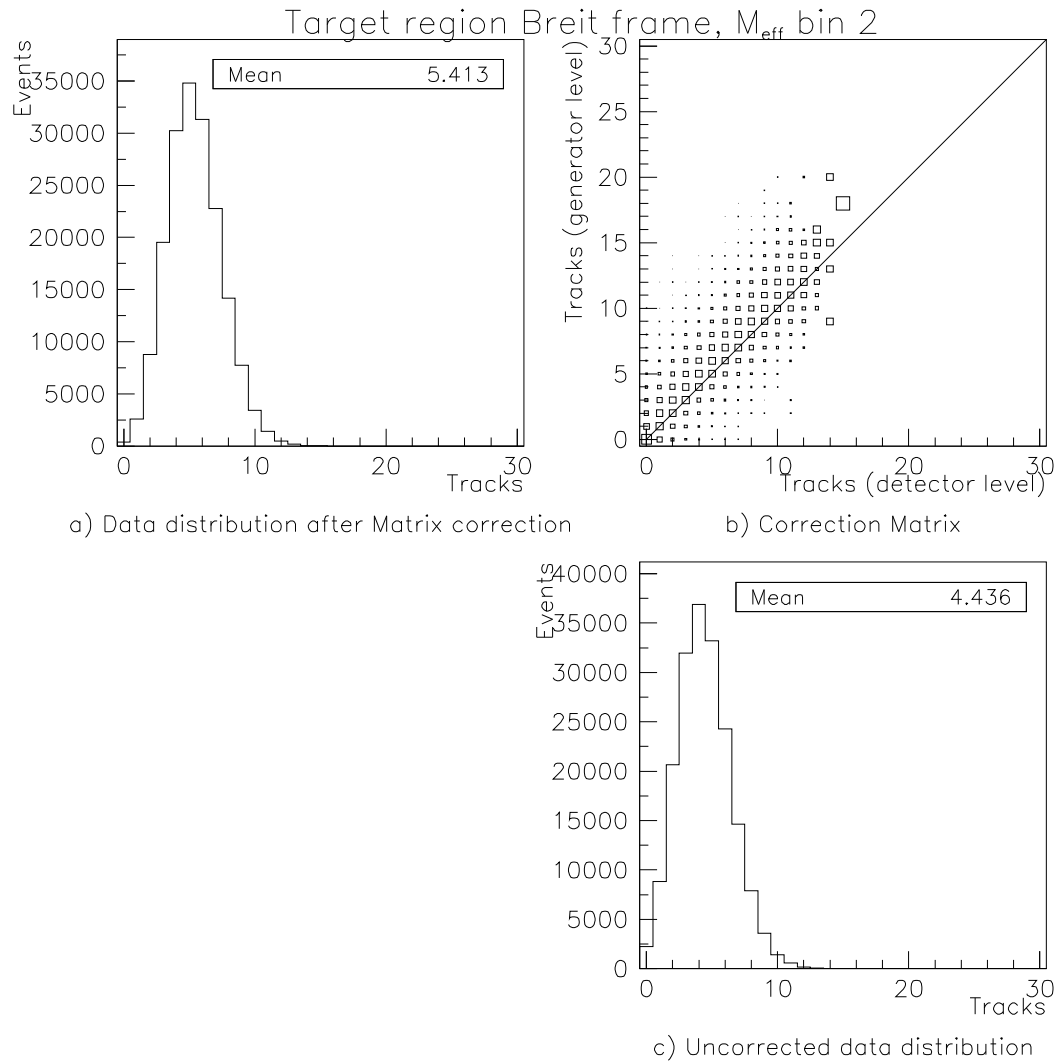
Figure A.10: Matrix correction for $\langle n_{\text{ch}} \rangle$ in the 4th bin of M_{eff} in the current region of the Breit frame (12 GeV $< M_{\text{eff}} <$ 20 GeV). The uncorrected number of tracks in the data (C) is multiplied by the normalized matrix (B) and the result is shown in (A).
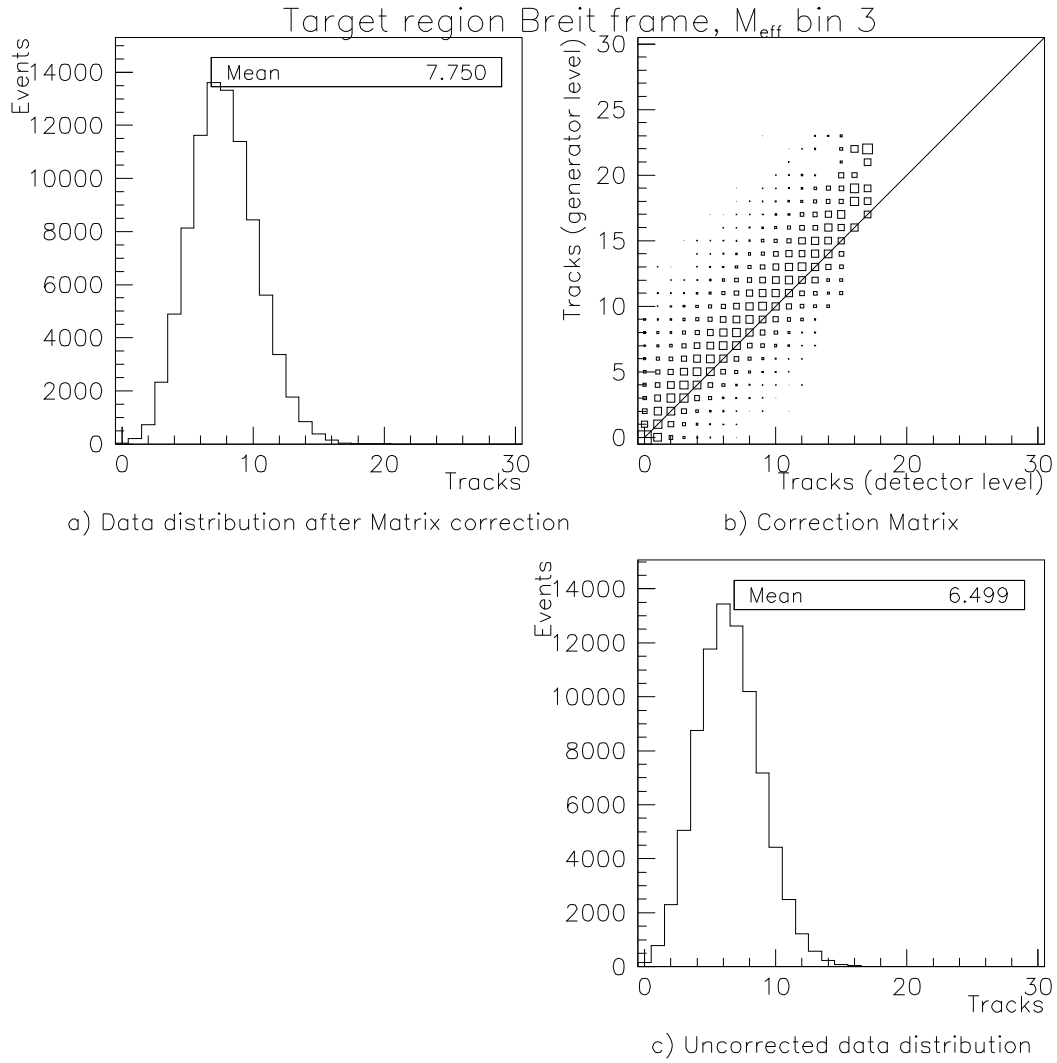
204
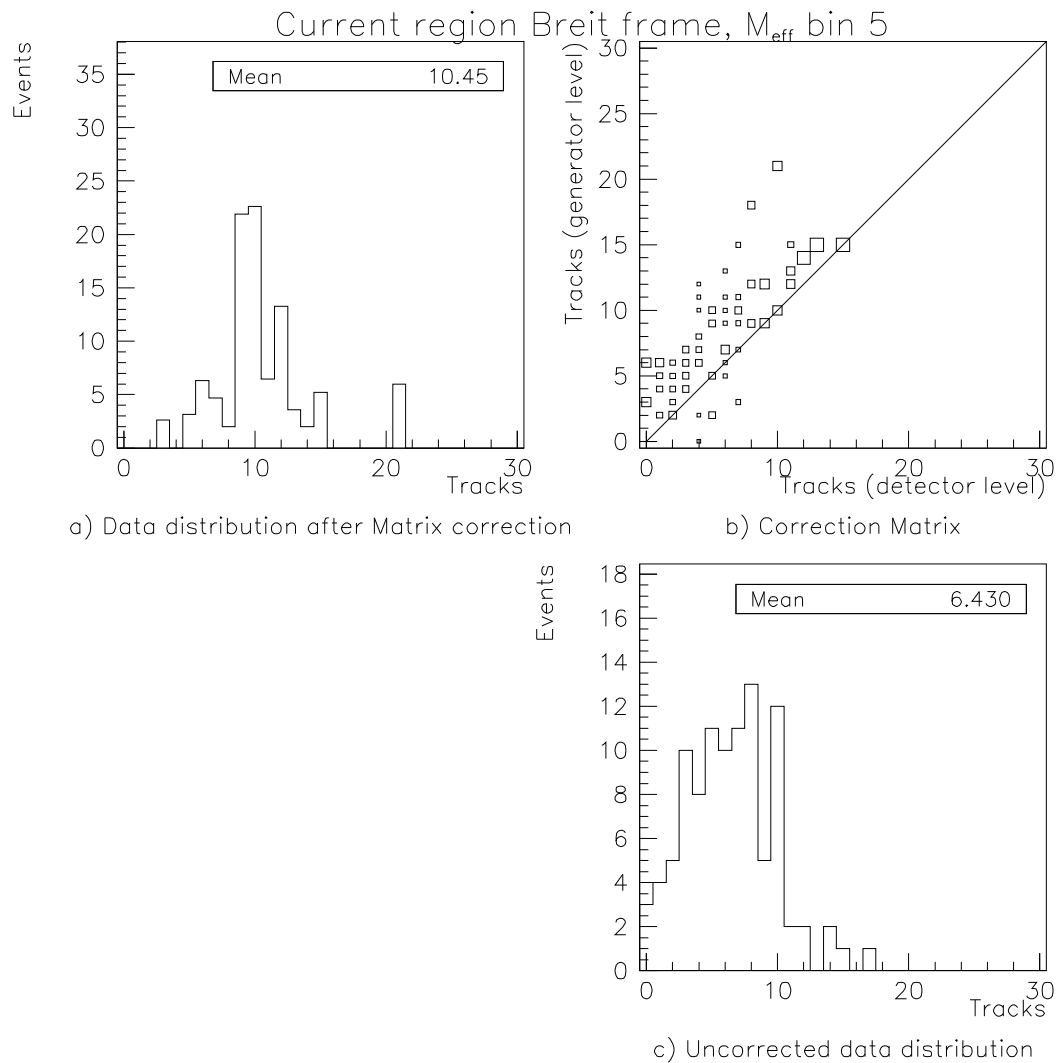
Figure A.11: Matrix correction for $\langle n_{\mathrm{ch}} \rangle$ in the 5th bin of M_{eff} in the current region of the Breit frame(20 GeV $< M_{\mathrm{eff}} <$ 30 GeV). The uncorrected number of tracks in the data (C) is multiplied by the normalized matrix (B) and the result is shown in (A).

a) Data distribution after Matrix correction   b) Correction Matrix

c) Uncorrected data distribution

Figure A.12: Matrix correction for $\langle n_{\mathrm{ch}} \rangle$ in the 1st bin of M_{eff} in the target region of the Breit frame (1.5 GeV $< M_{\mathrm{eff}} <$ 4 GeV). The uncorrected number of tracks in the data (C) is multiplied by the normalized matrix (B) and the result is shown in (A).
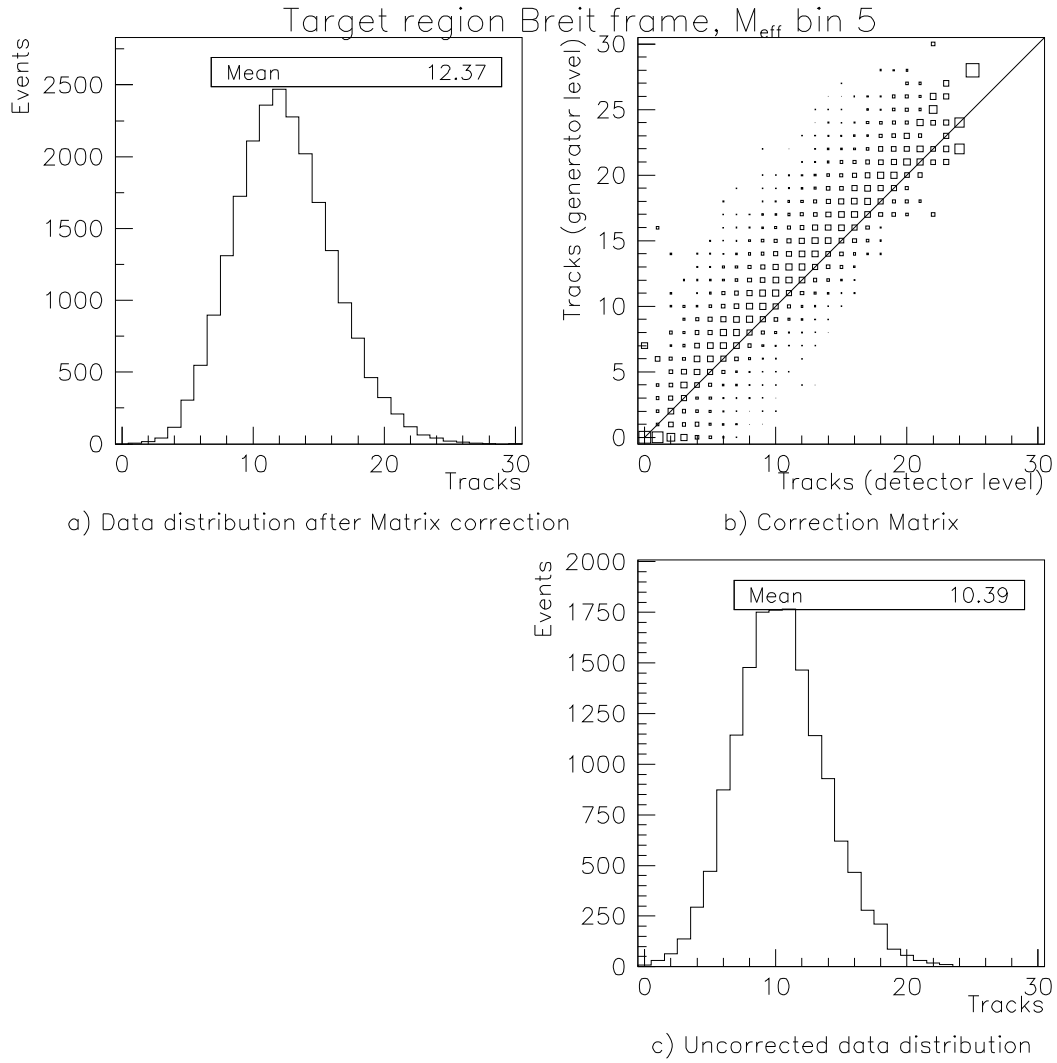
206

Figure A.13: Matrix correction for $\langle n_{\mathrm{ch}} \rangle$ in the 2nd bin of M_{eff} in the target region of the Breit frame (4 GeV $< M_{\mathrm{eff}} <$ 8 GeV). The uncorrected number of tracks in the data (C) is multiplied by the normalized matrix (B) and the result is shown in (A).

Figure A.14: Matrix correction for $\langle n_{\mathrm{ch}} \rangle$ in the 3rd bin of M_{eff} in the target region of the Breit frame (8 GeV $< M_{\mathrm{eff}} <$ 12 GeV). The uncorrected number of tracks in the data (C) is multiplied by the normalized matrix (B) and the result is shown in (A).

208

a) Data distribution after Matrix correction

b) Correction Matrix

c) Uncorrected data distribution
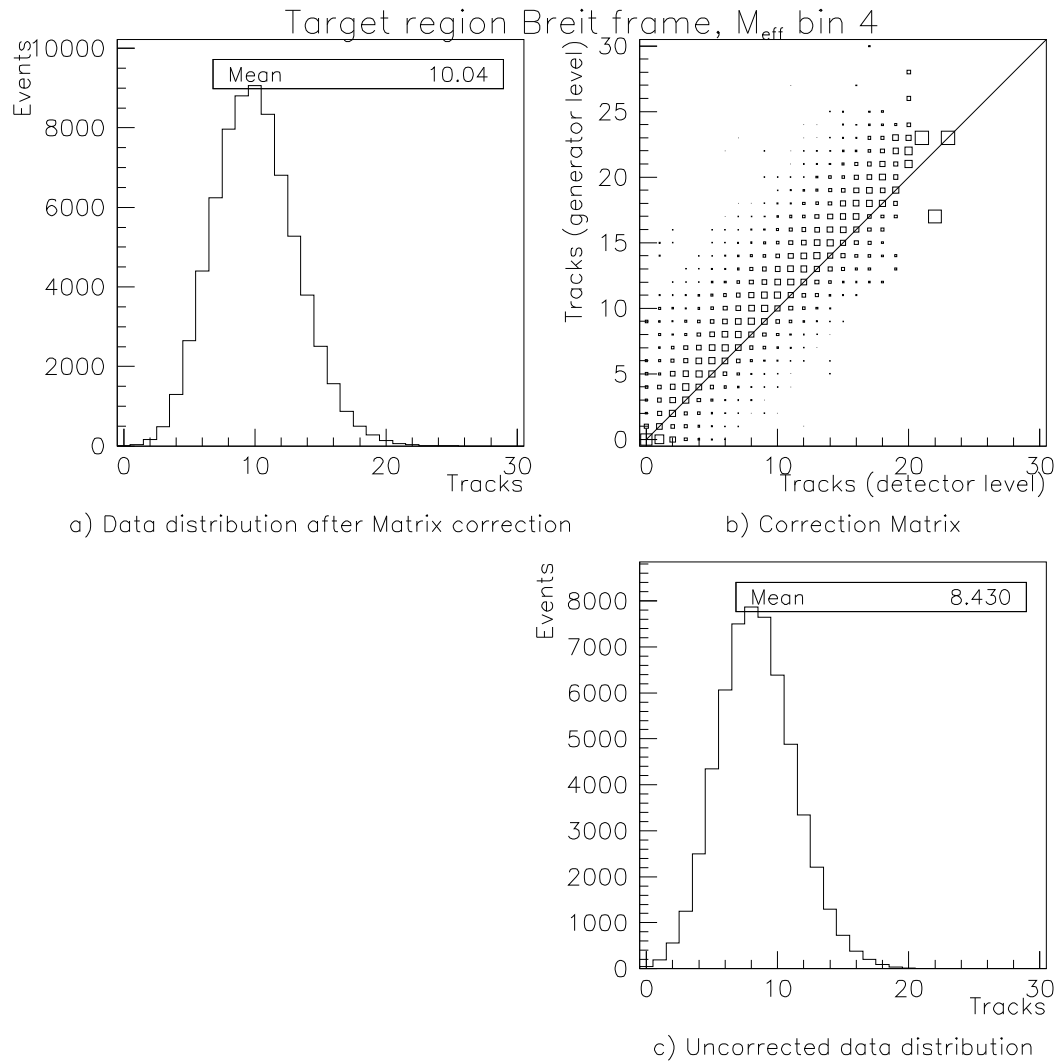
Figure A.15: Matrix correction for $\langle n_{\mathrm{ch}} \rangle$ in the 4th bin of M_{eff} in the target region of the Breit frame (12 GeV $< M_{\mathrm{eff}} <$ 20 GeV). The uncorrected number of tracks in the data (C) is multiplied by the normalized matrix (B) and the result is shown in (A).

a) Data distribution after Matrix correction

b) Correction Matrix

c) Uncorrected data distribution

Figure A.16: Matrix correction for $\langle n_{\mathrm{ch}} \rangle$ in the 5th bin of M_{eff} in the target region of the Breit frame (20 GeV $< M_{\mathrm{eff}} <$ 30 GeV). The uncorrected number of tracks in the data (C) is multiplied by the normalized matrix (B) and the result is shown in (A).

210
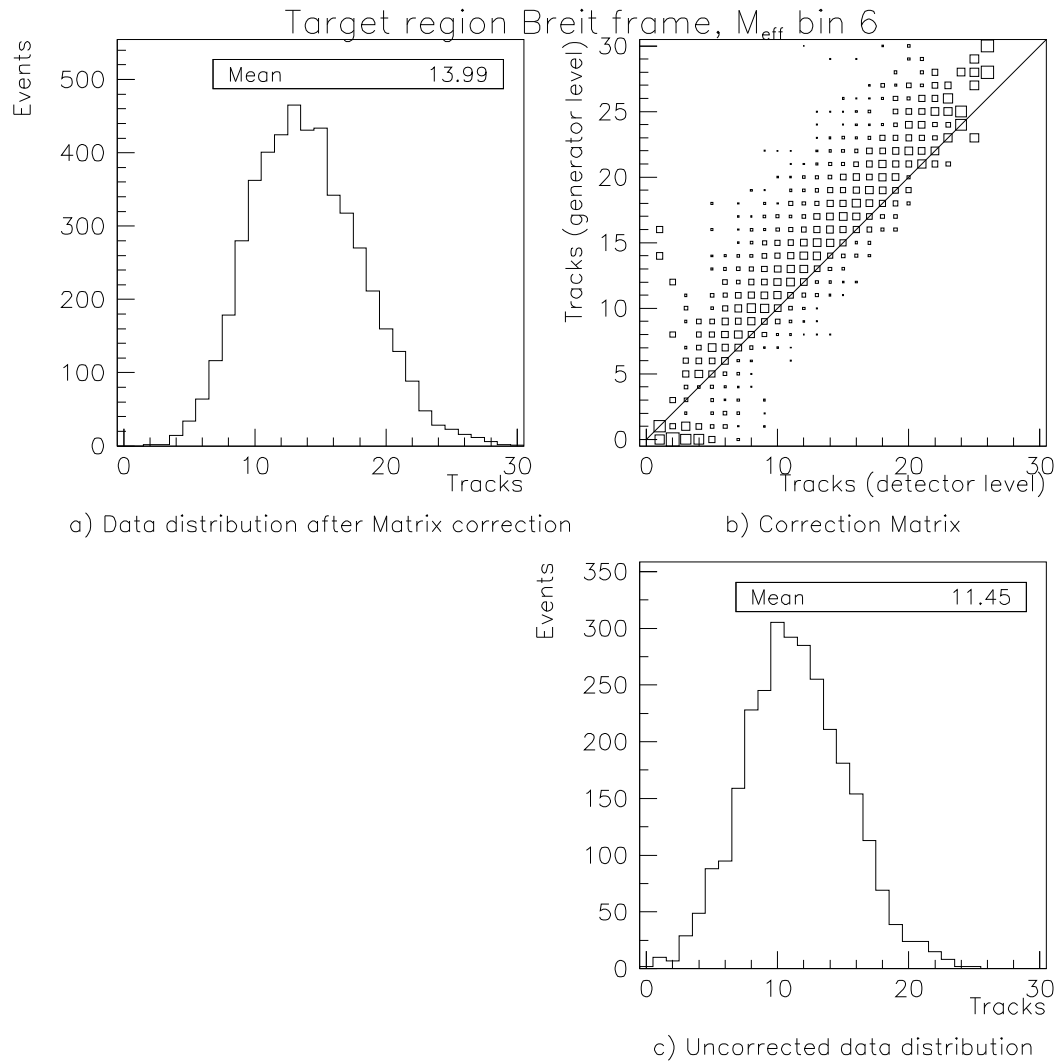
Figure A.17: Matrix correction for $\langle n_{\mathrm{ch}} \rangle$ in the 6th bin of M_{eff} in the target region of the Breit frame (30 GeV $< M_{\mathrm{eff}} <$ 45 GeV). The uncorrected number of tracks in the data (C) is multiplied by the normalized matrix (B) and the result is shown in (A).
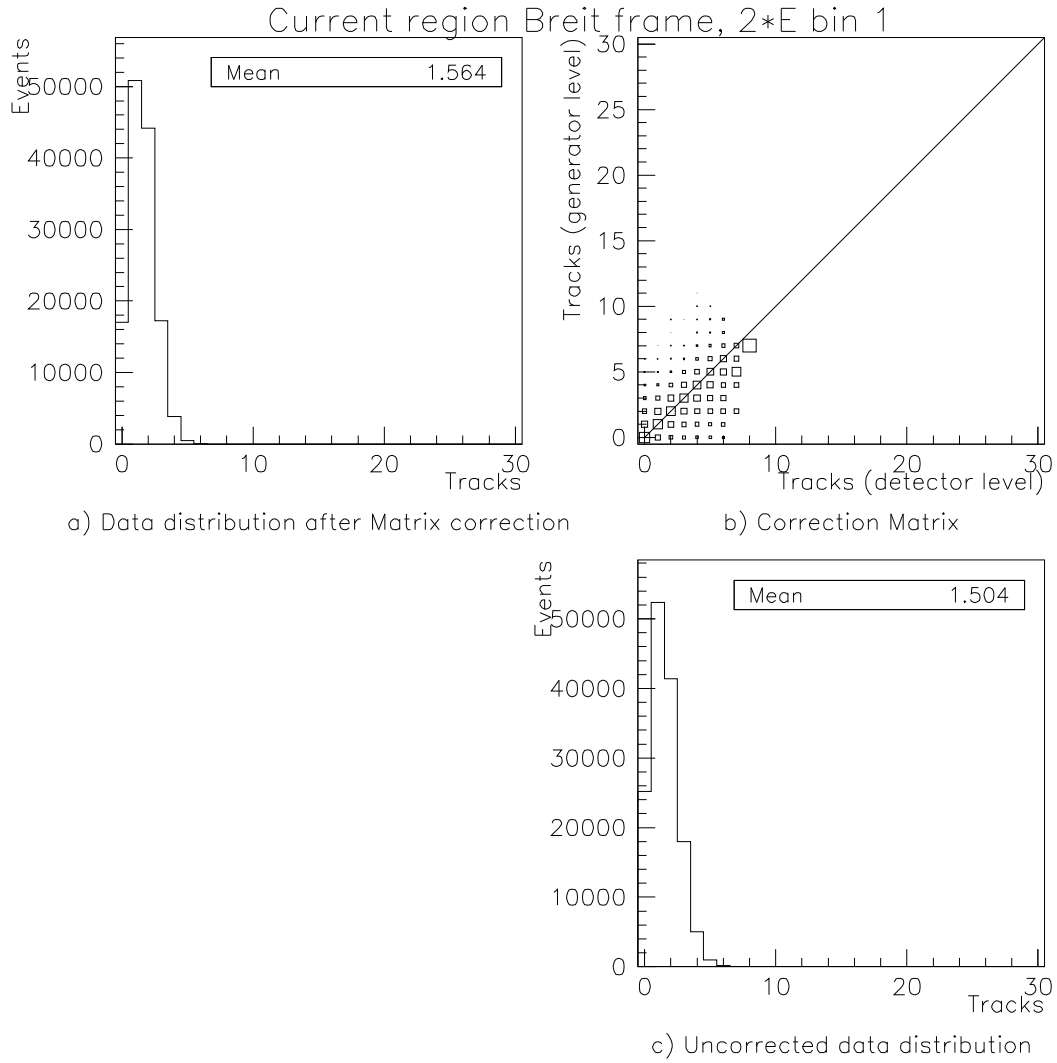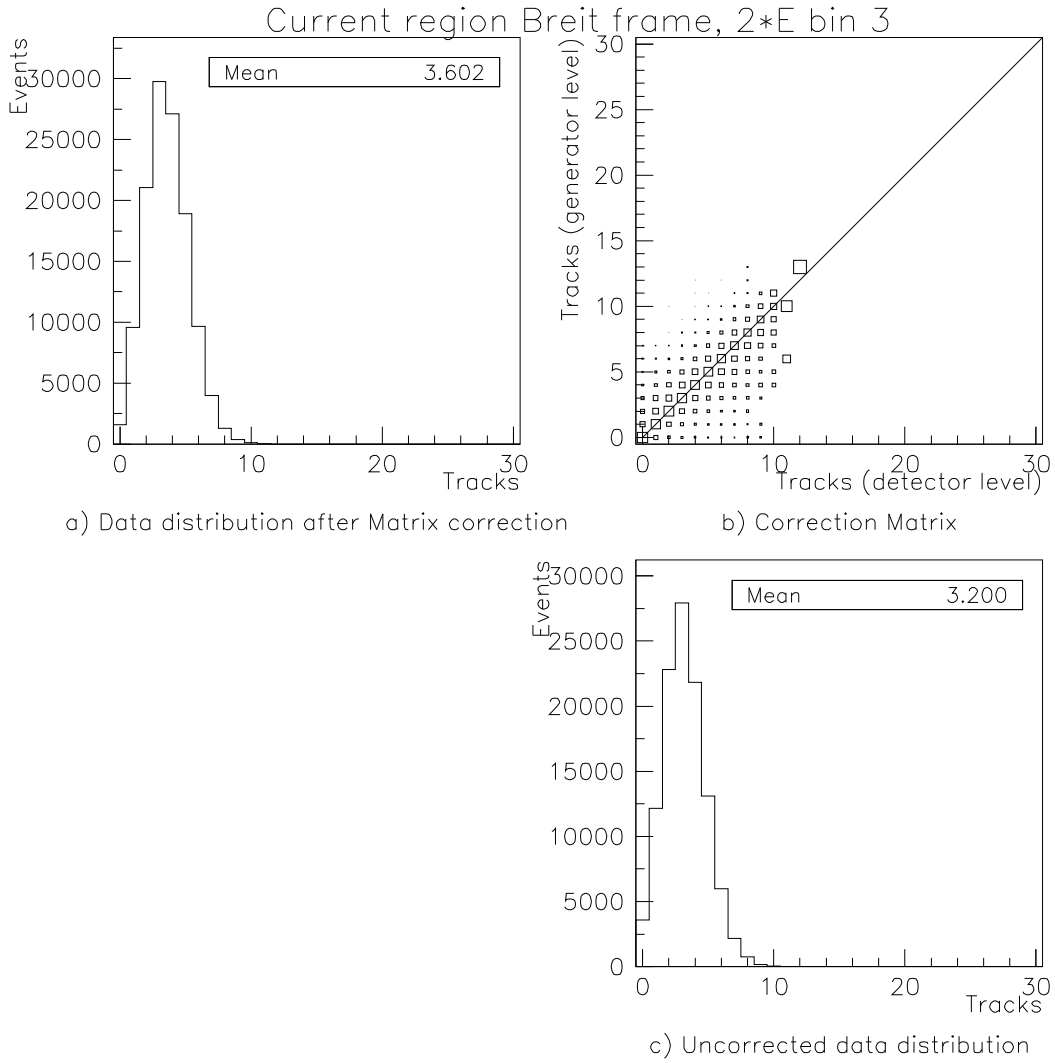
Figure A.18: Matrix correction for $\langle n_{\mathrm{ch}} \rangle$ in the 1st bin of $2 \cdot E_{\mathrm{Breit}}^{\mathrm{current}}$ in the current region of the Breit frame (1.5 GeV $< 2 \cdot E_{\mathrm{Breit}}^{\mathrm{current}} < 4$ GeV). The uncorrected number of tracks in the data (C) is multiplied by the normalized matrix (B) and the result is shown in (A).

212

a) Data distribution after Matrix correction

b) Correction Matrix

c) Uncorrected data distribution
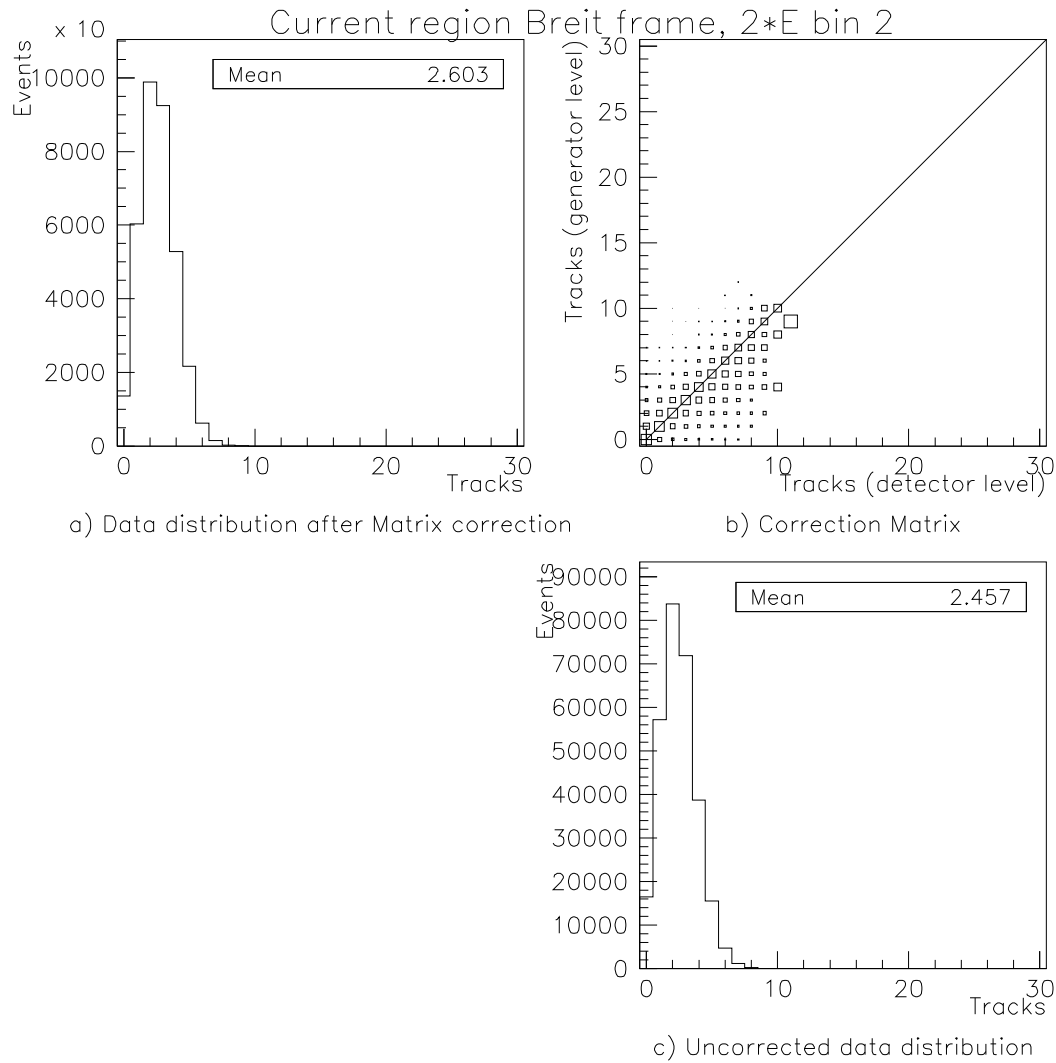
Figure A.19: Matrix correction for $\langle n_{\rm ch} \rangle$ in the 2nd bin of $2 \cdot E_{\rm Breit}^{\rm current}$ in the current region of the Breit frame (4 GeV $< 2 \cdot E_{\rm Breit}^{\rm current} <$ 8 GeV). The uncorrected number of tracks in the data (C) is multiplied by the normalized matrix (B) and the result is shown in (A).

Figure A.20: Matrix correction for $\langle n_{\text{ch}} \rangle$ in the 3rd bin of $2 \cdot E_{\text{Breit}}^{\text{current}}$ in the current region of the Breit frame ($8 \text{ GeV} < 2 \cdot E_{\text{Breit}}^{\text{current}} < 12 \text{ GeV}$). The uncorrected number of tracks in the data (C) is multiplied by the normalized matrix (B) and the result is shown in (A).
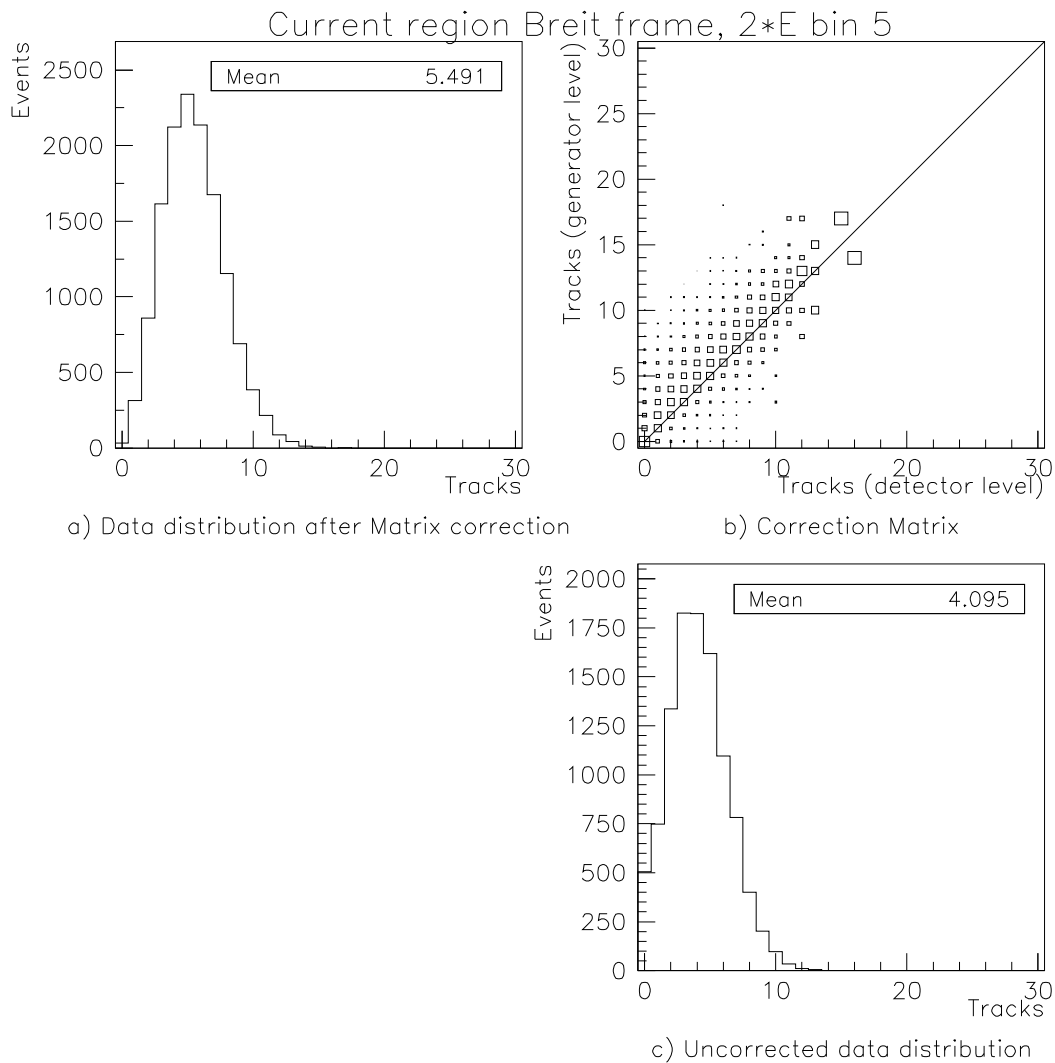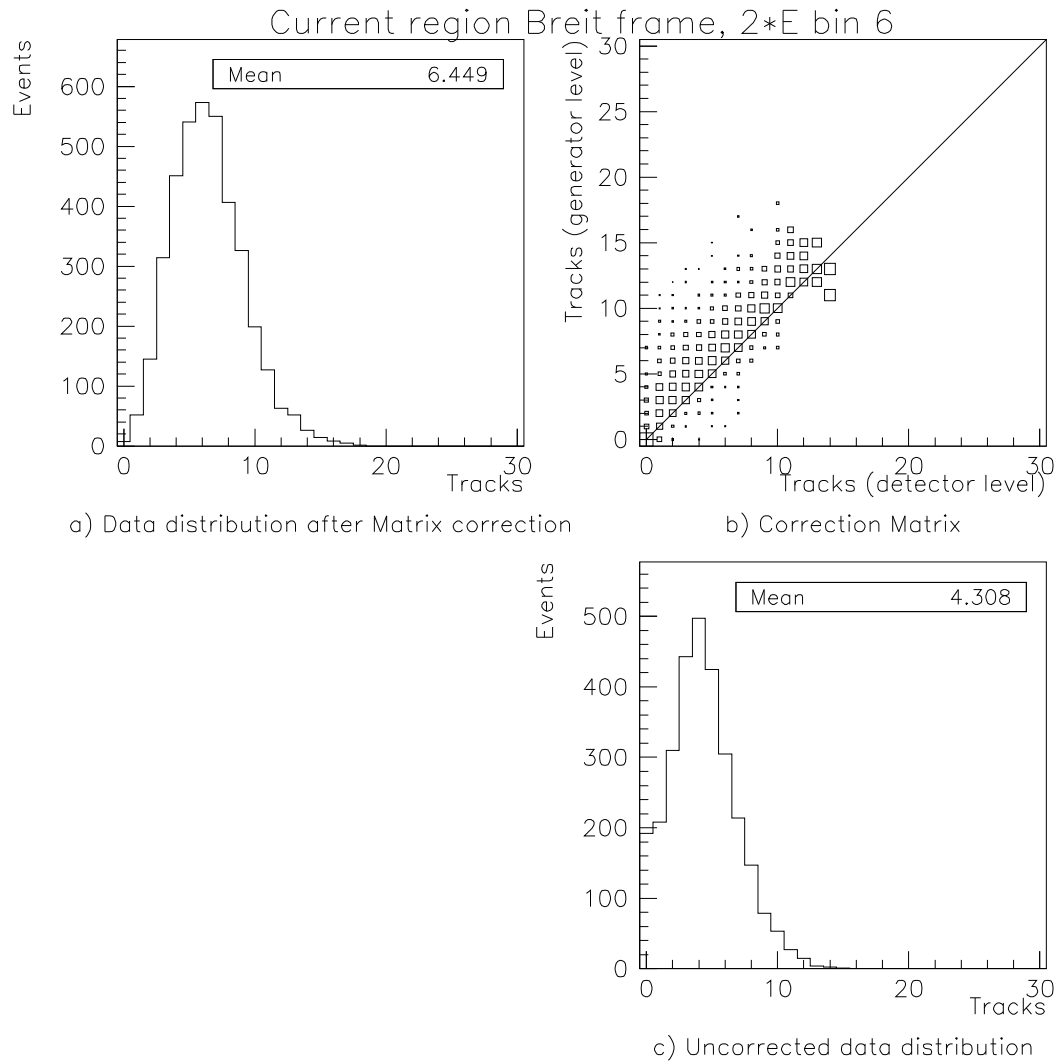
214
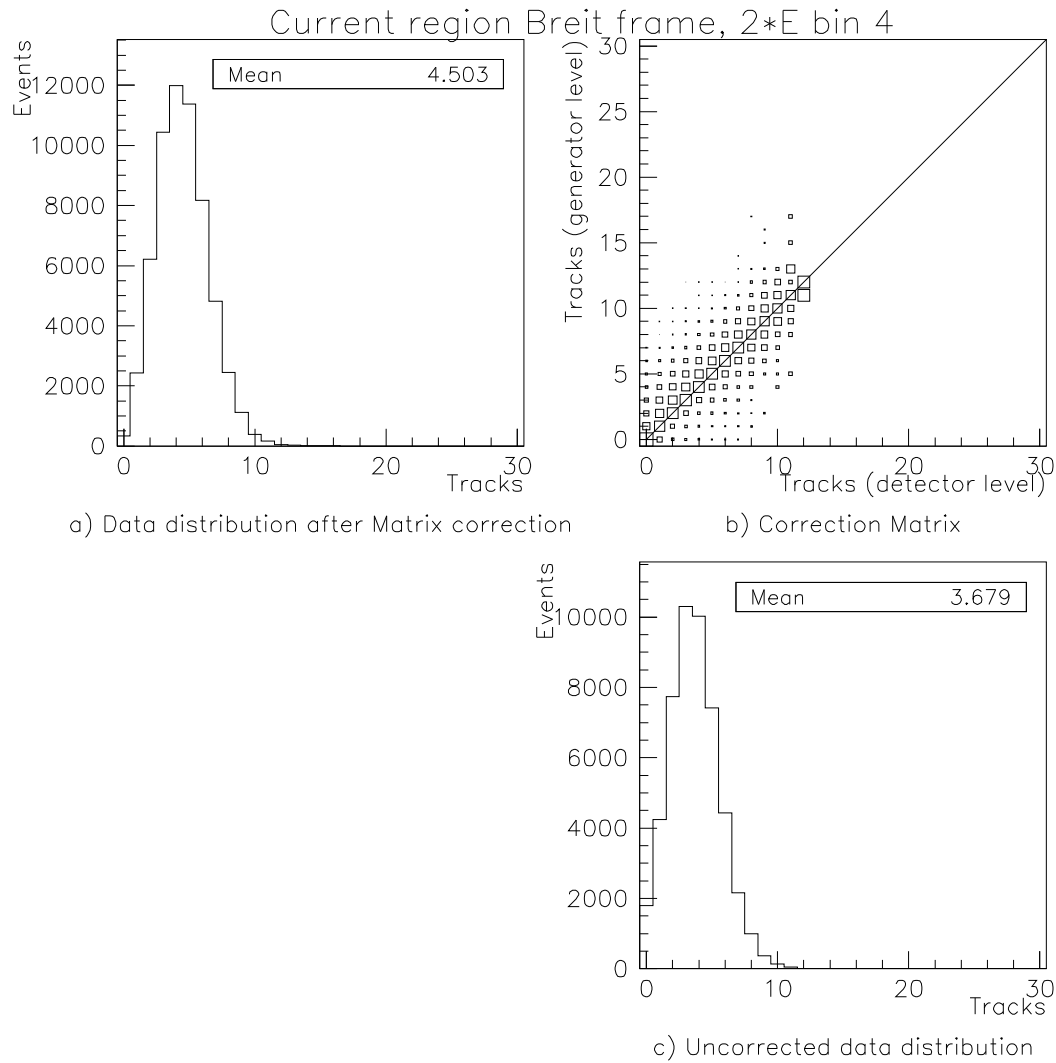
Figure A.21: Matrix correction for $\langle n_{\rm ch} \rangle$ in the 4th bin of $2 \cdot E_{\rm Breit}^{\rm current}$ in the current region of the Breit frame (12 GeV $< 2 \cdot E_{\rm Breit}^{\rm current} <$ 20 GeV). The uncorrected number of tracks in the data (C) is multiplied by the normalized matrix (B) and the result is shown in (A).

Figure A.22: Matrix correction for $\langle n_{\rm ch} \rangle$ in the 5th bin of $2 \cdot E_{\rm Breit}^{\rm current}$ in the current region of the Breit frame (20 GeV $< 2 \cdot E_{\rm Breit}^{\rm current} < 30$ GeV). The uncorrected number of tracks in the data (C) is multiplied by the normalized matrix (B) and the result is shown in (A).
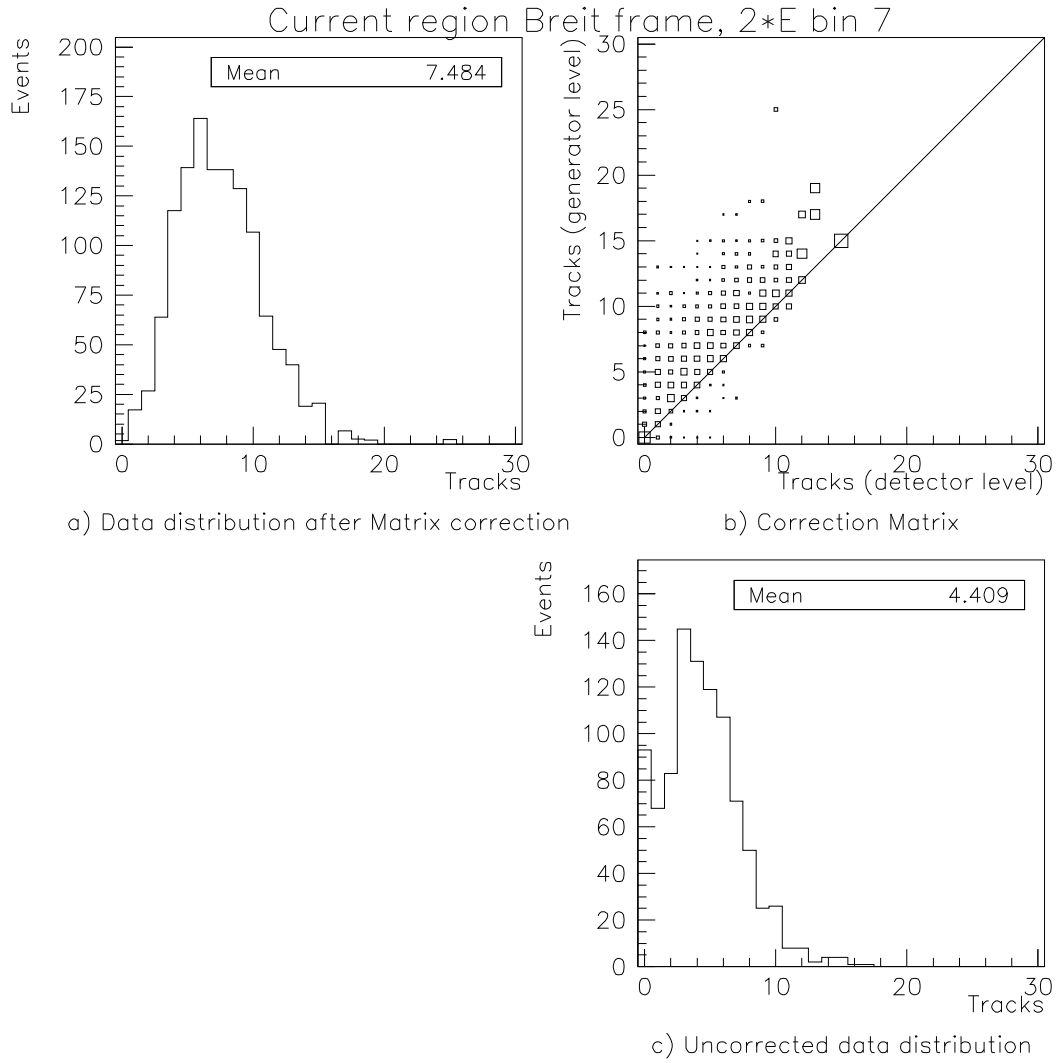
216

Figure A.23: Matrix correction for $\langle n_{\mathrm{ch}} \rangle$ in the 6th bin of $2 \cdot E_{\mathrm{Breit}}^{\mathrm{current}}$ in the current region of the Breit frame (30 GeV $< 2 \cdot E_{\mathrm{Breit}}^{\mathrm{current}} <$ 45 GeV). The uncorrected number of tracks in the data (C) is multiplied by the normalized matrix (B) and the result is shown in (A).
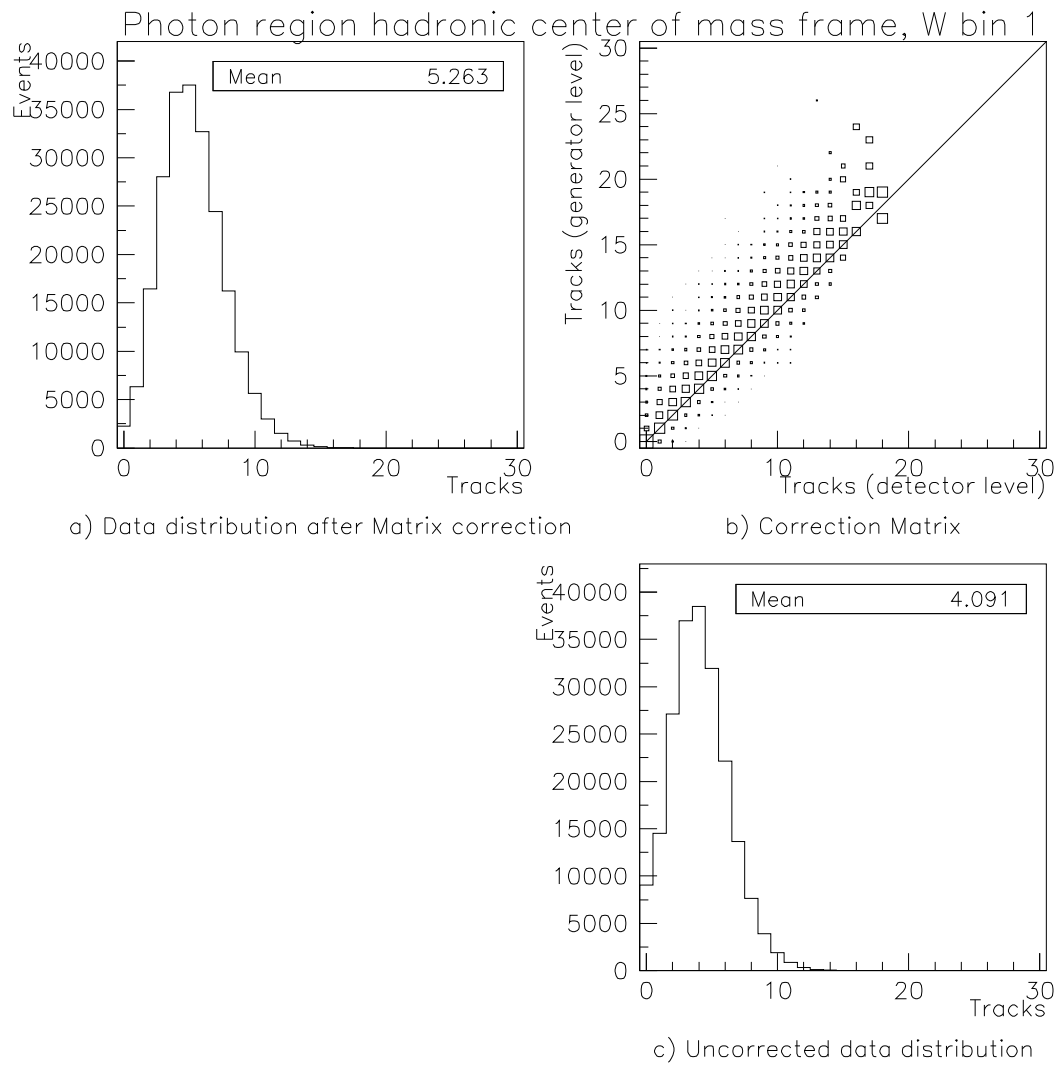
Figure A.24: Matrix correction for $\langle n_{\mathrm{ch}} \rangle$ in the 7th bin of $2 \cdot E_{\mathrm{Breit}}^{\mathrm{current}}$ in the current region of the Breit frame ($45\ \mathrm{GeV} < 2 \cdot E_{\mathrm{Breit}}^{\mathrm{current}} < 100\ \mathrm{GeV}$). The uncorrected number of tracks in the data (C) is multiplied by the normalized matrix (B) and the result is shown in (A).
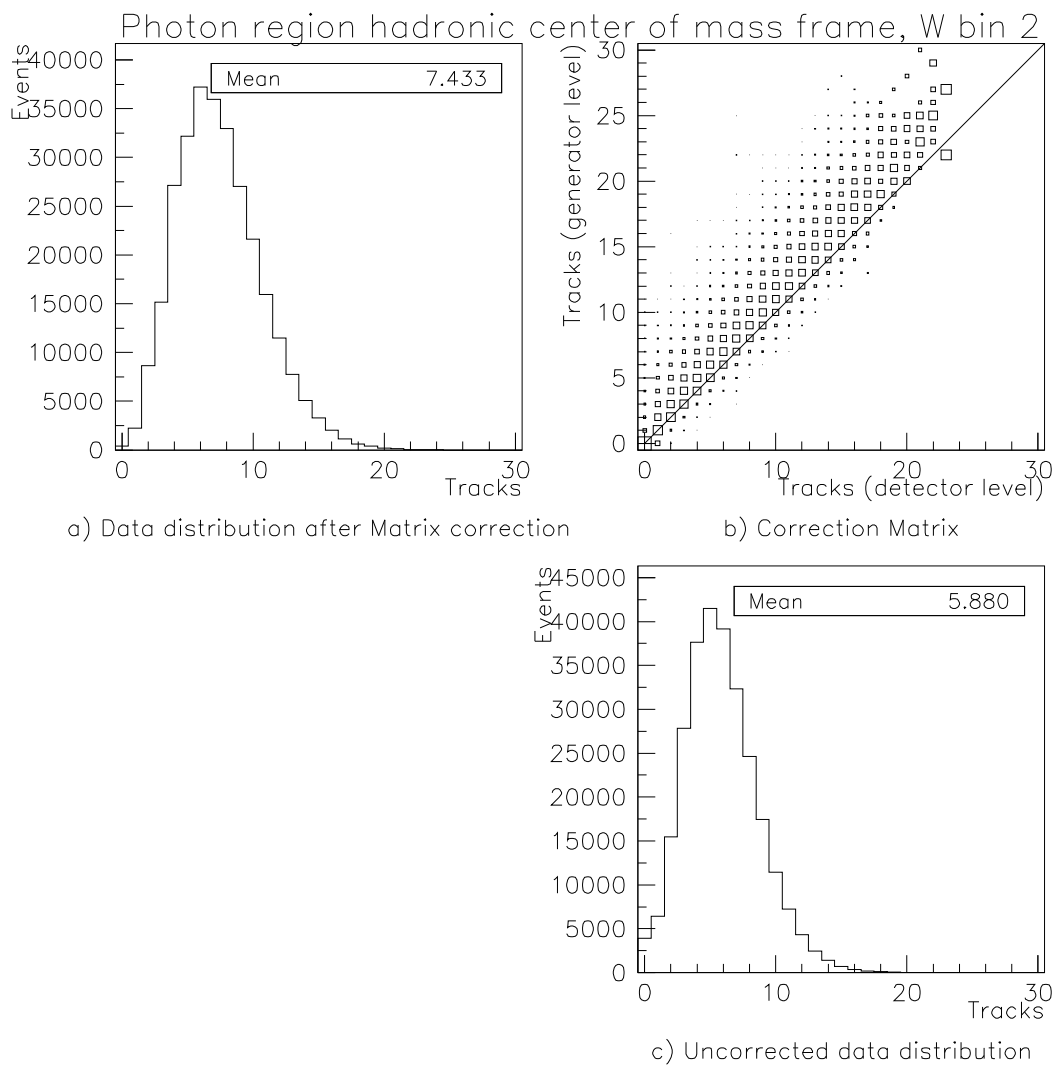
Photon region hadronic center of mass frame, W bin 1

a) Data distribution after Matrix correction

b) Correction Matrix

c) Uncorrected data distribution

Figure A.25: Matrix correction for $\langle n_{\mathrm{ch}} \rangle$ in the 1st bin of W in the photon region of the HCM frame (70 GeV $< W <$ 100 GeV). The uncorrected number of tracks in the data (C) is multiplied by the normalized matrix (B) and the result is shown in (A).

Photon region hadronic center of mass frame, W bin 2

a) Data distribution after Matrix correction

b) Correction Matrix

c) Uncorrected data distribution

Figure A.26: Matrix correction for $\langle n_{\mathrm{ch}} \rangle$ in the 2nd bin of W in the photon region of the HCM frame (100 GeV $< W <$ 150 GeV). The uncorrected number of tracks in the data (C) is multiplied by the normalized matrix (B) and the result is shown in (A).
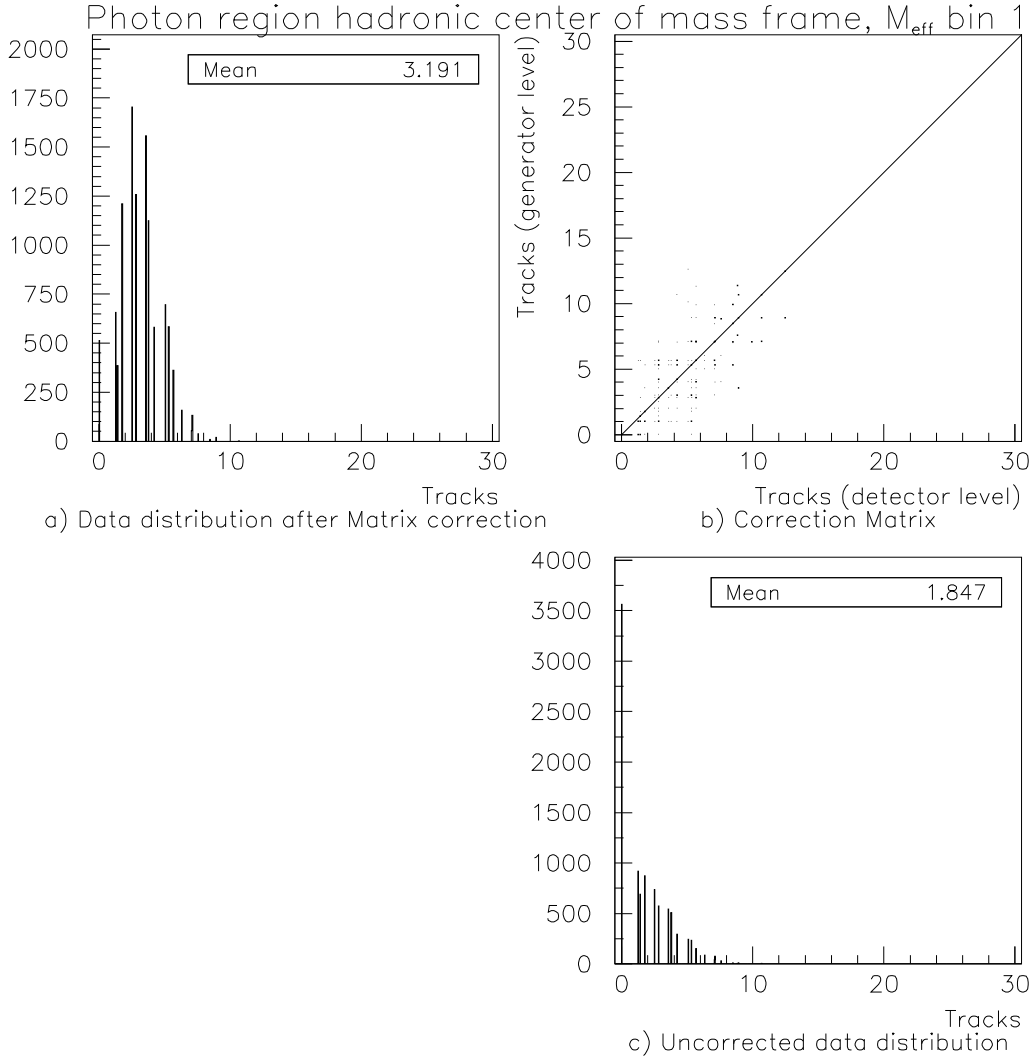
220
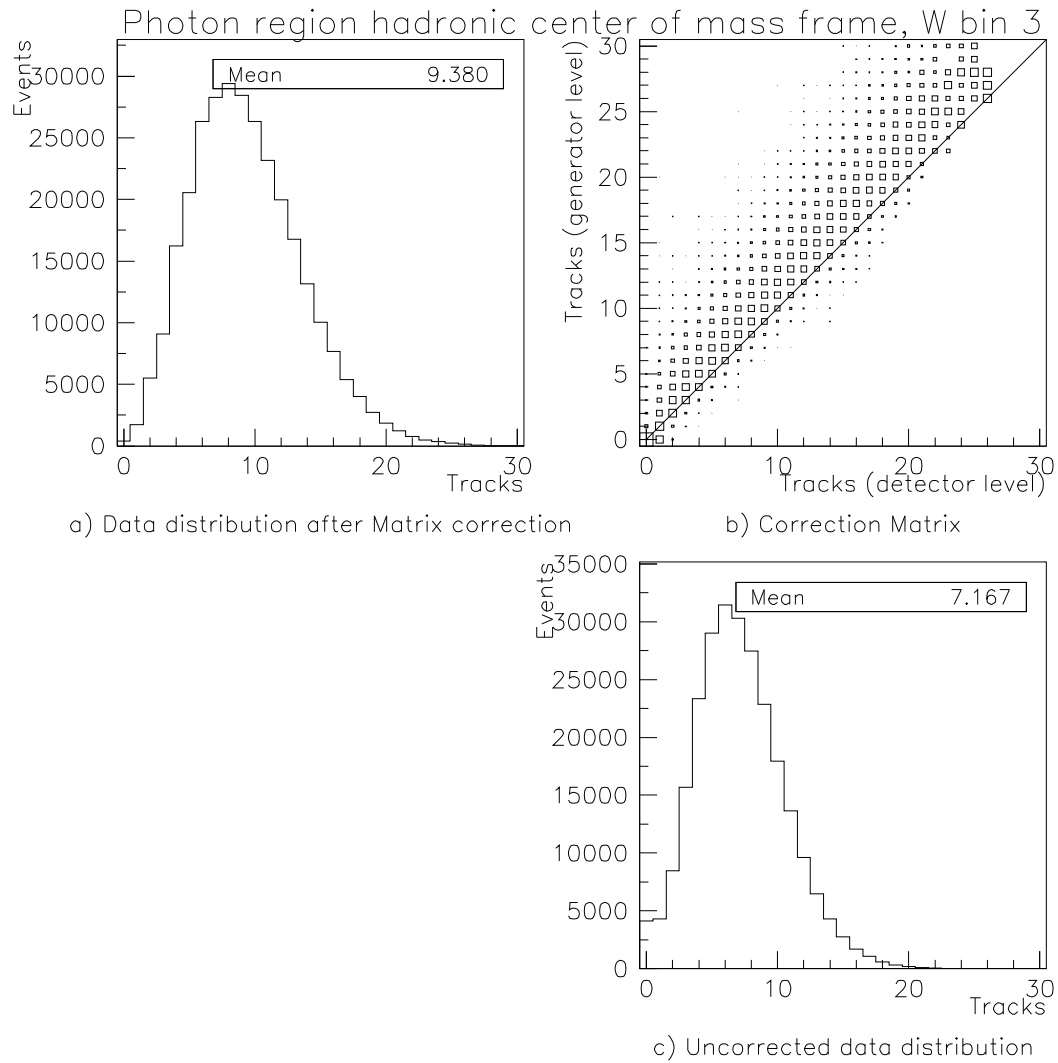
Figure A.27: Matrix correction for $\langle n_{\text{ch}} \rangle$ in the 3rd bin of W in the photon region of the HCM frame (150 GeV $< W <$ 225 GeV). The uncorrected number of tracks in the data (C) is multiplied by the normalized matrix (B) and the result is shown in (A).

Figure A.28: Matrix correction for $\langle n_{\mathrm{ch}} \rangle$ in the 1st bin of M_{eff} in the photon region of the HCM frame ($1.5 \text{ GeV} < M_{\mathrm{eff}} < 4 \text{ GeV}$). The uncorrected number of tracks in the data (C) is multiplied by the normalized matrix (B) and the result is shown in (A). The binning for these histograms is much finer than that for the other analyses due to the fact that there is a non-integer correction to the tracks applied before the matrix correction, as explained in section 8.5.
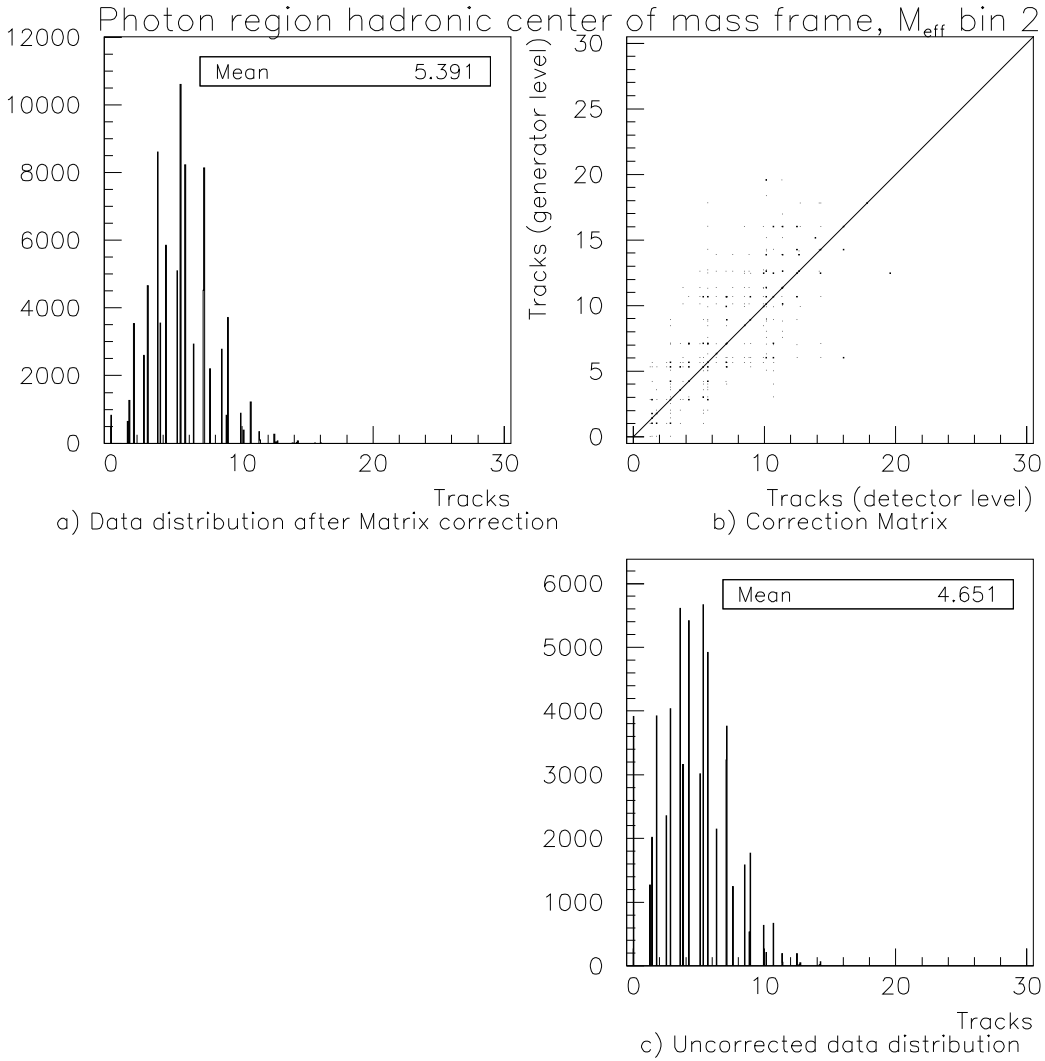
222

Figure A.29: Matrix correction for $\langle n_{\mathrm{ch}} \rangle$ in the 2nd bin of M_{eff} in the photon region of the HCM frame (4 GeV $< M_{\mathrm{eff}} <$ 8 GeV). The uncorrected number of tracks in the data (C) is multiplied by the normalized matrix (B) and the result is shown in (A). The binning for these histograms is much finer than that for the other analyses due to the fact that there is a non-integer correction to the tracks applied before the matrix correction, as explained in section 8.5.
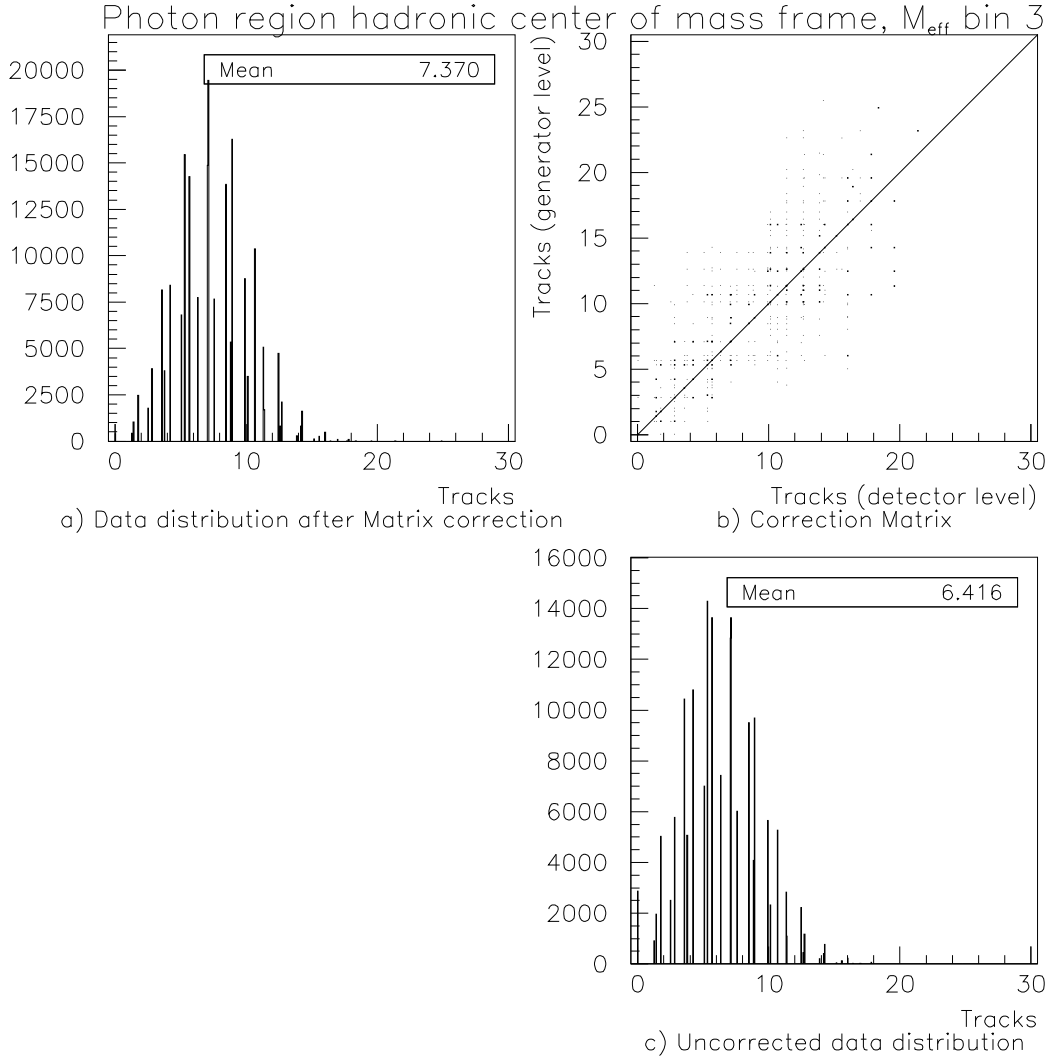
Figure A.30: Matrix correction for $\langle n_{\mathrm{ch}} \rangle$ in the 3rd bin of M_{eff} in the photon region of the HCM frame (8 GeV $< M_{\mathrm{eff}} <$ 12 GeV). The uncorrected number of tracks in the data (C) is multiplied by the normalized matrix (B) and the result is shown in (A). The binning for these histograms is much finer than that for the other analyses due to the fact that there is a non-integer correction to the tracks applied before the matrix correction, as explained in section 8.5.
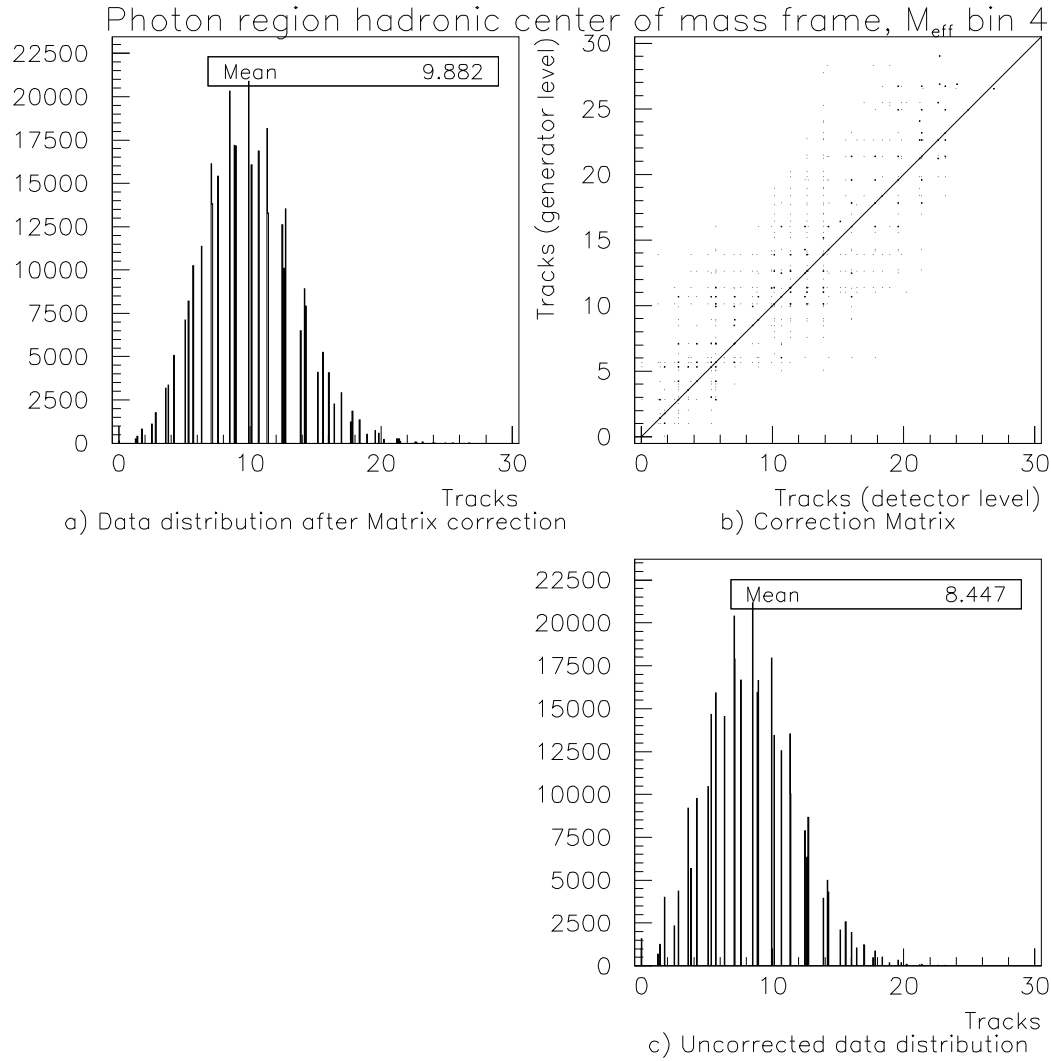
224

Figure A.31: Matrix correction for $\langle n_{\mathrm{ch}} \rangle$ in the 4th bin of M_{eff} in the photon region of the HCM frame (12 GeV $< M_{\mathrm{eff}} <$ 20 GeV). The uncorrected number of tracks in the data (C) is multiplied by the normalized matrix (B) and the result is shown in (A). The binning for these histograms is much finer than that for the other analyses due to the fact that there is a non-integer correction to the tracks applied before the matrix correction, as explained in section 8.5.
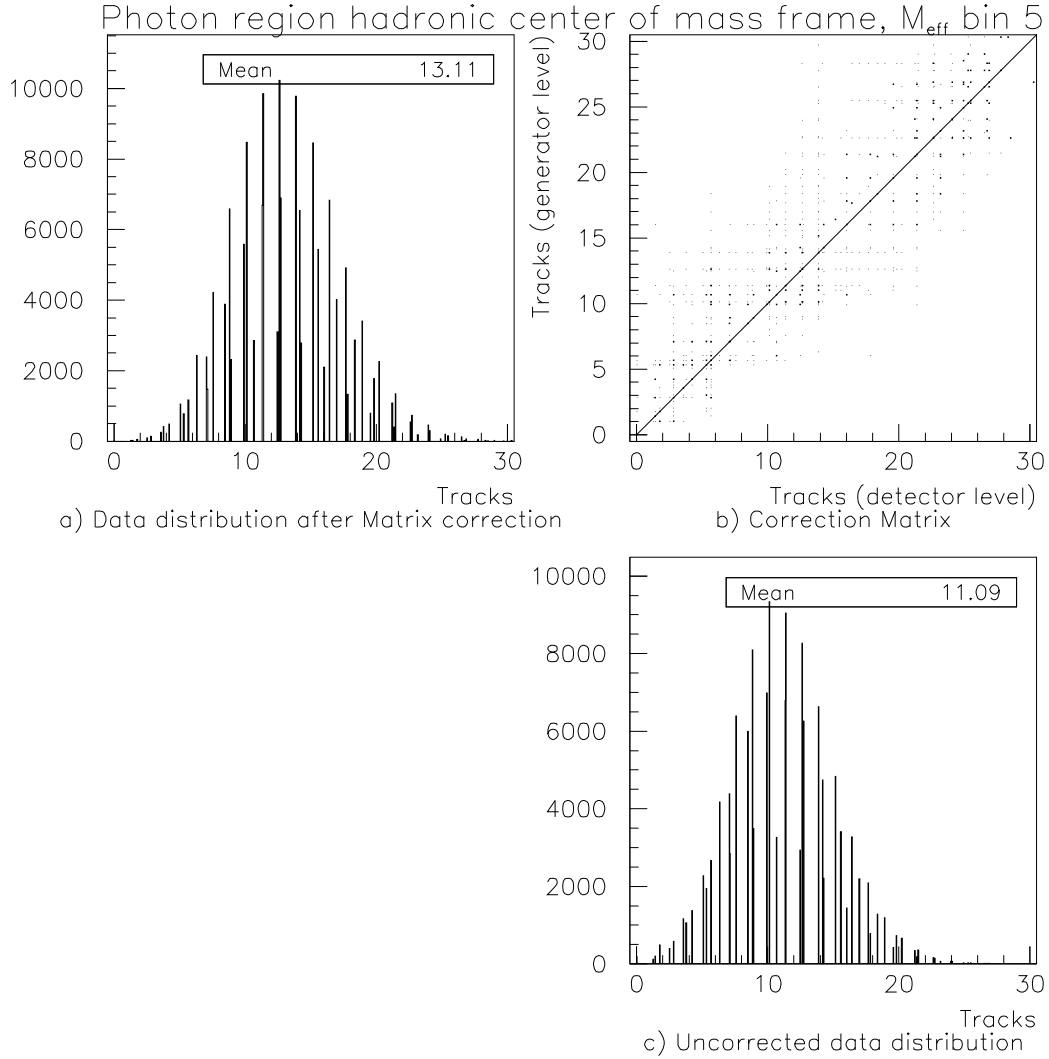
Figure A.32: Matrix correction for $\langle n_{\mathrm{ch}} \rangle$ in the 5th bin of M_{eff} in the photon region of the HCM frame (20 GeV $< M_{\mathrm{eff}} <$ 30 GeV). The uncorrected number of tracks in the data (C) is multiplied by the normalized matrix (B) and the result is shown in (A). The binning for these histograms is much finer than that for the other analyses due to the fact that there is a non-integer correction to the tracks applied before the matrix correction, as explained in section 8.5.
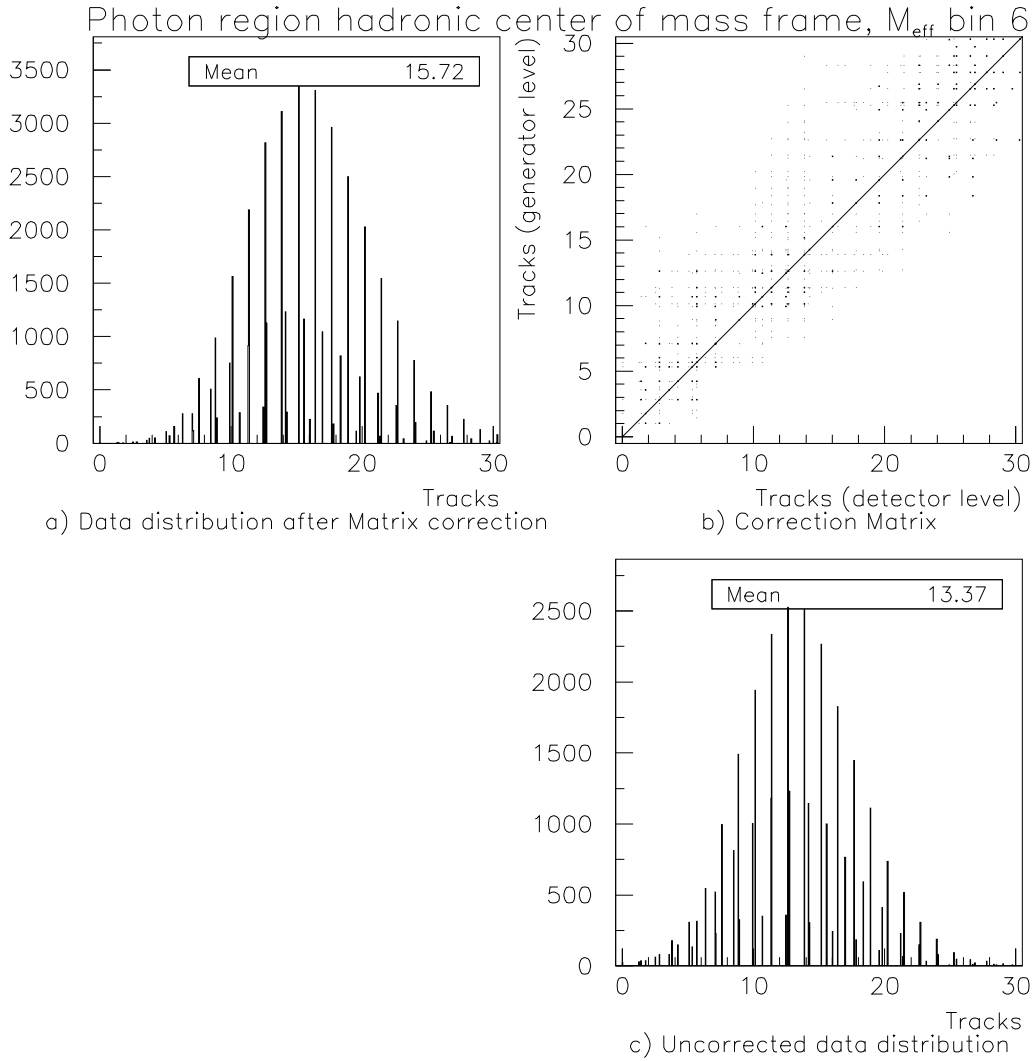
Figure A.33: Matrix correction for $\langle n_{\rm ch} \rangle$ in the 6th bin of $M_{\rm eff}$ in the photon region of the HCM frame (30 GeV $< M_{\rm eff} <$ 45 GeV). The uncorrected number of tracks in the data (C) is multiplied by the normalized matrix (B) and the result is shown in (A). The binning for these histograms is much finer than that for the other analyses due to the fact that there is a non-integer correction to the tracks applied before the matrix correction, as explained in section 8.5.
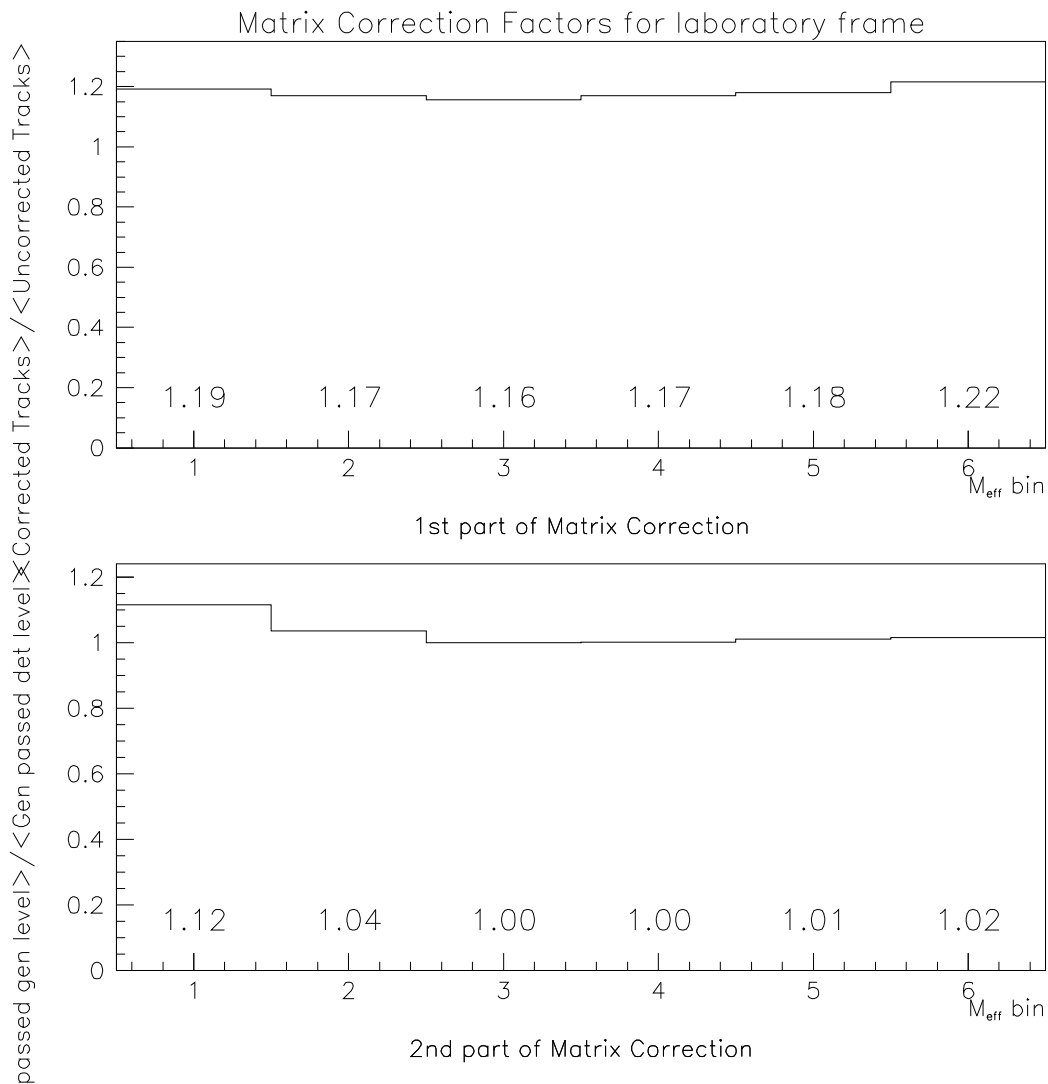
Figure A.34: Matrix correction factors for the laboratory frame in bins of M_{eff}. Shown in the upper plot is the average matrix correction factor, a ratio of the mean of the corrected track distribution to the mean uncorrected track distribution in each bin of M_{eff}. Shown in the bottom plot is the mean of the histograms of the correction factor, $C = \rho_{gen}/\rho_{rec}$, for the second part of the matrix correction. The M_{eff} bin ranges are given in section 6.6.1.
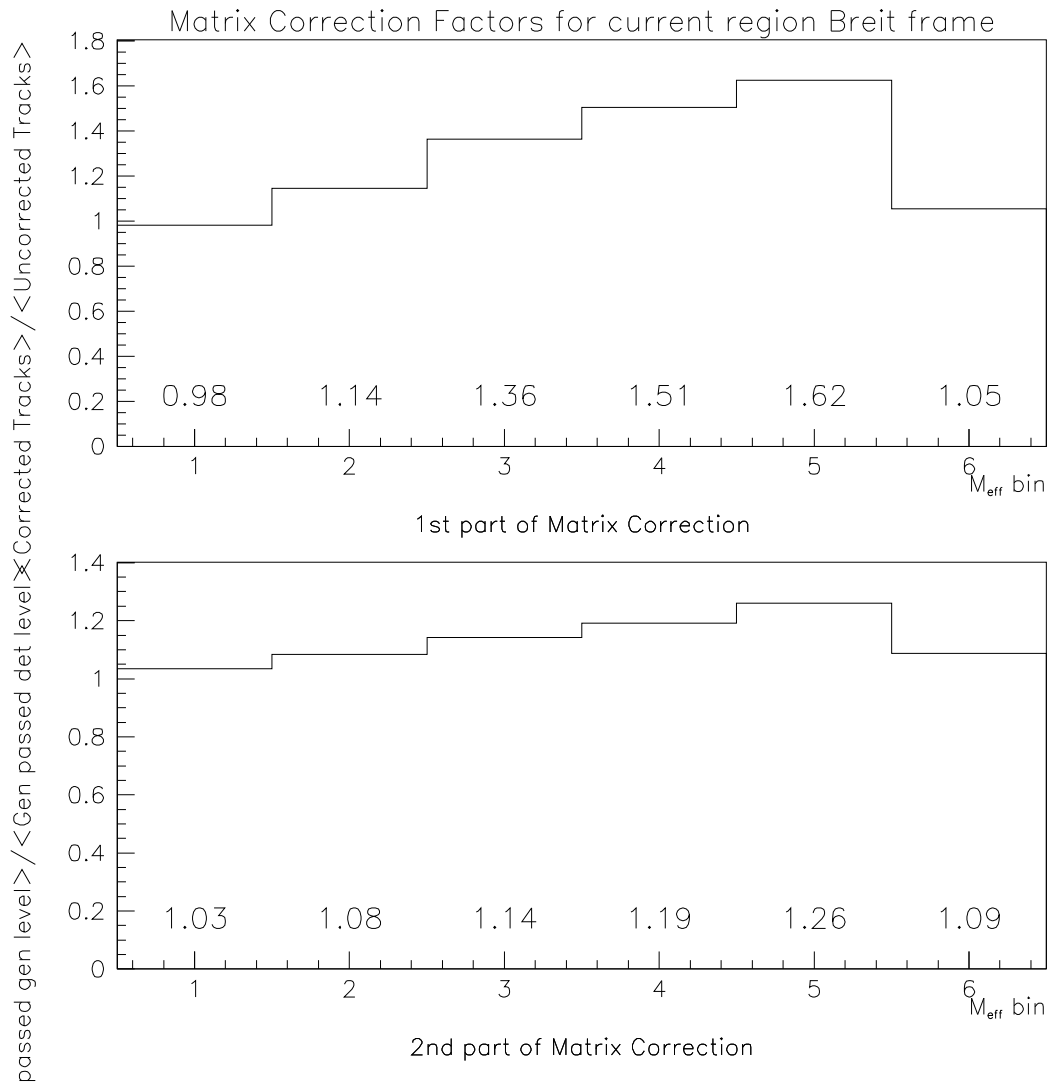
Figure A.35: Matrix correction factors for the current region of the Breit frame in bins of M_{eff}. Shown in the upper plot is the average matrix correction factor, a ratio of the mean of the corrected track distribution to the mean uncorrected track distribution in each bin of M_{eff}. Shown in the bottom plot is the mean of the histograms of the correction factor, $C = \rho_{gen}/\rho_{rec}$, for the second part of the matrix correction. The M_{eff} bin ranges are given in section 6.6.1.
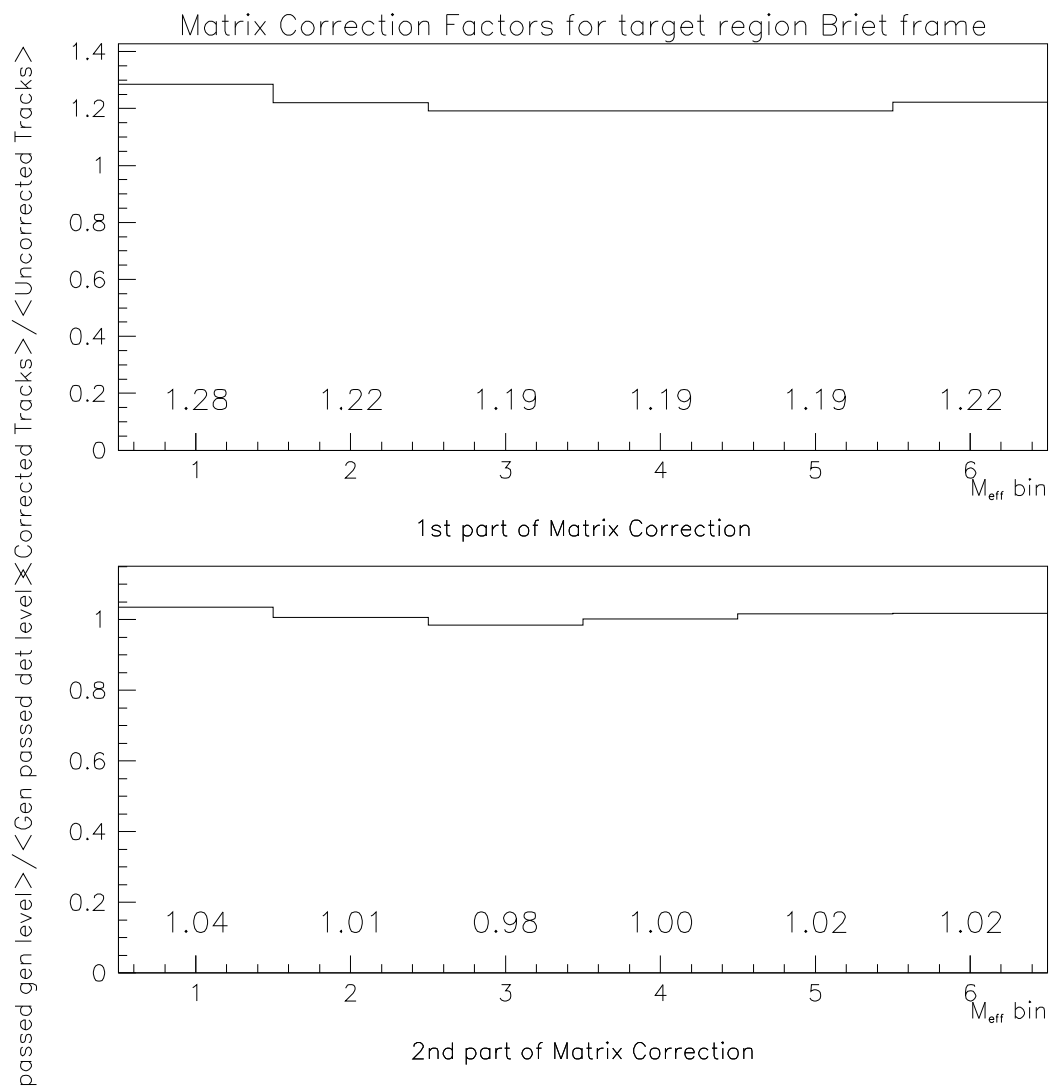
Figure A.36: Matrix correction factors for the target region of the Breit frame in bins of M_{eff}. Shown in the upper plot is the average matrix correction factor, a ratio of the mean of the corrected track distribution to the mean uncorrected track distribution in each bin of M_{eff}. Shown in the bottom plot is the mean of the histograms of the correction factor, $C = \rho_{gen}/\rho_{rec}$, for the second part of the matrix correction. The M_{eff} bin ranges are given in section 6.6.1.
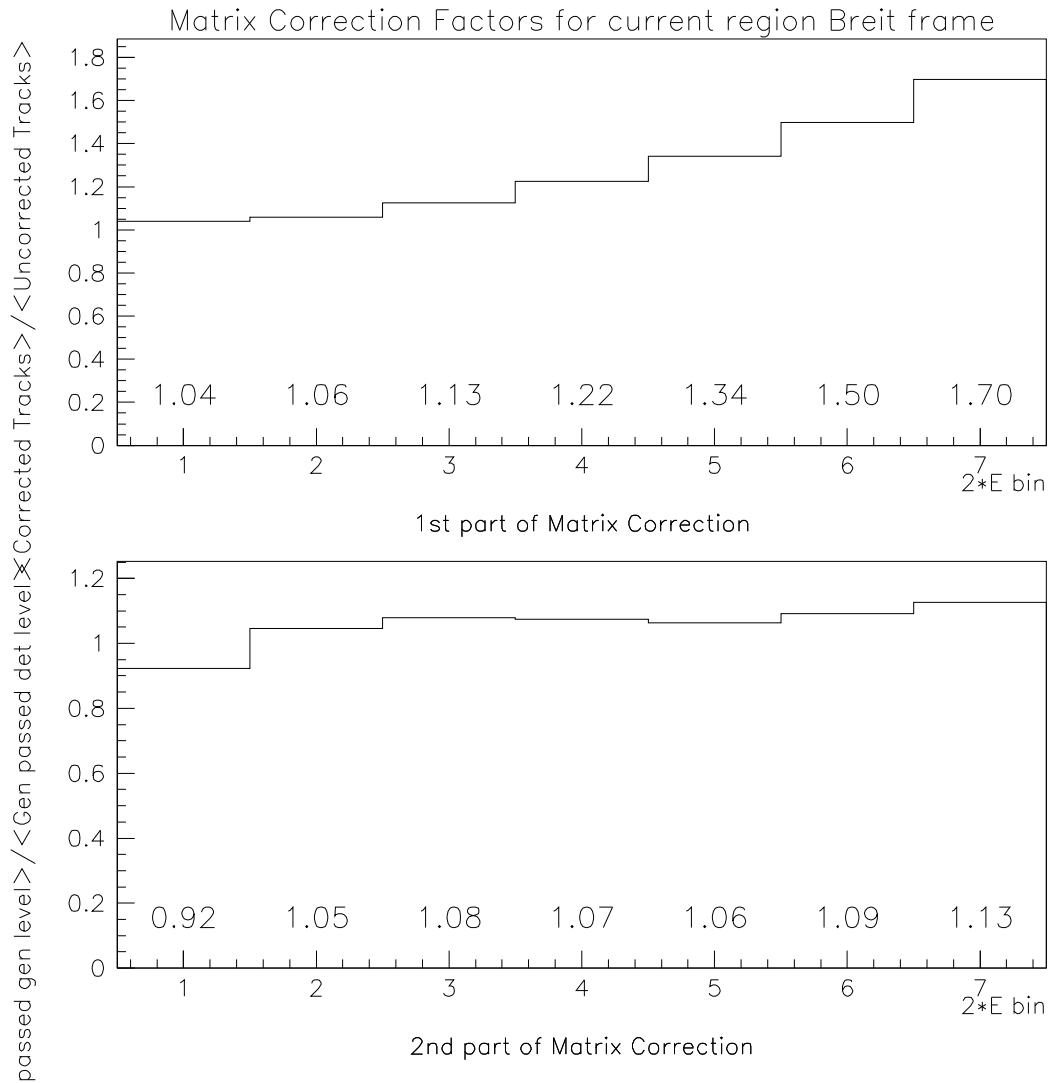
230

Figure A.37: Matrix correction factors for the current region of the Breit frame in bins of $2 \cdot E_{\mathrm{Breit}}^{\mathrm{current}}$. Shown in the upper plot is the average matrix correction factor, a ratio of the mean of the corrected track distribution to the mean uncorrected track distribution in each bin of M_{eff}. Shown in the bottom plot is the mean of the histograms of the correction factor, $C = \rho_{gen}/\rho_{rec}$, for the second part of the matrix correction. The $2 \cdot E_{\mathrm{Breit}}^{\mathrm{current}}$ bin ranges are given in section 6.6.1.
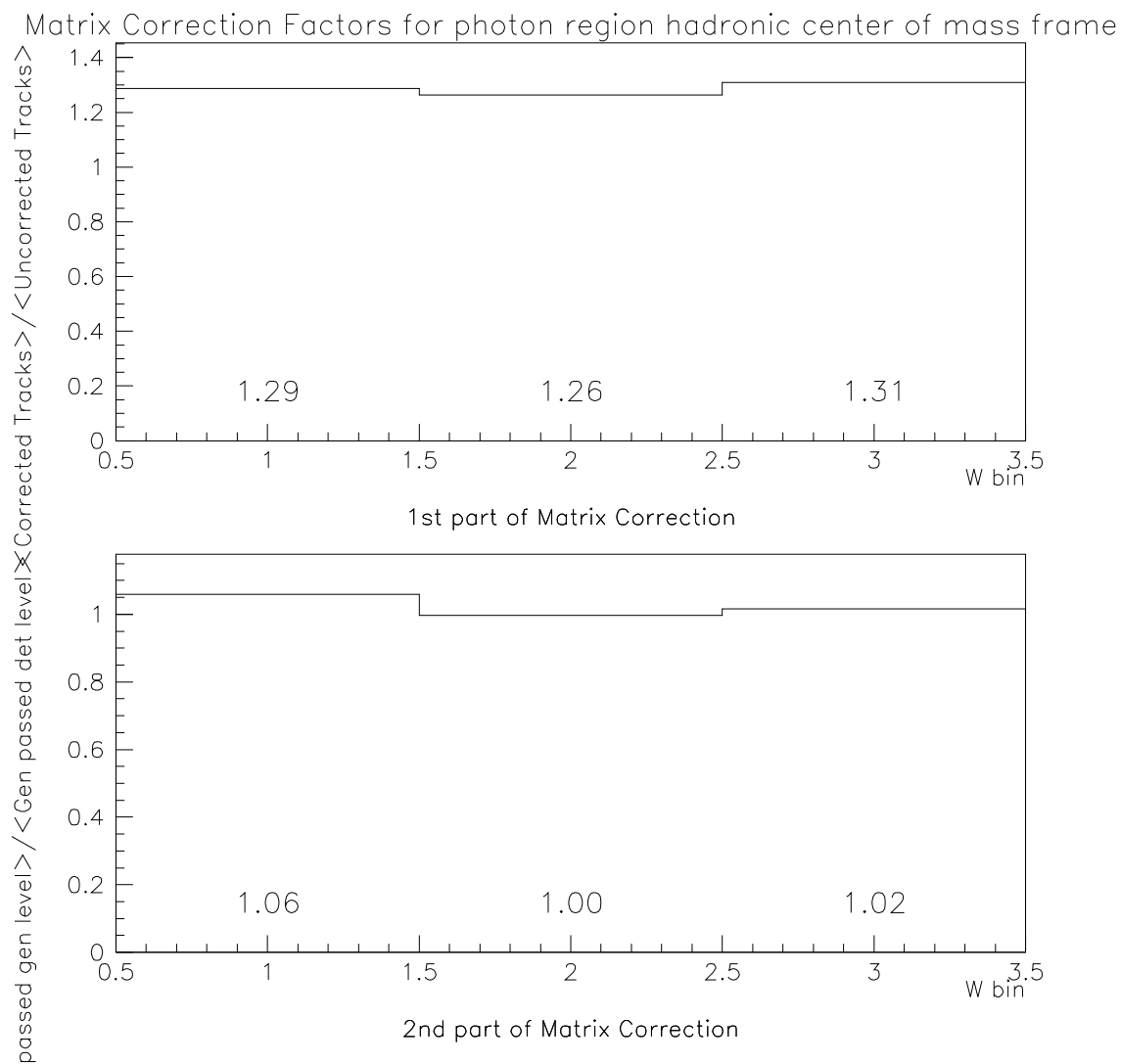
Figure A.38: Matrix correction factors for the photon region of the HCM frame in bins of W. Shown in the upper plot is the average matrix correction factor, a ratio of the mean of the corrected track distribution to the mean uncorrected track distribution in each bin of M_{eff}. Shown in the bottom plot is the mean of the histograms of the correction factor, $C = \rho_{gen}/\rho_{rec}$, for the second part of the matrix correction. The W bin ranges are given in section 6.6.1.
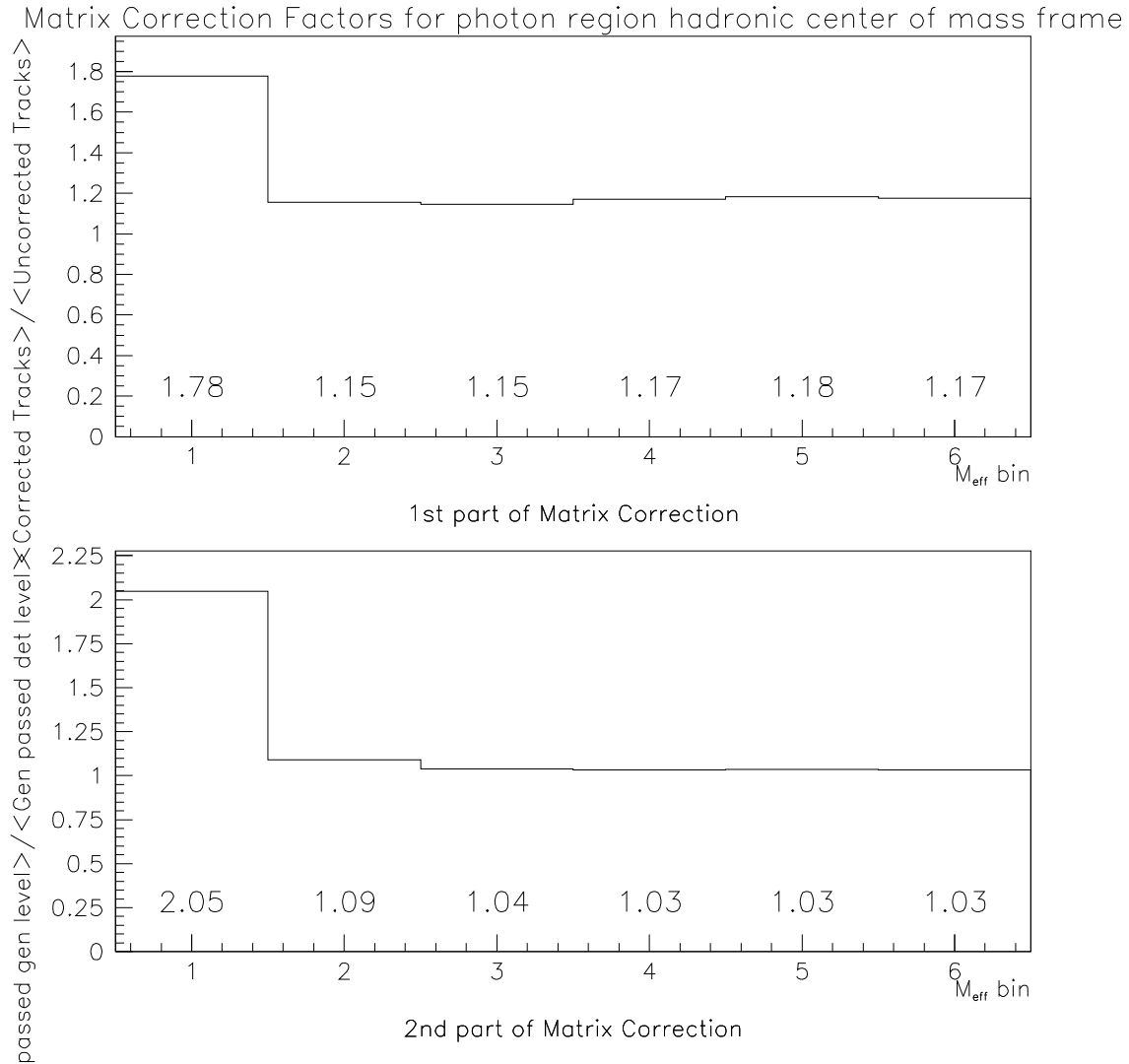
232

Figure A.39: Matrix correction factors for the photon region of the HCM frame in bins of M_{eff}. Shown in the upper plot is the average matrix correction factor, a ratio of the mean of the corrected track distribution to the mean uncorrected track distribution in each bin of M_{eff}. Shown in the bottom plot is the mean of the histograms of the correction factor, $C = \rho_{gen}/\rho_{rec}$, for the second part of the matrix correction. The M_{eff} bin ranges are given in section 6.6.1.

Appendix B

Modified Bin-By-Bin Correction Plots

Presented in this section are plots of the correction factors obtained using the modified bin-by-bin method as described in sec 8.3. The upper plot of the figures represents the average correction factor for detector effects. The lower plots are the correction for the hadrons with $p_T < 150\,\mathrm{MeV}$.

234
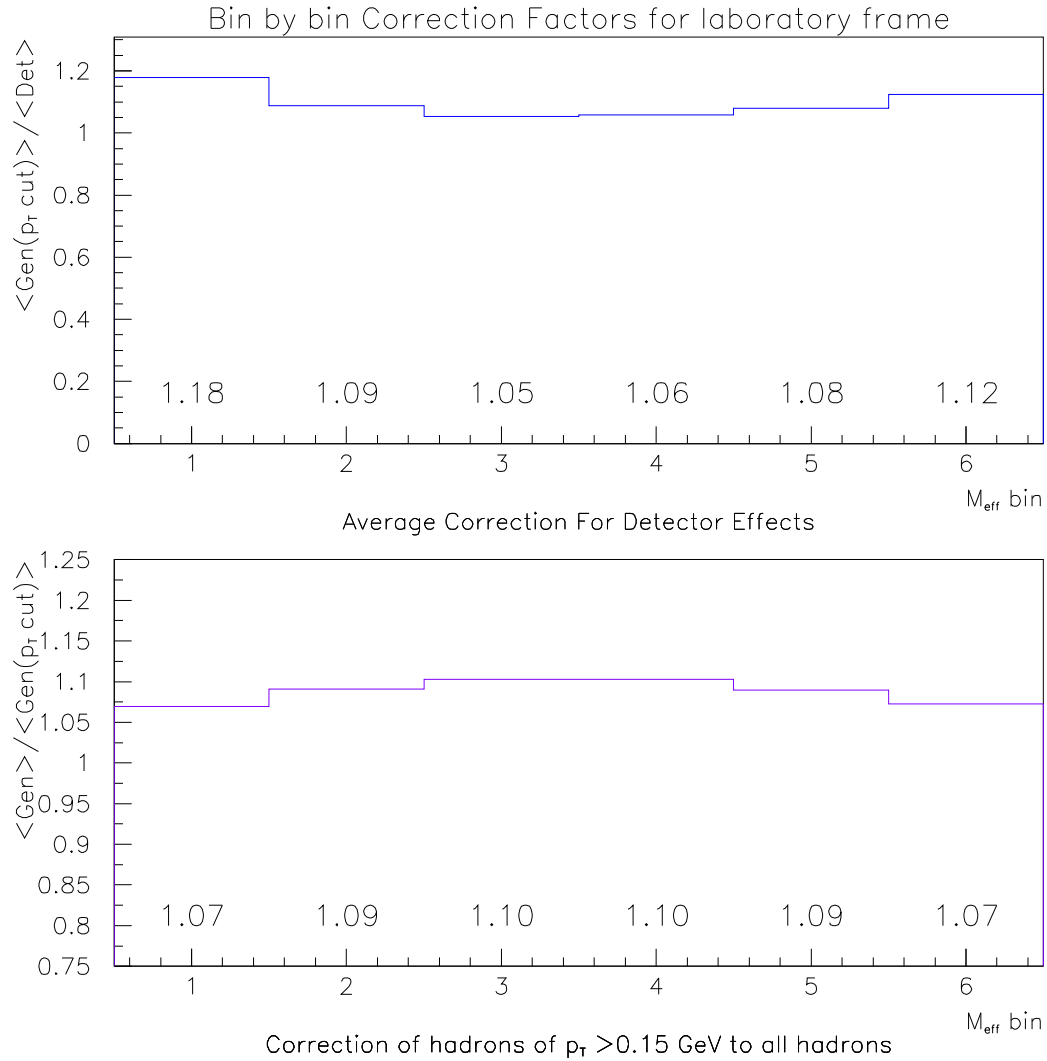
Figure B.1: Bin-by-bin correction factors for $\langle n_{\mathrm{ch}} \rangle$ in the laboratory frame in bins of M_{eff}. Shown in the upper plot is the average correction factor for detector effects, $\langle C_1 \rangle$ from equation 8.5. Shown in the bottom plot is the correction factor, C_2 from equation 8.6, for the hadrons with $p_T < 150\,\mathrm{MeV}$. The $/meff$ bin ranges are given in section 6.6.1.

Figure B.2: Bin-by-bin correction factors for $\langle n_{\mathrm{ch}} \rangle$ in the current region of the Breit frame in bins of M_{eff}. Shown in the upper plot is the average correction factor for detector effects, $\langle C_1 \rangle$ from equation 8.5. Shown in the bottom plot is the correction factor, C_2 from equation 8.6, for the hadrons with $p_T < 150\,\mathrm{MeV}$. The M_{eff} bin ranges are given in section 6.6.1.
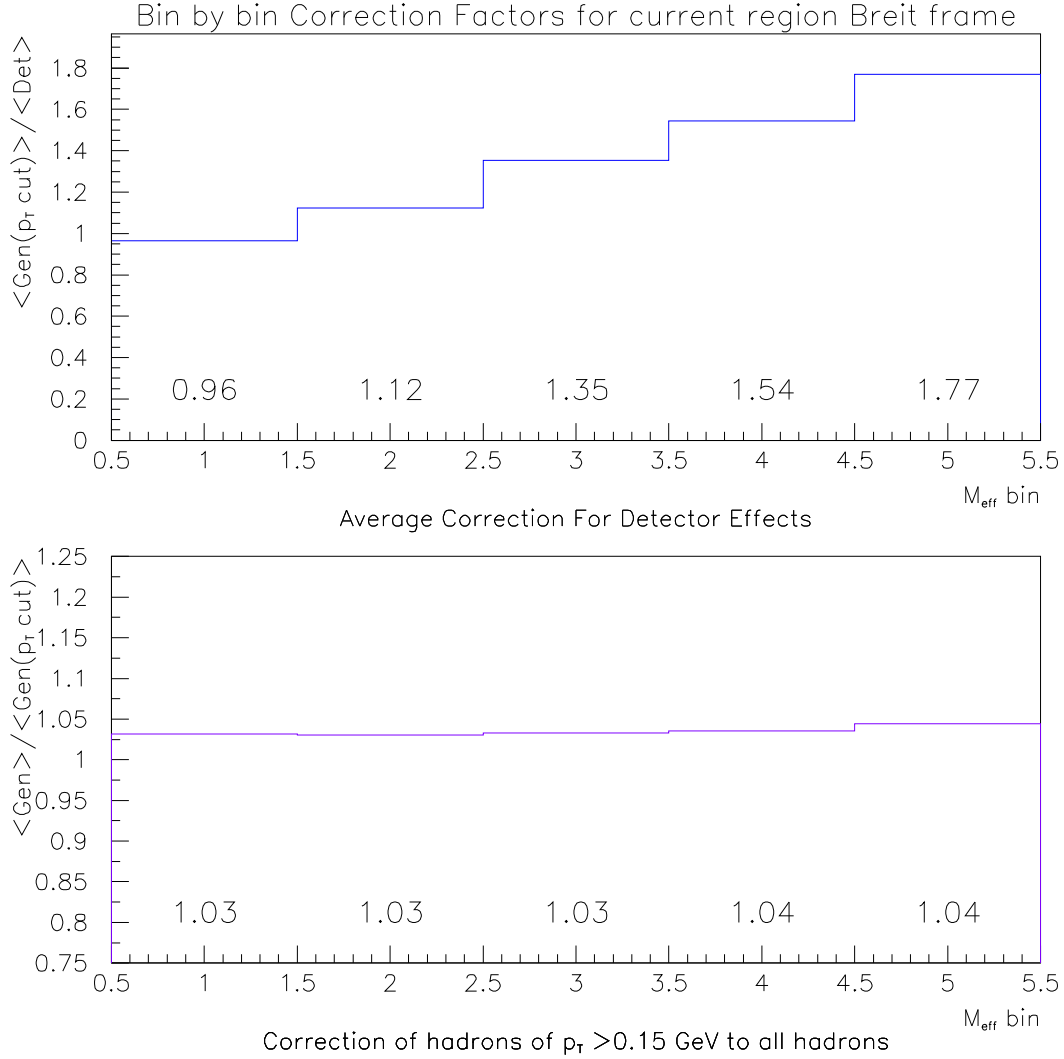
236

Figure B.3: Bin-by-bin correction factors for $\langle n_{\text{ch}} \rangle$ in the target region of the Breit frame in bins of M_{eff}. Shown in the upper plot is the average correction factor for detector effects, $\langle C_1 \rangle$ from equation 8.5. Shown in the bottom plot is the correction factor, C_2 from equation 8.6, for the hadrons with $p_T < 150\,\text{MeV}$. The M_{eff} bin ranges are given in section 6.6.1.

Figure B.4: Bin-by-bin correction factors for $\langle n_{\mathrm{ch}} \rangle$ in the current region of the Breit frame in bins of $2 \cdot E_{\mathrm{Breit}}^{\mathrm{current}}$. Shown in the upper plot is the average correction factor for detector effects, $\langle C_1 \rangle$ from equation 8.5. Shown in the bottom plot is the correction factor, C_2 from equation 8.6, for the hadrons with $p_T < 150\,\mathrm{MeV}$. The $2 \cdot E_{\mathrm{Breit}}^{\mathrm{current}}$ bin ranges are given in section 6.6.1.

238

Figure B.5: Bin-by-bin correction factors for $\langle n_{ch} \rangle$ in the photon region of the Breit frame in bins of W. Shown in the upper plot is the average correction factor for detector effects, $\langle C_1 \rangle$ from equation 8.5. Shown in the bottom plot is the correction factor, C_2 from equation 8.6, for the hadrons with $p_T < 150\,\text{MeV}$. The W bin ranges are given in section 6.6.1.
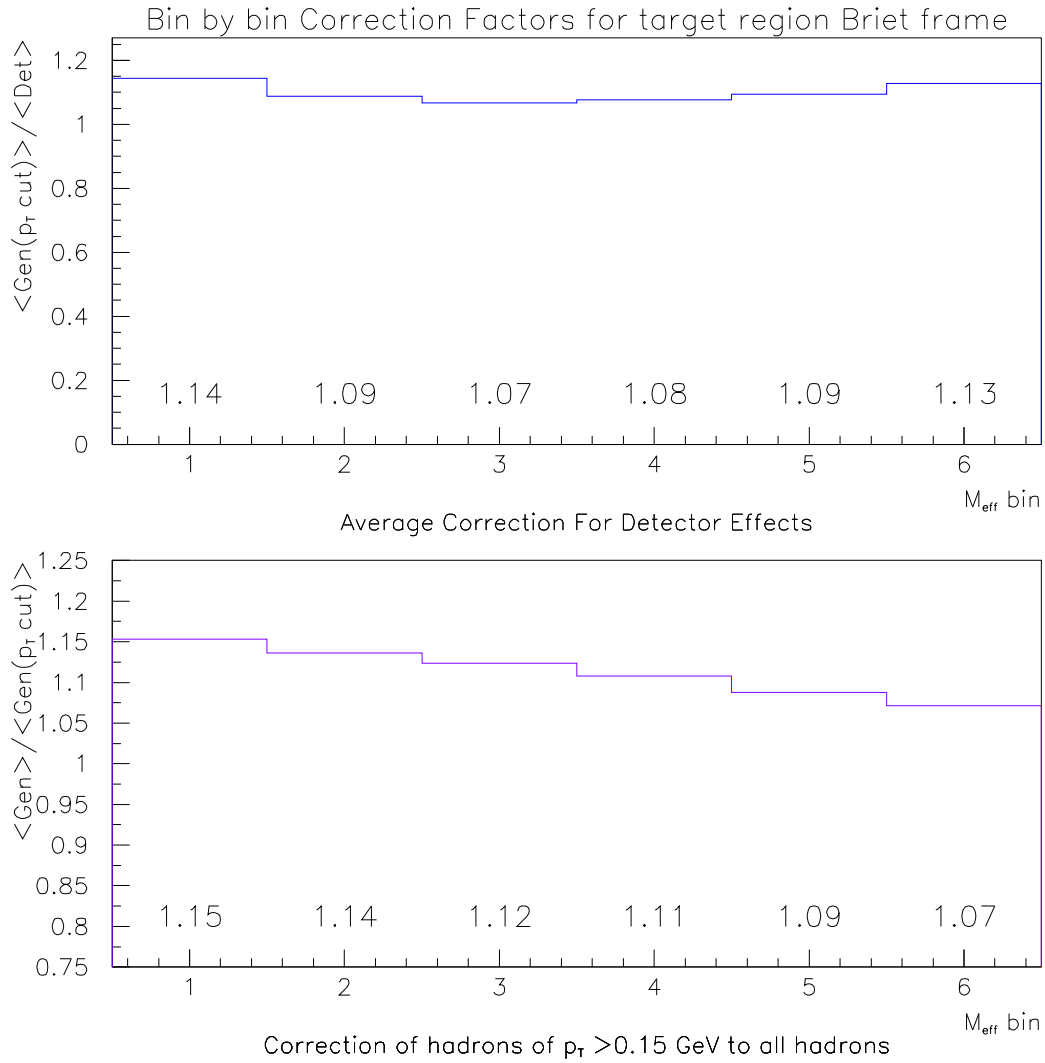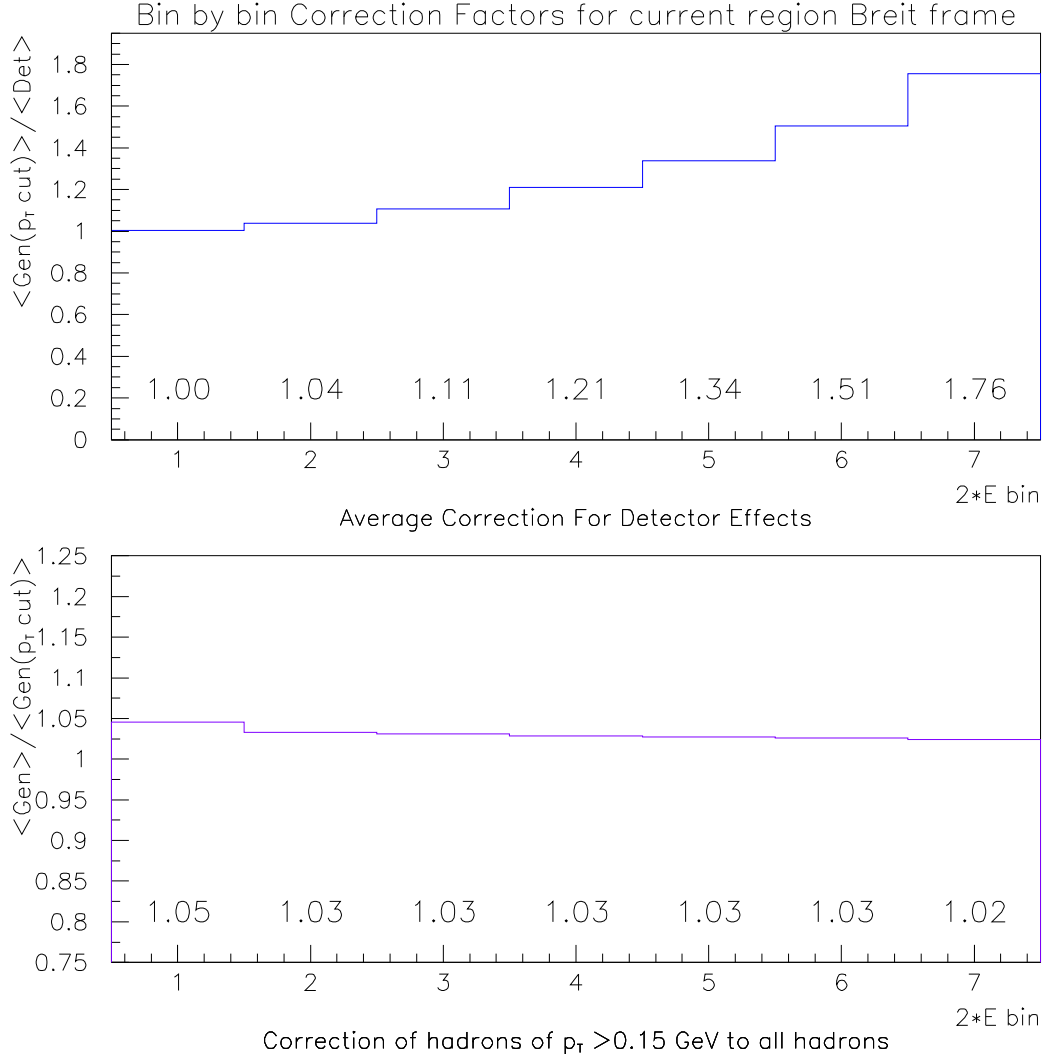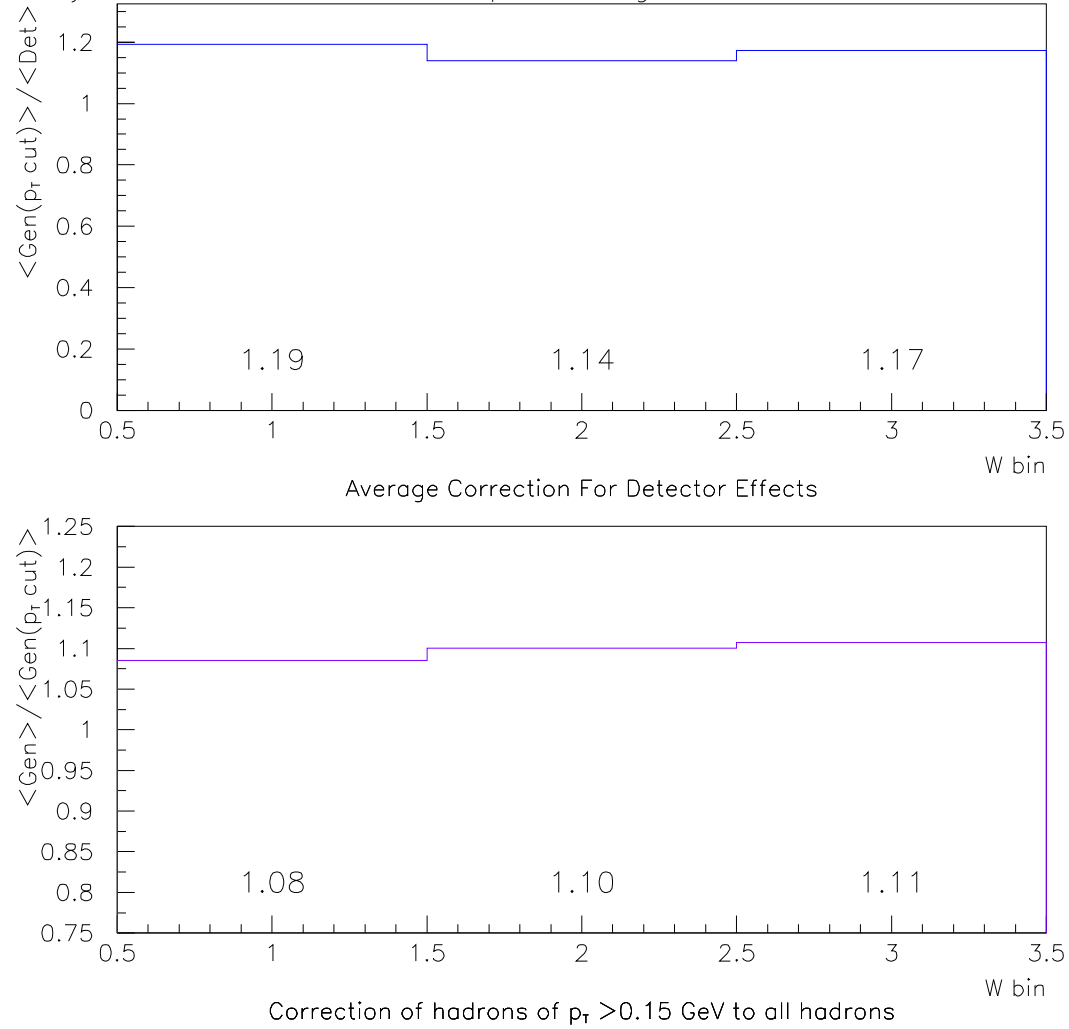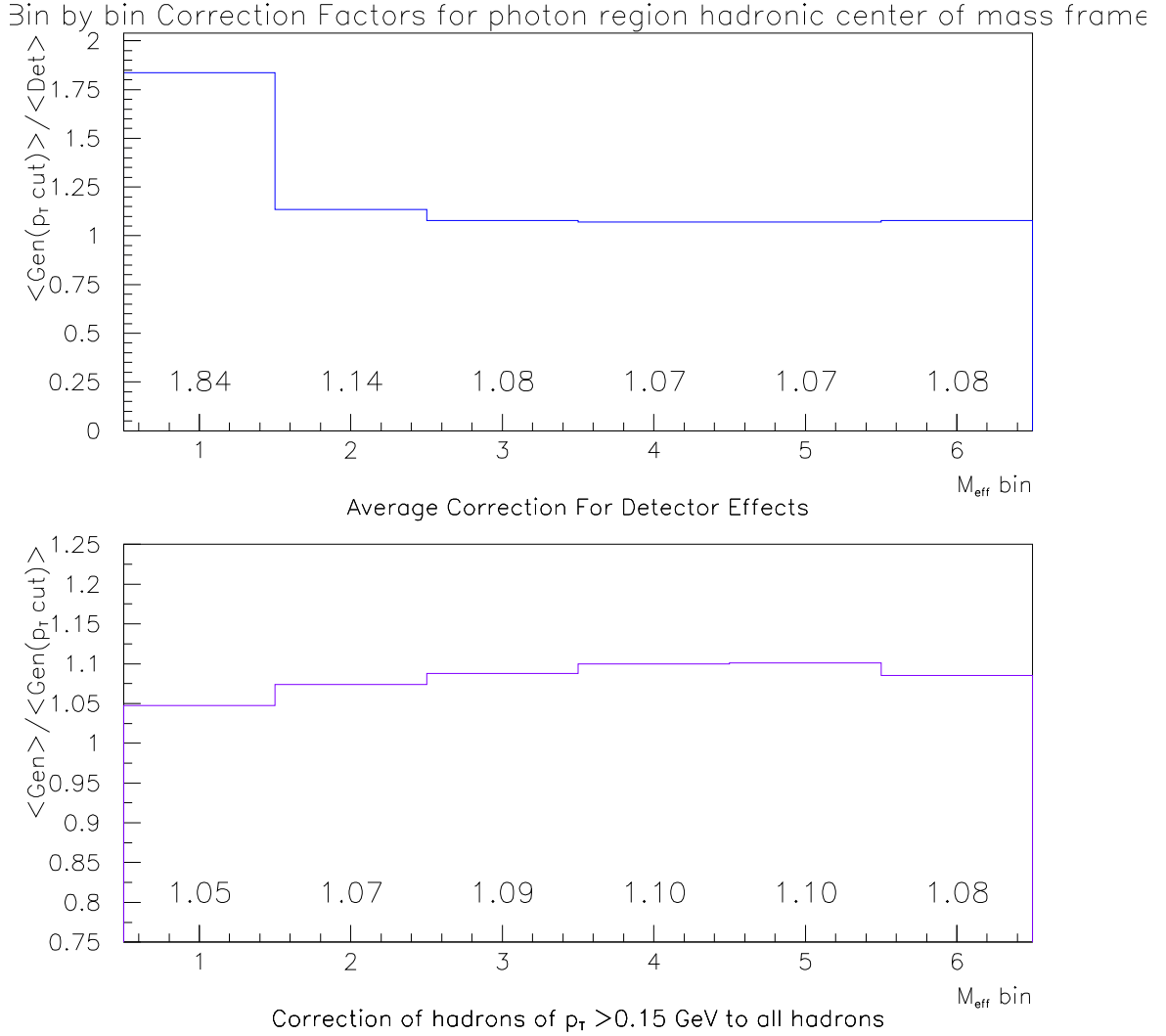
Figure B.6: Bin-by-bin correction factors for $\langle n_{\mathrm{ch}} \rangle$ in the photon region of the Breit frame in bins of M_{eff}. Shown in the upper plot is the average correction factor for detector effects, $\langle C_1 \rangle$ from equation 8.5. Shown in the bottom plot is the correction factor, C_2 from equation 8.6, for the hadrons with $p_T < 150\,\mathrm{MeV}$. The M_{eff} bin ranges are given in section 6.6.1.

Bibliography

[1] S.L. Glashow, Nucl. Phys. **22**, 579 (1961);
A. Salam, *Elementary Particle Physics.* (1968). Reprinted in Gauge Theory of Weak and Electromagnetic Interactions, C.H. Lai, ed.(Singapore: World Scientific, 1981);
S. Weinberg, Phys. Rev. Lett. **19**, 1264 (1967).

[2] F. Halzen and A.D. Martin, *Quarks and Leptons: An Introductory Course in Modern Particle Physics.* John Wiley & Sons, Inc, 1984;
D. Griffiths, *Introduction to elementary particles.* John Wiley & Sons, Inc., 1987.

[3] Taylor, Richard E., Rev. Mod. Phys. **63**, 573 (1991).

[4] Friedman, Jerome I., Rev. Mod. Phys. **63**, 615 (1991).

[5] M. Gell-Mann, Phys. Lett. **8**, 214 (1964);
Zweig, G. CERN-TH-412.

[6] Gell-Mann, Murray, Phys. Rev. **125**, 1067 (1962);
Ne'eman, Y., Nucl. Phys. **26**, 222 (1961).

[7] R.P. Feynman, Phys. Rev. Lett. **23**, 1415 (1969).

[8] J.D. Bjorken, Phys. Rev. **179**, 1547 (1969).

[9] Kendall, Henry W., Rev. Mod. Phys. **63**, 597 (1991).

[10] T. Eichten et al., Phys. Lett. **B 46**, 274 (1973).

[11] Martin, Alan D. Lectures given at 21st International Meeting on Fundamental Physics: Physics at HERA, Madrid, Spain, 9-15 May 1993.

[12] Brandelik, R. and others, Phys. Lett. **B86**, 243 (1979).

[13] H1 Coll., S. Aid et al., Nucl. Phys. **B 470**, 3 (1996).

[14] De Wolf, E. A. and Dremin, I. M. and Kittel, W., Phys. Rept. **270**, 1 (1996).

[15] B. Levtchenko, *The Breit System* (unpublished). ZEUS-94-099, 1994.

[16] Charchula, K., J. Phys. **G19**, 1587 (1993).

[17] MARK I Coll., V. Luth et al., Phys. Lett. **B 70**, 120 (1977);
JADE Coll., W. Bartel et al., Z. Phys. **C 20**, 187 (1983);
PLUTO Coll., Ch. Berger et al., Phys. Lett. **B 95**, 313 (1980);
TASSO Coll., W. Braunschweig et al., Z. Phys. **C 45**, 193 (1989).

[18] Aleph Coll., D. Decamp et al., Phys. Lett. **B 273**, 181 (1991);
Aleph Coll., D. Buskulic et al., Z. Phys. **C 73**, 409 (1997);
Delphi Coll., P. Abreu et al., Z. Phys. **C 50** (1991);
Delphi Coll., P. Abreu et al., Phys. Lett. **B 372**, 172 (1996);
Delphi Coll., P. Abreu et al., Phys. Lett. **B 416**, 233 (1998);
Delphi Coll., P. Abreu et al., Eur. Phys. J. **C 18**, 203 (2000);
L3 Coll., P. Achard et al., Phys. Lett. **B 577**, 109 (2003);
L3 Coll., M. Acciarri et al., Phys. Lett. **B 371**, 137 (1996);
L3 Coll., M. Acciarri et al., Phys. Lett. **B 404**, 390 (1997);
L3 Coll., M. Acciarri et al., Phys. Lett. **B 444**, 569 (1998);
Opal Coll., P. D. Acton et al., Z. Phys. **C 35**, 539 (1991);
Opal Coll., G. Alexander et al., Z. Phys. **C 72**, 191 (1996);
Opal Coll., K. Ackerstaff, Z. Phys. **C 75**, 193 (1997);
Opal Coll., G. Abbiendi et al., Eur. Phys. J. **C 16**, 185 (1999).

[19] PLUTO Coll., Ch. Berger et al., Phys. Lett. **B 95**, 313 (1980).

[20] Aleph Coll., D. Decamp et al., Phys. Lett. **B 273**, 181 (1991).

[21] Delphi Coll., P. Abreu et al., Z. Phys. **C 50** (1991).

[22] JADE Coll., W. Bartel et al., Z. Phys. **C 20**, 187 (1983).

[23] Thome, W. and others, Nucl. Phys. **B129**, 365 (1977).

[24] M. Basile et al., Nuovo Cimento **65A N3**, 293 (1981).

[25] M. Basile et al., Phys. Lett. **B 92**, 367 (1980);
M. Basile et al., Phys. Lett. **B 95**, 311 (1980);
M. Basile et al., Nuovo Cimento **A 67**, 244 (1982);
M. Basile et al., Lettere al Nuovo Cimento 41 **N. 9**, 293 (1984).

[26] ZEUS Coll., J. Breitweg et al., Eur. Phys. J. **C 11**, 251 (1999).

[27] L. Shcheglova, A. Solomin, S. Zotkin, *Multiplicity distribution in DIS at HERA* (unpublished). ZEUS-01-50, 2001.

[28] Aid, S. and others, Z. Phys. **C72**, 573 (1996).

[29] ZEUS Coll., U. Holm (ed.), *The ZEUS Detector. Status Report* (unpublished), DESY (1993), available on `http://www-zeus.desy.de/bluebook/bluebook.html`.

[30] Richard Wigmans, Ann. Rev. Nucl. Part. Sci. **41**, 133 (1991).

[31] M. Derrick et al., Nucl. Inst. Meth. **A 309**, 77 (1991);
A. Andresen et al., Nucl. Inst. Meth. **A 309**, 101 (1991);
A. Caldwell et al., Nucl. Inst. Meth. **A 321**, 356 (1992);
A. Bernstein et al., Nucl. Inst. Meth. **A 336**, 23 (1993).

[32] E. Bernardi, J. Engelen, R. van Stad, H. Tiecke, *Results on the Energy Resolution of a Test Calorimeter for ZEUS* (unpublished). ZEUS-87-039, 1987;
R. Klanner, Nucl. Inst. Meth. **A 265**, 200 (1988);
ZEUS Coll., Calorimeter group, G. d'Agostini et al., Nucl. Inst. Meth. **A 274**, 134 (1989).

[33] N. Harnew et al., Nucl. Inst. Meth. **A 279**, 290 (1989);
B. Foster et al., Nucl. Phys. Proc. Suppl. **B 32**, 181 (1993);
B. Foster et al., Nucl. Inst. Meth. **A 338**, 254 (1994).

[34] R. Hall-Wilton, N. McCubbin, P. Nylander, M. Sutton, M. Wing, *The CTD Tracking Resolution* (unpublished). ZEUS-99-024, 1999.

[35] W.H. Smith et al., Nucl. Inst. Meth. **A 355**, 278 (1995).

[36] G.P. Heath et al., Nucl. Inst. Meth. **A 315**, 431 (1992).

[37] H. Boterenbrood et al., Nucl. Inst. Meth. **A 332**, 263 (1993).

[38] H. Bethe and W. Heitler, Proc. Roy. Soc. Lond. **A146**, 83 (1934).

[39] D. Kisielewska et al., Nukleonika **31**, 205 (1986). Also in Report DESY-HERA-85-25.

[40] I. Ambats et al., Nucl. Inst. Meth. **A 368**, 364 (1996).

[41] G. F. Hartner, *VCTRAK Briefing: Program and Math* (unpublished). Zeus-98-058, internal ZEUS-note, 1998.

[42] A. Savin, *Study of Calorimeter Noise in the 1996 Data* (unpublished). ZEUS-98-007.

[43] D. Chapin, *A Measurement of Dijet Production in Neutral Current Deep Inelastic Scattering with ZEUS at HERA.* Ph.D. Thesis, Univeristy of Wisconsin, Madison, 2001. Unpublished.

[44] N. Tuning, *ZUFOs: Hadronic Final State Reconstruction with Calorimeter, Tracking and Backsplash Correction* (unpublished). ZEUS-Note-01-021, 2001.

[45] H. Abramowicz, A. Caldwell and R. Sinkus, Nucl. Inst. Meth. **A 365**, 508 (1995); R. Sinkus and T. Voss, Nucl. Inst. Meth. **A 391**, 360 (1997).

[46] M. Wodarczyk, *Measurement of the F_2 Structure Function of the Proton at HERA from 1996 and 1997 ZEUS Data.* Ph.D. Thesis, University of Wisconsin, 1999.

[47] F. Jacquet and A. Blondel, *Proc. the Study of an eP Facility for Europe*, U. Amaldi (ed.), p. 391. (1979). Also in preprint DESY 79-48.

[48] S. Bentvelsen, J. Engelen and P. Kooijman, *Proc. Workshop on Physics at HERA*, W. Buchmüller and G. Ingelman (eds.), Vol. 1, p. 23. Hamburg, Germany, DESY (1992).

[49] Collins, John C. and Soper, Davison E. and Sterman, George, Nucl. Phys. **B308**, 833 (1988).

[50] J. C. Collins, D. E. Soper and G. Sterman, Nucl. Phys. **B 261**, 104 (1985).

[51] V.N. Gribov and L.N. Lipatov, Sov. J. Nucl. Phys. **15**, 438 (1972); L.N. Lipatov, Sov. J. Nucl. Phys. **20**, 94 (1975); Yu.L. Dokshitzer, JETP **46**, 641 (1977); G. Altarelli and G. Parisi, Nucl. Phys. **B 126**, 298 (1977).

[52] E.A. Kuraev, L.N. Lipatov and V.S. Fadin, JETP **45**, 199 (1977); Ya.Ya. Balitskiĭ and L.N. Lipatov, Sov. J. Nucl. Phys. **28**, 822 (1978).

[53] H.L. Lai et al., Phys. Rev. **D 55**, 1280 (1997).

[54] ZEUS Coll., M. Derrick et al., Z. Phys. **C 65**, 379 (1994); H1 Coll., T. Ahmed et al., Nucl. Phys. **B 439**, 471 (1995).

[55] Sudakov, V. V., Sov. Phys. JETP **3**, 65 (1956).

[56] Gustafson, G., Phys. Lett. **B175**, 453 (1986); G. Gustafson and U. Pettersson, Nucl. Phys. **B 306**, 746 (1988); Andersson, Bo and Gustafson, Gosta and Lonnblad, Leif and Pettersson, Ulf, Z. Phys. **C43**, 625 (1989).

[57] B. Andersson et al., Phys. Rep. **97**, 31 (1983).

[58] Field, Richard D. and Wolfram, Stephen, Nucl. Phys. **B213**, 65 (1983); B. R. Webber, Nucl. Phys. **B 238**, 492 (1984).

[59] R.K. Ellis, W.J. Stirling and B.R. Webber, *QCD and Collider Physics*, Cambridge Monographs on Particle Physics, Nuclear Physics and Cosmology, Vol. 8. Cambridge University Press, 1996.

[60] R. Brun et al., GEANT3, Technical Report CERN-DD/EE/84-1, CERN, 1987.

[61] M. Wodarczyk, *Control Cards for the Zgana Simulation of the Calorimeter First Level Trigger (CFLT) and Calorimeter First Level Trigger Processor (CFLTP)* (unpublished). ZEUS-96-092, 1996.

[62] A. Kwiatkowski, H. Spiesberger and H.-J. Möhring, Comp. Phys. Comm. **69**, 155 (1992). Also in *Proc. Workshop Physics at HERA*, 1991, DESY, Hamburg;
H. Spiesberger, *An Event Generator for ep Interactions at HERA Including Radiative Processes (Version 4.6)*, 1996, available on http://www.desy.de/~hspiesb/heracles.html.

[63] H. Spiesberger, HERACLES *and* DJANGOH: *Event Generation for ep Interactions at HERA Including Radiative Processes*, 1998, available on http://www.desy.de/~hspiesb/djangoh.html;
K. Charchula, G.A. Schuler and H. Spiesberger, Comp. Phys. Comm. **81**, 381 (1994).

[64] L. Lönnblad, Comp. Phys. Comm. **71**, 15 (1992).

[65] G. Ingelman, A. Edin and J. Rathsman, Comp. Phys. Comm. **101**, 108 (1997).

[66] L. Lönnblad, *Workshop on Monte Carlo Generators for HERA Physics, Hamburg, Germany, April 1999*, p. 47. (1999). Also in preprint hep-ph/9908368.

[67] G. Marchesini et al., Comp. Phys. Comm. **67**, 465 (1992).

[68] C. Peter Fagerstroem, *Leading Neutron Production in DIS at HERA*. Ph.D. Thesis, University of Toronto, Report RAL-TH-97-004, 1999.

[69] ZEUS Coll., J. Breitweg et al., Phys. Lett. **B 414**, 428 (1997);
V.A. Noyes, *Measurement of Scaled Momentum Distributions in the Breit Frame at HERA Data Using the ZEUS Detector*. Ph.D. Thesis, Glasgow University, Report RAL-TH-97-004, 1997.

[70] K.H. Streng, T.F. Walsh, P.M. Zerwas, Z. Phys. **C 2**, 237 (1979).

[71] H1 Coll., S. Aid et al., Z. Phys. **C 72**, 573 (1996).

[72] Adams, M. R. and others, Z. Phys. **C76**, 441 (1997).

[73] Arneodo, M. and others, Z. Phys. **C35**, 335 (1987).

246

[74] Jones, G. T. and others, Z. Phys. **C54**, 45 (1992).

[75] ZEUS Coll., M. Derrick et al., Z. Phys. **C 67**, 93 (1995).

[76] H1 Coll., C. Adloff et al., Nucl. Phys. **B 504**, 3 (1997).

[77] S. Lammers and D. Chapin, *Jet Energy Scale Uncertainty* (unpublished). ZEUS-01-006, internal ZEUS-note, 2001.